Doctoral Dissertation
Doctoral Program in Civil and Environmental Engineering (33rd Cycle)

Performance of caisson foundations subjected to flood-induced scour

Andrea Ciancimino
* * * * * *

Supervisors
Prof. Sebastiano Foti
Prof. Ioannis Anastasopoulos
Prof. Alessandro Gajo

Doctoral Examination Committee:
Prof. Guido Musso, Politecnico di Torino (Italy)
Prof. Nikos Gerolymos, National Technical University of Athens (Greece)
Prof. Maria Rossella Massimino, Università degli Studi di Catania (Italy)
Prof. Federico Pisanò, Delft University of Technology (Netherlands)
Dr. Domenico Gaudio, Sapienza Università di Roma (Italy)

Politecnico di Torino
9th September 2021

I hereby declare that, the contents and organisation of this dissertation constitute my own original work and does not compromise in any way the rights of third parties, including those relating to the security of personal data.

…….....

Andrea Ciancimino

Turin, 9th September 2021

Abstract

This dissertation deals with the impact of foundation scour on the static and cyclic performance of bridge piers supported on caisson footings. Among the natural hazards, scouring is recognized as one of the main causes of bridge failure. The erosion of soil by flowing water changes the supporting conditions of the structure, deteriorating, in turn, its static and seismic performance. It is then of paramount importance to be able of quantifying its mechanical consequences on the response of the structure.

The first goal of this research was to investigate experimentally the two aspects of the problem: the hydraulic phenomenon, which concerns the erosive process around the foundation, and its mechanical consequences which affect the performance of the structure. A hybrid 2-step experimental methodology was developed to this end. The first step studies the hydraulic process of local scour around a bridge pier in *1g* using a Miniaturized Tidal Generator (MTG) recently developed at the ETH Zurich. The results of the experimental tests are used to produce a 3D-printed mould of the scour hole to recreate the actual shape of the scour hole in physical models suitable for testing in a geotechnical drum centrifuge. The mechanical consequences of scouring are then investigated in the second step through *Ng* models, thus achieving proper stress scaling.

The methodology was applied to study the performance of a caisson foundation supported on dense sand before and after local scour. The centrifuge tests consisted of vertical, lateral monotonic, and slow-cyclic pushover tests. In addition to the impact of local scour, the effects of general (uniform) scour were also investigated by removing a soil layer of constant thickness. The results of the vertical tests showed that local scour has a minor effect on the vertical bearing capacity. Conversely, the lateral response of the structure is significantly affected in terms of both moment capacity and monotonic (or cyclic) rocking stiffness. General scour is even more detrimental, leading to a massive reduction of the foundation capacity and a substantial increase in the rate of cyclic settlement accumulation.

The experimental tests provided relevant insights regarding the effects of scouring. Nevertheless, some aspects required further investigation. The subsequent step of the research was then to calibrate a numerical model able to reproduce the main features of the phenomenon. The constitutive model employed to simulate the stress-strain response of the soil is the Severn-Trent sand model. The constitutive

parameters were firstly calibrated on a set of element tests performed on the same sand used in the physical model tests. The numerical model was then validated against the results of the centrifuge tests. The comparison between the simulations and the centrifuge tests proved the ability of the numerical model in capturing the response of the foundation for a wide range of problems. The outcomes of the analyses have confirmed what was speculated from the experimental tests: local scour mainly affects the resistance exerted by the soil along the sides of the caisson, whereas general scour has also a major impact on the bearing capacity mechanism developing below the foundation.

The abovementioned conclusions are valid for the specific situation investigated through the experimental tests. A parametric study was then performed to extend the results of the analyses to more general conclusions. In particular, the study focused on the effects of scouring on the performance of bridge piers characterized by different vertical loads (and, thus, vertical safety factors FS_v) and slenderness ratios (i.e. the embedment-to-diameter ratio of the caisson d/D_f). The results revealed that the differences between local and general scour are less pronounced for lightly loaded foundations, where the sides resisting mechanism becomes more relevant. Conversely, the effects of local scour on the response of the foundation are less significant (but still relevant) for heavily loaded piers, where the bearing capacity mechanism is predominant. However, this holds as long as FS_v (computed for the unscoured reference situation) is larger than 3. For very heavily loaded piers, the asymmetry of the local scour hole leads to the accumulation of permanent rotations under just the dead load of the superstructure and, eventually, to its collapse. At the same time, the reduction of the vertical bearing capacity due to general scour leads to instability of the heavily loaded pier which may result, again, in the collapse of the structure. Interestingly, local scour has proven to strongly affect also the response of slender caisson foundations. With increasing d/D_f, the prevailing resisting mechanism under lateral loadings becomes the lateral mechanism mobilized along the sides of the caisson. The soil thrusts substantially decrease due to scouring, even if the scour depth is relatively small compared to the embedment depth of the footing. As a consequence, the entire moment capacity of the caisson is severely reduced.

Overall, the research shows that the effects of local scour differ substantially from those of general scour, recalling attention to the common simplification of ignoring the geometry of the scour hole. Realistic modelling of the physical phenomenon should therefore link the hydraulic scenario which leads to foundation scour to its mechanical consequences on the performance of the structure.

Table of Contents

List of Figures

List of Tables

Notation

$\boldsymbol{\alpha}$	unit vector defining the position of the yield surface in the normalized stress space
α	constitutive parameter of the Severn-Trent model controlling the exponent of the hyperbolic stiffness relationship
a	width of the pier
A	multiplier in flow rule of the Severn-Trent model
$A_{\max}$	maximum output amplitude measured by the accelerometer in the RC tests
A_c	cross-sectional area of the sample
A_G	calibration parameter of the Hardin and Richart (1963) equation for the small-strain shear modulus
β	distance of $\bar{\boldsymbol{\sigma}}$ from its conjugate stress $\bar{\boldsymbol{\sigma}}_c$, equal to $\mathbf{Q}\cdot\left(\bar{\boldsymbol{\sigma}}_c-\bar{\boldsymbol{\sigma}}\right)$
$\beta_{\max}$	maximum value that β can assume, equal to $\left(1-R\right)\mathbf{Q}\cdot\left(\hat{\bar{\boldsymbol{\sigma}}}_c-\bar{\boldsymbol{\sigma}}_c\right)$
B	Skempton B-parameter
B	constitutive parameter of the Severn-Trent model controlling hyperbolic stiffness relationship
B_{eq}, L_{eq}	equivalent dimensions of the foundation for which the vertical loading is centred
$\mathbf{B}$	second-order, positive-definite fabric tensor
$\mathbf{B}_0$	initial fabric tensor
c_v	consolidation coefficient
C_c	curvature coefficient
C_u	uniformity coefficient
CSL	Critical State Line
δ_{n+1}	logarithmic decrement between two successive cycles

δu_p	incremental horizontal translation of the caisson
$\delta\theta_p$	incremental horizontal rotation of the caisson
d	embedment depth
d_{10}	grain size corresponding to a passing percentage of 10%
d_{30}	grain size corresponding to a passing percentage of 30%
d_{50}	mean grain size, corresponding to a passing percentage of 50%
d_{60}	grain size corresponding to a passing percentage of 60%
$d_{\max}$, $d_{\min}$	maximum and minimum grain size
d_s	average scour depth
$d_{s,\max}$	maximum local scour depth
$d_{s,\max}\left(f_{cl}=0\right)$	maximum local scour depth at complex piers neglecting the shielding effect
$d_{s,c}$, $d_{s,pc}$, $d_{s,pg}$	single components of the local scour depth (Arneson et al., 2012)
D	damping ratio
D_f	diameter of the foundation
D_0	small-strain damping ratio
D_e	equivalent diameter of the complex pier (after Coleman, 2005)
D_p	diameter of the pier
D_{pc}	diameter of the pile-cap or caisson foundation
D_{pg}	equivalent diameter of the pile group
D_R	relative density
D_S	diameter of the sample
ε_{ax}	axial strain
$\dot{\varepsilon}_{ax}$	axial loading rate
ε_{vol}	volumetric strain
ε_s	shear strain in a triaxial test
$\boldsymbol{\varepsilon}^p$	plastic volumetric strain tensor
$\dot{\boldsymbol{\varepsilon}}^p$	plastic strain rate tensor
e	void ratio
e_0	initial void ratio
e_{CS}	void ratio at critical

$e_{\max}$, $e_{\min}$	maximum and minimum void ratio
e_n	net eccentricity
E_a	aluminium Young's modulus
E_m	Young's modulus of the membrane
E_R	constitutive parameter of the Severn-Trent model defining the fraction of G_0 used in computations
E_s	steel Young's modulus
φ'_{CS}	Critical State friction angle
φ'_{peak}	peak friction angle
$\varphi\left(\boldsymbol{\varepsilon}^e, \boldsymbol{\varepsilon}^p\right)$	free-energy density function
f	loading frequency
f_0	first torsional resonance frequency
f_{cl}	extension length of the pile-cap (or the caisson foundation) to the diameter of the column
$\overline{f}\left(\overline{\boldsymbol{\sigma}}, \boldsymbol{\alpha}\right)$	yield surface of the Severn-Trent model in the normalized plane
$F\left(e\right)$	void ratio function
Fr	Froude number, equal to $\overline{v}/\sqrt{g \cdot y}$.
FS_v	purely vertical safety factor
$\overline{F}\left(\overline{\boldsymbol{\sigma}}\right)$	strength surface of the Severn-Trent model in the normalized plane
γ	shear strain
γ_c	cyclic shear strain amplitude
$\gamma_{\max}$	maximum shear strain
γ'	soil unit weight under buoyancy equals to $g(\rho_s - \rho_w)$
γ_{tl}	linear cyclic threshold shear strain
γ_{tv}	volumetric cyclic threshold shear strain
γ_w	water unit weight
γ , η , ζ , λ	constitutive parameters of the Severn-Trent model defining the elastic behaviour
g	gravitational acceleration
G_0	small-strain shear modulus
G_S	secant shear modulus
G_s	specific Gravity of the grains

h	height of the structure, from the top of the footing to the mass centre of the deck
h_{act}	distance between the actuator and the bottom of the footing
h_G	height of the mass centre of the structure from the bottom of the footing
h_L	distance between the horizontal lasers
$h_{t,i}$	height of the column of water in the *i-th* pump-tank
H	horizontal load
H_{act}	horizontal load applied by the actuator
H_s	height of the sample
$\mathbf{I}$	second-order unity tensor
k	constitutive parameter of the Severn-Trent model defining the link between changes in state parameter and current size of the yield surface
k_d	state parameter contribution in the flow rule of the Severn-Trent model
K_1, K_2, K_3	correction factors of the scour depth for shape, angle of attack of the water flow and bed transport conditions (after Richardson and Davis, 2001)
K_4	correction factors of the scour depth for the armoring effect (after Richardson and Davis, 2001)
K_{yb}	flow-depth pier size factor (after Melville, 1997)
K_I	flow intensity factor (after Melville, 1997)
K_D, K_S, K_θ, K_G	correction factors for sediment particle size, foundation shape, foundation alignment, and channel geometry (after Melville, 1997)
K_h	correction factor for the shielding effect (after Arneson et al., 2012)
K_W	correction factor of the scour depth for wide piers in shallow flows (after Johnson and Torrico, 1994)
K_P	passive thrust coefficient
$K_{r,c}$	secant cyclic rocking stiffness
$K_{r,m}$	secant monotonic rocking stiffness
$K_{r,m}(\theta = 0)$	small-strain rocking stiffness
K_v	tangent vertical stiffness of the footing
λ	slope of the CSL in the volumetric plane
μ	interface friction coefficient

m	constitutive parameter of the Severn-Trent model controlling the deviatoric section of the yield surface
m_1	mass of the deck
m_2	mass of the column
m_3	mass of the footing
M	rotational moment
M_{CS}	slope of the CSL in the $q-p$ plane, equal to $\left(6\sin\varphi'_{CS}\right)/\left(3-\sin\varphi'_{CS}\right)$
M_{ult}	ultimate moment capacity of the structure
$M_{ult}^{\exp}$	ultimate moment capacity of the structure as obtained from the centrifuge tests
M_{ult}^{num}	ultimate moment capacity of the structure as obtained from the numerical simulations
M_{base}	moment exerted by the resisting mechanism developing below the base of the foundation
M_{sides}	moment exerted by the resisting mechanism developing along the sidewall of the foundation
$\Delta M\left(\delta\right)$	second-order moment
MRD	Modulus Reduction and Damping curves
M_{CS}	stress ratio at critical
M_{peak}	stress ratio at peak
M_s	dry mass of the sample
ν	Poisson's ratio
n_G	exponent of the confining pressure of the Hardin and Richart (1963) equation for the small-strain shear modulus
N	centrifugal acceleration level
N_γ, N_c, N_q	bearing capacity factors
NCL	Normal Consolidation Line
p	mean total stress
p_{atm}	atmospheric pressure
p'	mean effective stress
p'_0	initial mean effective stress
p'_{CS}	mean effective stress at critical
p'_{peak}	mean effective stress at peak
$P-\delta$	second-order effects

PI	Plasticity Index
PSD	Particle Size Distribution
$\mathbf{P}$	plastic flow direction
q	deviatoric stress
$q_{\lim}$	bearing capacity of the foundation according to Brinch Hansen (1970)
q_{CS}	Critical State deviatoric stress
q_{peak}	peak deviatoric stress
ρ	soil density
$\rho_{\min}$	minimum density of the dry soil
ρ_w	water density
ρ_s	density of the soil grains
θ_s	rotation of the sample in a RC test
θ_σ	Lode's angle
θ	rotation of the structure
θ_c	cyclic rotational amplitude
θ_{ult}	ultimate rotation angle at incipient overturning of the structure
$\bar{Q}$	mean flow rate
$\mathbf{Q}$	gradient of the yield function: $\partial f / \partial \boldsymbol{\sigma}$
r	ratio of sizes of the strength surface and the critical-state surface, equal to $1 - k\Psi$
r_M	moment overstrength ratio defined as the increase in the cyclic moment capacity divided by the monotonic ultimate moment
$R*$	Grains Reynolds' number, equal to $U_c \cdot d / \upsilon$
RC	Resonant Column
R	size of the yield surface respect to the size of the strength surface
$s_{\gamma,c,q}$, $i_{\gamma,c,q}$, $b_{\gamma,c,q}$, $g_{\gamma,c,q}$, $d_{\gamma,c,q}$	corrective factors, respectively, for the shape of the foundation, the inclination of the load, the inclination of the base, the slope of the soil, and the presence of soil along the sides of the foundation
σ_{ax}	axial stress
σ_g	geometric standard deviation of the particle size distribution
σ_{rad}	radial stress

$\boldsymbol{\sigma}$	*true* stress state
$\overline{\boldsymbol{\sigma}}$	*normalized* stress state
$\overline{\boldsymbol{\sigma}}_c$	conjugate normalized stress
σ'_h	horizontal effective stress
σ'_v	vertical effective stress
τ	shear stress
τ_c	cyclic shear stress amplitude
τ_{crit}	critical bed shear stress
t	time
t^*	normalized time equal to $t \cdot \overline{v}/D_c$
t_{90}	time to 90% of the first consolidation
t_m	thickness of the membrane
T	height of the pile-cap or the caisson foundation
T_α	fourth-order projection tensor
υ	kinematic viscosity of the fluid
u_{L1} , u_{L2}	horizontal displacements measured by lasers L_1 and L_2, respectively
u_{tot}	total displacement field
u_w	pore water pressure
U_c	critical flow velocity for entrainment of bed sediment
v	specific volume
v_{CS}	specific volume at critical
v_λ	intercept of the CSL in the volumetric plane
$\overline{v}$	mean flow velocity
V	vertical load
V_s	volume of the sample
V_S	small-strain shear wave velocity
V_{ult}	vertical bearing capacity of the footing
V_{ult}^{num}	vertical bearing capacity of the footing as obtained from the numerical simulations
V_{ult}^{exp}	vertical bearing capacity of the footing as obtained from the centrifuge test
V_{ult}^{BH}	vertical bearing capacity of the footing as obtained from the analytical solution of Brinch Hansen (1970)

V_w	total volume of water discharged in a time $\overline{t}$
w	settlement
w_c	settlement per cycle
$\overline{w}_c$	average settlement per cycle within one package of 10 cycles at constant loading amplitude
w_{L3}	vertical displacements measured by laser L_3
w_{ult}	ultimate settlement associated with the vertical bearing capacity of the footing
$\xi_{r,h}$	hysteretic rocking damping ratio
ψ_{peak}	dilatancy angle at peak
Ψ	state parameter
y	water-flow depth
$\overline{y}_0$	mean flow depth
Y	foundation top elevation
W_1	weight of the deck
W_2	weight the column
W_3 '	net weight of the footing
W_{tot}	total weight of the pier
z_n	peak Amplitude associated with the *n-th* cycle measured by the accelerometer in a RC test
z_p	depth to the rotation pole of the caisson

Chapter 1

Introduction

1.1 Motivation

The safety of infrastructures is strictly connected to the ability of highway bridges to withstand different hazards during their life cycles (Alampalli and Ettouney, 2008). Furthermore, the serviceability of transportation networks is also a key aspect for emergency operations in the aftermaths of major natural events, such as floods and earthquakes. At the design stage of a bridge, the performance of its components have therefore to be carefully evaluated, from the *hydraulic*, *structural* and *geotechnical* points of view.

It is also essential ensuring the stability and functionality of the structure over time. The performance of the bridge components indeed evolves during its service life due to both structural damage and variation of the supporting conditions. As a consequence, the static and seismic vulnerability of the entire structure can increase over time, leading, eventually, to its collapse.

Several studies highlight that the majority of bridge failures usually takes place as a consequence of flood events (Wardhana and Hadipriono, 2003; Imhof, 2004). The presence of a structure in a channel represents an obstacle for the uniform water flow, inducing the development of turbulences around piers and abutments. Such vortices increase the erosive power of the flow, which may locally exceed the shear strength of the riverbed material gaining the energy to excavate and carry out the soil. This phenomenon, usually termed as *local scour* at bridges, keeps going on until the local equilibrium is re-established. In addition to local scour, aggradation and degradation phenomena, together with the reduction of the channel section, may result in a global erosion of the riverbed usually identified as *general scour* (Ettema, 1980; Melville and Coleman, 2000; Richardson and Davis, 2001).

The riverbed erosion progressively modifies the mechanical behaviour of the foundations. Its effect is mainly related to the soil erosion, in terms of loss of material and change of geometry, but it also changes the stress state of the remaining

soil (e.g., Lin et al., 2010; Lin et al., 2014a; Qi et al., 2016b; Liang et al., 2017). The deterioration of the supporting conditions may affect the overall performance of the bridge, especially in the presence of other natural hazards as earthquakes (e.g. Alipour and Shafei, 2012; Wang et al., 2012; Banerjee and Ganesh Prasad, 2013). Consequently, the seismic vulnerability of scoured structures has to be re-assessed in the aftermaths of major floods.

Predicting the time-evolution of the supporting conditions *a priori* is a nontrivial task, which involves the definition of a design flood scenario and the evaluation of its hydraulic consequences, in terms of scour depth and shape of the scour hole. Monitoring is thus crucial to guarantee the safety and serviceability of infrastructures. Traditional investigation techniques typically provide useful information about the actual ground surface elevation, but deeper knowledge on the influence of scouring is required to evaluate the vulnerability of the bridge *a posteriori*.

During the last decade or so, vibration-based monitoring techniques have been proposed to study the evolution with time of the dynamic response of bridges due to the progress of scouring (e.g., Foti and Sabia, 2010; Briaud et al., 2011; Prendergast and Gavin, 2014; Bao and Liu, 2017). The results have proven that the erosive process affects the static and seismic performance of the soil-structure system, leading to a significant reduction of foundation stiffness. The dynamic parameters may therefore be used to infer the scour depth evolution.

The detrimental impact of scouring is nowadays well-recognized in the scientific literature (e.g., Breusers and Raudkivi, 1991; Melville and Coleman, 2000; Sheppard and Renna, 2005). Despite that, the localized loss of support is still recognized as one of the main causes of bridge failure (Wardhana and Hadipriono, 2003; Imhof, 2004). This is partly due to the budget constraints which often prevent a simultaneous implementation of risk mitigation measures, leading to an increase of the bridge vulnerability to subsequent extreme events (Macky, 1990). On the other side, there is still a lack of knowledge on the actual influence of scouring on the structural performance of bridge piers.

1.2 Research Objectives

Local scour phenomena have been extensively investigated from the hydraulic point of view (e.g., Breusers and Raudkivi, 1991; Melville and Coleman, 2000; Sheppard and Renna, 2005). Conversely, only a few experimental studies have focused on their mechanical consequences (e.g. Prendergast et al., 2013; Qi et al., 2016b; Chortis et al., 2020). In addition, some numerical studies have been devoted to evaluating the performance of bridge piers subjected to foundation scour (e.g. Ganesh Prasad and Banerjee, 2013; Wang et al., 2014a; Klinga and Alipour, 2015).

In common practice, the two aspects of the problem are often investigated independently. Predictive equations and empirical methods are used to study the hydraulic problem with the purpose of estimating the maximum scour depth. The local scour hole is thus modelled (experimentally or numerically) in a crude manner: either by removing a constant thickness soil layer (without any distinction

between general and local scour) or by considering an idealized scour hole geometry. The simplified model of the scoured pier is then used to evaluate the performance of the structure.

Although this approach has the undeniable advantage to be easy to implement, it neglects the real geometry and asymmetry of the scour hole. Recent studies (Foti and Sabia, 2011; Liang et al., 2019) however suggest that the latter may have a significant effect on the mechanical response of the soil-structure system. The mechanical problem is a direct consequence of the hydraulic process and, therefore, the two aspects has to be examined together.

The present research fits within this framework, focusing on scour at bridge piers founded on caissons. Specifically, the study was developed in an attempt to answer the following main questions:

- Which are the main mechanisms affecting the performance of bridge piers subjected to flood-induced scour?
- Is it possible to accurately reproduce such mechanisms through a numerical model to predict the mechanical consequences of scouring?

The first issue was experimentally investigated through the development of a 2-step hybrid methodology. The methodology studies both aspects of the problem: the *hydraulic* phenomenon and its *mechanical* consequences. The first step reproduces the hydraulic process of local scour at bridge piers in 1*g* using a Miniaturized Tidal Generator recently developed at the ETH Zurich. The results of the hydraulic tests are then used to evaluate the impact of scouring on the performance of the pier in a geotechnical drum centrifuge, thus achieving proper stress scaling.

The centrifuge tests were then used to study the performance of the caisson foundation against vertical, lateral monotonic, and lateral slow-cyclic loadings before and after scouring. Although the research is mainly focused on local scour, the effects of general scour (i.e., erosion of a constant thickness soil layer) were also evaluated to reveal and quantify the differences between these two processes.

To address the second question, a numerical model of the prototype problem was developed by adopting an advanced constitutive model able to simulate the sand stress-strain behaviour for a wide range of problems. The model was firstly calibrated on an independent set of soil element tests. Subsequently, the results of the centrifuge tests were used for its validation. Finally, further numerical simulations were performed to study the effects of scouring on structures with different characteristics and subjected to different loading conditions.

1.3 Dissertation Outline

The dissertation starts with a discussion on the hydraulic process of scour at bridge piers and its mechanical consequences. In particular, Chapter 2 focuses on the genesis of the phenomenon, examining the main factors influencing the evolution of local scour around bridge piers. The most common methods for predicting the expected maximum scour depth are then introduced. Chapter 3 is devoted to the

impact of foundation scour on the mechanical response of the structure. The attention is firstly focused on the identification of the failure modes and the associated main features, which lead to the collapse of bridges due to scour. Experimental and numerical studies on the mechanical consequences of scouring are then presented, together with the approaches adopted in common practice to assess the vulnerability of scoured bridges.

Chapter 4 summarizes the properties of the sand used in the physical models, including basic index properties and stress-strain characteristics. Specifically, the sand behaviour is analyzed in the light of laboratory tests reported in the literature and new tests carried out within the framework of the present thesis.

Chapter 5 presents the physical model implemented to assess the changes induced by foundation scour on the performance of a prototype bridge pier. The experimental methodology is firstly introduced. The hydraulic 1*g* tests, which serve as a basis to study the mechanical problem, are then reported. Finally, the chapter presents the results of the centrifuge tests.

The second part of the study deals with the numerical simulations of the performance of scoured caisson foundations. Chapter 6 provides an overview of the advanced constitutive model adopted to simulate the sand stress-strain behaviour, along with the calibration procedure carried out to define the constitutive parameters. The validation of the numerical model is then presented in Chapter 7, which compares the results of the centrifuge tests with the predictions given by the simulations. The validated model is eventually used to carry out a parametric study on the performance of scoured caisson foundations. The simulations focused on the vertical safety factor and the slenderness ratio of the foundation, and the results are presented in Chapter 8.

Finally, Chapter 9 summarizes and discusses the main conclusions of the research, along with some indications on possible future studies on the topic.

Appendix A reports the approaches adopted in the common practice to estimate the capacity of caisson foundations.

Chapter 2

Scour at bridge piers

The construction of resilient infrastructures has always been a major task for civil engineers, either from a structural, a geotechnical or a hydraulic point of view. At the design stage of a bridge, it is of paramount importance to be able to evaluate its performance against both static and seismic actions. At the same time, it is also essential to ensure its stability and functionality over time.

Safety and serviceability of infrastructures are, in fact, strongly influenced by their ability to withstand different hazard demands. The performance of a bridge evolves during its life-cycle due to both the damaging of structural components and changing of the supporting conditions, increasing its static and seismic vulnerability. The latter frequently takes place when soil is eroded around bridge piers and abutments by flowing water. This phenomenon is usually identified as *scour at bridges.*

This chapter introduces the phenomenon of scour at bridges, focusing mainly on the hydraulic process itself. The discussion starts with the analysis of the dynamics and the main mechanisms governing the evolution of the phenomenon. Section 2.2 is devoted to an examination of the most important factors influencing the evolution of local scour around bridge piers. Subsequently, the most common methods for predicting the expected maximum scour depth are introduced, distinguishing between local scour at uniform or complex piers. The attention is specifically focused on local scour around circular piers supported on caisson foundations, which is the main topic of this thesis.

2.1 Basic concepts

The construction of a structure in a channel represents an obstacle for the river itself, inducing an alteration of the initial uniform pattern of the streamflow. As a consequence, turbulences develop around piers and abutments and the flow acquires a stronger erosive power which, in some cases, exceeds the shear strength capacity of the riverbed. If that is the case, the flow has the energy to excavate and carry away the material and scour takes place, in particular around the most prominent obstacles as the bridge piers and abutments.

To identify the different processes responsible for the riverbed erosion, the total scour at bridge crossings can be conveniently broken down into three components (Hoffmans and Verheij, 1997; Melville and Coleman, 2000): *long-term degradation of the riverbed*, *contraction scour*, and *local scour* (Figure 2.1).

Long-term streambed elevation changes are the result of aggradation and degradation phenomena, which occur either naturally in riverbeds or consequently to changes in the hydraulic parameters of the channel. Degradation usually occurs if the sediment load present in the flow is lower than the actual transport capacity. To reduce the longitudinal gradient of the channel, the riverbed upstream is progressively eroded until an approximate equilibrium is reached. The equilibrium condition can, however, be disturbed by human activities, triggering again the process.

Contraction scour is due to the reduction of the river cross-section as a result of the construction of the bridge. A constriction of the flow implies an increase in velocity and therefore in bed shear stress.

The third component, *local scour*, refers to the localized erosion around bridge piers and abutments, caused by the flood-induced vortices around their base. The alteration of the uniform flow field leads to a local increase of the flow velocity and, thus, to larger erosive forces in the proximity of the obstacles. As a result, a local lowering of the riverbed relative to the general level of the channel takes place around the structure.

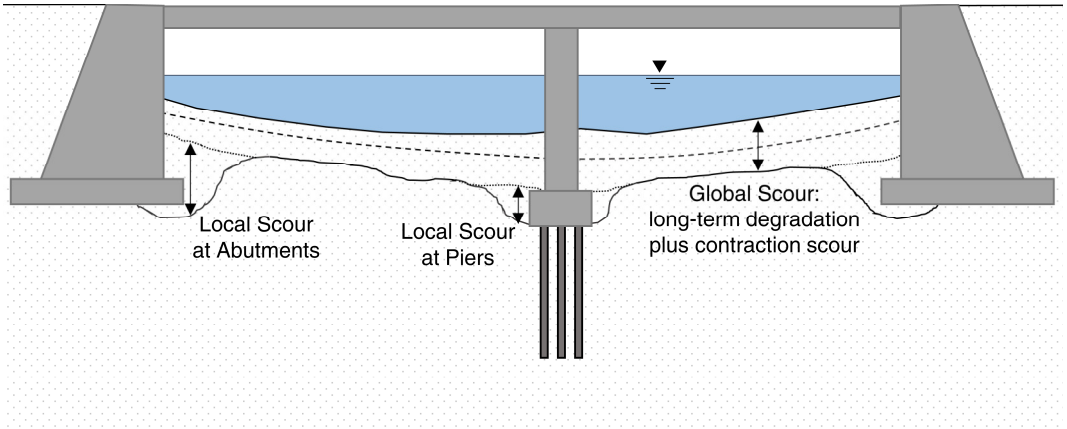

Figure 2.1: Main components constituting the total scour at bridges.

Total scour at bridge piers is the result of the three components, which may occur either simultaneously or independently according to the main features of the flow. Both of the first two components lead to a global lowering of the riverbed and are thus usually identified as *general* or *global scour*. Conversely, local scour causes the development of a very localized scour hole around bridge piers, which compromises the local supporting conditions of the structure (Figure 2.2).

Both global and local scour are usually quantified through the *maximum scour depth*, considered as a measure of the severity of the scour process in terms of exposure of the bridge foundation system. However, the effects of a global lowering of the riverbed on the mechanical response of a structure can significantly differ from a local deterioration of the supporting conditions.

2.2 Local scour at bridge piers

2.2.1 Hydraulic processes

Focusing on local scour around bridge piers, it is possible to identify the main features of the flow field responsible for the scour hole development. The system of vortices depends on the geometry of the pier and the characteristics of the flow, but it is usually composed of three main individual systems (Graf, 1998; Melville and Coleman, 2000; Ettema et al., 2011): (i) the *horse-shoe vortices* forming at the base of the pier; (ii) the *wake-vortex* system downstream of the pier; and (iii) the *surface rollers*. Figure 2.3 depicts the main complex flow field generated by the presence of a narrow cylindrical pier.

Figure 2.2: Effects of local scour around a bridge pier (from Sheppard and Renna, 2005).

The uniform flow, approaching the pier, is partially diverted around the pier, and partially deflected vertically. The upward flow is deflected towards the free surface, forming the surface rollers, while the downward vertical component is directed towards the riverbed.

The main responsible for local scour is precisely the vertical downward component which interacts with the riverbed, forming the horse-shoe vortices. The vortices intensify the local flow velocities, resulting in the local erosion of the soil adjacent to the upstream side of the pier (Melville and Coleman, 2000).

On the contrary, the wake-vortex system is generated by the interaction between the flow separated around the sides of the pier and the pier itself (Shen et al., 1969). The vortices are characterized by an almost vertical rotation axis and act somehow like a vacuum system that removes the streambed material and transport downstream the sediment (Melville and Coleman, 2000). This system is usually considered responsible for the development of scouring along the flanks and downstream to the pier. However, as the wake-vortices move away from the pier, they expand in diameter, dissipate and then break up, resulting in sediment deposition (Ettema et al., 2011).

The flow features previously described always exist in presence of an obstacle such as a bridge pier, but their relative importance can vary depending on the pier width a (being equal to the diameter of the pier for cylindrical piers), and on the flow depth, y. For shallow water flows, the vortex systems start to interact one each other, reducing their erosive capacity. In particular, reference is usually made to three categories of the pier flow field, namely: *narrow piers* ($y/a > 1.4$); *transitional piers* ($0.2 < y/a < 1.4$); and *wide piers* ($y/a < 0.2$) (Ettema et al., 2011).

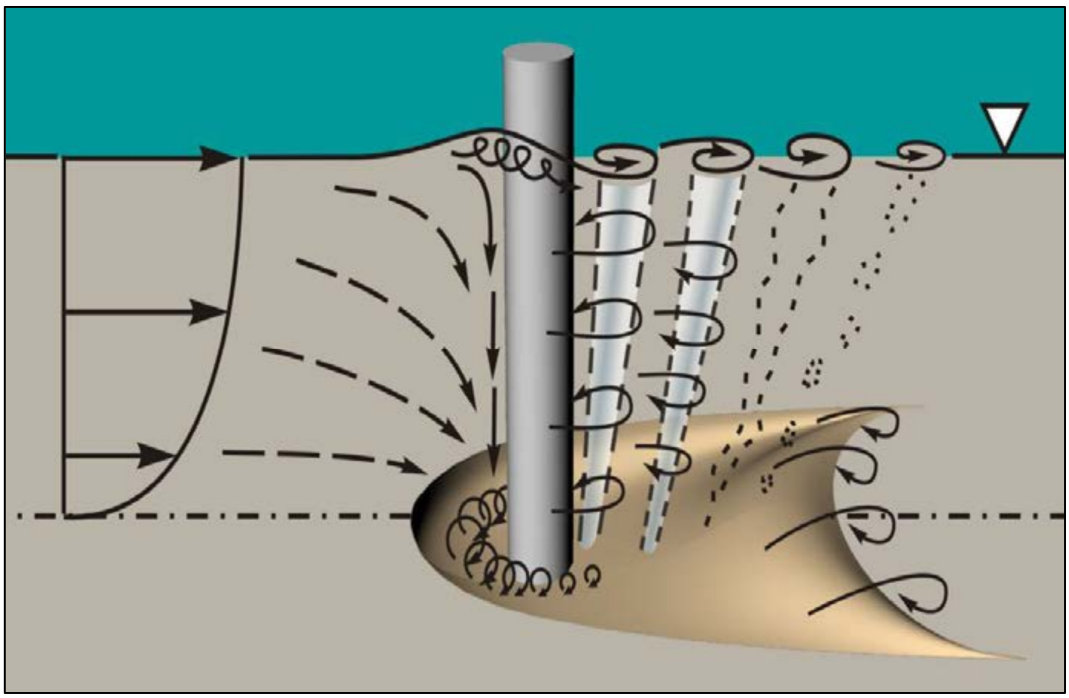

Figure 2.3: Localized erosion at a narrow cylindrical pier: main flow features forming the altered flow field (from Ettema et al., 2011).

At a narrow pier, the horse-shoe vortices assume the maximum relative importance, inducing a maximum scour depth typically at the upstream pier face. Conversely, scour induced by the wake-vortices is of secondary importance. As the width of the pier decreases, the downward flow approaching the pier tends mainly to flow laterally, and the vertical component becomes less significant. At a wide pier, the capacity of the horse-shoe vortices of eroding the bed material is then decreased, resulting in general in shallower scour holes which are deeper along the pier flank.

These trends, nowadays well-recognized by the scientific community, have been highlighted in the past by many studies, including Laursen (1963); Shen et al. (1969); Hancu (1971); Ettema (1980); Chiew (1984); Breusers and Raudkivi (1991).

2.2.2 Time scale

Time plays a crucial role in the development of scour around bridge piers. Quite generally, after that a scour process is triggered, it will keep going on until an equilibrium between the erosive capacity of the flow and the shear resistance of the bed material will be re-established (Melville and Coleman, 2000; Richardson and Davis, 2001).

In the particular situation of a constant, almost steady, water-flow the equilibrium is progressively attained through erosion of the flow boundary, as the scour depth increases (Melville and Chiew, 1999). Conversely, in reality, flood events of different magnitude can occur in sequence, preventing the equilibrium condition from being achieved (May et al., 2002). Consequently, it is important to study the time-scale of a scour process, to be able to properly identify the consequences of a specific hydraulic scenario, characterized by a flow of given features lasting for a finite time.

2.2.2.1 Transport conditions

Two different local scour regimes can be identified (e.g., Melville and Chiew, 1999; Melville and Coleman, 2000; Richardson and Davis, 2001): (a) *clear-water* when no sediments are transported by the water flow (or at most, when the soil is transported in suspension); and (b) *live-bed* scour, when sediments delivered by the river interact with the scour process. The clear-water regime takes place when the mean flow velocity is lower than the critical approach flow velocity for entrainment of bed sediment. Conversely, live-bed conditions are expected for flow velocities larger than U_c (Melville and Chiew, 1999).

Figure 2.4 depicts the typical time-evolution of the scour depth as a function of the flow velocity. Under clear-water conditions, the scour depth increases slowly until the equilibrium between the erosive capacity and the shear bed resistance is reached, corresponding to the equilibrium scour depth. The latter increases almost linearly with the flow velocity attaining its peak value at the threshold flow velocity.

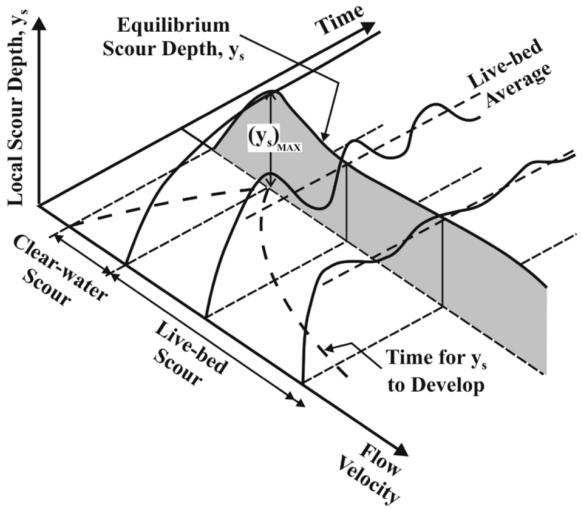

Figure 2.4: Time evolution of scour depth under clear-water or live-bed conditions (from Melville and Chiew, 1999)

As the velocity exceeds this threshold value, the live-bed regime is achieved and the interaction between the scour process and the transported sediments leads to a partial, cyclic, refilling of the scour hole. The scour depth thus oscillates around an equilibrium value, corresponding to a balance between the sediment supply and the eroded material. This equilibrium value initially decreases with the flow velocity, then increases again until a second peak value is reached, anyway smaller than the first one. The time necessary to reach the equilibrium condition increases rapidly with flow velocity under clear-water regime, while it decreases for velocities larger than U_c.

The findings here discussed have been experimentally observed and explained by many Authors in the past, including Shen et al. (1969); Breusers and Raudkivi (1991); Melville and Chiew (1999); Melville and Coleman (2000); Richardson and Davis (2001); May et al. (2002); Ettema et al. (2011); Arneson et al. (2012).

2.2.2.2 Critical flow velocity for entrainment of bed sediment

The definition of the threshold critical velocity for the incipient motion of granular material on a flat bed is a nontrivial task. In his pioneering study, Shields (1936) proposed his criterion to define the condition of incipient motion for uniform granular material. The Author defined an entrainment function, relating the nondimensional critical shear stress (also called Shield parameter) to the Reynolds grain number, R^*:

$$\frac{\tau_{crit}}{\gamma'_S d} = f\left(R^*\right) = f\left(\frac{U_c \cdot d}{\upsilon}\right) \tag{2.1}$$

where $\tau_{crit} = U_c^2 \cdot \rho_w$ is the critical bed shear stress (being ρ_w the water density), d is the sediment grain size, $\gamma'_S = g(\rho_s - \rho_w)$ is the submerged specific weight of grains (being g the gravitational acceleration and ρ_s the density of the grains), and υ is the kinematic viscosity of the fluid.

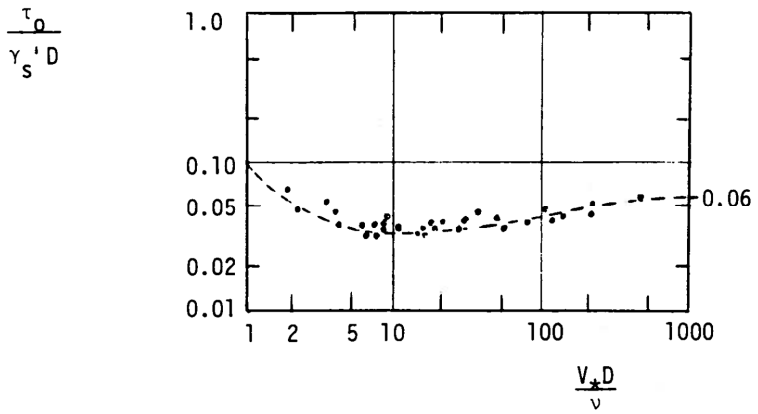

Figure 2.5: Shields diagram as reported by Neill (1968) (the notation "V∗" in the abscissa stands for "U_c").

The experimental data points, originally reported by the Author, were subsequently fitted by Rouse (1939), defining a family of curves usually quoted (Neill, 1968) as *Shields diagram* (Figure 2.5).

Since 1936, many studies have focused on the topic trying to extend the original study and adding more experimental observations (e.g., Liu, 1957; Liu, 1958; Yalin, 1972). Although the Shields' framework is actually well-accepted, many Authors in the past questioned his basic assumptions. A comprehensive historical account on Shields' work can be found in Kennedy (1995).

Nowadays, several equations exist to define the critical velocity, many of which are based on the Shields' framework (e.g., Hancu, 1971; Breusers et al., 1977; Jain, 1981). However, there are still some discrepancies among them. As further clarified in the next sections, U_c is a crucial parameter in evaluating the expected maximum scour depth. Consequently, care should be exercised in using these predictive equations.

Among the different possible approaches, two of the most quoted methods are the Neill's equation (1967) and the method proposed in the Hydraulic Engineering Circular Nr.18, HEC-18, of the Federal Highway Administration (Arneson et al., 2012). Both the methods are based on the Shields' framework and allow to predict the critical flow velocity U_c as a function of both the characteristics of the flow and the properties of the riverbed material. The following equation has been proposed by Neill in 1967:

$$U_c = \sqrt{2.5\left(G_S - 1\right) \cdot g \cdot d_{50}} \cdot \left(\frac{y}{d_{50}}\right)^{0.1} \tag{2.2}$$

where d_{50} is the mean grain size of the soil and G_S is the specific gravity of the grains. Alternatively, U_c can be computed according to the HEC-18 method (Arneson et al., 2012) through the following equation:

$$U_c = 6.19 \cdot y^{1/6} \cdot {d_{50}}^{1/3} \tag{2.3}$$

using the S.I. units.

2.2.2.3 Time evolution of the scour hole

As the scour process proceeds not only the scour depth increases, but also the geometry of the scour varies. Zanke (1978) identified four different phases in the evolution of local scour: (i) an *initial* phase, (ii) a *development* phase, (iii) a *stabilization* phase, and (iv) an *equilibrium* phase. The different stages of the process, subsequently clarified by Hoffmans and Verheij (1997), have been defined based on clear-water scour experiments from Breusers (1966) and Dietz and Wittke (1969).

The initial phase is characterized by the maximum erosive capacity. Scouring starts from the upstream side of the pier, where the eroded bed material is transported in suspension. Afterwards, during the development phase, a significant increase of the scour depth with time is observed. No significant changes are anyway observed in terms of the shape of the scour hole and the inclination of the upstream slope tends to remain constant. In the stabilization phase, the rate of increase of the maximum scour depth is considerably reduced. Conversely, the longitudinal dimension of the scour hole tends to increase, being higher the erosive capacity of the downstream flow. Finally, the equilibrium phase is achieved if the scour hole does no longer change (Hoffmans and Verheij, 1997).

2.2.2.4 Influence of cohesion on scour rate

The observations discussed up to this point refer mainly to local scour at piers on granular, non-cohesive, material. As a matter of fact, the vast majority of scour-prone bridges are founded on alluvial sediments, at least as regards the upper layers of the soil profile. Consequently, most of the studies focused on granular material, neglecting the effects of soil cohesion.

As a conservative approach, in the common practice, the maximum scour depth expected around bridge piers on cohesive soils is often estimated through the same usual approaches developed for alluvial bed materials (Ansari et al., 2002; Brandimarte et al., 2012).

Figure 2.6 depicts the local scour hole formed at a cylindrical pier founded either on sand or clay. Although the maximum scour depth appears to be on the same order of magnitude, some differences are observed in terms of shape. For clayey materials, the scour hole is less regular and reaches its maximum value around the piers flanks, where steeper slopes are observed with respect to scour holes on sandy materials (Ettema et al., 2011).

Besides these minor differences in terms of the shape of the scour hole, the bed material becomes relevant when the scour rate is considered: the additional resistance offered by the soil cohesion results in fact in a much slower progression of the scour process (Briaud et al., 1999b; Ansari et al., 2002; Brandimarte et al., 2006). While the maximum scour depth on alluvial material is attained after some hours, for piers on cohesive soils the scour process can last even several days, thus preventing the full development of the scour hole (Briaud et al., 1999b). As a consequence, scour on alluvial beds is, in general, considered the most critical situation.

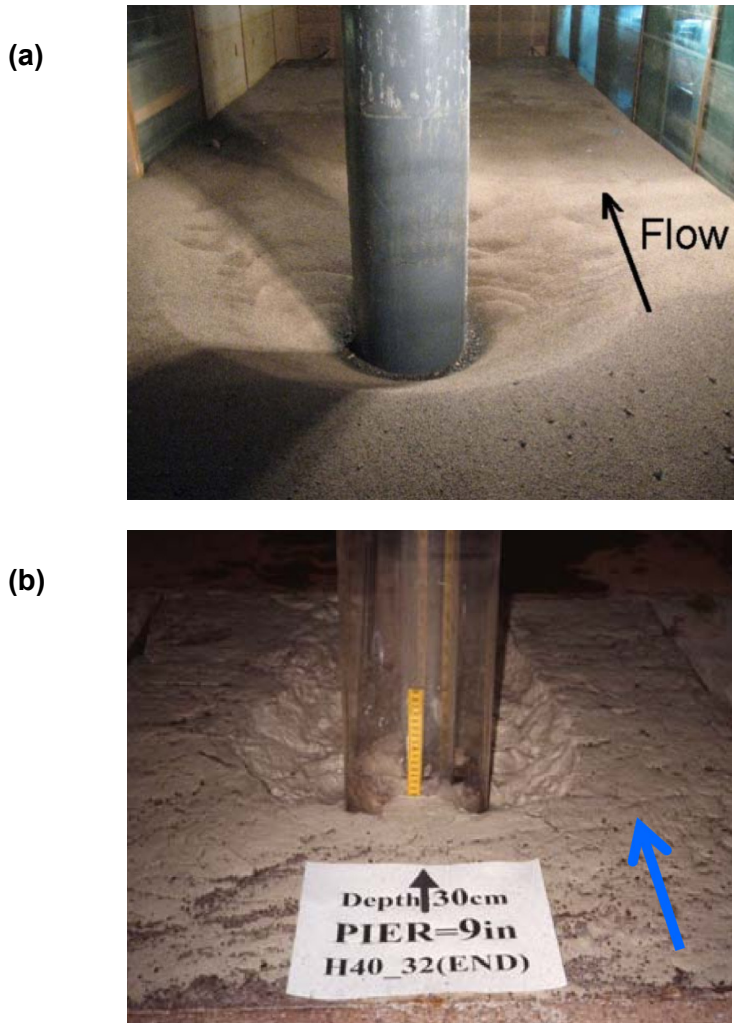

Figure 2.6: Local scour hole at a cylindrical pier founded on (a) sand bed and (b) clay bed as observed by Briaud et al. (2004) (modified from Ettema et al., 2011).

Recently, several studies focused on the effects of cohesion on the scour process (e.g., Briaud et al., 1999a; Briaud et al., 1999b; Ansari et al., 2002; Briaud et al., 2004; Brandimarte et al., 2006). Among them, one of the most used approaches is the Scour Rate in Cohesive Soils (SRICOS) method, initially developed by Briaud et al. (1999b) for single piers and subsequently extended to predict local scour at complex piers (Briaud et al., 2004) and contraction scour (Briaud et al., 2005). The method is based on the concept that to estimate the evolution of scour with time it is possible to cumulate the effects of different flood events lasting for specific periods.

2.2.3 Geometry of the scour hole

The shape of a scour hole around a bridge pier is primarily influenced by the characteristics of the pier itself. However, other factors play a role in the definition of the scour slopes such as the bed material and the features of the water flow. The base case of a single cylindrical pier founded on uniform bed material and subjected to a uniform flow has been extensively studied in the past (e.g., Shen et al., 1969; Breusers et al., 1977; Melville and Sutherland, 1988; Sumer et al., 2007).

A detailed description of the geometry of the scour hole for the base case is given by Dargahi (1990) and subsequently adopted by Hoffmans and Verheij (1997) in their reference book. The shape of the scour hole can be schematized in a horizontal cross-section as a half-circle at the upstream side, connected to a half ellipse downstream (Figure 2.7). The lower part of the upstream slope is usually steeper than the upper part, while in the proximity of the bridge pier a concave region develops. The average slope of the downstream side is about half of the upstream slope, the latter being almost equal to the constant volume friction angle of the bed material φ'_{cs}. A deposition area is present downstream at the end of the scour hole, as a result of the dissipation and the consequent break-up of the wake-vortices.

Having defined the maximum equilibrium scour depth and the φ'_{cs} of the bed material, it is then possible to estimate the expected shape of the scour hole. Clearly, moving from the reference case (i.e. cylindrical pier on uniform bed material) towards a more complex situation (e.g., pier founded on caisson or pile foundation) could result in a significantly different shape of the scour hole (e.g. Liang et al., 2019). Specific hydraulic studies are thus necessary to define in such complex situations the geometry of the scour hole.

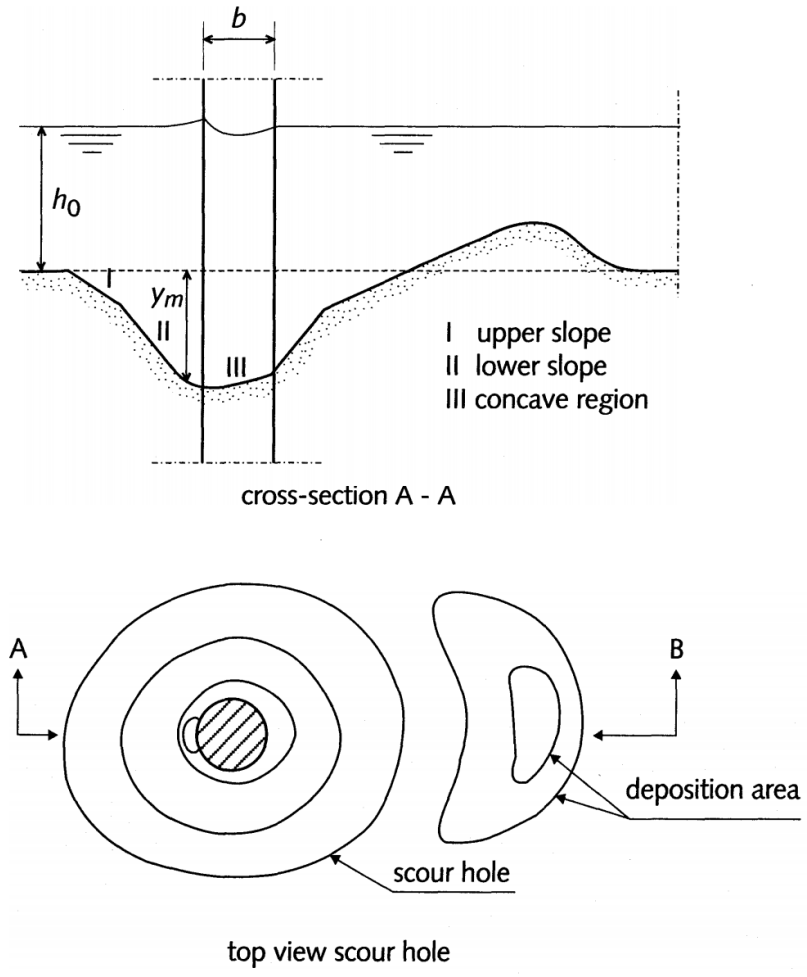

Figure 2.7: Geometry of a scour hole around a cylindrical bridge pier (from Hoffmans and Verheij, 1997).

2.3 Evaluating the local scour depth

As previously discussed, the severity of local scour at bridge piers is quantified through the *local scour depth at equilibrium* (or just *local scour depth*), which refers to the depth of the deepest point of the local scour hole, usually occurring along the upstream side of the bridge pier (Sheppard and Renna, 2005). The latter gives a measure of the exposure of the bridge foundation system due to scouring and can be used also as a starting point to define the geometry of the scour hole.

For a specific bridge that crosses a river characterized by a given hydrological regime, the most reliable method for predicting the equilibrium scour depth would be certain to develop a proper physical model of the system. The direct modelling of the problem is, however, a nontrivial task and it necessitates advanced laboratory equipment which is not generally available in the common practice.

As a consequence, several different approaches have been developed in the past decades for evaluating the maximum equilibrium scour depth. The possible approaches can be classified according to three different categories (Brandimarte et al., 2012): (i) *empirical methods*; (ii) *numerical methods*; and (iii) *data-driven methods*.

The empirical methods provide easy-to-use equations, calibrated on results of laboratory tests, for predicting the scour depth as a function of the flow characteristics, the riverbed material properties, and the bridge geometry. However, some limitations affect these formulations, mainly due to the complexity of the scour phenomenon (Brandimarte et al., 2012).

Some of these limitations can be overcome by performing advanced 3D numerical analyses to simulate the complex turbulent flow around the pier. The hydrodynamic model can thus accurate reproduce the dynamics of the vortex systems and the consequent development of the scour hole (e.g. Khosronejad et al., 2012). These models are anyway still under development and affected by heavy computational costs, preventing their use in practice.

Recently, some studies have addressed the possibility to use data-driven methods (i.e. Artificial Neural Networks) for predicting the scour depth without defining an *a priori* relationship between the input parameters and the output scour depth (e.g., Bateni et al., 2007; Toth and Brandimarte, 2011). Although Artificial Neural Networks have shown their capability in predicting the scour depth, the limited amount of available data restricts their general use for design purposes (Brandimarte et al., 2012).

A comprehensive discussion about the existing approaches for predicting the maximum scour depth (for which reference can be made to Brandimarte et al., 2012) is beyond the scope of this section. As appears from the previous discussion, to date the empirical methods are the only ones being used in practice. In the following, the most used empirical equations are thus introduced. In particular, the focus will be on the methods for predicting the local scour depth under clear-water conditions at cylindrical piers founded on caisson foundations (as in the case analysed in the present study).

2.3.1 Factors influencing the equilibrium scour depth

The local scour depth depends on many different parameters. Quite generally, the relationship for predicting the maximum scour depth $d_{s,\max}$ can be written as follows (Melville and Coleman, 2000):

$$d_{s,\max} = f\left(\rho_w, \upsilon, \overline{v}, y, g;\ d_{50}, \sigma_g, \rho_s, U_c;\ a, Sh, Al\right) \tag{2.4}$$

where the groups of parameters refer, respectively, to the water flow features (being ρ_w the water density, υ is the kinematic viscosity of the fluid, $\overline{v}$ the mean flow velocity, y the flow depth, and g the gravitational acceleration), to the riverbed material (being d_{50} the mean grain size, σ_g the geometric standard deviation of the particle size distribution, ρ_s the soil density, and U_c the critical velocity), and to the bridge pier geometry (being a the pier width, Sh a parameter describing the pier shape, and Al a parameter describing the pier alignment).

The abovementioned parameters can be combined to obtain a reduced number of dimensionless groups governing the scour depth equation. To this end, a variety of different combinations have been proposed in the past.

Assuming that the sediment particles are nearly uniform and neglecting the viscous effects, the scour depth at a cylindrical pier of diameter D_c can be rewritten as a function of three dimensionless groups (Melville and Coleman, 2000):

$$\frac{d_{s,\max}}{D_c} = f\left(\frac{\overline{v}}{U_c}, \frac{y}{D_c}, \frac{d_{50}}{D_c}\right) \tag{2.5}$$

where the three groups are usually termed, respectively, as *flow intensity*, *flow shallowness*, and *sediment coarseness*.

The flow intensity factor defines the scour regime (i.e., clear-water or live-bed, see Section 2.2.2.1). Figure 2.8.a depicts the influence of the factor on the equilibrium scour depth. Under clear-water conditions the scour depth increases almost linearly up to a threshold peak value, occurring for a mean flow velocity equal to the critical velocity. For larger intensity factors, the local scour develops under live-bed conditions. The scour depth initially decreases, then it increases again up to a second peak (Melville and Coleman, 2000).

The flow shallowness influences the intensity of the vortex systems forming at the base of the pier (see Section 2.2.1). At narrow piers (i.e., $y/D_c > 1.4$) the horseshoe vortices and the surface rollers do not interfere one each other and the flow depth does not influence the scour depth (Figure 2.8.b). As the flow depth decreases, the vortex systems, characterized by different directions of rotation, start to interact, reducing the erosive capacity of the flow. Within this range of flow shallowness factors (i.e., $0.2 < y/D_c < 1.4$), the scour depth depends on both the flow depth and the pier diameter, and the pier is identified as a transition pier. Finally, for very shallow flows at wide piers (i.e., $y/D_c < 0.2$), the surface rollers become dominant and the scour depth is mainly influenced by the flow depth (Melville and Coleman, 2000; Ettema et al., 2011).

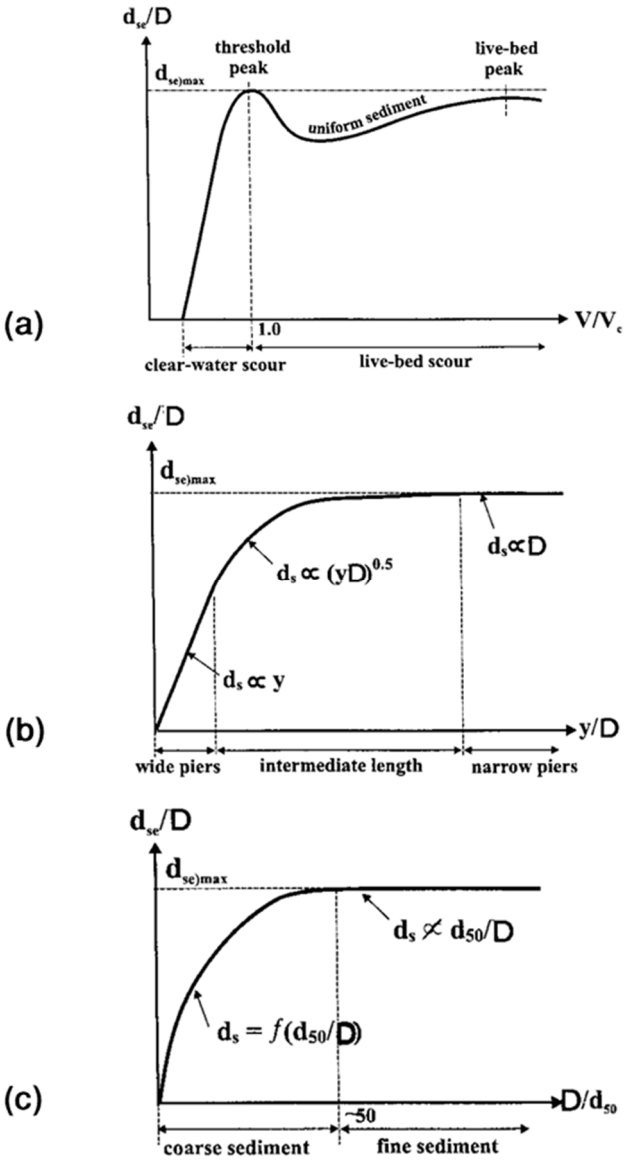

Figure 2.8: Influence of (a) flow intensity, (b) flow shallowness, and (c) sediment coarseness at a cylindrical pier on uniform bed material (modified from Melville and Chiew, 1999).

Figure 2.8.c reports the influence of the sediment coarseness on the scour depth for uniform bed materials. For usual values of the sediment coarseness (i.e. $d_{50}/D_c < 1/50$), the scour depth is not influenced by the sediment size. The latter becomes relevant for very coarse materials when the single grains are large compared to the dimension of the turbulences to dissipate the flow energy upstream (i.e. armouring of the bed material), thus reducing the flow erosive capacity (Ettema, 1980).

2.3.2 Predicting the local scour depth at cylindrical piers

Several empirical methods have been developed in the past fifty years for predicting the local scour depth in the reference case of a cylindrical pier founded on a uniform, cohesionless material (e.g., Shen et al., 1969; Hancu, 1971; Breusers et al.,

1977; Melville and Sutherland, 1988; Breusers and Raudkivi, 1991; Melville and Coleman, 2000; Arneson et al., 2012). The empirical equations are mostly calibrated on the results of laboratory tests conducted under specific conditions. Most of the formulations express the scour depth as a function of the dimensionless groups introduced in the previous section (e.g., Melville and Coleman, 2000; Arneson et al., 2012).

The simplicity of these approaches made them very popular unless they are affected by several limitations. It is important to point out that the estimated scour depth should be seen as a reference, generally conservative, value rather than an actual specific prediction.

A thorough review of the existing empirical methods can be found in some reference studies, for instance: Brandimarte et al., 2012; Sheppard et al., 2014; Qi et al., 2016a. In the following, the focus will be on two of the most used models, which serves also as a base for the methods for predicting the scour depth at complex piers that will be introduced in Section 2.3.3.

2.3.2.1 Melville (1997) equation

The method, initially proposed by Melville (1997) and subsequently integrated into Melville and Coleman (2000) (as it is usually referred to), takes into account the influence of the different parameters on the local scour depth through a series of empirical factors. The method can be used to assess the scour depth at both piers and abutments. The resulting equation for the local scour depth at equilibrium is the following:

$$d_{s,\max} = K_{yb} \cdot K_I \cdot K_D \cdot K_S \cdot K_\theta \cdot K_G \tag{2.6}$$

where K_{yb} is the flow-depth pier size factor, K_I is the flow intensity factor, and K_D, K_S, K_θ, and K_G are correction factors for sediment particle size, foundation shape, foundation alignment, and channel geometry, respectively.

Consistently with Figure 2.8.b, the flow-depth pier size factor is independent from the flow depth at narrow piers, while it becomes predominant for wide piers. The equations suggested for K_{yb} by the Author, considering a cylindrical pier, are the following:

$$\begin{aligned} K_{yb} &= 2.4 D_c && D_c/y < 0.7 \\ K_{yb} &= 2 \cdot \sqrt{y D_c} && 0.7 < D_c/y < 5 \\ K_{yb} &= 4.5 y && D_c/y > 5 \end{aligned} \tag{2.7}$$

In the case of a uniform riverbed material, the flow intensity factor K_I is simply defined as the ratio $\overline{v}/U_c$ under clear-water conditions, while it is equal to 1 if a live-bed scour regime is achieved.

Specific equations and charts are proposed for the other correction factors in Melville (1997) and Melville and Coleman (2000). However, if a cylindrical pier founded on uniform, relatively fine (i.e. $d_{50}/D_c < 1/50$), cohesionless soil is considered, the factors reduce to unity and the scour depth is just a function of $\overline{v}/U_c$, D_c and y.

2.3.2.2 Richardson and Davis (2001) equation

The Richardson and Davis (2001) method relies on the relationship colloquially termed as CSU (Colorado State University) equation. The equation, initially proposed by the Authors in 1975, has been updated several times to take into account all the parameters influencing the scour depth. The final equation is included in the updated version of the Hydraulic Engineering Circular Nr.18, HEC-18, of the Federal Highway Administration (Arneson et al., 2012). The scour depth can be computed as:

$$\frac{d_{s,\max}}{D_c} = 2 \cdot K_1 \cdot K_2 \cdot K_3 \cdot K_4 \cdot K_W \cdot \left(\frac{y}{D_c}\right)^{0.35} Fr^{0.43} \tag{2.8}$$

where K_1, K_2, and K_3 are correction factors for the shape, the angle of attack of the water flow and the bed transport conditions, K_4 takes into account the armouring effect for very coarse materials, K_W is a correction factor for wide piers in shallow flows, and Fr is the Froude number equal to $\overline{v}/\sqrt{g \cdot y}$. For a cylindrical pier under clear-water conditions supported on relatively fine material, K_1, K_2, K_3 and K_4 are equal to 1, 1, 1.1, and 1 respectively.

The correction factor for wide piers K_W has to be applied when $y/D_c < 0.8$ and $D_c/d_{50} > 50$. In such a situation, Richardson and Davis (2001) adopt the formulation proposed by Johnson and Torrico (1994):

$$\begin{aligned} K_W &= 2.58\left(\frac{y}{D_p}\right)^{0.34} \cdot Fr^{0.65} \quad \overline{v}/U_c < 1 \\ K_W &= \left(\frac{y}{D_p}\right)^{0.13} \cdot Fr^{0.25} \qquad \overline{v}/U_c \geq 1 \end{aligned} \tag{2.9}$$

2.3.3 Predicting the local scour depth at complex piers

Most of the existing equations for local scour apply to bridge piers with a constant cross-section, termed as *uniform piers*. The equations generally include a corrective factor to consider the pier geometry, but the factor is used to consider different shapes of the pier (for instance square-nose piers or cylindrical ones) rather than changes of the geometry itself along the length of the pier.

In reality, bridge piers are usually nonuniform, being supported on caisson or pile foundations. For these piers, termed *complex piers*, specific methods are necessary to predict the local scour depth.

Chabert and Engeldinger (1956) firstly investigated the local scour depth at a cylindrical column founded on a larger diameter caisson foundation. The study revealed a reduction of the scour depth at complex piers when the top of the footing is at or below the level of the channel before scouring. This beneficial effect (sometimes quoted as *shielding effect*) has been observed experimentally also by other Authors (e.g. Tsujimoto, 1987; Jones et al., 1992; Parola et al., 1996). The caisson foundation intercepts the pier downflow, partially protecting the bed at the upstream side from the pier-generated horseshoe vortices (Parola et al., 1996). Breusers and

Raudkivi (1991) observed anyway that care should be exercised when the scour-depth reduction is applied in practice, given the difficulties in predicting the actual level of the riverbed during a flood event.

A practical approach to estimate the scour depth at piers founded on caisson foundations has been firstly proposed by Melville and Raudkivi (1996). The Authors identified three different configurations according to the foundation top elevation *Y*. If the top of the caisson foundation is below the channel level after scouring, the foundation will not influence the scour process and the scour depth will be equal to that at a uniform pier (with the same diameter as the column). When the foundation top elevation is lower than the expected scour depth, the caisson interacts with the scour process due to interception of the downflows, having initially a beneficial effect on the scour depth. However, as the caisson protrudes into the flow its influence becomes predominant and the scour depth increases again, reaching a limit maximum value equal to the scour depth that would have been produced by a uniform pier with the same size of the caisson foundation.

These considerations have been subsequently extended by Melville and Coleman (2000) to the more general case of a column supported on a pile-cap founded on a pile group. In total, five possible cases exist, according to the position of the pile-cap relative to the expected scour depth (Figure 2.9.a).

In Figure 2.9.b is represented the expected trend for the scour depth as a function of foundation top elevation. The trend is equivalent to the one previously identified by Melville and Raudkivi (1996) as long as the pile group is not exposed to the flow (cases I and II). As the pile group gets exposed (within Case III), a reduction of the scour depth is produced by the pile group (Fotherby and Jones, 1993). Afterwards, for case IV, the reduction becomes predominant and the scour depth tends to the one produced by a pile group having the pile-cap above the water level (Case V).

Melville and Coleman (2000) give a conservative prediction of this trend, neglecting the reduction of the scour depth due to the shielding effect of the caisson foundation (acting within cases II and III). Moreover, the reduction observed when the pile group gets fully exposed (Case V) is also neglected and the limit scour depth, in this case, is computed considering an equivalent caisson foundation with the same width of the pile group.

As it emerges from the previous discussion, different approaches have to be applied for predicting the maximum scour depth at complex piers according to the foundation top elevation. In the following, the two most used empirical approaches are discussed, namely, the methodology suggested by Coleman (2005) and the one proposed in the updated version of the HEC-18 (Arneson et al., 2012). Attention is focused on the particular case of cylindrical piers supported on cylindrical caisson foundations.

2.3.3.1 *Coleman (2005) methodology*

The method proposed by Coleman (2005) is based on the concept of an equivalent pier width, as the width of a single column that would produce the same scour depth with the complex pier. The method has been developed mainly for local scour under clear-water conditions and it incorporates existing equations previously derived for the specific cases of local scour at uniform piers, caisson-founded piers and pier on pile groups.

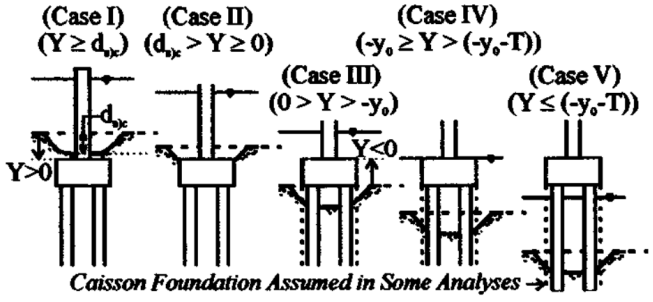

a) Pier components exposed with varying pile-cap elevation

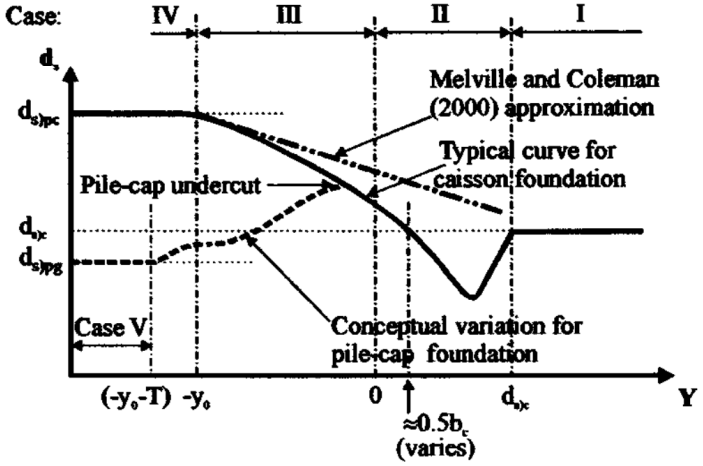

b) Conceptual variation of local scour with pile-cap elevation

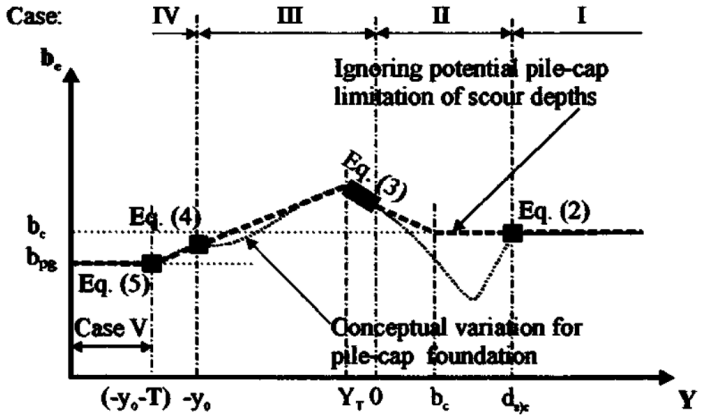

c) Conceptual variation (heavy dashed line) of b$_e$ with pile-cap elevation

Figure 2.9: Local-scour variation with complex-pier pile-cap elevation (from Coleman, 2005).

For the specific case of a cylindrical column on a cylindrical pile-cap or caisson foundation, the equivalent width corresponds to an equivalent diameter D_e. The latter is defined through a set of equations as a function of the foundation top elevation Y (Coleman, 2005):

$$\begin{aligned} D_e &= D_c && Y \geq D_c \\ D_e &= D_c \left(\frac{D_c}{D_{pc}} \right)^{\left(D_c/D_{pc}\right)^3 + 0.1 - 0.47\left(0.75 - Y/D_c\right)^{0.5}} && 0 > Y \geq Y_T \\ D_e &= \frac{0.52 \cdot T \cdot D_{pc} + D_{pg}\left(y - 0.52 \cdot T\right)}{y} && Y = -y \\ D_e &= D_{pg} && Y \leq -y - T \end{aligned} \tag{2.10}$$

being: D_c the diameter of the column; D_{pc} the diameter of the pile-cap (or the foundation for caisson-founded piers); D_{pg} the equivalent diameter of the pile group; T the height of the pile-cap; Y the foundation top elevation (Figure 2.9.a); Y_T the pile-cap elevation Y at which the pile group is exposed to the flow; and y the flow depth. The D_e is assumed to vary linearly outside of the ranges covered by Eq. (2.10).

The trend identified by Coleman (2005) is depicted in Figure 2.9.c (where the set of equation is termed as Eq. 2-5), accordingly to the five cases introduced by Melville and Coleman (2000). Once the equivalent pier diameter D_e is computed, the local scour depth at the complex pier can be evaluated applying Eq. (2.7) as proposed by Melville (1997) for local scour at uniform piers.

The prediction does not take into account the shielding effect given by the pile-cap (or the caisson foundation) in case II. An expression is however suggested by the Author to consider the reduction of the local scour depth. The equation is calibrated on the results of Parola et al. (1996), and it defines the ratio between the actual scour depth $d_{s,\max}$ (including the shielding effect) and the scour depth computed from Eq. (2.7) $d_{s,\max}\left(f_{cl}=0\right)$ as a function of the extension length f_{cl} of the pile-cap (or the caisson foundation) with respect to the diameter of the column:

$$\begin{aligned} &\left\{1 - \left[\frac{d_{s,\max}}{d_{s,\max}\left(f_{cl}=0\right)} \right] \right\} = 0.089 \cdot \left(f_{cl}/D_c\right)^{2.76} && f_{cl}/D_c < 2.5 \\ &d_{s,\max} = 0 && f_{cl}/D_c \geq 2.5 \end{aligned} \tag{2.11}$$

2.3.3.2 The HEC-18 complex-pier methodology

The methodology proposed in the HEC-18 of the Federal Highway Administration (Arneson et al., 2012) relies on the hypothesis of superposition of scour components, according to which the equilibrium scour depth can be computed separately for the column ($d_{s,c}$), the pile-cap or the caisson foundation ($d_{s,pc}$), and the pile group ($d_{s,pg}$). The total maximum scour depth at the complex pier is then simply obtained as the sum of the components:

$$d_{s,\max} = d_{s,c} + d_{s,pc} + d_{s,pg} \tag{2.12}$$

The single components of the scour depth can be computed as scour depth at uniform piers according to the Richardson and Davis (2001) equation (2.8), making sure to adopt the right values for the pier width and the flow depth and velocity.

Specifically, to compute the column scour depth component the actual diameter of the column D_c and the mean flow depth y have to be used in Eq. (2.8). Moreover, an additional coefficient K_h has to be adopted to account for the shielding effect offered by the foundation overhang distance f_{cl} in front of the pier. The coefficient can be obtained from charts provided in the HEC-18 circular as a function of f_{cl} and the ratio between the height of the pier stem above the bed and the pier width.

As regards the scour depth component given by the pile-cap or the caisson foundation, the methodology distinguishes between two cases: bottom of the pile-cap (or caisson foundation) above or below the level of the channel after scouring.

If the pile-cap is fully exposed to the flow, an equivalent pier width has to be used in the computation. The equivalent width can be obtained using charts provided in the circular. Moreover, adjusted values of the flow depth and the flow velocity have to be computed. In the second case (bottom of the pile-cap below the scour depth), the foundation is treated as a wide, short, pier in a shallow stream of depth equal to the exposed part of the foundation. Consequently, the actual diameter of the foundation is adopted, but the average velocity in the portion of the profile approaching the foundation has to be used.

Finally, the scour depth component due to the presence of the pile-group is computed adopting an effective width of an equivalent full-depth pier which considers both the number of pile rows and the pile spacing. The flow-depth and the velocity have thus to be adjusted consistently. Clearly, this component has to be computed only if the pile-cap is fully exposed.

Chapter 3

Influence of foundation scour on the mechanical response of bridges

The development of scour holes around bridge piers may severely affect the static and seismic response of the whole structure. As it emerges from the previous chapter, several studies have been devoted in the past to investigate the phenomenon from a hydraulic point of view. However, although the scour processes are now well-known, it is very difficult to properly predict the time-evolution of the supporting conditions at the pier foundation. As a consequence, several techniques have been proposed over the years to monitor the evolution of the scour hole at bridge piers.

The localized loss of support caused by scouring is still recognized as one of the main causes of bridge failure. This is partly due to the budget constraints which often prevent a simultaneous implementation of risk mitigation measures, leading to an increase of the bridge vulnerability to subsequent extreme events. On the other hand, there is still a lack of understanding of the actual influence of scouring on the global response of the structure.

In this chapter, the impact of foundation scour on the response of bridges is firstly analyzed with reference to well-documented case-histories. The attention is then focused on the identification of the key factors leading to the collapse of bridges due to scour and to the associated failure modes. Section 3.2 presents the main studies regarding the mechanical consequences of scouring, regarding both numerical simulations and experimental studies. Finally, approaches adopted in common practice to assess the vulnerability of scoured bridges are discussed.

3.1 Bridge damages and failures due to scour

3.1.1 Overview

The localized loss of support caused by scouring around bridge foundations is recognized as one of the main sources of bridge failures (Ballio et al., 1998; Melville and Coleman, 2000; Arneson et al., 2012). Wardhana and Hadipriono (2003) analyzed the main causes of bridge failures on the basis of 503 cases that occurred in the United States between 1989 and 2000. The statistical analysis of the case-histories revealed that 48% of the total failures were caused by flooding and scour. According to a comprehensive database of worldwide bridge collapses, Imhof (2004) comes to similar conclusions: flooding and scour seem to be responsible for about 60% of the worldwide failures caused by natural hazards.

Failures of bridges result in loss of human lives and great financial loss. The average annual cost for flood damage repairs in the US is estimated at approximately $50 US million (Lagasse et al., 1995). For example, the 1993 flood in the upper Mississippi basin was held responsible for 23 bridge failures, the majority of whom attributed to abutment or pier scour. The total estimated damage was about $15 million (Arneson et al., 2012).

The notorious case-history of the Schoharie Creek Bridge is probably the most famous bridge failure due to foundation scour (Thornton-Tomasetti, 1987; WJE and MR, 1987). The bridge collapsed on the morning of April 5, 1987, after an intensive spring flood event, leading to the fall of five vehicles into the river and the consequent death of ten people (Figure 3.1).

Figure 3.1: Collapse of the Schoharie Creek Bridge (from Delatte, 2008).

The structure consisted of five simply supported spans on concrete pier frames, consisting of two tapered columns and tie beams. The columns were supported by a plinth on a shallow spread foundation over layers of gravel, sand, and silt (Thornton-Tomasetti, 1987; Storey and Delatte, 2003). In the Spring of 1987, the combination of heavy rainfall and snowmelt produced an estimated 50-year flood, which in turn led to the development of an about 3 m deep scour hole around the third pier. The collapse started with the toppling of the pier, followed by the sudden collapse of the two corresponding spans. About ninety minutes later, the second pier and the second span collapsed. Finally, about two hours later, also the first pier and the first span dropped into the river (Thornton-Tomasetti, 1987; Storey and Delatte, 2003). Six days later part of the Mill Point Bridge (located about 5 km upstream of the Schoharie Creek Bridge) collapsed, once again due to foundation scour (WJE and MR, 1987).

The causes of the failure were investigated in the aftermath of the event by Thornton-Tomasetti (1987) and WJE and MR (1987). The collapse was mainly attributed to the extensive local scour around the third pier (Figure 3.2), caused by several design and maintenance deficiencies. The scouring process began soon after the bridge construction, due to a 100-year flood event in 1955. The flood removed the riprap protection layer, not adequately designed, from around the foundation (WJE and MR, 1987). The protection was never restored, leaving exposed the erodible backfill materials (i.e. layers of gravel, sand, and silt). As a consequence, subsequent floods led to the development of a local scour hole that was periodically refilled by sediment settling after the floods (WJE and MR, 1987).

Figure 3.2: Pier local scour holes at Schoharie Creek Bridge (from Lagasse and Richardson, 2001).

During the flood in 1987, the scour hole around pier three reached a depth of 3 meters and a length of, approximately, 7.5 to 9 meters. The scour hole affected substantially the bearing capacity of the not sufficiently embedded spread foundation, leading to the toppling of the pier (WJE and MR, 1987; Storey and Delatte, 2003). Besides, an insufficient design of the superstructure was also observed. The connection bearings, for instance, allowed for the uplift and the slide of the spans simply supported. Moreover, the lightly reinforced concrete piers led to a brittle failure instead of a ductile hinging of the piers (Storey and Delatte, 2003; Lin et al., 2014b).

The aforementioned case-history is a clear example of a poor hydraulic and structural design of a bridge exacerbated by inadequate inspections of the structure. The hydraulic processes responsible for scour at bridges are nowadays well-recognized, and several approaches are available to predict the expected scour depth at the design stage of a structure (see Chapter 2).

Nevertheless, as noticed by Brandimarte et al. (2012) regarding the Imhof (2004) data, bridge failures due to natural hazards and in particular to foundation scour seem to be increasing with time. This is mainly attributed to the ageing of the structures and the lack of maintenance. For instance, according to a survey produced by the roading authorities, the main part of the average cost due to bridge scour in New Zealand (about NZ $36 million in total) is related to damage repairs, rather than maintenance works (Macky, 1990).

The budget constraints, in fact, often prevent a simultaneous implementation of risk mitigation measures, as in the case of the Schoharie Creek bridge. As a consequence, the effects of subsequent floods are added together, leading to a substantial increase of the bridge vulnerability and, in turn, to an increase of bridge failures.

3.1.2 Key factors responsible for bridge failures

The mechanical performance of bridges is severely affected by flood-induced scour. Fortunately, the consequences of scouring not necessarily results in damage or collapse of the structure. Many different factors are, in fact, responsible for a substantial increase in bridge vulnerability, leading to its failure. Lin et al. (2014b), based on 36 well-documented case-histories, analyzed the main factors associated with scour-induced bridge collapses. The Authors identified three different conditions associated with failures: (i) *hydraulic*; (ii) *geotechnical*; and (iii) *structural*.

3.1.2.1 Hydraulic factors

The necessary prerequisite for the development of scouring is a water-flow with an erosive power stronger than the shear strength capacity of the riverbed material. According to the hydraulic features of the river, three different types of scour can occur either simultaneously or individually, namely: long-term degradation, contraction scour, and local scour (see Section Chapter 2 for further details). However, even in the general case of a combination of different scour-types, there is frequently a dominant one for a given bridge (Lin et al., 2014b).

In most of the cases (i.e. about 64%) examined by Lin et al. (2014b), local scour was the dominant component leading to failure. A global lowering of the riverbed (as in the case of long-term degradation and contraction scour) can have a major effect on the response of the structure. However, it is quite straightforward to identify its occurrence and measure its depth as it extends along the whole section of the river and it is the result of relatively slow processes. On the other hand, local scour leads to a very localized erosion around piers and abutments as a result of intensive flood events (Arneson et al., 2012). It is then quite difficult to rapidly quantify its actual extent, especially during major floods.

The traditional scour monitoring techniques are based on the direct or indirect measurement of the level of the streambed (e.g., Brandimarte et al., 2012; Prendergast and Gavin, 2014). The instrumentation is constituted by underwater devices which require expensive installation and maintenance costs and which are difficult to be used during flood events. Moreover, local scour holes tend to be refilled in aftermath of the floods (as in the case of the Schoharie Creek bridge), so the maximum scour extent reached during the flood may not be recorded by the depth-measuring instrumentation.

Recent studies identify the vibration-based monitoring techniques as viable options to monitor the scour progress (e.g. Foti and Sabia, 2010; Briaud et al., 2011; Prendergast and Gavin, 2014; Bao and Liu, 2017). Experimental data from vibration monitoring are used to study the evolution over time of the dynamic parameters of the bridge and, in turn, the evolution of scour at piers. Moreover, the data can be safely acquired even during extensive floods, guaranteeing a rapid quantification of the scour depth. Nevertheless, these techniques are still a long way from being applied in common practice.

Other hydraulic aggravation factors are the accumulation of debris during floods and the presence of water flow with an angle of attack to the bridge (e.g. Lin et al., 2014b). The presence of debris leads to a local increase in the flow velocity due to the restriction of the river channel. In addition, it induces lateral forces acting on the piers, increasing the lateral demand at the foundation system. Similarly, skewed flows tend to increase the scour rate at piers and abutments. Moreover, they induce additional torsional actions on the structure (Lin et al., 2014b).

3.1.2.2 Geotechnical factors

The geotechnical features of the foundation system influence both the development of scouring and the vulnerability of the structure. The soil type forming the riverbed material strongly influences the hydraulic processes responsible of scouring, especially in terms of scour rate (Briaud et al., 1999b; Ansari et al., 2002; Brandimarte et al., 2006). Fine-grained materials are characterized by a much slower progression of the scour process when compared to alluvial materials (see also Section 2.2.2.4). Consequently, larger scour depths are usually observed for bridges founded on sandy soils. This also entails a major number of scour-induced bridge failures observed for structures founded on alluvial materials (Lin et al., 2014b).

Besides the differences in terms of hydraulic processes due to the soil type, it is clear that the features of the foundation system are strongly related to the impact of scour on the vulnerability of the bridge. Lin et al. (2014b) observed that shallow foundations are, in general, strongly affected by foundation scour. However, several failures also occurred in bridges with piers supported on piles.

The effects of scouring on the response of spread foundations are often catastrophic. The progressive removal of soil from the sides of the foundation results in a reduction of both pure vertical and horizontal bearing capacity. Under extreme circumstances, local scour can undermine the pier causing the failure of the whole structure due to just the dead load of the bridge itself. This is the case, for example, of the third pier of the Schoharie Creek Bridge (WJE and MR, 1987). Conversely, in presence of deep foundations, the development of a local scour hole mainly implies a deterioration of the horizontal response of the foundation system, leading to structural hinging or pushover failure (Lin et al., 2014b; Qi et al., 2016b). The impact of scour on the different types of foundation systems is specifically treated in Section 3.1.3.

3.1.2.3 Structural factors

Scour-induced bridge failures usually initiate at a specific bridge component. Lin et al. (2014b) observed that in most cases (i.e. about 61%) the collapse is triggered by the failure of one or more piers (Figure 3.3). Once the failure starts at a component, it tends to propagate throughout the entire structure. However, different features of the superstructure can lead to different consequences. Girder bridges with simply supported spans, for example, are more affected by scouring with respect to ones with continuous spans (Lin et al., 2014b). This is probably due to the presence of a superstructure that can substantially restrain the movement of the pier (Tanasić and Hajdin, 2018).

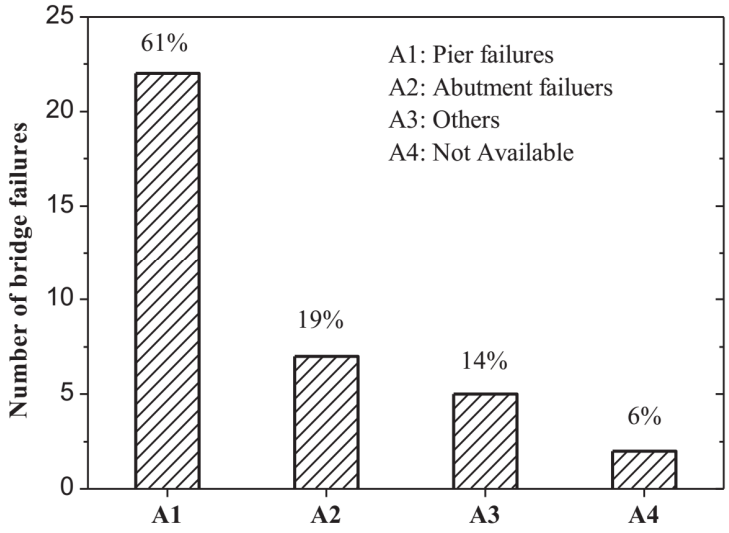

Figure 3.3: Failure of the components triggering the scour-induced collapse of the bridge (from Lin et al., 2014b).

The presence of the superstructure can be seen as an additional resisting system, able to redistribute the forces in the bridge after that a flood event deteriorates the performance of the piers. Nevertheless, the bridge resistance can be attained just in case a sufficient redundancy is present in the structural scheme. In this regard, a proper structural design and a good level of maintenance of joints and bearings are crucial to avoid catastrophic brittle failures (Tanasić and Hajdin, 2018).

3.1.3 Failure modes

Piles and embedded foundations of bridge piers are usually overdesigned to avoid the development of brittle bearing-capacity failure mechanisms which would result in the collapse of the structure. This is usually achieved by adopting conventional capacity design criteria: conservative safety factors have to be guaranteed when designing the foundation system, while the possible failure is guided towards ductile structural members (e.g., Priestly et al., 1996; Anastasopoulos et al., 2010). However, in presence of severe foundation scour, these criteria can be reversed.

Scour-induced failures are usually triggered by extreme flood events which deteriorates the performance of the foundation system of the piers. If this reduction is such that the demand acting on the pier exceeds the remaining resistance of the foundation system, the bridge gets damaged and, eventually, collapses.

Different failure modes can be observed based on the foundation type and the main actions acting on the pier. Lin et al. (2014b) identified, in total, four different structural failure modes of scoured bridge piers, namely: (i) *vertical failure*; (ii) *lateral failure*; (iii) *torsional failure*; and (iv) *bridge-deck failure*.

The first three mechanisms are related to the collapse of the foundation system and will be treated in detail in the following sections. Conversely, a bridge-deck failure is the result of the direct action of the flood acting on the deck. In the case of simply-supported spans, if the deck is not monotonically connected to the piers it can be washed out by the flood (Lin et al., 2014b).

3.1.3.1 Vertical failure

A pure vertical failure is observed when the pier collapses under just the dead load of the deck. It usually takes place when a shallow or a moderately embedded, foundation system is severely scoured, to such an extent that the footing is undermined (Figure 3.4.a) and the vertical bearing capacity of the soil is dramatically reduced (Lin et al., 2014b).

This is, for instance, the case of the Schoharie Creek Bridge, where the failure was triggered by the collapse of the third pier due to the undermining of the spread footing (Thornton-Tomasetti, 1987; WJE and MR, 1987). It is evident that a pure vertical failure can occur just in very extreme conditions as a result of a serious lack of maintenance and inspections. The bridge has to be subjected to exceptional floods in absence of any kind of monitoring system.

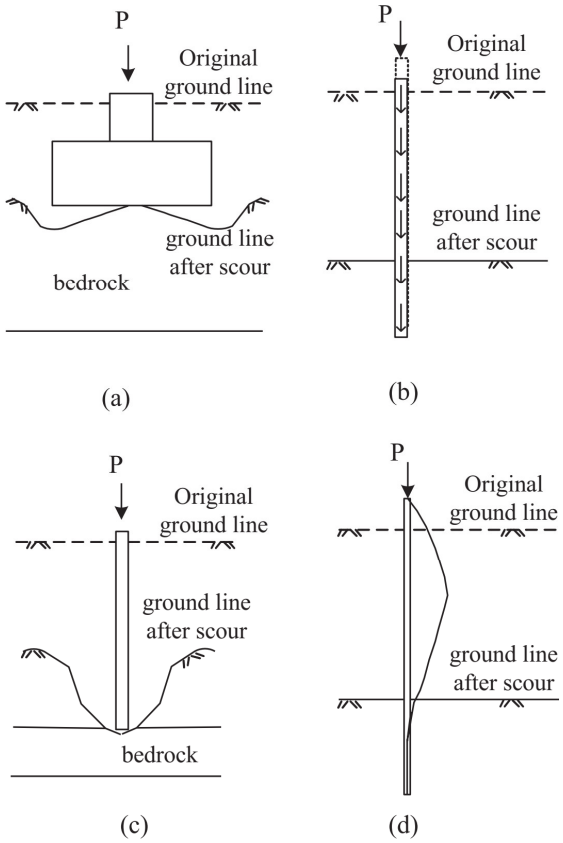

Figure 3.4:Vertical failure modes of scoured piers: (a) undermining of the spread footing; (b) penetration of friction piles; (c) undermining of pile tip; (d) buckling of piles (from Lin et al., 2014b).

The vertical capacity of pile foundations is also affected by scour. This is, for instance, the case of friction piles (Figure 3.4.b) where the skin friction resistance is reduced by the erosion of the surrounding soil, causing an increase of the settlement which can lead to the collapse of the pier. In very extreme cases, the scour depth can even reach the entire length of the piles, undermining their tips (Figure 3.4.c). The consequence is the total loss of the end-bearing resistance (Lin et al., 2014b).

The vertical failure of piers supported on deep foundations is also observed as a result of the buckling of slender piles (Figure 3.4.d). Local scour increases the free length of the piles, which can buckle under the actions transmitted by the pile cap tend (Lin et al., 2014b).

3.1.3.2 Lateral failure

The lateral supporting conditions of bridge piers are significantly reduced when the soil is eroded from the sides of the footing. While it is usually necessary a very severe foundation scour (until the undermining of the footing) to observe a pure vertical failure, even the development of a medium-deep scour hole can compromise the resistance of the pier in the horizontal direction, especially for simply supported short-span bridges (e.g. Wang et al., 2012).

A lateral failure can occur as a consequence of a pushover failure of the scoured piers, either for deep or spread foundations (Lin et al., 2014b). The erosion of the

soil around the foundation system implies a reduction of the lateral pushover capacity. At the same time, the presence of debris and the increased free length of the pier involve additional horizontal demands on the foundation. If the two effects are significant, the lateral demand can overcome the pushover capacity of the pier, leading to the toppling of the pier.

The development of structural hinging at piles or columns can also occur in the case of excessive displacement or rotation of the foundation. Even if the reduction of the pushover capacity and the increased horizontal demand do not directly lead to the collapse of the pier, they may result in a rotation of the foundation towards the upstream side (the direction where the maximum scour depth is usually observed) and, consequently, in structural hinging of the piles or the column itself (Melville and Coleman, 2000; Lin et al., 2014b).

3.1.3.3 Torsional failure

The last failure mode identified by Lin et al. (2014b) is the torsional failure of the structure. It is the result of skewed flows which can induce an additional torsional action acting on the foundation system (Melville and Coleman, 2000; Lin et al., 2014b). As also recognized by the Authors, it is not a frequent failure mode. However, the additional torsional action can play a role when it is added to other preexisting actions acting on the foundation.

3.2 Evaluation of the performance of scoured bridges

The previous sections analyzed the strong impact of scouring on the mechanical response of bridges, in the light of well-documented case-histories documented by previous studies. The deterioration of the performance of the foundation system can lead to accumulation of permanent displacements, damaging of the superstructure and, ultimately, failure of the bridge. However, available information about the failure mechanisms is mainly qualitative.

In the following, the principal studies regarding a quantitative estimate of the effects of scouring on the performance of the foundation system are presented, together with approaches usually adopted in the common practice to assess the vulnerability of scoured bridges.

3.2.1 Experimental evidence of the effects of scouring

Over the last years, several experimental studies on existing structures have been devoted to investigating the influence of scouring on the dynamic response of the structure (e.g. Foti and Sabia, 2010; Chen et al., 2014; Li et al., 2017; Kariyawasam et al., 2019). These studies mainly focused on the changes in the small-strain parameters of the pier due to the evolution of the scour hole. Such changes can, in fact, be used to infer *a posteriori* the scour depth. Nevertheless, the acquired data also provide interesting insights regarding the influence of scouring on the global behaviour of the structure. Consequently, they can serve as a basis for developing

appropriate models able to capture the response of scoured foundations also at large strains.

Foti and Sabia (2011) presented the case history of a five-span simply supported bridge in Turin, Italy, constructed in 1965. The original pier foundation system was constituted by a mat on 24 piles 15 m long, with a diameter of 0.6 m. Soon after the construction, 55 piles were placed around the original foundations as a scour protection measure. Nevertheless, the piers were affected by general and local scour over time, which caused the exposure of the top 2-3 m of the piles. In 2000, after a major flood event, the second pier (P2) was severely affected by localized scour, leaving exposed the top 5 m of the piles. A monitoring plan was then developed to measure the rotations of the piers. The critical pier continued to rotate consistently over time, reaching settlements of 16 mm and 44 mm, respectively for the downstream and the upstream side. In contrast, the other piers were not affected by significant rotations. In 2004 the pier P2 was replaced, incorporating the old foundation mat into a new one constituted by 6 piles 47 m long. Before and after the retrofitting, the dynamic response of the bridge under traffic-induced vibrations was studied.

Experimental data were interpreted in the light of two different approaches: the modal identification of the superstructure and the analysis of the local dynamic response of the pier foundation. The comparison between modal parameters identified before and after the retrofitting revealed that the first and the third vibrating mode of the superstructure were particularly sensitive to the scouring of the pier P2 foundation. Before the retrofitting, the second span exhibited a lower vibration frequency and an anomalous modal shape for the first mode of vibration. The lower stiffness of the foundation system was attributed to the loss of lateral support caused by the development of the scour hole. After the retrofitting, the modal shape appeared more regular and the anomaly disappeared (Foti and Sabia, 2011).

The Authors analyzed then the local dynamic response of the piers regarding experimental data and results from a simplified numerical model. The development of the scour hole in the numerical model was simulated removing the springs used to model the interaction between the piles and the surrounding soils.

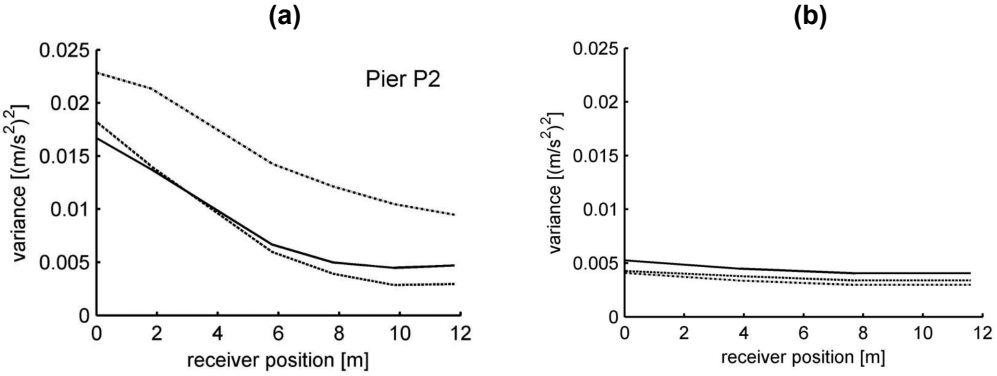

Figure 3.5: Experimental dynamic response of the pier P2 (a) before and (b) after the retrofitting of the foundation; traffic on the upstream carriageway (modified from Foti and Sabia, 2011).

A simple time-history of vertical external forces was applied to the two sides of the numerical model to simulate the traffic load imposed by a moving truck. Vertical acceleration time-histories were computed in the numerical model in six points of the foundation mat, the same locations where experimental data were collected through an array of vertical receivers during the passing of a real truck. Both the numerical model and the experimental data clearly showed an asymmetrical behaviour of the pier, especially for traffic on the upstream side of the carriageway (i.e. the same side of the scour hole). The experimental dynamic response of the pier before the retrofitting is shown in Figure 3.5.a in terms of variance of the signals for three different records. The asymmetrical response, as also highlighted by the progressive rotation of the pier, is the result of the different supporting conditions around the foundation: local scour holes are usually asymmetrical, with a maximum scour depth on the upstream side (Melville and Coleman, 2000). Finally, results of the experimental tests conducted after the retrofitting of the foundation (Figure 3.5.b) showed a significantly different response in terms of both variance amplitude (i.e. amplitude of the recorded signals) and symmetry (Foti and Sabia, 2011).

The study showed the influence of scouring on the dynamic (i.e. small-strain) stiffness of the foundation and its impact on the overall response of the structure. Specifically, the local behaviour of the pier seems to be particularly sensitive to the evolution of the scour hole after flood events. Furthermore, the experimental data showed a strong asymmetry of the response, suggesting that the shape of the scour hole can have major implications on the performance of the foundation.

Chen et al. (2014) presented an interesting example of the use of vibration data to calibrate a numerical model able to reproduce, at least in the small-strain field, the response of a scoured bridge. The application is based on the case study of the Kao-Ping-His bridge, an unsymmetrical single-pylon cable-stayed bridge in southern Taiwan, with a total length of 2617 m. The Authors studied the dynamic behaviour of the first of six units that constitute the bridge, which pier P2 was subjected to local scour.

The bridge dynamic response was first experimentally investigated using two sets of 3D measurements, located longitudinally on the bridge decks. In addition, two sections were selected and instrumented inside the steel box girder with vertical 1D sensors to identify the torsional response of the bridge. The monitoring data were used to detect the main vibration modes, together with the associated dominant frequencies, of the structure. A simplified numerical model was developed neglecting the influence of the pier P2 and substituting it with equivalent boundary conditions. Conversely, the pier P1 was included in the model and the surrounding soil was simulated through equivalents springs with coefficients initially derived from available information of drilling reports. The boundary conditions were then calibrated through a model updating procedure.

Subsequently, the pier P2 was also included in the model. The modal analysis of the whole model revealed that the global dynamic parameters were approximately equal to the ones obtained in the simplified model, confirming the initial

hypothesis about the slight influence of the pier P2 on the global bridge response. The comprehensive model was further used to calibrate the stiffness of the soil. Finally, the Authors evaluated the scour conditions at pier P2 minimizing the error between the vibration frequencies of two local vibration modes of the pier. The optimal scour depth obtained was 3.3 m. Subsequent measurements of the scour extent through underwater investigations revealed a consistent scour depth ranging from 3.4 m to 4.3 m.

This example provides interesting inputs to the discussion about the impact of scouring on the response of the structure. The case study emphasizes, firstly, that the influence of the scour depth on the response of the structure is evident when the local response of the pier is analyzed, but it can be hard to detect if the whole bridge is analyzed. The second emerging issue is that the dynamic response of the pier is strongly correlated to the stiffness of the remaining soil layers. Changes in the soil stiffness involve changes in the support conditions. Vibration-based data are useful tools to calibrate numerical models of scoured piers, but care should be exercised when they are used in absence of a reliable description of the soil properties.

Following the path defined by the experimental results on real structures, several small-scale physical models were carried out to evaluate the impact of scouring under controlled (i.e. laboratory) conditions (e.g. Briaud et al., 2011; Prendergast et al., 2013; Elsaid and Seracino, 2014).

Briaud et al. (2011) developed a small-scale model to compare different scour monitoring techniques, either traditional or vibration-based methods. Two laboratory experiments were performed in a 2D flume: the first with a shallow foundation constituted by the end of the column; the second with a deep pile foundation. The bridge pier (Figure 3.6.a) was reproduced by a concrete column with a diameter of 0.45 m and length of 4 m, while the deck was simulated with two prefabricated concrete elements installed end-to-end on the top of the pier. A fine clean and uniform silica sand was used to simulate the riverbed material. The bridge pier was instrumented with float-out devices, sonar-sensors, tilt sensors, and a 3D accelerometer installed on the top of the pier (Figure 3.6.b).

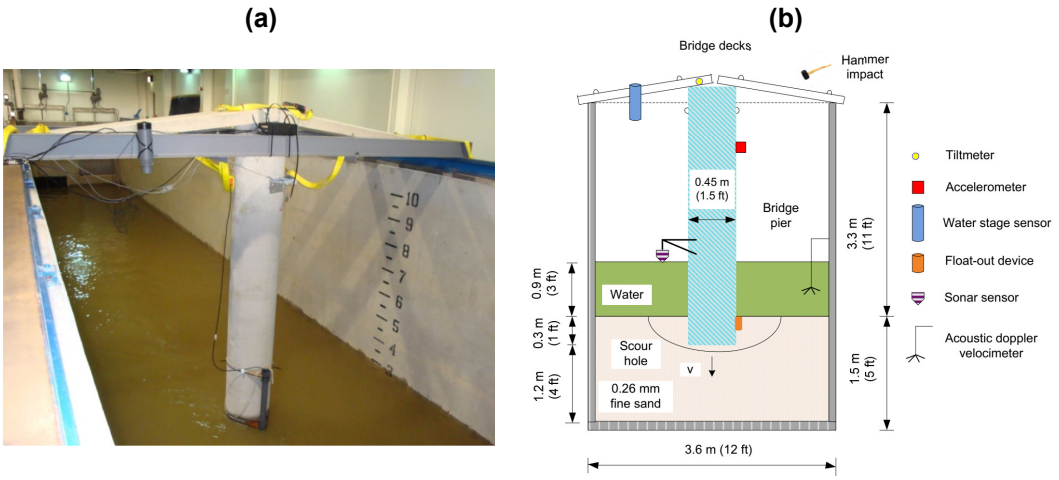

Figure 3.6: Experimental set-up (a) and instrumentation location (b) of the shallow foundation model (modified from Briaud et al., 2011).

After the construction of the model, the experiment was carried out increasing the velocity of the flood to induce foundation scour under controlled conditions. The dynamic response of the model was registered by the accelerometer as the scour hole progressed. Traffic loadings were simulated by impacting various points with a rubber hammer. The acceleration time-histories in the three directions were analyzed in terms of frequency content and Root Mean Square, RMS, ratios of the acceleration measured in two directions. The objective was to highlight the modal parameter changes in the three main directions (i.e., flow direction, traffic direction, and vertical direction) at different moments of the two experiments. The natural frequencies measured in the flow direction resulted to be particularly sensitive to the progress of scour in both the shallow and the deep foundation experiments. Conversely, in the transversal direction (concerning the flow), the restraint given by the deck partially limits the influence of the scour hole. Finally, when the scour depth reaches the base of the shallow foundation (i.e. it starts to undermine the footing), notable changes both in natural frequencies and in RMS ratios are detected (Briaud et al., 2011).

Based on the experimental results obtained by Briaud et al. (2011) for the shallow foundation model, Bao and Liu (2017) developed a coupled 3D FE model to get insights on the response of scoured piers. The soil was modelled adopting a perfectly plastic Mohr-Coulomb constitutive model, while an elastic homogeneous constitutive relationship was assumed for the deck and the pier. The soil-structure interaction was simulated using a hard contact in the normal direction and a penalty frictional algorithm in the tangential direction. After the validation phase, the model was used to investigate, firstly, the physical significance of the predominant natural frequencies measured during the experimental tests. The comparison revealed that the detected vibration frequencies correspond to the third modal frequency, which probably contributes the most to the dynamic response of the pier. Then, the FE model was used to study the influence of the sensor location. The preferred location should be at the top of the pier, where high vibration amplitudes are expected. Finally, the influence of the shape of the scour holes in terms of symmetry was investigated. A consistent asymmetric shape of the scour hole was obtained through a series of small-scale laboratory tests and then implemented in the finite element model. Results indicated that the natural frequencies tend to decrease with the progress of the scour depth in a different way when symmetric or asymmetric scour conditions are considered, suggesting again that the shape of the scour hole plays an important role.

The effect of scouring on the dynamic response of a driven pile was investigated by Prendergast et al. (2013) through laboratory and field tests. Firstly, a medium-scale model of a 1.26 m long pile was developed in laboratory. The pile was driven in a sandbox to an embedment depth of 490 mm, subsequently the scour progress was modelled by gradually removing the sand in 50 mm increments until a total of 200 mm of sand was removed. The pile was impacted at each stage with an impulse force applied through a swinging arc mechanism, and the dynamic response was recorded using uniaxial horizontal accelerometers. The results

confirmed again the influence of scouring on the natural vibration frequency (and thus on the stiffness) of the foundation.

A field investigation was subsequently undertaken by the Authors on a real-size model. The model was realized in a well-known test site near Dublin, consisting of a very dense, fine sand deposit with a groundwater table approximately 13 m below the ground level. An 8.76 m long steel pile with a diameter of 0.36 m was installed to an initial embedment depth of 6.5 m and was instrumented with 4 horizontal accelerometers. Thirteen scour levels were tested considering scour increments of 0.5 m. At each level, an impulse force was applied using a modal hammer, and the response of the pile was recorded. Again comparison between experimental data and results from simplified numerical simulations highlighted the importance of selecting appropriate parameters to model the soil-structure interaction. The differences between numerical and experimental results are in fact significantly reduced if the stiffnesses of the springs are selected using experimental measurements rather than empirical correlations.

The experimental studies previously discussed suggest that to properly model in laboratory the changes in the response of piers induced by scouring, it is crucial to reproduce correctly the soil-structure interaction phenomena. This is usually difficult to achieve in 1$\boldsymbol{g}$ physical models given the dependency of the soil behaviour from the confining pressure. A viable option to overcome this issue is to carry out centrifuge tests at $N\boldsymbol{g}$, to obtain a proper stress field in the small-scale model at the foundation level (Madabhushi, 2014).

Very recently, Kariyawasam et al. (2020) carried out a centrifuge study to assess the natural frequency sensitivity of bridge piers supported on sand to local and global scour. The Authors studied the response of a two-span integral bridge model supported on pile foundations and then compared it to three different standalone foundations, namely: monopile, pad foundation, and pile bent. The local scour process was modelled by progressively removing soil from around the piers up to a maximum depth of about 1/3 of the pile length and up to the foundation level for the pad. A simplified scour hole shape was considered by sloping the sides of the hole at 30° (i.e. approximately the critical state friction angle of the sand used in the experiments).

Finally, a constant soil layer was removed to simulate global scouring. The analysis of the behaviour of the integral bridge revealed that its natural frequency is significantly sensitive to local scour, especially when it affects both piers and abutments. The sensitivity is higher when global scour is considered, even if it does not seem to be extremely significant. Similar results are obtained in the tests performed on the standalone foundations. However, the shallow foundation seems to be less sensitive to scour when compared to the pile bent or the monopile.

3.2.2 Influence of scouring on the performance of the foundation

Soil scour around bridge foundations can significantly compromise the performance of the piers, especially in terms of lateral response. Consequently, practical approaches are necessary to include its effects when both deep and shallow foundations are studied.

In the case of pile foundations, scour basically reduces the pile embedment depth, modifying the soil lateral resistance profiles and increasing the horizontal displacements of the pile (e.g. Qi et al., 2016b). It is clear that its impact is different if local or general scour affects the foundation.

The problem was analyzed numerically and analytically by Lin et al. (2010; 2014a). When a layer of constant thickness is eroded from around the foundation, the confining pressure of the remaining soil is drastically reduced and the lateral response of the piles can be treated as such as a pile with an embedment decreased by the scour depth. The only major difference is related to the overconsolidation effects on the remaining soil. Conversely, the presence of the soil above the scour level for localized scour holes can significantly enhance the lateral resistance (Lin et al., 2010; Lin et al., 2014a).

The impact of scouring on the horizontal response of a shallowly embedded pile in sand has been recently investigated by Qi et al. (2016b) through a series of centrifuge tests. In particular, the Authors studied the effects of both local and general scour on the load-deflection (*p*-*y*) curves. General scour has shown to change mainly the pile embedment depth and the load eccentricity, proving that, in such conditions, the response of the scoured foundation can be modelled just by removing the eroded soil (without any additional effect). Conversely, under local scour the resistance of the soil at a given depth is somehow in the middle between the initial one (i.e. before scouring) and the one corresponding to general scour conditions.

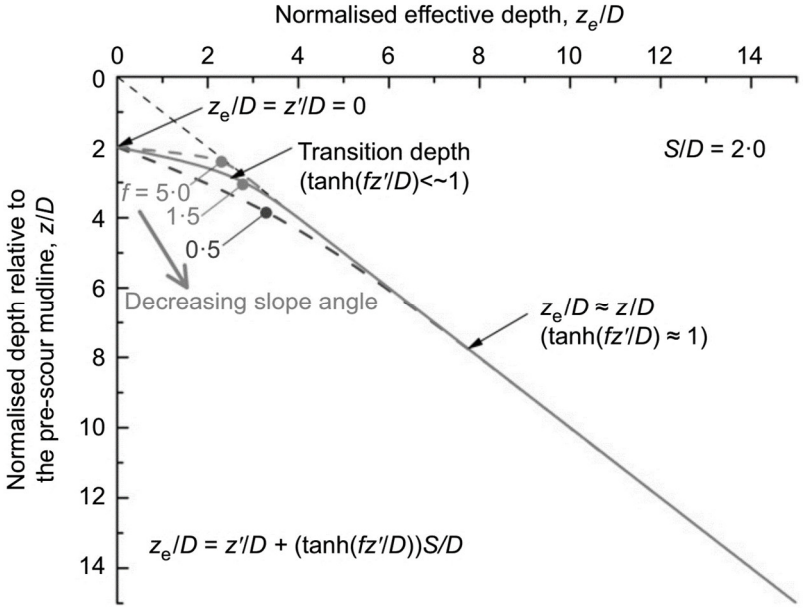

Figure 3.7: Definition of the normalised effective depth (from Qi et al., 2016b).

As a practical approach to estimate the *p-y* curves for piles under scouring conditions, the Authors introduced the concept of an *effective soil depth* as the weighted average value of the soil depth relative to the pre-scour level and to the soil depth below the current scour depth. The concept is well-explained in Figure 3.7. Just below the scour hole, the effect of scouring is maximized and the lateral response of the soil can be modelled by referring to an effective depth z_e (and, in turn, confining pressure) equal to the scoured one (i.e. equal to zero at the base of the scour hole). At much higher depths (well below the scour hole) the effects of scouring vanishes and the resistance of the soil profile corresponds to the unscoured one, so the effective depth z_e is equal to the initial (pre-scour) depth z. Finally, in the middle, it is present a transition zone that is more or less steep according to a parameter f defined as a function of the slope angle of the scour hole (i.e. equal to 0 for general scour and 1.5 for local scour with an average slope of 30°).

Following the path defined by Qi et al. (2016b), Li et al. (2020) and Chortis et al. (2020) conducted a series of centrifuge tests to study the lateral response of a rigid monopile subjected to global and local scour. Global scour is modelled removing a constant thickness soil layer, while in the case of local scour two different shapes are considered (namely, narrow scour hole and wide scour hole) by varying the distance from the pile to the base of the side slope.

Based on the experimental results, the Authors come to general conclusions similar to the previous findings: the effect of scour is more pronounced in shallower soil layers while it becomes less relevant at higher depths. The study also adds an interesting contribution to the discussion about the importance of the shape of the scour hole. According to the experimental results, the usual distinction between local and global scour seems not to be sufficient in defining the response of the monopile. The lateral resistance of the monopile subjected to local wide scour is, in fact, significantly lower (i.e. about 20%) with respect to the case of the narrow scour hole. Therefore, the shape of the scour hole should be realistically modelled as it plays a crucial role in defining the ultimate resistance of the foundation.

As opposed to piles or monopile foundations, very few studies focused on the influence of scouring on the response of embedded caisson foundations (e.g., Zhang et al., 2019; Tu et al., 2020). An interesting experimental study on the lateral performance of caisson and composite caisson-pile foundations on sand has been presented by Zhang et al. (2019). Based on the project of a cable-stayed bridge in the Qiongzhou strait, the Authors defined three different foundation models: a cylindrical caisson, a composite caisson supported on four piles, and a composite caisson supported on eight piles. The models were subjected to monotonic and cyclic lateral loadings considering different unsymmetric loading protocols. The results of the tests showed a progressive accumulation of residual lateral displacements for all the foundation types, with the best performance observed for the composite caisson-pile foundation. With increasing cycles, however, a stiffening effect is observed in the horizontal response of the foundation and the rate of accumulation tends to decrease. The effects of local scour (modelled forming a local scour hole with sides sloped at 30°) have been specifically considered by the Authors just for the

composite caisson foundation on eight piles. The increase of the scour depth has been shown to have a significant effect on the monotonic capacity of the composite foundation. The long-term cyclic performance is also dramatically affected by local scour, showing a substantial increase in terms of accumulated rotations and displacements under unsymmetric loadings. In this regard, a more accurate representation of the cyclic behaviour of scoured caisson foundations should refer to the ratio between the monotonic capacity after scouring and the cyclic loading.

3.2.3 Risk assessment under combined scour and seismic hazard

In the State-of-the-Practice, natural hazards are considered as independent actions on the structure, given the relatively small joint probability that two exceptional events act at the same time. Nevertheless, budget constraints often prevent the immediate retrofitting of scoured bridges after flood events. In such cases, the deterioration of the performance of the foundation system, especially in the horizontal direction, increases the seismic vulnerability of the damaged structures. For this reason, many studies have been recently developed to assess specific combined risks for bridge management (e.g. Alampalli and Ettouney, 2008). Multi-Hazard strategies in bridge management have the goal to increase safety and security at reasonable costs, ensuring an adequate bridge capacity during its life-cycle. Moreover, they constitute a significant budgetary control instrument to plan appropriate retrofitting measures on the most damaged structures.

The seismic vulnerability of bridges is usually expressed using seismic fragility curves, i.e. the conditional probability of failure as a function of a seismic demand parameter (e.g., Shinozuka et al., 2000). Different methodologies have been developed and employed to obtain the fragility curves, from empirical to analytical methods, under different conditions (e.g., Muntasir Billah and Shahria Alam, 2015). Within this framework, flood-induced scour and seismic hazards are usually combined evaluating the variations of the probability of failure due to scour effects (e.g., Alipour and Shafei, 2012; Ganesh Prasad and Banerjee, 2013; Wang et al., 2014a).

The main characteristics of this approach are common to all the studies in the literature. For this reason, just the approach described by Wang et al. (2014b) is here presented to give an idea of the methodology usually adopted to define the seismic risk of bridges subjected to scouring.

The response of a bridge under seismic hazard is described through a Probabilistic Seismic Demand Model, PSDM, which defines a relationship between the peak demand at a given component of the bridge and the ground motion intensity measure. A common seismic demand parameter for bridge piers is, for example, the maximum curvature of the column. At this step, also the input uncertainties are introduced into the model, related to the choice of adopting a given intensity measure as representative of the seismic action. The influence of scour can be implicitly included in the probabilistic analysis by assuming an initial scour depth in the numerical model used to predict the response of the bridge. Alternatively, a

Multi-Hazard PSDM, MH-PSDM, can be defined by modelling explicitly the dependence of the demand from the scour depth.

Once defined the seismic demand, a capacity model for the bridge component is defined to compute the failure probability. In the study of Wang et al. (2014b), for instance, the ultimate curvature limit state of the column was defined accordingly to the strain limit of the concrete and the longitudinal reinforcements. The conditional probability of failure is finally computed by combining the probability of occurrence of a given seismic (and scour in case of a MH-PSDM) demand with the capacity of the component. The product of a PSDM is a family of fragility curves (one for each scour depth considered) which defines the probability of failure of a bridge as a function of the intensity measure (Figure 3.8.a). On the other side, when the scour depth is explicitly included, the MH-PSDM provides a unique failure surface describing the probability of failure under a given combination of scour depth and intensity measure (Figure 3.8.b).

Finally, the combined risk is assessed through a convolution of the failure curve (or surface) and the seismic (and scour) hazard curves, which describes the annual exceedance probability of the hazard intensity measure (i.e. seismic intensity or scour depth).

The two types of risk analysis (i.e. PSDM or MH-PSDM) can also be considered representative of two different conditions. When a new bridge has to be designed no information about the effective scour depth at piers is available. As a consequence, the only way to assess *a priori* the combined seismic and scour risk is to develop a MH-PSDM, considering the uncertainties related to the expected scour depth. On the contrary, in the aftermath of a major flood, the seismic fragility assessment of an existing bridge has to be re-evaluated to consider the impact of the scour progress on the response of the bridge and, in turn, to plan eventual retrofitting activities. The scour depth, in this case, is known and the *a posteriori* assessment of the seismic risk can be undertaken considering the scour hazard as an additional boundary initial condition rather than a proper hazard (as in the case of a PSDM).

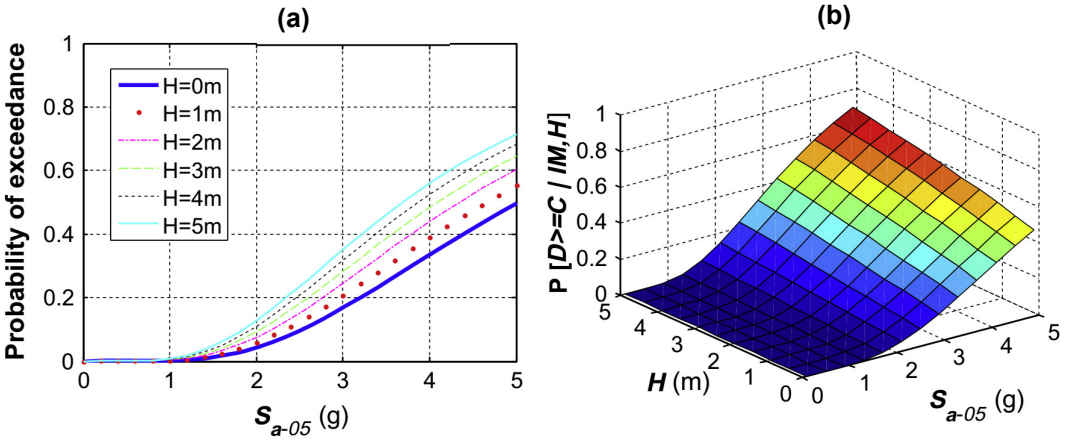

Figure 3.8: (a) Fragility curves and (b) fragility surface of a short-span bridge under combined scour and seismic hazard (from Wang et al., 2014b).

Wang et al. (2014a) assessed the combined seismic and scour risk for three different types of RC bridges (i.e. single concrete box-girder bridges with a shaft foundation, multi-span simply supported, concrete girder bridges with pile foundations, and multi-span continuous, concrete girder bridges with pile foundations) with short- and medium-span layouts. The soil-structure interaction was modelled through *p-y, t-z,* and *q-z* springs, which are progressively removed to model increasing scour depths. The Authors initially analysed the changes in the natural vibration periods of the first six modes of the structures with increasing scour depths. In each case, the scour progress affected significantly only the first few vibration modes in the longitudinal and transversal directions, lengthening the vibration periods. Subsequently, the fragility curves have been obtained for the six models, considering different scour depths and components of the bridges. The results highlight that a lower probability of failure of the column is expected with increasing scour depths. This is due to the isolation effect of the foundation system that counters the degradation of the support conditions. Conversely, the probability of a structural failure of the piles always increases with the scour depth.

Klinga and Alipour (2015) investigated numerically the lateral response of scoured bridges modelling all the components of the bridge (i.e. abutments, pile foundations and superstructure). The influence of scouring on the response of the structure was studied via pushover, buckling and modal analyses, considering five different soil profiles, namely four uniform soil profiles composed by medium/stiff clay or medium/dense sand and one non-uniform profile. The seismic performances of a pile-group foundation were analysed for all the soil profiles, while a single pile shaft foundation was studied only for two uniform soil profiles. The soil-structure interaction was again simulated through springs with properties calculated accordingly to the hypothetical soil profiles. Results showed, firstly, that the scour process results in a degradation of the lateral support conditions of the structure with a significant decrease of the foundation stiffness. Moreover, increasing shear forces and bending moments were observed in the piles, causing large strains and ultimately, structural hinging. However, the analyses also highlighted a decrease in the shear force acting on the column.

Although the growing interest regarding the combined risk assessment, most of the numerical studies totally neglect the effects of scouring on the remaining soil layers. Moreover, no distinction is usually made between general and local scour. The scouring process is often simulated by simply removing the springs and the dashpots until to the scour depth. However, as shown in the experimental studies by Qi et al. (2016b), scouring affect the response of remaining layers of soil differently if general or local scour affect the pier. Moreover, even in the specific case of local scour the shape of the hole can significantly change the effects of foundation scour (Chortis et al., 2020). This can have a major impact on the results of risk analyses. For instance, general scour significantly reduces the lateral response of the remaining soil, potentially increasing the failure probability of the foundation. In turn, the isolation effect protects the column and, in general, the superstructure. The relative entity of these two effects can be different if local scour is considered.

Unfortunately, it is not possible to define *a priori* which is the most critical situation, as often when dealing with seismic analyses. Consequently, it is crucial to be able to model the response of scoured foundations as accurate as possible.

Chapter 4

Characterization of the Perth sand

A thorough understanding of the behaviour of the sand used in the physical models is necessary to properly interpret and analyze the outcomes of the experimental tests. Moreover, it is fundamental to calibrate and validate a constitutive model able to predict the response of the material both at an element level and in a boundary value problem.

The sand used in the present experimental work is fine silica sand from Western Australia, close to Perth (hereafter, Perth sand). This sand has been widely adopted in the past for centrifuge modelling at ETH Zurich because of its physical properties which make it stable during the preparation and the installation of the models in the geotechnical drum centrifuge (e.g., Laue et al., 2002; Nater, 2005; Buchheister, 2009; Morales, 2015; Taeseri et al., 2018).

This section summarizes the main properties of the Perth sand, including basic index properties and stress-strain characteristics. The behaviour of the Perth sand is analyzed in the light of laboratory tests reported in the literature and new tests carried out in the geotechnical laboratory of the Politecnico di Torino within the framework of the present study.

Specifically, isotropically consolidated drained and undrained monotonic compression triaxial tests were carried out in an effort to identify the critical state conditions of the sand not only in terms of critical state friction angle, φ'_{CS}, but also in the compression ($v - \log p'$) plane. The identification of the Critical State Line, CSL, is fundamental to define the current state of a soil, characterized by an initial void index, e, and a mean effective confining stress, p', and to predict its evolution under external loadings. This is, of course, a nontrivial task, leading in the past to speculate the existence of a "zone" of critical states rather than a unique CSL (e.g. Konrad, 1993).

Although the uniqueness of the CSL for a given sand is nowadays recognized, the tendency of the sand to localise shear strains and the limitations associated to the instrumentation at very high axial strains imply high uncertainties in the

definition of the critical state, especially in volumetric terms (e.g. Verdugo and Ishihara, 1996).

In addition to the triaxial tests, a set of Resonant Column, RC, tests is also presented. The results of the tests have made it possible to define the dynamic properties of the Perth sand as a function of p', namely: the small-strain shear modulus G_0, the damping ratio D_0, and the Modulus Reduction and Damping (MRD) curves.

4.1 Index Properties

4.1.1 Particle Size Distribution

The Perth sand is a fine silica sand from the coast near Perth, Western Australia. The sand was observed to be rounded in grain shape, as depicted in Figure 4.1 in a picture taken with an environmental scanning electron microscope. The shape of the grains is probably a consequence of the aeolian transportation of the particles (Buchheister, 2009).

The Particle Size Distribution, PSD, of the material was investigated by Buchheister (2009) through different techniques, namely through a sieve analysis, a laser diffractometer analysis and an automatic evaluation based on zoomed pictures. The results are in general in good agreement, although some differences were observed especially for the curve obtained with the laser diffractometry. The PSD curve obtained by the Author through a sieving analysis is compared with the one declared by the sand manufacturer in Figure 4.2. The comparison is quite satisfactory, thus the PSD obtained by sieving is considered representative of the Perth sand.

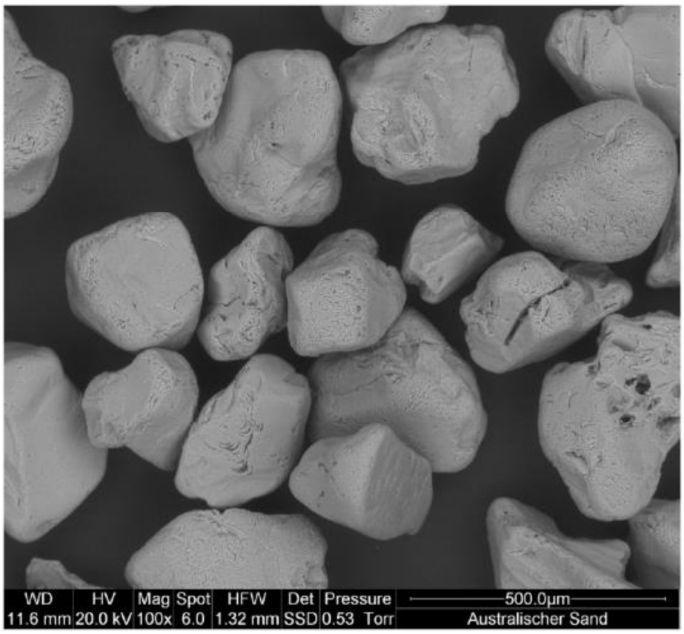

Figure 4.1: Image of Perth sand grains taken with an environmental scanning electron microscope (from Buchheister, 2009).

The Perth sand is characterized by a mean grain size, d_{50}, of 0.23 mm, while the minimum and maximum grain sizes, $d_{\min}$ and $d_{\max}$, are equal, respectively, to 0.08 and 0.5 mm. The Uniformity Coefficient, C_u, defined as the ratio between d_{60} and d_{10}, is equal to 1.79, while the Curvature Coefficient, C_c, defined according to Eq. (4.1), is equal to 1.26.

$$C_c = \frac{{d_{30}}^2}{d_{60} \cdot d_{10}} \tag{4.1}$$

The soil can then be classified as a poorly graded clean sand, according to the Unified Soil Classification System (ASTM D2487-17).

4.1.2 Specific Gravity

The Specific Gravity, G_s, of the Perth sand was measured through the water pycnometer technique, according to the specification given by ASTM D854-14. The resulting average value, equal to 2.65, is fully consistent with the value reported by Buchheister (2009) and, generally speaking, with the G_s expected for pure silica sand.

4.1.3 Minimum and maximum void ratios

The definition of the minimum and maximum void ratios, respectively $e_{\min}$ and $e_{\max}$, is necessary to compute the relative density, D_R, of the soil via the following equation:

$$D_R = \frac{e_{\max} - e}{e_{\max} - e_{\min}} \tag{4.2}$$

where e is the void ratio corresponding to a particular state of the soil.

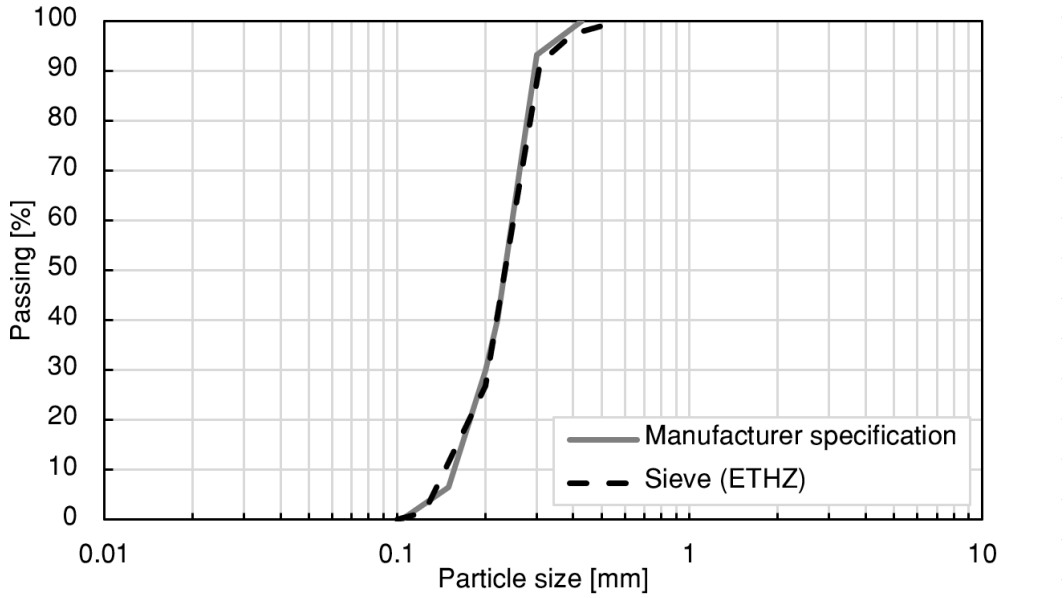

Figure 4.2: Particle Size Distribution curves of the Perth Sand (modified from Buchheister, 2009).

The e_{max} of a clean sand typically lies on a range between 0.75 and 1.1, while e_{min} ranges between 0.4 and 0.65. As regards the Perth sand, Morales (2015) reports an e_{min} of 0.50 and an e_{max} equal to 0.75. The two values were defined averaging the results of the measurements carried out by Nater (2005) and Buchheister (2009). The reported value of e_{min} appears to be quite reasonable, falling within the range of the expected values for clean sands, while the e_{max} value corresponds to the lower limit of the expected range. Moreover, as will be discussed in the next section, significantly larger values of e were achieved through the moist tamping method adopted to prepare the samples tested at the Politecnico di Torino.

Consequently, it was decided to perform a new determination of the e_{max}. Three measurements were carried out through Method A suggested by the ASTM D425-16. The test allows the determination of the minimum density, ρ_{min}, of the dry soil. The e_{max} can thus be computed through the following equation:

$$e_{max} = \frac{G_s \rho_w}{\rho_{min}} - 1 \tag{4.3}$$

where ρ_w is the density of water.

The obtained e_{max} values range from 0.85 to 0.87. The relatively high scattering of the results is associated with the well-known difficulties in the execution of replicable tests. The differences are anyway lower than the limit values reported in ASTM D425-16 and the results are thus valid. It was then decided to adopt an e_{max} equal to 0.87 (the maximum of the three determinations), in light also of the high e achieved in the triaxial tests and reported in the following.

4.1.4 Summary

The Index Properties of the Perth sand are summarized in Table 4.1. Hereafter, these values will be used as reference values (in defining, for instance, the D_R of the sand).

Table 4.1: Index Properties of the Perth sand.

d_{50} [mm]	d_{min} [mm]	d_{max} [mm]	C_u [-]	C_c [-]	G_s [-]	e_{min} [-]	e_{max} [-]
0.23	0.08	0.50	1.79	1.26	2.65	0.50	0.87

4.2 Triaxial tests

In this section, the mechanical behaviour of the Perth sand is analyzed in light of results from triaxial tests. An introduction about the main features of the stress-strain behaviour of sands is first given. The results of an experimental laboratory study conducted at the Politecnico di Torino are then presented, together with previously published results present in literature. Finally, the stress-strain behaviour of the soil is analyzed in an effort of defining the Critical State parameters of the Perth sand.

4.2.1 Stress-strain behaviour of sands

The mechanical behaviour of granular materials is known to be both pressure- and density-dependent. The influence of the initial state on the behaviour of sands was firstly studied by Casagrande (1936) comparing the results of drained strain-controlled monotonic tests. Sand samples initially consolidated at the same p', show different mechanical responses during the shearing phase depending on whether the initial state is loose or dense (Figure 4.3).

Loose sands exhibit a contractive behaviour (i.e. characterized by positive volumetric strains, ε_v) with a monotonic increase of deviatoric stress q, defined as $\sigma_1' - \sigma_3'$. On the other side, dense samples tend to dilate, experiencing an initial increase of q up to a peak value and a subsequent softening. The peak is attained in correspondence to the maximum dilatancy. At large strains, both dense and loose sands tend to reach the same state, termed c*ritical state*, corresponding to the same critical state void ratio e_{CS}, and the same state of stress defined by p'_{CS} and q_{CS}.

The concept was subsequently formalised by Roscoe et al. (1958), which defines the critical state as the state at which the soil continues to deform at constant stress, without further changes in volume. The e_{CS} depends on the confining pressure p'_{CS}, and their relationship defines the locus of the possible critical states for a sand. The latter is usually represented in the $e - \log p'$ plane (or equivalently in the $v - \log p'$ plane) and is called Critical State Line (CSL).

In a drained monotonic compression test, the higher is the p' after the consolidation, the higher will be the p'_{CS} and, thus, the e_{CS}. As a consequence, at high confining pressures the tendency of a dense sand to dilate will decrease and, eventually, will disappear. By knowing the position of the CSL and the initial state of the soil, it is then possible to know whether the soil will exhibit a contractive or a dilative behaviour.

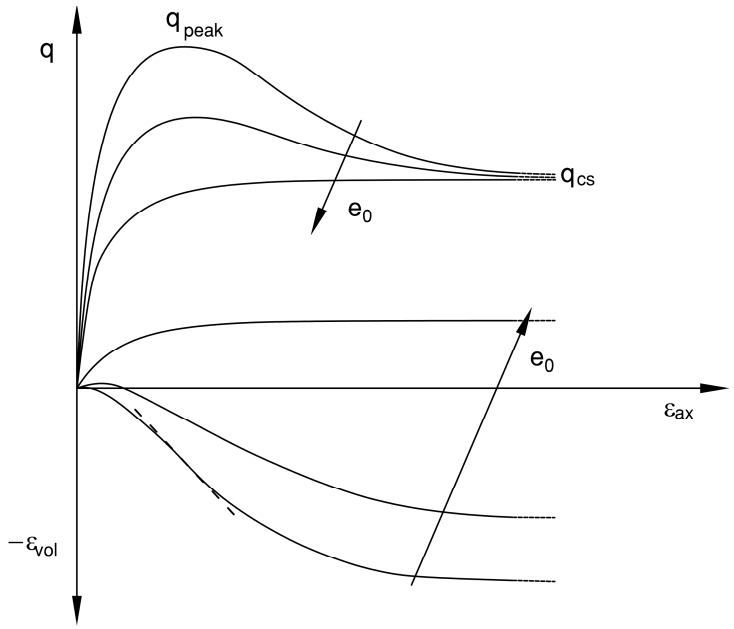

Figure 4.3: Influence of the initial state on the behaviour of sands in drained triaxial compression tests.

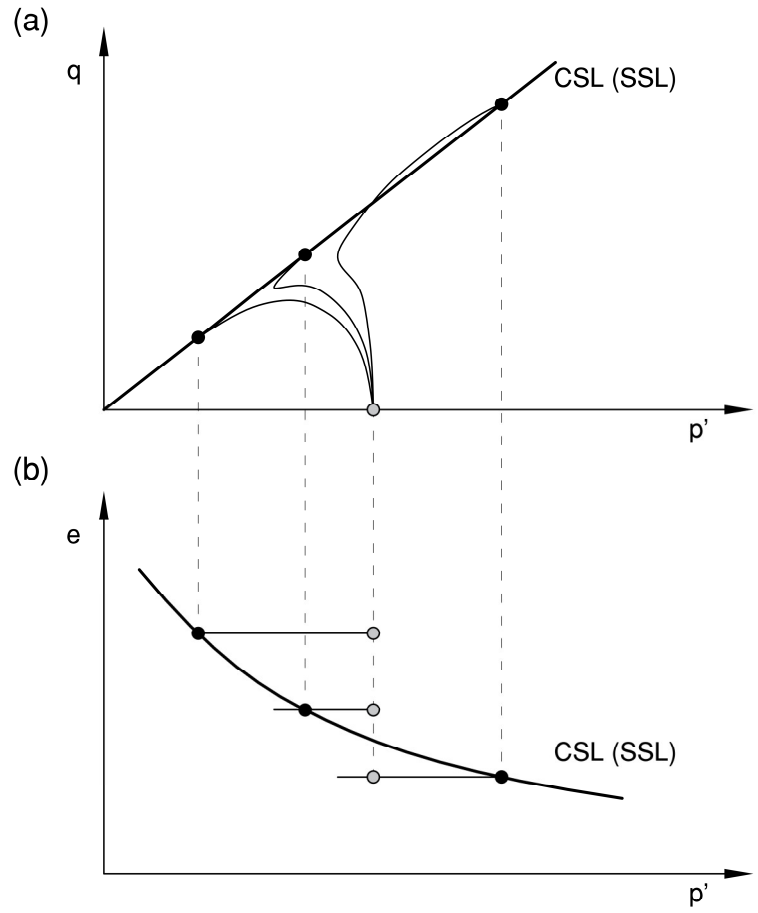

Figure 4.4: Influence of the initial state on the behaviour of sands in undrained triaxial compression tests: (a) stress paths in the $q - p'$ plane; (b) representation in the $e - p'$ plane.

A complementary behaviour was observed by Castro (1969) in undrained conditions through load-controlled triaxial tests. In Figure 4.4 the typical behaviour of sands in undrained conditions is shown concerning the possible stress paths in the $q - p'$ plane and in volumetric terms.

At a given confining pressure, a very loose sand characterized by a void ratio larger than e_{cs} tends to contract. Consequently, a positive increase of the pore water pressure, and in turn a decrease of the confining pressure, takes place due to the kinematic limitation given by the undrained conditions. Once that the peak deviatoric stress is reached, a significant softening takes place as a consequence of the pore water pressure build-up. At high strains, the sand reaches the Steady State, characterized by a continuous deformation of the sample at constant volume, constant normal effective stress and constant velocity (Poulos, 1981).

The significant loss of strength is commonly indicated as liquefaction of the material. However, it has to be pointed out that the concept of liquefaction, strictly speaking, is associated with flow-type failures of soils that exhibit a total loss of strength, behaving as liquids (Ishihara, 1993).

Conversely, dense samples exhibit a dilative tendency, constrained by the build-up of negative pore pressures in undrained conditions, and an associated

hardening. Castro (1969) also observed that a medium-dense sample with an initial state close to the critical condition experiences limited liquefaction. Initially, the deviatoric stress increases up to a peak value. A positive increase of the pore water pressure takes then place, inducing a temporary flow failure. The state corresponding to the minimum deviatoric stress is commonly referred to as Quasi-Steady State (Alarcon-Guzman et al., 1988; Ishihara, 1993; Verdugo and Ishihara, 1996). The sample experience then a *phase transformation*, shifting from a contractive to a dilative behaviour and recovering its strength and stability.

At high strains, all the tests showed an almost constant state of stress, the value of which depends only on the initial void ratio. The correlation between the void ratio and the final, constant, state of stress was identified by the Author as the Steady State Line. Subsequently, Been et al. (1991) clarified that the concepts of steady or critical state coincide and, thus, the two corresponding lines are equivalent.

It is clear that knowing only the relative density of a sand is not sufficient to determine his state, given the dependency of e_{CS} on p'. A state parameter, Ψ, was then proposed by Been and Jefferies (1985) considering as a reference to the Critical State condition:

$$\Psi = e_0 - e_{CS} \tag{4.4}$$

where e_0 is the void ratio before shearing.

A sand in an initial state characterized by a positive Ψ will show a tendency to contract during shearing. Conversely, negative values of Ψ are related to sands that will exhibit a dilative behaviour (Figure 4.5). The CSL is usually perceived as a straight line in the $e - \log p'$ plane, parallel to the Normal Consolidation Line, NCL. However, the experimental evidence highlights a change in the gradient of the curve for high confining pressures (e.g., Verdugo and Ishihara, 1996; Konrad, 1998). The latter is commonly associated with the onset of grain crushing for p' larger than 1 Mpa (Coop, 2005).

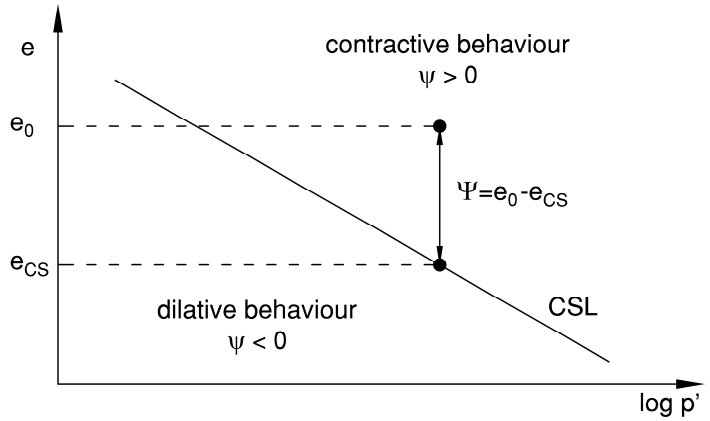

Figure 4.5: State parameter concept (after Been and Jefferies, 1985).

4.2.2 Triaxial tests on medium-loose samples of Perth sand

The tests reported in this section were carried out within the framework of the present thesis using the triaxial cell for sands of the Geotechnical Laboratory of the Politecnico di Torino (Figure 4.6). The cell was specifically developed for testing sand samples in stress or strain control. All the tests here presented were anyway carried out under strain control, applying the displacements at a constant strain rate through a digital press. A full description of the apparatus can be found in Puci (1999) and Carrera (2008). The tests were performed according to the prescriptions given in ASTM D7181-20.

4.2.2.1 Laboratory equipment

A brief description of the instrumentation used to measure the parameters of interest of the test is here reported:

- The backpressure, as well as the radial pressure, are measured through Druck pressure transducers with a full-scale pressure of 1 MPa and an accuracy of ±0.5 kPa.

Figure 4.6: Triaxial cell for sands of the Geotechnical Laboratory of the Politecnico di Torino.

- The deviatoric load is measured through a load cell mounted at the base of the sample, below the porous stone. The instrument is a Maywood cell characterized by a maximum load of 10 kN and an accuracy of ±0.7 N.
- An LVDT (Linear Variable Differential Transformer) rigidly connected to the load arm measures the axial strain with an accuracy of ±1 μm.
- The local radial strains are measured with two non-contact proximity Kaman transducers. The latter are piezoelectric ceramics transducers mounted through a couple of external bars at a height corresponding to half height of the sample. The transducers measure the distance from a reference small piece of aluminium glued on the membrane, allowing the determination of the changes in the diameter of the sample under the assumption of cylindrical deformations.
- The two Kaman transducers are characterized by accuracy of ±1 μm and a relatively small full range of 2.5 mm, making it necessary to place them close to the sample. Before starting with the shearing, a mechanical system has thus to be used to get them away from the sample, avoiding possible disturbance effects.
- The volume strain is measured through a volume gauge. The volume gauge is constituted by a cell full of water connected to the pore water in the sample. The pressure of the water inside the volume gauge is externally controlled, therefore in drained conditions it controls also the pore water pressure, namely the backpressure. An LVDT is used to measures the changes in height, and thus in volume, of the water exchanged between the volume gauge and the sample. The volume gauge has a capacity of 50 cm^3 and an accuracy of ±0.04 cm^3.

4.2.2.2 Sample preparation

The moist tamping method was adopted to prepare the samples. The method has the main advantage of permitting to control the relative density obtaining very loose, homogeneous samples (Yang, 2005). On the other side, very loose samples appear to be externally layered and it creates a honeycomb structure not fully consistent with the one typically obtained in field (Casagrande, 1976).

The preparation method is known to be a potential factor of influence in the behaviour of sands. This may result in differences in the results of triaxial tests performed on samples characterized by the same initial state (i.e. samples of a given relative density, consolidated at the same confining pressure), but prepared using different methods. Yang (2005) ascribed the potential differences to the anisotropy due to the orientation of the grains. Carrera (2008) however showed that the behaviour of a sand rounded in grains is independent of the preparation method, probably because of the absence of a favourite orientation of the spherical particles.

The total weight of soil needed to achieve the objective relative density is firstly computed by knowing the expected volume of the sample. The total amount of material is split into 10 equal parts, the specimen is in fact prepared to create several

layers of constant height to ensure an adequate homogeneity. A 5% in weight of water is then added to the soil layer to generate an apparent cohesion necessary to achieve low relative densities. The soil is left to rest for about 12 hours in sealed containers to ensure a homogeneous water content throughout the sand.

A standard latex membrane (0.25 mm thick) is then mounted on the base of the cell and applied via vacuum against the wall of a cylindrical split mould mounted on the base of the cell (Figure 4.7a). The soil corresponding to the first layer is placed on a disk of filter paper above the porous stone and the layer is levelled up to the desired height using a flat-bottom tamper. The material necessary to form the following layer is then placed and the procedure is repeated until the total specimen is created.

After the moist tamping, the specimen can be closed. The top cap initially blocked, is attached to a load arm passing through a guiding system. A counterbalance is then mounted to release the cap and to put it in contact with the soil sample without undesired disturbance effects given by the weight of the top cap itself (Figure 4.7b). After that the contact is made, the sample can be closed and set under negative pressure of about -30 kPa, which makes it stable during the assembly of the apparatus.

At this point, the actual initial dimensions of the specimen are measured considering, as representative values, the average of three determinations. The height is measured through a calliper, while a *π-tape* is used for the diameter. Both the instruments have a precision of ±0.01 mm. The samples prepared in this study are characterized by an initial height of about 140 mm and a diameter of about 70 mm. Henceforward, the variations in the dimensions of the sample will be recorded by the instruments described in Section 4.2.2.1.

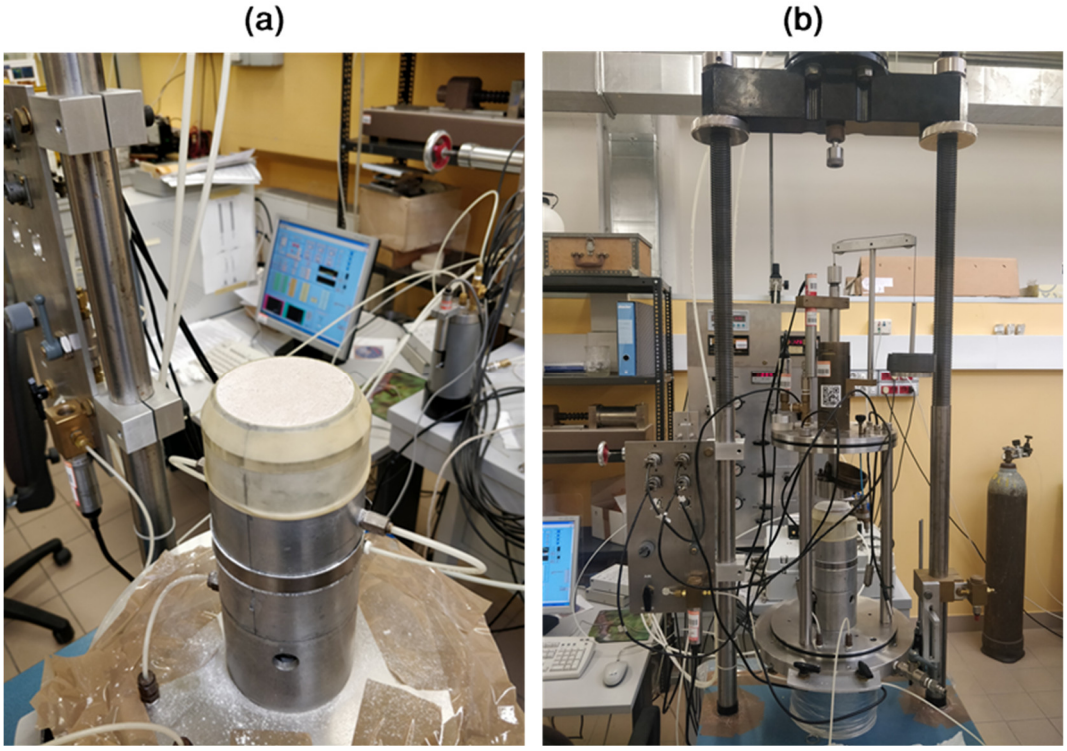

Figure 4.7: Preparation of a test: (a) preparation of a sample; (b) assembly of the cell.

After all the sensors are mounted, the cell is sealed positioning the external plexiglass. The chamber is then filled with water to ensure correct control of the radial pressure. The load arm is, temporarily, blocked to remove the counterbalance while it is connected to the pneumatic jack that governs the axial stress during the saturation and consolidation phases. Subsequently, the load arm will be rigidly connected to a crossbar to counter the press during the compression under strain control. The negative internal pressure is now gradually removed and the radial pressure is simultaneously increased. The test can, thus, start.

4.2.2.3 Testing procedure

Saturation

The samples are firstly flushed with CO_2 for about 1 hour to facilitate the subsequent saturation process. Afterwards, the water flushing takes place using de-aired water under a gradient of about 4 kPa between the bottom and the top of the samples. When, at least, two times the volume of the specimen in water passes through the sand the flushing is stopped (according to the prescriptions given in ASTM D7181-20).

A backpressure procedure is then carried out to fully saturate the sample. Initially, both the radial pressure and the backpressure are simultaneously increased, keeping constant the effective pressure at almost 30 kPa. After about 30 min the drainage valve is closed and the backpressure is monitored. If the change in the backpressure over 2 min is smaller than the 5% of the effective pressure, the pore water pressure is considered to be stable and the Skempton B-parameter can be measured. If this is not the case, the procedure is repeated.

The total confining pressure p, is then increased in undrained conditions of Δp and the B-value is calculated as:

$$B = \frac{\Delta u_w}{\Delta p} \tag{4.5}$$

where Δu_w is the pore water pressure build-up after its stabilization.

The drainage is then opened keeping constant the effective pressure in the specimen. If the B-value obtained is larger than 0.95, the saturation phase of the test is considered to be concluded. Otherwise, the drainage is again opened, keeping constant the effective pressure. The step is then repeated after a while, to permit the water to flow inside the sample.

In all the tests here presented a B-value of, at least, 0.97 has been achieved.

Consolidation

All the tests were isotropically consolidated. For the undrained tests, a multistep consolidation is carried out. Both the radial and the axial pressure are increased in undrained steps of 10-30 kPa until the desired value of effective confining pressure is reached. After each step, the drainage is opened for the time necessary to ensure the dissipation of the excess pore water pressure (i.e. until the stabilization of the volumetric deformation of the specimen, monitored through the strain gauge). This

procedure has made it possible to follow the consolidation process also in the $e - \log p'$ plane.

Conversely, for the drained tests, the consolidation is performed in a single step. This is done to define the maximum loading rate which will allow pore pressure to dissipate during the shearing of the sample. Assuming that the failure will take place for an axial deformation of 4%, the axial loading rate, $\dot{\varepsilon}_{ax}$, can be computed as (ASTM D7181-20):

$$\dot{\varepsilon}_{ax} = \frac{4\%}{16 \cdot t_{90}} \tag{4.6}$$

where t_{90} is the time to 90% of the first consolidation, obtained by applying the Taylor (1942) method. A loading rate of 3.8 %/hour (i.e. 0.08 mm/hour) is thoroughly sufficient to ensure the pore pressure dissipation. The same rate was adopted also for the undrained tests.

Shearing

After the consolidation of the sample, the shearing phase takes place. The shearing is carried out under strain control using a digital press. The press moves upwards the cell while the top cap is held in place through the loading arm, the latter rigidly connected to a crossbar above the cell.

Data are recorded in this phase with a time rate of 5 sec, allowing the definition of the stress-strain curve with a resolution of about 0.005% in axial strain.

4.2.2.4 Analysis of the data

The variables of interests describing the stress-strain behaviour of the soil are defined as follows:

- *Axial strain,* ε_{ax}: computed as:

$$\varepsilon_{ax} = \frac{\Delta H_s}{H_{s,0}} \tag{4.7}$$

  where ΔH_s (positive in compression) is measured through the LVDT and $H_{s,0}$ is set equal to the height of the sample before shearing.

- *Volumetric strain,* ε_{vol}: during the flushing and the saturation phases, the changes in volume are monitored through the geometrical deformations measured by the axial LVDT and the two horizontal Kaman transducers. The volume of the sample can be computed as:

$$V_s = \frac{\pi\left(\Delta D_s + D_{s,0}\right)^2 \left(\Delta H_s + H_{s,0}\right)}{4} \tag{4.8}$$

  where D_s is the diameter of the sample. Subsequently, the sample is considered to be fully saturated and the changes in volume, ΔV_s, (positive in compression) are directly measured through the volume gauge. The volumetric strain at shearing is then computed as:

$$\varepsilon_{vol} = \frac{\Delta V_s}{V_{s,0}} \tag{4.9}$$

where V_0 is set equal to the sample volume before shearing.

- *Shear strain,* ε_s: computed as:

$$\varepsilon_s = \frac{3\varepsilon_{ax} - \varepsilon_{vol}}{3} \tag{4.10}$$

- *Void ratio,* e: computed as:

$$e = \frac{V_{s,0}\left(1-\varepsilon_{vol}\right)}{M_S / \left(G_s \cdot \rho_w\right)} - 1 \tag{4.11}$$

where M_S is the dry mass of the soil.

- *Radial pressure,* σ_{rad}: directly measured through the pressure transducer.
- *Deviatoric stress,* q: computed as:

$$q = \frac{F}{A_c} \tag{4.12}$$

where F is the load measured by the load cell, while A_c is the cross-sectional area. The values obtained through Eq. (4.14) are subsequently corrected to consider the restraining effect given by the stiffness of the membrane. The correction is computed according to the specifications given in ASTM D7181-20:

$$\Delta q = \frac{4E_m t_m \varepsilon_{ax}}{D_{s,0}} \tag{4.13}$$

where t_m and E_m are the thickness and the Young's Modulus of the membrane, equal to 0.25 mm and 1400 kPa, respectively.

- *Cross-sectional area,* A_c: computed via Eq. (4.14) assuming a cylindrical deformation of the specimen, according to the ASTM D7181-20 standard.

$$A_c = A_0\left(\frac{1-\varepsilon_{vol}}{1-\varepsilon_{ax}}\right) \tag{4.14}$$

t_m This assumption is certainly valid for the preliminary phases of the test (i.e., flushing, saturation and consolidation). Conversely, during shearing, the cross-section of the specimen is not constant along its length and the sample ceases to deform cylindrically, due to the friction with both the top cap and the base of the cell (Figure 4.8).
Although corrections for full barreling deformation are available in the literature (e.g. Georgopoulos and Vardoulakis, 2005), it was decided to assume a cylindrical deformation to homogenize the results without assuming a predefined reference cross-section at failure. Furthermore, the assumption is consistent with the adopted volumetric and axial strains, which are computed as average values for the sample.

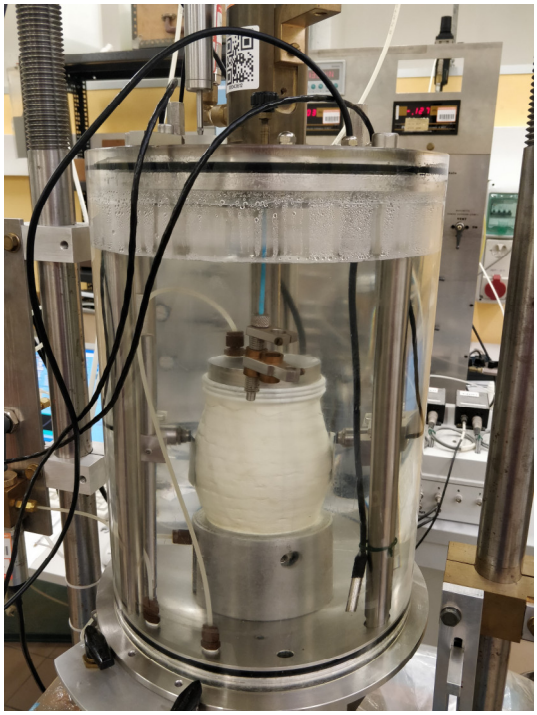

Figure 4.8: Shape of the specimen at the end of a test due to barreling deformation.

- *Axial pressure,* σ_{ax}: computed as:

$$\sigma_{ax} = \sigma_{rad} + q \tag{4.15}$$

- *Pore water pressure,* u_w: directly measured through the pressure transducer.
- Mean effective confining pressure, p': computed as:

$$p' = \frac{\sigma_{ax} + 2\sigma_{rad}}{3} - u_w \tag{4.16}$$

4.2.2.5 Results

The main objective of the laboratory investigation was the definition of the CSL both in the $q - p'$ and in the $e - \log p'$ plane. Defining the correct position is anyway very difficult, especially in volumetric terms. The main problems associated to the identification of the critical state condition are: (i) the tendency of the sand to localize the shear strains and (ii) the necessity to reach high strains to achieve the critical state at high confining pressures (Verdugo and Ishihara, 1996).

A dense (i.e. dilative) sand sample sheared in both drained and undrained conditions will eventually reach the critical state at really high strains, beyond the limits given by both the instrumentation and the assumptions usually made to interpret the results. Moreover, the development of shear bands inside a dense sample implies the necessity of defining the void ratio, and thus the volumetric strains, locally, even when the samples are sheared in undrained conditions and the total volumetric strains of the sample are null (Desrues et al., 1996). Conversely, a very loose sample that reaches the critical state in undrained conditions liquefies at low to medium shear strains, in correspondence of low values of p'_{CS}, without the development of shear bands.

Consequently, to study the position of the CSL, it was decided to perform mainly undrained tests on loose (i.e. contractive) samples, looking for a total, or at least partial, liquefaction of the specimen. In total, five isotropically consolidated triaxial tests were performed, only one of which under drained conditions. All the tests were sheared in compression. A summary of the tests is given in Table 4.2.

Table 4.2: Summary of the triaxial tests carried out at the Politecnico di Torino.

Test name	Drainage	p'_0 [kPa]	e_0	D_R [%]
TX-PoliTO-01	Undrained	99	0.70	45.9
TX-PoliTO-02	Undrained	199	0.72	40.5
TX-PoliTO-03	Undrained	299	0.79	21.6
TX-PoliTO-04	Drained	300	0.79	21.6
TX-PoliTO-05	Undrained	198	0.84	8.1

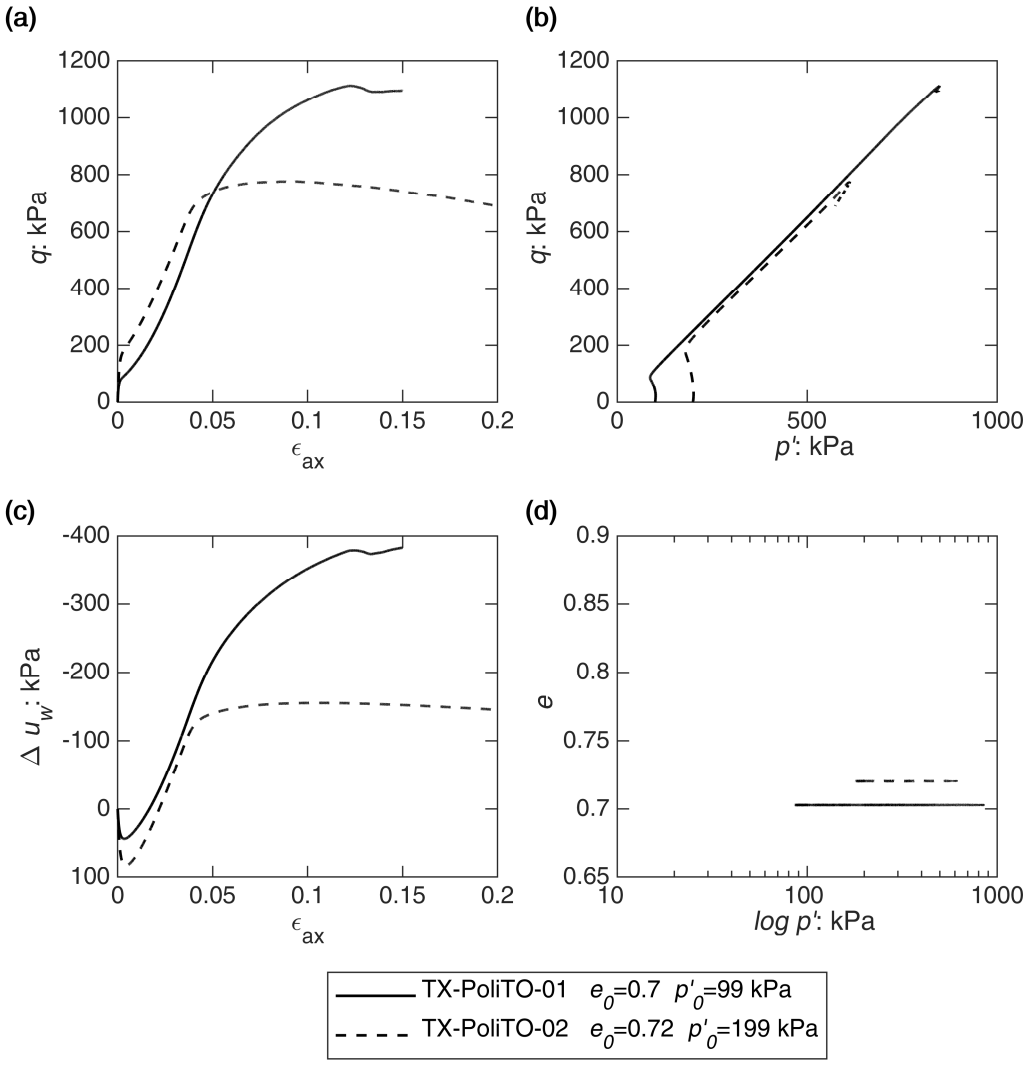

Figure 4.9: Undrained triaxial tests on medium dense (i.e. D_R of 40.5-45.9%) samples of Perth sand: (a) deviatoric stress vs axial strain; (b) effective stress paths; (c) pore water pressure build-up vs axial strain; (d) void ratio vs mean effective confining stress.

The first two tests (namely, TX-PoliTO-01 and -02) were performed on samples with an e_0 of about 0.7 and a p'_0 of about 100 and 200 kPa. The two samples showed a dilative behaviour, clearly identifiable in terms of both negative pore pressure build-ups (Figure 4.9.c) and effective stress paths (Figure 4.9.b). The behaviour is typical of a medium-dense sand: the samples exhibit an initial increase of Δu_w up to the phase transformation, followed by a dilative tendency (i.e. a decrease of Δu_w down to negative values) and a consequent significant hardening (Figure 4.9.a). In test TX-PoliTO-01, the denser state of the soil and the lower confining pressure result in larger negative Δu_w respect to the test TX-PoliTO-02.

The critical state condition for test TX-PoliTO-01 is not clearly identifiable, even if the state seems to be stabilizing at the end of the test. Conversely, in test TX-PoliTO-02 the critical state seems to be reached for an ε_{ax} of about 0.06, after which Δu_w is almost stable, while q slightly decreases. The decrease of q could be anyway related to the hypothesis of full barrelling, which results in a larger increase of the cross-sectional area at high strains.

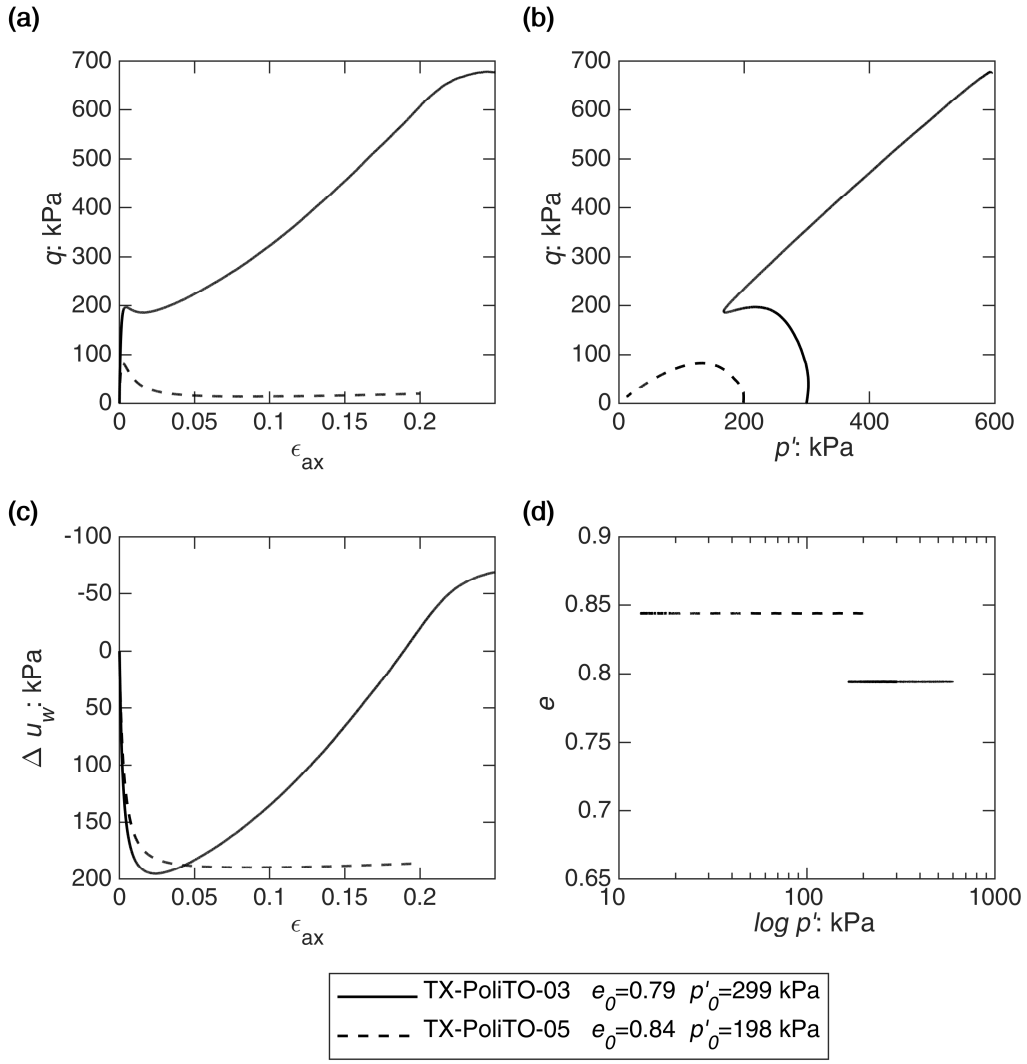

Figure 4.10: Undrained triaxial tests on loose (i.e. D_R of 8.1-21.6%) samples of Perth sand: (a) deviatoric stress vs axial strain; (b) effective stress paths; (c) pore water pressure build-up vs axial strain; (d) void ratio vs mean effective confining stress.

Figure 4.10 reports the results of two tests (namely, TX-PoliTO-03 and -05) carried out on very loose samples of Perth sand, characterized by a D_R of 8.1% and 21.6% and a p'_0 of about 300 and 200 kPa, respectively.

In test TX-PoliTO-03 the sand experiences temporary liquefaction: a rapid increase of q is followed by a softening and temporary stabilization of Δu_w, which subsequently decreases again causing a further hardening. At really high strains, both q and Δu_w show a progressive stabilization, apparently approaching to a steady-state condition for an ε_{ax} of about 0.25. Conversely, in test TX-PoliTO-05 the very loose initial state of the sand turns out in complete liquefaction, with an almost total loss of strength. After the peak, both q and Δu_w become stable and the sand reaches, and continues to maintain, a clear critical state condition.

Finally, the contractive behaviour of a loose (i.e., D_R of 21.6%) sand sample was investigated in drained conditions in test TX-PoliTO-04 (Figure 4.11). The sand exhibits a monotonic increase of q up to a value of about 600 kPa. The Critical State condition seems to be reached at for an ε_{ax} of about 0.1, after which q is almost constant.

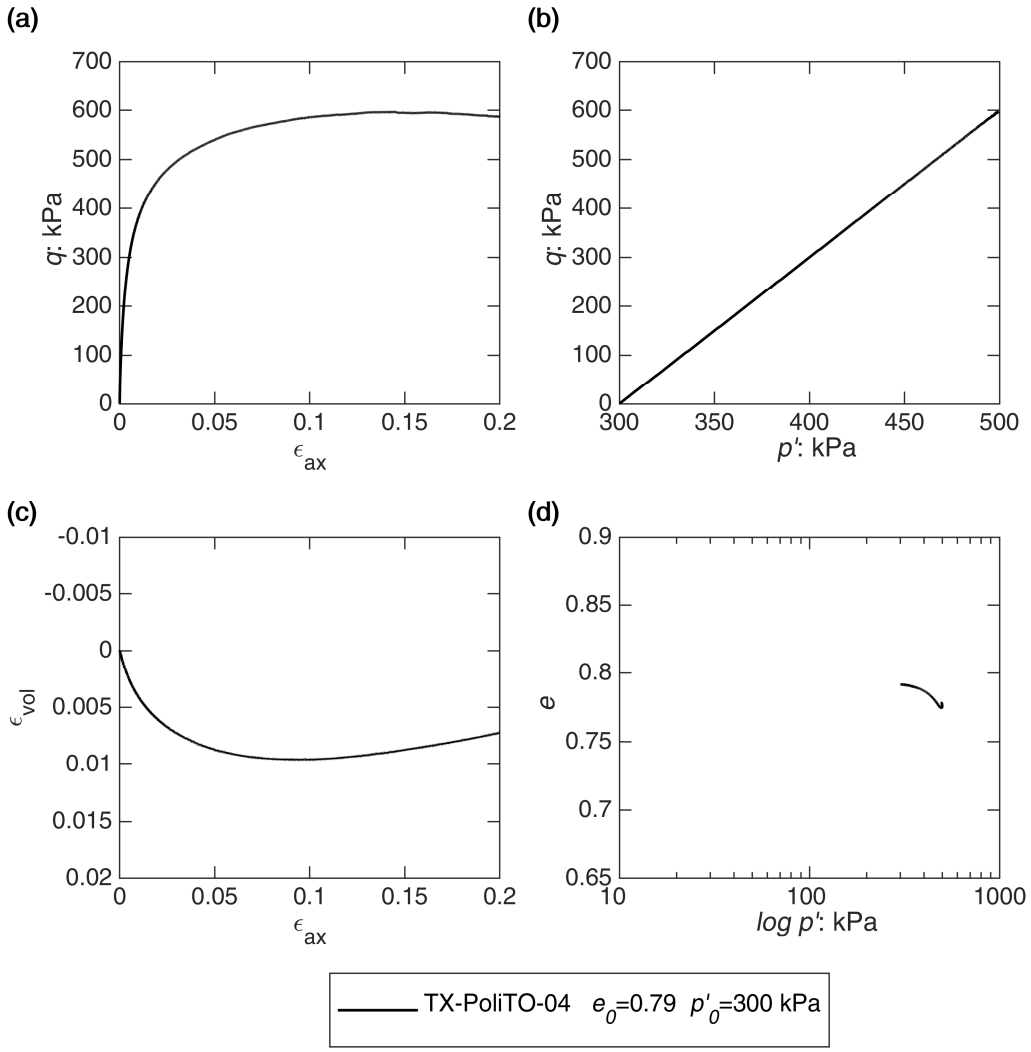

Figure 4.11: Triaxial test on a loose (i.e. D_R of 21.6%) sample of Perth sand: (a) deviatoric stress vs axial strain; (b) effective stress paths; (c) volumetric strain vs axial strain; (d) void ratio vs mean effective confining stress.

In volumetric terms, the sand experiences a contraction up to a maximum ε_{vol} of about 0.010 and then it slightly decreases down to 0.007. It is worth noticing that although the decrease of ε_{vol} is apparently substantial, it corresponds to a change of 0.004 in void ratio and it is thus practically negligible. In this specific test, the initial state of the soil was probably really close to being critical and low volumetric strains developed during the test. Consequently, the constant volume condition seems to be verified.

4.2.3 Triaxial tests on dense samples of Perth sand

The stress-strain response of Perth sand samples denser than critical is analyzed in this section regarding the results of a set of triaxial tests carried out by Bühler et al. (2019) at the Institute for Geotechnical Engineering of the ETH Zurich.

The samples were prepared through the wet pluviation technique, in contrast to the samples prepared at the Politecnico di Torino. The technique consists of pluviating the sand into a mould using an immersed tube filled with water to obtain an almost saturated homogeneous sample. During the pluviation, the mould is tapped to achieve the desired relative density. Further details about the technique and the experimental procedure can be found in Bühler et al. (2019).

As regards to the analysis of the data, the variables of interest were computed accordingly with the procedures reported in Section 4.2.2.4. It is worth mentioning that the results were reprocessed assuming a cylindrical deformation of the samples.

A summary of the tests is given in Table 4.3. In total, reference is made to the results of six drained triaxial tests (namely, from TX-ETH-01 to -06). The D_R in the Table is computed accordingly to the results reported in Section 4.1.3.

In the Table the results of the tests are reported in terms of the peak deviatoric stress, q_{peak}, the corresponding mean confining stress, p'_{peak}, and the peak friction angle, φ'_{peak}, computed as:

$$\varphi'_{peak} = \arcsin\left(\frac{3 \cdot M_{peak}}{6 + M_{peak}}\right) \tag{4.17}$$

where M_{peak} is the stress ratio at peak.

Table 4.3: Results of the triaxial tests carried out on dense samples of Perth sand (modified from Bühler et al., 2019).

Test name	Drainage	p'_0 [kPa]	e_0	D_R [%]	q_{peak} [kPa]	p'_{peak} [kPa]	φ'_{peak} [°]	ψ_{peak} [°]
TX-ETH-01	Drained	50	0.58	78.6	188	112	40.9	16.0
TX-ETH-02	Drained	100	0.54	88.1	387	230	41.1	17.2
TX-ETH-03	Drained	50	0.52	93.7	218	123	43.2	19.3
TX-ETH-04	Drained	200	0.53	93.2	776	459	41.3	18.2
TX-ETH-05	Drained	400	0.51	96.6	1476	893	40.4	17.2
TX-ETH-06	Drained	101	0.53	92.7	393	232	41.4	18.1

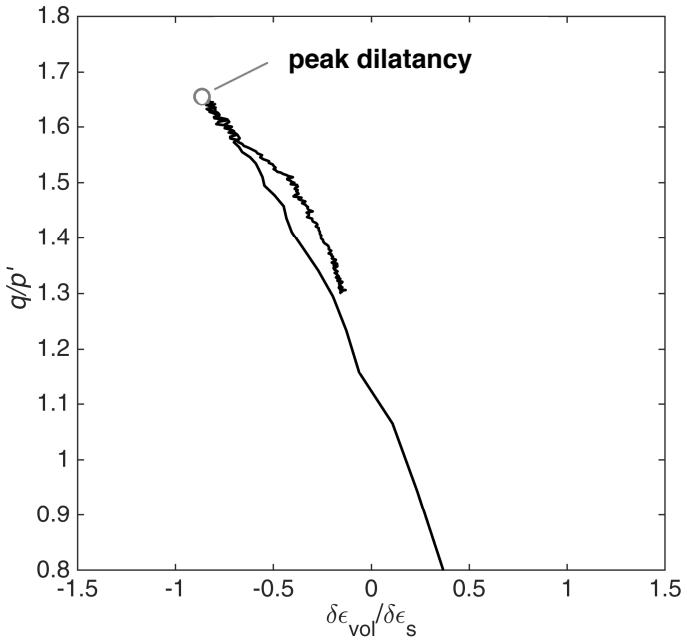

Figure 4.12: Stress-dilatancy plot for test TX-ETH-05 (data from Bühler et al., 2019).

Table 4.3 also reports the dilatancy angle at peak, ψ_{peak}. The latter is defined via Eq. (4.18), according to the approach proposed by Bolton (1986) based on the Rowe's (1962; 1964) stress-dilatancy theory:

$$\psi_{peak} = \arcsin\left(\frac{-\left(\delta\varepsilon_{vol}/\delta\varepsilon_{ax}\right)_{peak}}{2-\left(\delta\varepsilon_{vol}/\delta\varepsilon_{ax}\right)_{peak}}\right) \tag{4.18}$$

where $\delta\varepsilon_{vol}$ and $\delta\varepsilon_{ax}$ are the volumetric and axial strain increments at peak.

The peak condition was identified by looking at the stress-dilatancy plots during shearing. Figure 4.12 reports, as an example, the results for test TX-ETH-05. Initially, the dilatancy rapidly increases, together with the stress ratio. At peak, both q/p' and the dilatancy reach the maximum, corresponding to ψ_{peak} and φ'_{peak}. Subsequently, q/p' decreases again, eventually reaching the critical state value for a null dilatancy (i.e. constant volume condition).

Unfortunately, in all the tests here reported the critical state condition was not achieved, although the high axial strain levels reached.

The tests from TX-ETH-03 to -06 were performed starting from a e_0 of 0.51-0.53 with p'_0, ranging from 50 to 400 kPa. In tests TX-ETH-01 and -02 the initial states were slightly looser (i.e. e_0 of 0.58 and 0.54, respectively).

The results of the tests carried out on very dense (i.e. D_R ranging from 92.7% to 96.6%) samples are reported in Figure 4.13. As expected, q increases monotonically up to the peak value, q_{peak}, after which all the samples experience a significant softening, moving towards the critical state condition. By increasing p'_0 from 50 to 400 kPa, the tendency of the sand to dilate is slightly inhibited, reducing ψ_{peak} from 19.3 to 17.2°. As a consequence, φ'_{peak} also decreases from 43.4 to 40.4°. On the other side, q_{peak} increases with p'_0. Moreover, the larger is the p'_0 the larger is the axial strain needed to reach the peak condition.

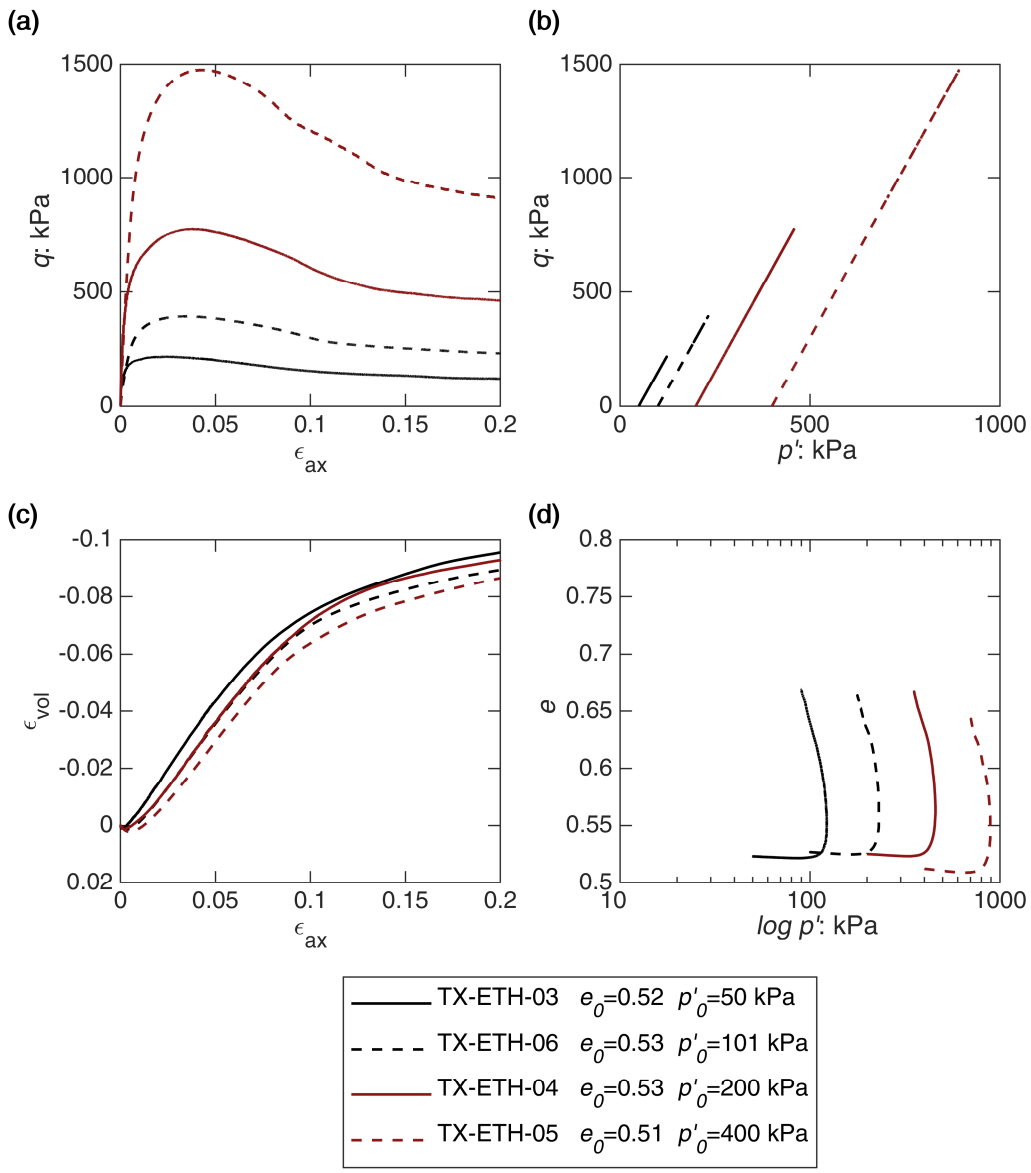

Figure 4.13: Triaxial test on very dense (i.e. D_R of 92.7-96.6%) samples of Perth sand: (a) deviatoric stress vs axial strain; (b) effective stress paths; (c) volumetric strain vs axial strain; (d) void ratio vs mean effective confining stress (data from Bühler et al., 2019).

Figure 4.14 reports the results of tests TX-ETH-01 and -02, carried out on samples with a D_R of 78.6 and 88.1% at a p'_0 of 50 and 100 kPa, respectively. In test TX-ETH-02, the initial state is significantly looser to the other tests. As a consequence, although the test was performed at confining pressure of 50 kPa, the sample exhibits a lower tendency to dilate and a φ'_{peak} of 40.9°.

Conversely, the initial state in test TX-ETH-02 is quite close to the one in test TX-ETH-06, performed on a sample slightly denser. Consequently, the stress-strain behaviour observed in the two tests is similar, with both φ'_{peak} and ψ_{peak} just lower in test TX-ETH-01.

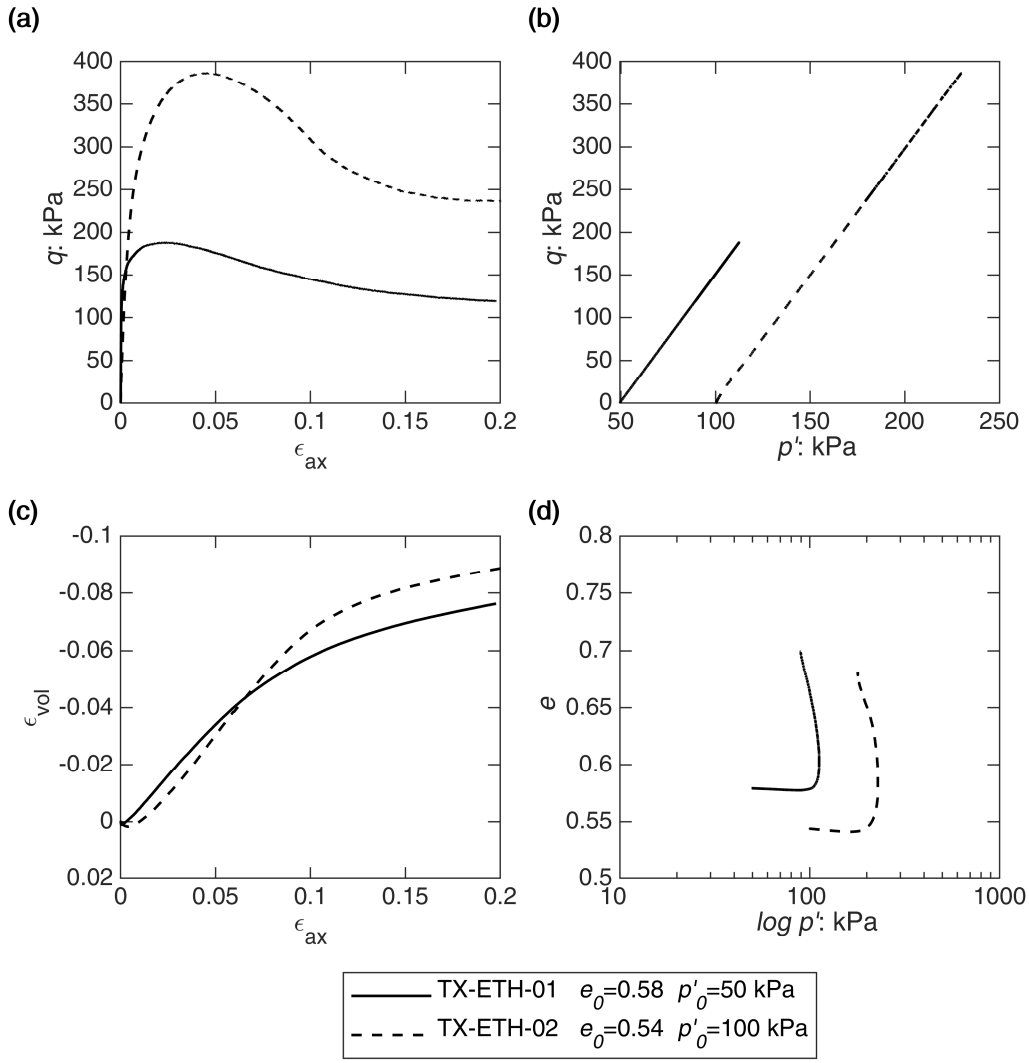

Figure 4.14: Triaxial test dense (i.e. D_R of 78.6 and 88.1%) samples of Perth sand: (a) deviatoric stress vs axial strain; (b) effective stress paths; (c) volumetric strain vs axial strain; (d) void ratio vs mean effective confining stress (data from Bühler et al., 2019).

4.2.4 Critical State Line of the Perth sand

The position of the Critical State Line is studied in this section with reference to the results of the triaxial tests performed at the Politecnico di Torino. The graphs of q and ε_{vol} (or Δu_w in drained conditions) versus ε_{ax} have to be observed to define whether the critical state was reached or not during a test.

However, the assessment of the critical state condition is somehow really difficult and affected by significant uncertainties. The stress-dilatancy plots (i.e. q/p' versus $\delta\varepsilon_{vol}/\delta\varepsilon_s$ in drained conditions or, equivalently, q/p' versus $\delta\Delta u_w/\delta\varepsilon_s$ in undrained conditions) are helpful to better identify, together with the other graphs, the onset of the critical state.

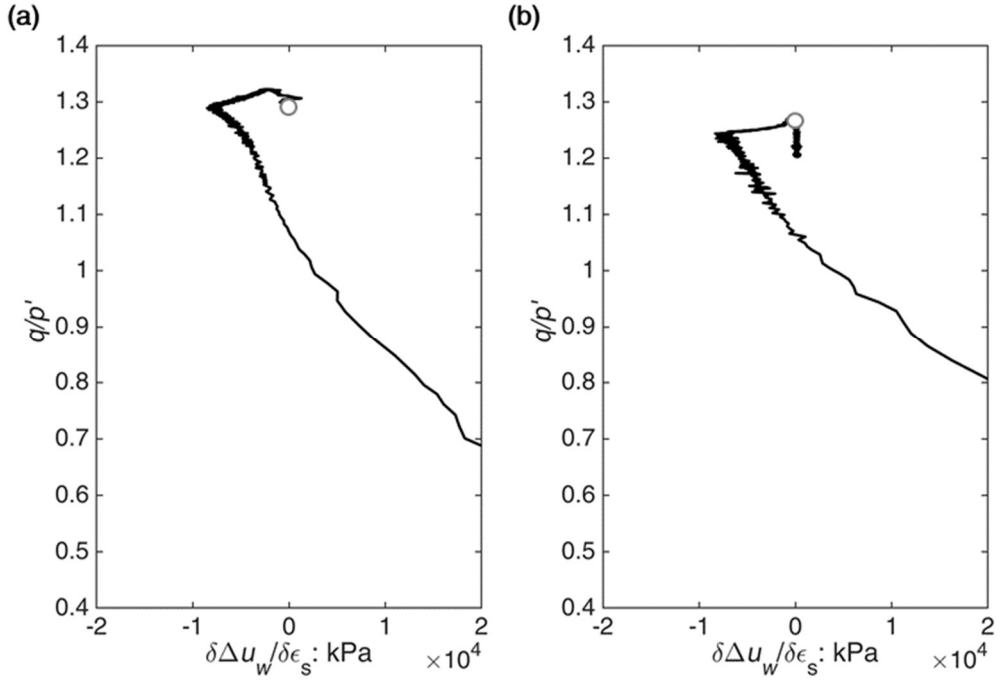

Figure 4.15: Stress ratio vs pore pressure build-up rate: (a) test TX-PoliTO-01; (b) test TX-PoliTO-02.

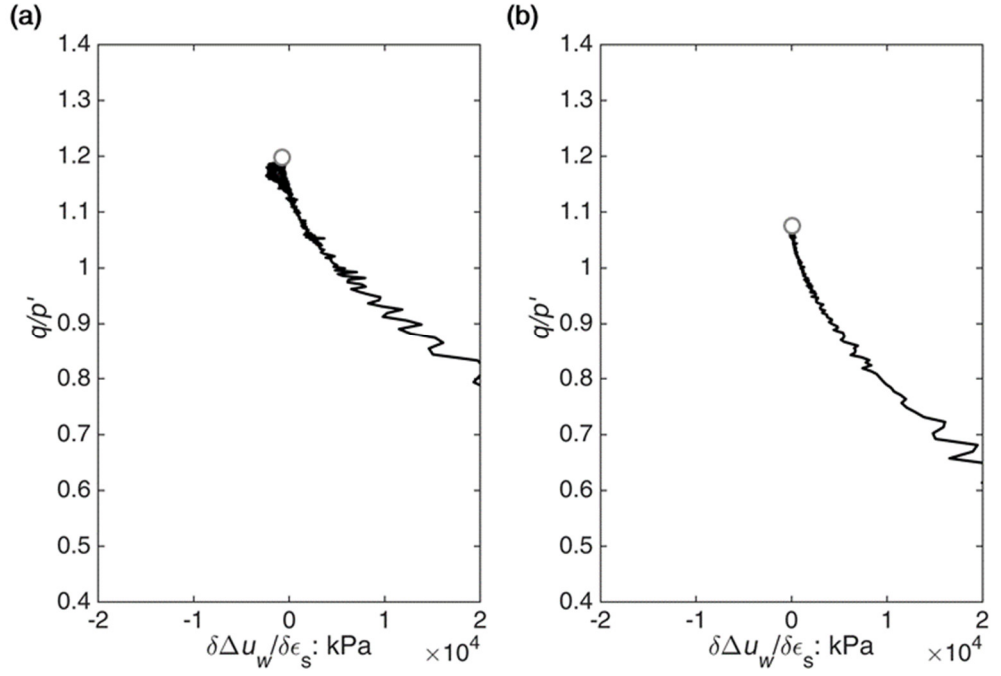

Figure 4.16: Stress ratio vs pore pressure build-up rate: (a) test TX-PoliTO-03; (b) test TX-PoliTO-05.

Figure 4.15 reports the plots for the two tests carried out on medium-dense sand samples (i.e., TX-PoliTO-01 and -02). Both the tests show an initial increase of the stress ratio together with an increase of the negative pore pressure build-up rate. The latter increases up to a peak negative value, corresponding to the peak dilatancy in drained condition. Subsequently, the negative $\delta\Delta u_w/\delta\varepsilon_s$ drop, reaching a zero value at the onset of the critical state. For the two tests, these points (represented with grey circles in the figure) were identified as critical state points. In the test TX-

PoliTO-02, the onset of the critical state condition is quite clear also in terms of stabilization of q and Δu_w. Conversely, it is not so clear if the critical state was effectively reached at the end of test TX-PoliTO-01 (see Figure 4.9).

The two very loose samples (i.e., TX-PoliTO-03 and -05) showed a different behaviour. In test TX-PoliTO-03 the sample experiences temporary liquefaction, identified in the stress-dilatancy plot by a progressive decrease of the positive $\delta\Delta u_w/\delta\varepsilon_s$ to zero (Figure 4.16.a). This point is referred to as Quasi-Steady State and is followed by a further increase of the deviatoric stress due to the phase transformation (see Figure 4.10). In contrast, in test TX-PoliTO-05 the sample exhibits complete liquefaction, reaching and maintaining the critical state characterized by a null $\delta\Delta u_w/\delta\varepsilon_s$ (Figure 4.16.b).

The stress-dilatancy plot of test TX-PoliTO-04 is presented in Figure 4.17. The loose sample exhibit a contractive behaviour characterized by an initial positive $\delta\varepsilon_{vol}/\delta\varepsilon_s$. The stress-ratio progressively increases, reaching an almost constant value for a null dilatancy. After this point also q and Δu_w are almost stable, as shown in Figure 4.11. This point was then identified as a critical state point.

A summary of the critical state points is given in Table 4.4. It is worth emphasising that it was not always straightforward to identify a point as critical, so significant uncertainties could affect the results. Moreover, for the two tests performed on medium-dense samples, it is not possible to properly identify the void ratios at critical. The tendency of medium-dense samples to dilate implies, under undrained conditions, a continuous decrease of the back-pressure until the critical state is reached (Figure 4.9.c). As observed by other Authors in the past (e.g., Whitman and Healy, 1962; McManus and Davis, 1997; Gawin and Sanavia, 2010), the latter could lead to cavitation of the pore fluid and, in turn, to partially drained conditions. No values of void ratios at critical are thus reported for these tests in the table.

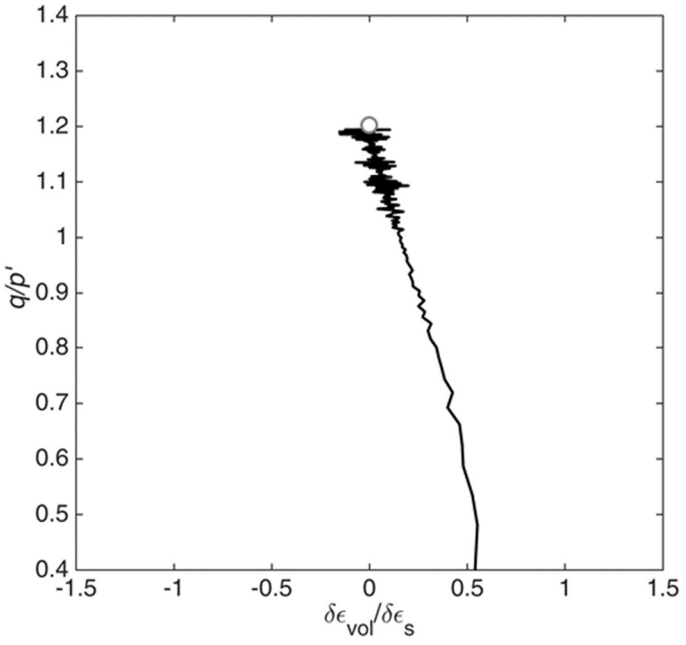

Figure 4.17: Stress-dilatancy plot for test TX-PoliTO-04.

Table 4.4: Results of the triaxial tests carried out at the Politecnico di Torino.

Test name	Drainage	p'_0 [kPa]	e_0	D_R [%]	p'_{CS} [kPa]	q_{CS} [kPa]	e_{CS}
TX-PoliTO-01	Undrained	99	0.70	45.9	840*	1092*	-
TX-PoliTO-02	Undrained	199	0.72	40.5	611	769	-
TX-PoliTO-03	Undrained	299	0.79	21.6	168**	186**	0.79**
TX-PoliTO-04	Drained	300	0.79	21.6	496	586	0.77
TX-PoliTO-05	Undrained	198	0.84	8.1	13	14	0.84

* Critical State not clearly identified, point not used for the statistical regression
** Quasi-Steady State point

The CSL of the Perth sand is represented in Figure 4.18. The slope of the line corresponding to the critical state stress ratio, M_{CS}, was obtained through a least-square regression of the three critical state points clearly identified. In the plot, the quasi-steady state point obtained from test TX-PoliTO-03 is also reported for comparison. Once obtained M_{CS}, the critical state friction angle, φ'_{CS}, was computed as:

$$\varphi'_{CS} = \arcsin\left(\frac{3 \cdot M_{CS}}{6 + M_{CS}}\right) \tag{4.19}$$

A M_{CS} of 1.225 was obtained through the regression, corresponding to a φ'_{CS} of 30.6°. The associated standard deviation is equal to ±0.7°.

The position of the Critical State Line in the $v - \log p'$ plane is analyzed in Figure 4.19. In the plot, both the quasi-steady and the critical state points are reported, together with the paths followed by the samples during the compression phase.

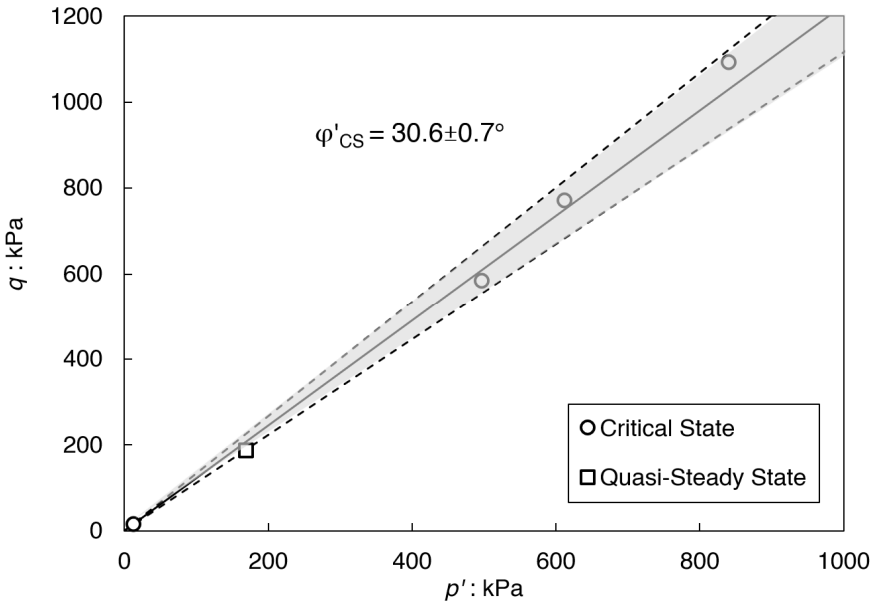

Figure 4.18: Critical State Line of the Perth sand in the $q - p'$ plane with the associated 95% confidence interval.

The projection of the CSL in the volumetric plane is usually described as (Been and Jefferies, 1985):

$$v_{CS} = v_\lambda - \lambda \cdot \ln p' \tag{4.20}$$

where v_λ and λ are the calibration parameters.

For the two tests carried out on medium-dense sand samples localized volumetric strains are thought to have originated during the compression due to cavitation of the pore fluid. The actual critical state specific volumes are thus expected to be higher, consistently with the dilative behaviour of the samples. By excluding also the quasi-steady state point, just two points can be used to define the CSL.

Figure 4.19 reports an estimation of the CSL according to these points. By expressing the confining pressure in kPa, the calibration parameters v_λ and λ are equal to 1.89 and 0.02, respectively. The position of the line appears to be reasonable and the intercept is quite close to the maximum specific volume associated with the loosest possible state (see Section 4.1.3). However, it is worth noticing that the number of points used is not sufficient to accurately evaluate the CSL. The equation here proposed has thus to be considered just a rough estimate of the CSL and care must be taken when it is adopted in practice.

4.3 Resonant Column tests

A set of Resonant Column, RC, tests was carried out aiming at investigating the cyclic behaviour of the Perth sand. In this section, an introduction to the cyclic stress-strain response of soils is firstly given. The experimental methodology adopted is then reported, together with the testing programme. Finally, the results of the tests are analyzed to identify the dynamic properties of the Perth sand.

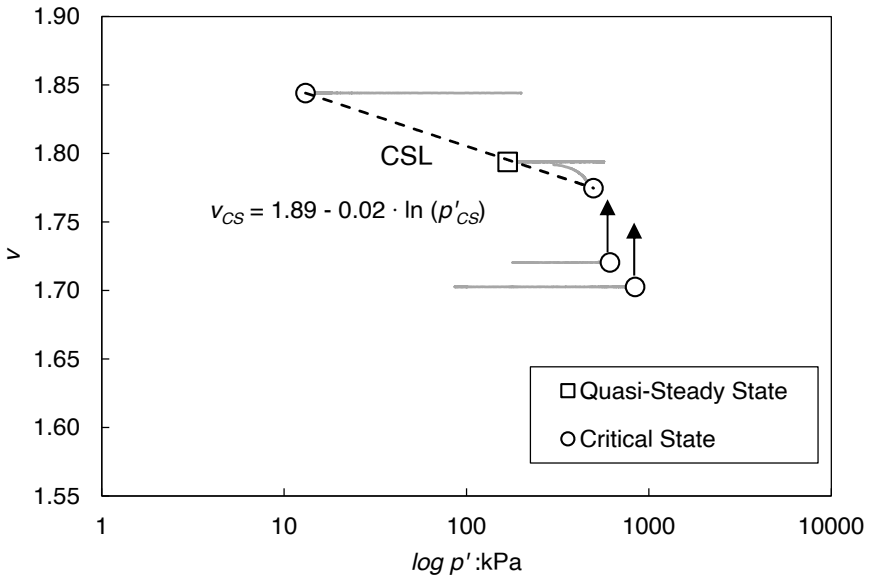

Figure 4.19: Estimate of the Critical State Line of the Perth sand in the $v - \log p'$ plane.

4.3.1 Stress-strain behaviour of soils under cyclic and dynamic loadings

The behaviour of soils under cyclic and dynamic loadings is quite complex and characterized by pronounced nonlinearity, degradation of the mechanical properties and coupling between shear and volumetric strains if the volumetric strain threshold is exceeded.

The soil response in dynamic conditions can be analyzed in analogy with an idealized hysteresis stress-strain loop, where τ and γ are the shear stress and the shear strain, respectively, while τ_c and γ_c are the cyclic shear stress amplitude and the cyclic shear strain amplitude, respectively (Figure 4.20). The cycle is usually described adopting as reference parameters the secant shear modulus, G_S, and the material damping ratio, D. At very small strains approaching zero, the behaviour of the soil is almost linear and G_S assumes its maximum value, G_0. At higher shear strains, the nonlinearity of the stress-strain relationship is typically described by a normalized modulus reduction curve, $G_S/G_0 - \gamma_c$ (Seed and Idriss, 1970).

The material damping ratio represents the energy internally dissipated by the soil under cyclic loading conditions, as a consequence of friction between soil particles, nonlinearity and viscous effects. By virtue of the mathematical convenience of a visco-elastic formulation, the soil damping at a given cyclic shear strain amplitude is usually computed in analogy to the equivalent viscous damping ratio. The latter is the critical damping ratio of a Single-Degree-Of-Freedom system constituted by a mass connected to a linearly elastic spring and a viscous dashpot. If the system is subjected to harmonic vibrations, the stress-strain curve at resonance is described by an ellipse. The damping ratio can thus be evaluated as:

$$D = \frac{W_D}{4\pi W_S} \tag{4.21}$$

where W_D and W_S are, respectively, the energy dissipated and the maximum elastic energy stored in one cycle.

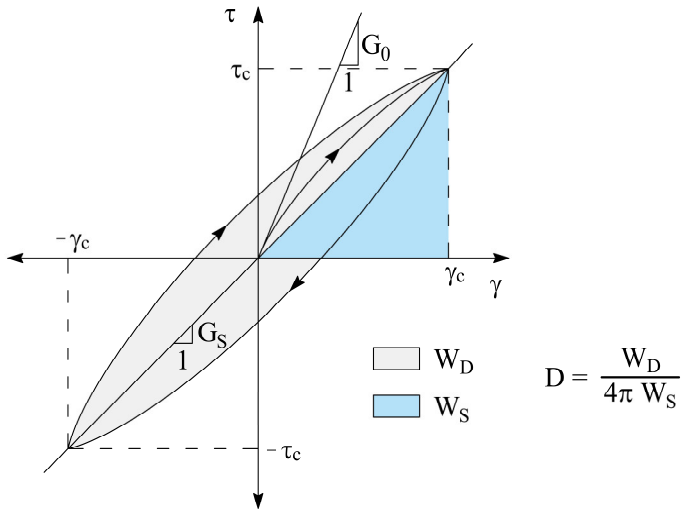

Figure 4.20: Parameters describing an idealized hysteretic stress-strain loop (from Ciancimino et al., 2019).

The hysteresis loop typically described by soils under cyclic loadings (Figure 4.20) is similar to the ellipse described by the SDOF system and the material damping can, therefore, be expressed in terms of the area of the loop.

Nonlinearity in the stress-strain soil behaviour leads to an increase of the area enclosed by one cycle and, thus, of D. The relationship between D and γ_c is represented by the material damping curve, $D-\gamma_c$. Both the modulus reduction and the damping (MRD) curves are usually represented in a semi-logarithmic plot.

By knowing the MRD curves and the G_0, it should be possible, in principle, to predict the response of soils under cyclic and dynamic loadings, at least in the small-to-medium strain range.

The behaviour of soils is strongly dependent on the cyclic strain amplitude, not only because of the shear modulus decay but also in terms of volumetric strains. Silver and Seed (1971) and Youd (1972) firstly noticed the existence of a volumetric shear strain threshold in dry sands, above which soils experience significant cyclic compression. Then, Stoll and Kald (1977) reported the presence of a cyclic threshold shear strain in a cohesionless silty soil associated with the pore water pressure build-up in undrained conditions. The presence of the two abovementioned shear strain limits in sands was subsequently fully confirmed by Dobry et al. (1982) from both the experimental and the theoretical point of view. The Authors also established the coincidence of the two thresholds.

The concept was addressed also by Lo Presti (1989, 1991) who highlighted the dependency of threshold strains in clayey soils from soil plasticity. The issue of threshold strains was then thoroughly examined by Vucetic (1992, 1994) as well as the dependency of the cyclic thresholds on the plasticity index. The larger is the plasticity index of a soil, the larger is the volumetric threshold. As a consequence, lower shear strain amplitudes are necessary to trigger the tendency of sands to densify (Hsu and Vucetic, 2004). Vucetic (1994) also introduced the idea of dividing the cyclic soil behaviour into three different domains, namely very small, small-to-medium and medium-to-large strains.

At very small strains, below the linearity threshold, the soil behaves almost linearly and G_S can be approximated to its constant, small-strain, value G_0. Because of this convenient engineering approximation, from a mathematical point of view, the area inside the hysteresis loop is null at very small strains, hence no dissipation should take place. However, the experimental evidence highlighted a minimum amount of energy dissipated, given mainly by friction between particles and viscosity. The damping in the small-strain range is thus usually approximated to a constant minimum value, D_0. Between the linear and the volumetric threshold, the soil behaves nonlinearly and the hysteretic behaviour is characterized by minor changes in the microstructure. Above the volumetric threshold, at medium-to-large strains, soils exhibit a gradual degradation behaviour, experiencing permanent changes in the microstructure and, in drained conditions, volume variation. Vucetic (1994) and more recently Tabata and Vucetic (2010) and Mortezaie and Vucetic (2016) distinguished the amplitude below which there is practically no degradation, defined as cyclic degradation threshold shear strain, and the amplitude below which

there is practically no permanent cyclic pore water pressure build-up (or, equivalently, no volumetric strains), known as cyclic pore pressure generation threshold shear strain.

4.3.2 Factors affecting the dynamic parameters of soils

Many research efforts have been devoted in the past to identifying the key parameters affecting the cyclic behaviour of soils, namely: the plasticity index, PI, the initial effective confining pressure, p'_0, the loading frequency, f, the number of loading cycles, and the over-consolidation ratio.

Kokusho et al. (1982) firstly showed the influence of the plasticity index on the normalized modulus reduction curves of fine-grained soils. Soils characterized by high PI exhibit higher G_S/G_0 at a given γ_c amplitude. The correlations between the MRD curves and PI, at a given γ_c were subsequently presented by Dobry and Vucetic (1987) and Vucetic and Dobry (1991), showing that PI is the most influent parameter governing the nonlinear dynamic behaviour. The effect of p'_0 was recognized by Ishibashi and Zhang (1993) and Lanzo et al. (1997). Specifically, $G_S/G_0-\gamma_c$ curves tend to be higher with increasing p'_0, while lower $D-\gamma_c$ curves are expected. The influence of p'_0 is significant especially for non-plastic soils (e.g., Lanzo et al., 1997). The over-consolidation ratio is recognized as an increasing factor of G_S/G_0 in fine-grained soils, although it is considered to be a secondary parameter (e.g., Kokusho et al., 1982; Vucetic and Dobry, 1991; Darendeli, 2001). The characteristics of the dynamic loading also affect the nonlinear behaviour of soils (e.g., Isenhower and Stokoe, 1981; Stokoe et al., 1999; Lo Presti et al., 1997; Matešić and Vucetic, 2003). Its influence on G_S/G_0 is usually neglected, but it is considered a relevant parameter on D_0 (e.g., Darendeli, 2001; Ciancimino et al., 2019). Finally, the number of cycles becomes relevant above the cyclic degradation threshold (Tabata and Vucetic, 2010; Mortezaie and Vucetic, 2016).

The abovementioned parameters affect the dynamic properties of a variety of soils, ranging from fine-grained to granular materials. However, it is important to analyze their specific influence on the behaviour of sandy materials, together with the influence of the physical properties of the soils.

The main factors affecting the G_0 of sands are the void ratio and the effective confining pressure. Hardin and Richart (1963) for first pointed out their influence on the small-strain shear wave velocity, V_S, and thus on G_0. The latter increases for denser sands and with higher p'. Based on their experimental results, Hardin and Black (1966) proposed a relationship to estimate G_0, that can be written in a general, normalized, form as:

$$G_0 = A_G \cdot F(e) \cdot \left(\frac{p'}{p'_{atm}} \right)^{n_G} \tag{4.22}$$

where p'_{atm} is the atmospheric pressure, A_G and n_G are calibrated coefficients depending on the specific material, and $F(e)$ is the void ratio function. Several expressions were proposed in the past for $F(e)$. The original ones suggested by the Authors are:

$$F(e)=\frac{(2.97-e)^2}{1+e} \tag{4.23}$$

$$F(e)=\frac{(2.17-e)^2}{1+e} \tag{4.24}$$

proposed, respectively, for sand rounded in grains and angular quartz sand.

The parameters A_G and n_G depends mainly on the particle shape and the gradation of the granular material. Higher G_0 are expected for angular materials and for sands characterized by larger mean grain size, D_{50}. The two parameters have then to be defined specifically for each particular material. For reconstituted sands, A_G showed to range from 33 to 90 (with G_0 expressed in Mpa), while the exponent n_G is equal to about 0.4-0.6 (Hardin and Black, 1966; Iwasaki et al., 1978; Kokusho, 1980; Yu and Richart Jr, 1984; Santamarina et al., 2005).

The damping at small strains is also affected by the particle gradation and p'. Menq (2003) suggested that D_0 decreases with increasing p' and D_{50}, but increases with increasing C_u. The aforementioned dependencies were then included by the Author in the following empirical predictive equation:

$$D_0 = 0.55 \cdot C_u^{\,0.1} \cdot D_{50}^{\,-0.3} \cdot \left(\frac{p'}{p'_{atm}}\right)^{-0.08} \tag{4.25}$$

Additionally, Shibuya et al. (1995) showed that D_0 is also affected by the loading frequency. The Authors suggested the existence of three different branches of influence: (i) at low frequencies (<0.1Hz) the damping ratio tends to decrease with increasing frequencies; (ii) in the medium range (between 0.1 and 10 Hz, the typical seismic bandwidth) D_0 is almost constant, irrespectively of the loading frequency (iii) at frequencies larger than 10 Hz D_0 increases with f because of viscous effects. This effect exists independently from the strain level, but it becomes less relevant at high strains when the hysteretic damping increases.

In terms of MRD curves, the main parameters affecting the behaviour of granular materials are the confining pressure and the particle gradation. Menq (2003) showed their influence on the reference cyclic shear strain associated to G_S/G_0 of 0.5. With increasing p'_0, the reference cyclic shear strain increases, enlarging the almost linear strain range. Similarly, uniform sands characterized by low C_u present a wider linear range with respect to well-graded sands. Based on the framework previously defined by Darendeli (2001), the Author proposed an empirical model able to predict the MRD curves for sandy and gravelly soils as a function of the abovementioned main factors.

4.3.3 Resonant Column tests carried out at the Politecnico di Torino

A set of RC tests was carried out to study the cyclic behaviour of the Perth sand both at small strains and in the medium-to-large strain range. The tests were carried out using the combined Resonant Column and Torsional Shear device of the Geotechnical Laboratory of the Politecnico di Torino (Figure 4.21). The device is a

modified version of the free-fixed type apparatus designed at the University of Texas at Austin and described by Isenhower (1979). A full description of the device can be found in Pallara (1995). The tests were performed and processed according to the prescriptions given in ASTM D4015-15.

4.3.3.1 Laboratory equipment

A brief description of the instrumentation installed in the experimental device is here reported:

- An electromagnetic Stokoe-type driving system (SBEL, Arizona) is used to apply the torque at the top of the specimen. The driving system is constituted by eight coils and four magnets (Figure 4.21) and it is based on the interaction between the magnets and the magnetic field generated by the AC passing through the solenoids. The resulting motion of the magnets generates the torque applied to the sample. The motor is driven by an arbitrary function generator and a power amplifier, both computer-controlled. The loading amplitude is changed through the power amplifier to analyze the response of the sample at different strain levels, while the actual torque applied to the specimen is computed using a torque-voltage calibration curve (Lo Presti et al., 1993). The system can apply sinusoidal loadings within a wide range of frequencies, with a maximum amplitude of 1.1 Nm and an accuracy of $2.5 \cdot 10^{-5}$ Nm.
- The backpressure, as well as the radial pressure, are measured through Druck pressure transducers with a full-scale pressure of 1 MPa and an accuracy of ±0.5 kPa.
- An LVDT (Linear Variable Differential Transformer) rigidly connected to the top cap measures the axial strain with a full-scale of 4 mm and an accuracy of ±1 μm.
- The local radial strains are measured with two non-contact proximity Kaman transducers. The latter are piezoelectric ceramics transducers mounted in the cylindrical aluminium support at half the height of the sample. The transducers measure the distance from a small piece of aluminium glued on the membrane, allowing the determination of the changes in the diameter of the sample under the assumption of cylindrical deformations. The two transducers are characterized by a full range of 2.5 mm and an accuracy of ±1 μm.
- A pair of Kaman transducers measure the rotation at the top of the sample. The targets are rigidly connected to the driving system (and, thus, to the sample) at a radial distance of about 30 mm. The transducers can measure rotations up to 0.05 rad with an accuracy of about $1.7 \cdot 10^{-5}$ rad.
- An accelerometer, rigidly connected to the driving system, tracks the response of the sample to define the amplitude versus frequency response.

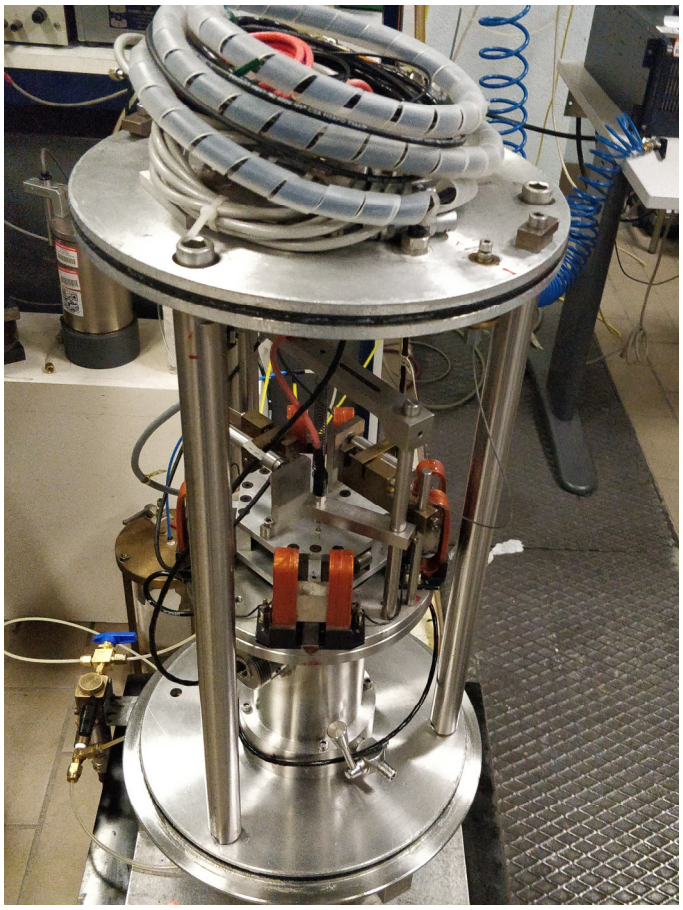

Figure 4.21: Combined Resonant Column and Torsional Shear device of the Geotechnical Laboratory of the Politecnico di Torino.

4.3.3.2 Sample preparation

The reconstituted specimens were prepared through the dry pluviation technique to achieve high relative densities maintaining an acceptable degree of homogeneity of the sample. The technique is fully consistent with the one used to prepare the centrifuge models.

The dry sand is poured into a latex standard membrane 0.25 mm thick, applied via vacuum against the wall of a cylindrical split mould mounted on the base of the cell (Figure 4.22.a). By adjusting the falling height and the openings of the container (directly related to the falling rate) it is possible to achieve a wide range of void ratios. The system was calibrated to obtain samples with void ratios close to the one used in the centrifuge tests (i.e. about 0.56).

The RC device is not equipped with a water flushing system. Therefore, the sample is saturated after the dry pluviation, letting the water flow from the porous stone at the bottom. When the water reaches the top surface, the drainage is closed, and the top cap is placed. After that the contact is made, the sample can be closed and set under negative pressure of about -30 kPa, which makes it stable during the assembly of the apparatus (Figure 4.22.b).

The actual initial dimensions of the specimen are measured considering, as representative values, the average of three determinations. The height is measured through a calliper, while a *π-tape* is used for the diameter. Both the instruments

have a precision of ±0.01 mm. The cylindrical samples have an initial height of about 100 mm and a diameter of about 50 mm. Henceforward, the variations in the dimensions of the sample are recorded by the instruments described in Section 4.3.3.1. At the end of the test, the sand will be collected and dried in a hoven at a constant temperature of 100C° to measure the dry mass of the sample and back-calculate the initial void ratio.

An aluminium cylindrical support is placed on the base of the device. The latter contains the sample and it is filled with oil to avoid possible passage of air through the membrane in case of tests executed on dry samples. The last part of the apparatus is then finally installed and the electromagnetic driving system is placed above the cylindrical support. The system is supported by a vertical spring to avoid undesired axial loadings and it is connected to the top cap.

After that all the sensors are mounted, the cell is sealed positioning an external steel cylinder. The negative internal pressure can then be gradually removed and the cell pressure simultaneously increased.

4.3.3.3 Testing procedure

Saturation

In the absence of a water flushing system, the samples are saturated directly after the dry pluviation. The saturation system allows to obtain reasonable initial degrees of saturation, but a further backpressure procedure has to be carried out to fully saturate the sample. The procedure is described in Section 4.2.2.3.

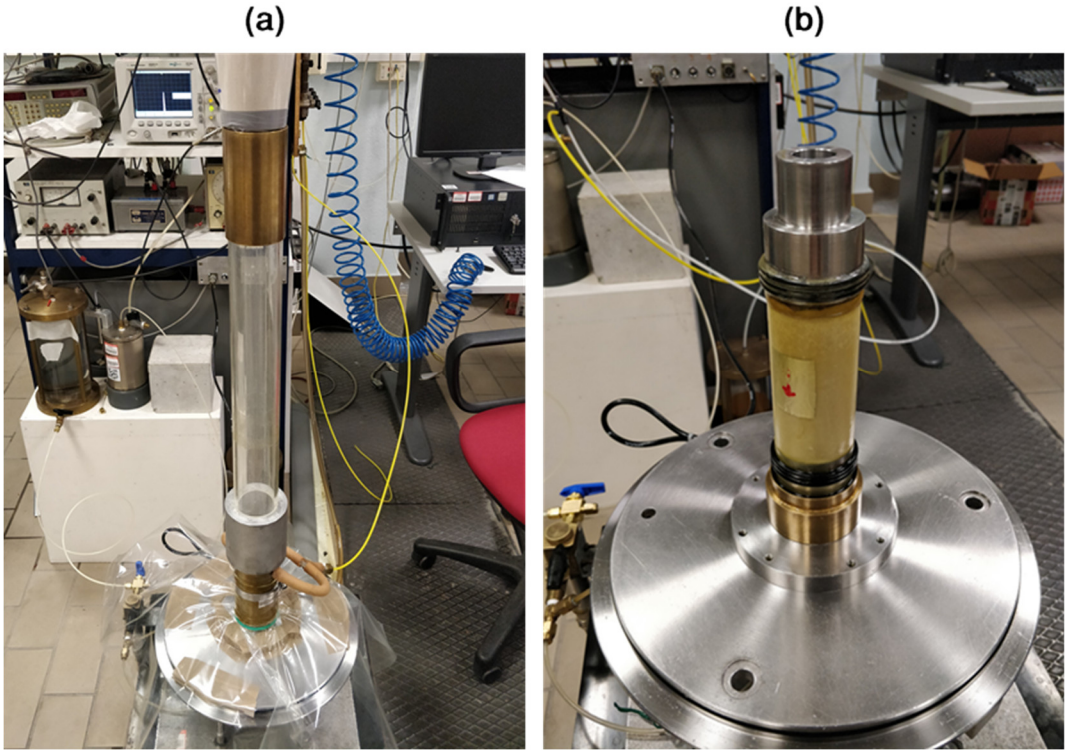

Figure 4.22: Sample preparation: (a) dry pluviation; (b) reconstituted sample.

Consolidation

All the tests were isotropically consolidated. The cell pressure is increased in undrained steps of 10-30 kPa until the desired value of effective confining pressure is reached. After each step, the drainage is opened for the time necessary to dissipate the excess pore water pressure (i.e. until the stabilization of the pore water pressure).

When the final effective confining pressure is reached, a further time of about one hour is waited in drained conditions to ensure that both the pore water pressure and the dimensions of the specimen are stable.

Cyclic loading

The electromagnetic driving system is used to excite the sample at the free top. The test is performed under loading control, applying torques with increasing amplitudes. The bottom of the specimen is fixed to ensure adequate (i.e., well-defined) boundary conditions.

For a given loading amplitude, a wide range of frequencies is analyzed to clearly identify the resonance condition of the first torsional mode of the specimen. Specifically, for each loading amplitude, a frequency sweep is applied around the expected resonance frequency. The sweep investigates a range of 40 Hz with a frequency-step of 0.1 Hz (i.e. 400 frequencies are investigated for each loading amplitude). For each frequency, 20 cycles of forced vibrations are applied, followed by 10 cycles of free vibrations. The loading amplitude is then increased and a new frequency sweep is applied. The apparatus can investigate cyclic shear strain amplitudes ranging from 10^{-5} to 0.5 %.

The tests are performed in undrained conditions and the eventual pore water pressure build-up is recorded. At the end of the test, the behaviour of the specimen at small-strains is again investigated ta analyze possible differences induced by the test. The same initial small-strain resonance frequency is expected if neither degradation nor pore pressure build-up took place.

4.3.3.4 Analysis of the data

The main parameters describing the state of the sand during the test are computed as follows:

- *Axial strain,* ε_{ax}: computed as:

$$\varepsilon_{ax} = \frac{\Delta H_s}{H_0} \tag{4.26}$$

  where ΔH_s (positive in compression) is measured through the LVDT and $H_{s,0}$ is set equal to the height of the sample after the consolidation.

- *Volumetric strain,* ε_{vol}: the changes in volume are monitored through the geometrical deformations measured by the axial LVDT and the two horizontal Kaman transducers. The volume of the sample, assuming cylindrical deformations, can be computed as:

$$V_s = \frac{\pi\left(\Delta D_s + D_{s,0}\right)^2 \left(\Delta H_s + H_{s,0}\right)}{4} \tag{4.27}$$

where D_s is the diameter of the sample.

- *Void ratio,* e: computed as:

$$e = \frac{V_{s,0}\left(1-\varepsilon_{vol}\right)}{M_S / \left(G_s \cdot \rho_w\right)} - 1 \tag{4.28}$$

where M_S is the dry mass of the soil.

- *Radial pressure and axial pressure,* σ_{rad} and σ_{ax}: both equal to the cell pressure (i.e. test carried out under isotropic conditions) directly measured through the pressure transducer.
- *Pore water pressure,* u_w: directly measured through the pressure transducer.
- Mean effective confining pressure, p': computed as:

$$p' = \frac{\sigma_{ax} + 2\sigma_{rad}}{3} - u_w \tag{4.29}$$

4.3.3.5 Determination of the dynamic properties

The dynamic properties of the soil are obtained applying the theory of torsional waves propagation in a linear visco-elastic medium in steady-state conditions (Richart et al., 1970).

The output Amplitude, A, given by the accelerometer is proportional to the rotation of the sample and can thus be used to track the soil response. In total, 20 cycles of forced vibrations are applied for each loading frequency, followed by 10 cycles of free vibrations recorded. As an example, Figure 4.23.a reports the time-history of A for one loading frequency.

The cyclic amplitude, characteristic of the response of the sample, is then computed as the *Root Mean Square* of the last 15 cycles of forced vibrations. The first 5 cycles are excluded because the motion of the sample could still be in the transient phase. The computation is repeated for each loading frequency and the amplitude versus frequency curve is plotted to identify the first torsional resonance frequency of the sample, f_0, corresponding to the maximum amplitude, $A_{\max}$ (Figure 4.23.b).

The V_s is then computed via the equation of motion for torsional vibrations, assuming the soil as a linear visco-elastic medium (Richart et al., 1970):

$$\frac{I_\theta}{I_t} = \frac{2\pi f_0 H}{V_S} \cdot \tan\left(\frac{2\pi f_0 H}{V_S}\right) \tag{4.30}$$

where I_θ is the mass polar moment of inertia of the specimen, I_t is the driving system polar moment of inertia and H is the height of the specimen.

The G_S can then be obtained through the well-known relationship:

$$G_S = \rho \cdot V_S^2 \tag{4.31}$$

being ρ the density of the soil.

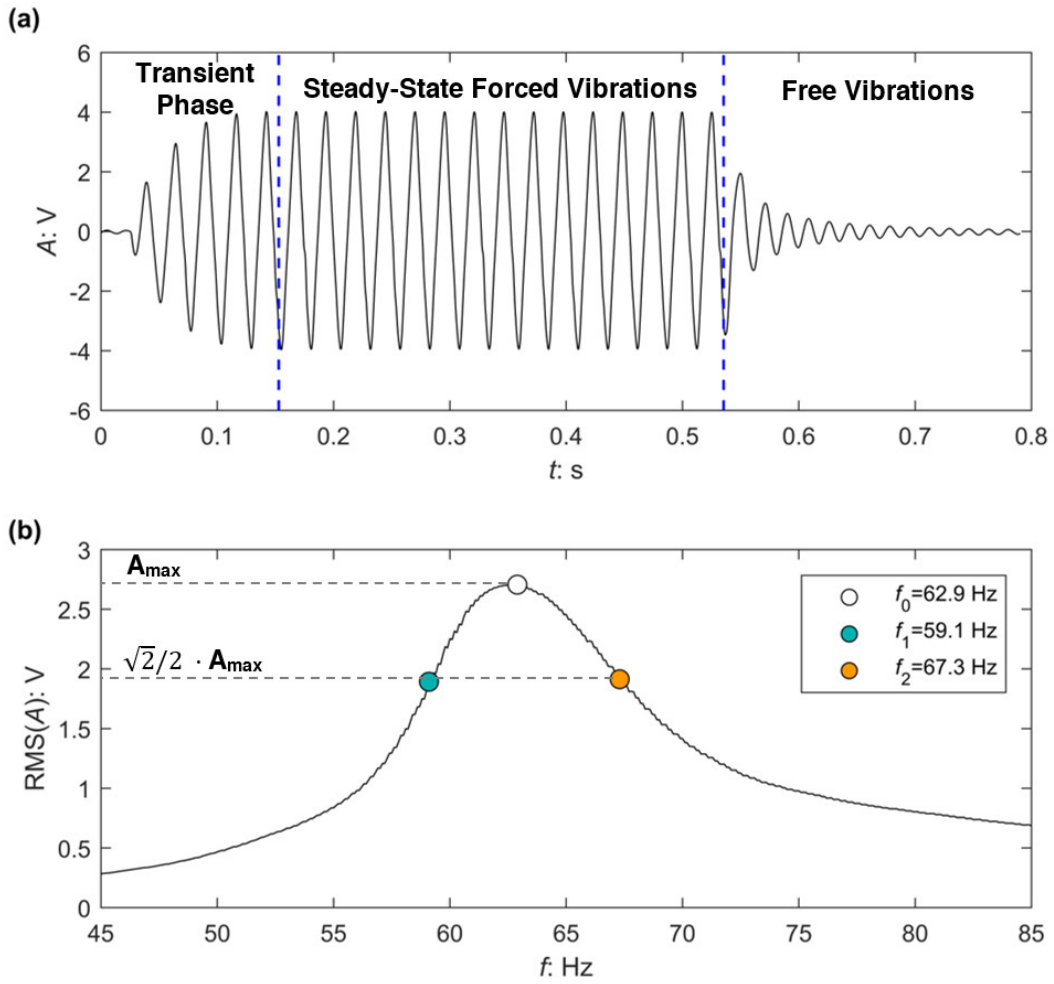

Figure 4.23: Typical results of a RC test at a given loading amplitude: (a) time-history of the accelerometer output amplitude for one loading frequency; (b) amplitude versus frequency response curve.

The shear strain is not constant in a full cylinder subjected to a torsional motion but increases radially (Figure 4.24). For a given horizontal section, a reference cyclic shear strain amplitude, γ_{max}, has thus to be computed. The latter is usually defined as 2/3 of the maximum shear strain, γ_{max} (Hardin and Drnevich, 1972).

In a fixed-free device the waveform is almost linear along the vertical direction, so γ_{max} is almost constant (Woods, 1978) and can be computed as:

$$\gamma_{max} = \frac{\theta_s \cdot D_s}{2 \cdot H} \tag{4.32}$$

where θ_s is the maximum rotation of the sample, obtained by double integrating the angular acceleration defined through the accelerometer.

The damping ratio can be obtained using two different methods, namely the half-power bandwidth and the free-vibration decay method. In the half-power bandwidth method, the connection between the shape of the frequency response curve and the dissipated energy is exploited (Figure 4.23.b). The soil is assumed to behave linearly: the method is therefore reliable only in the small-strain range.

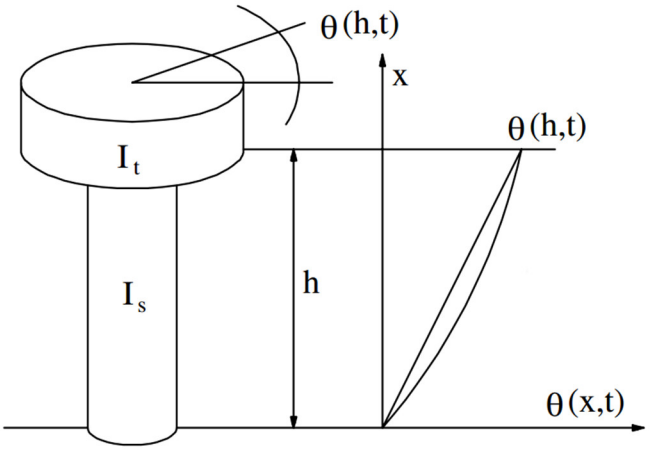

Figure 4.24: Fixed-free Resonant Column scheme (from Pallara, 1995).

It can be shown that, for small values of the damping ratio, the latter can be evaluated as:

$$D = \frac{f_2 - f_1}{f_0} \tag{4.33}$$

where f_1 and f_2 are the frequencies associated with an amplitude equal to $\sqrt{2}/2\, A_{\max}$.

Alternatively, the free-vibration decay method can be used to obtain the damping ratio from the amplitude decay of the torsional oscillations at the resonance frequency. At the end of the forced vibrations, the input current is switched off and 10 cycles of damped free vibrations are recorded by the accelerometer. By knowing two successive peak amplitudes (z_n and z_{n+1} corresponding, respectively, to the *n*-th and *n+1*-th cycle), the logarithmic decrement δ_{n+1} can be computed as:

$$\delta_{n+1} = \ln\left(\frac{z_n}{z_{n+1}}\right) \tag{4.34}$$

The logarithmic decrement is obtained for the first three successive peaks (and valleys), then an average value, δ, is used to obtain the damping ratio as:

$$D = \frac{\delta}{2\pi} \tag{4.35}$$

The two values obtained considering both the first three peaks and valleys are finally averaged to get the damping ratio. Figure 4.25 reports as an example the application of the method for a loading amplitude.

The two methods are characterized by different advantages and disadvantages. When the free-vibration method is used the average strain amplitude decays at each cycle. As a consequence D slightly decreases from a peak to another, especially at high strains. Conversely, the linear visco-elastic assumption inherent in the half-power bandwidth method is acceptable just for small D values, when the shape of the amplitude versus frequency curve is still symmetric.

Moreover, a well-recognized source of error in RC measurements of D from forced vibrations arises from the use of an electromagnetic driving system to provide the torsional excitation (e.g., Kim, 1991; Hwang, 1997; Cascante et al., 2003; Meng and Rix, 2003; Wang et al., 2003).

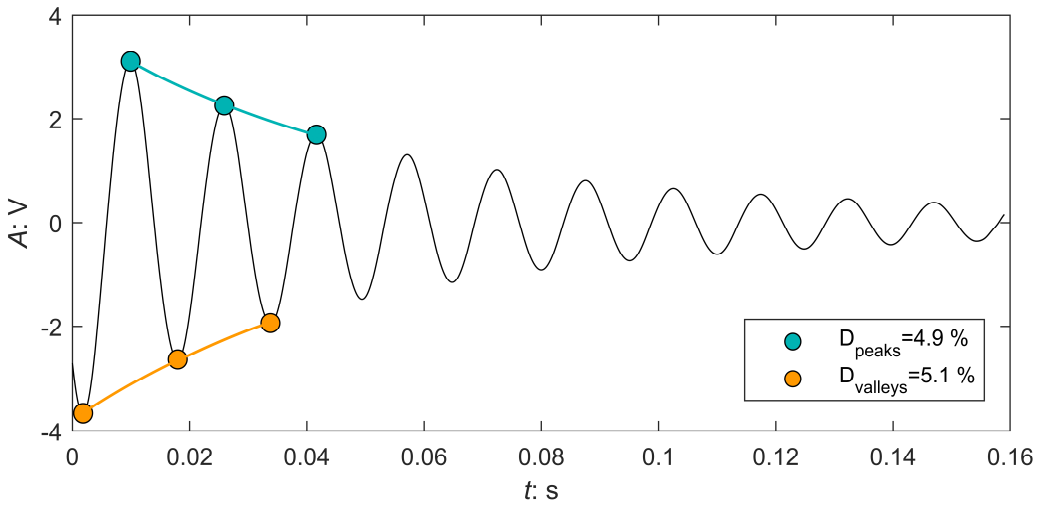

Figure 4.25: Free-vibration decay method.

The driving system is based on the interaction between the magnets and the magnetic field generated by the AC passing through the solenoids. The driving torque applied to the sample is given by the resulting motion of the magnets. Meanwhile, the motion of the magnets induces an electromagnetic force which is opposed to the motion. The phenomenon results in equipment-generated damping which is added to the actual material damping. The bias can be substantial, especially in the small-strain range where small values of material damping are expected. Different studies suggested correcting the results of the RC test by subtracting the equipment generated damping. The latter has to be obtained through a calibration procedure of the apparatus as a function of the loading frequency (e.g., Kim, 1991; Hwang, 1997; Wang et al., 2003). However, the extent of the bias is not yet totally understood.

In the present work, reference is made just to the results of the free-vibration decay method, which is supposed to be less affected by possible biases.

4.3.3.6 Results

The experimental investigation focuses on the determination of the dynamic properties of the Perth sand in a dense state, as close as possible to the one obtained in the centrifuge models. Two full multistage tests were initially carried out on saturated samples, namely RC-PoliTO-01 and -02. A full multistage test comprises a series of RC tests carried out at increasing initial confining pressures. One stage includes an initial consolidation phase up to p'_0 (e.g. 25 kPa), followed by a full RC test performed in undrained mode. At the end of the stage, keeping the drainage closed, the small-strain behaviour of the sample is again investigated to study the changes induced by the eventual pore water pressure build-up. Subsequently, the drainage is opened to allow the sample to change in volume and, then, to dissipate the excess pore water pressure. Afterwards, a new stage starts consolidating the sample to a larger p'_0.

The multistage procedure allows investigating the cyclic behaviour of the sample at increasing confining pressures. Analogous testing programmes were already

successfully applied in the past by other Authors to define the MRD curves of sands for a range of p'_0 (e.g., Molina-Gómez et al., 2020).

Some doubts could anyway arise about eventual disturbance effects induced by the previous stages on the tests performed at larger p'_0. As already stated, when a sand sample is excited in undrained conditions it exhibits, above the volumetric threshold, a pore pressure build-up. Subsequently, during the consolidation phase, the sample experiences permanent changes in the microstructure and further densification. These changes can strongly affect the dynamic parameters of the soil measured in the subsequent stages of the tests. The changes in volume due to the densification of the sample are usually recorded by the instrumentations and can, in principle, be taken into account in the analysis of the experimental results. Conversely, the effect of the alteration of the initial microstructure of the soil is difficult to be considered although it can strongly affect the cyclic soil behaviour, especially in terms of G_0 distribution.

As a consequence, it was decided to carry out one more multistage test with a different experimental procedure to define the actual distribution of the small-strain dynamic parameters. The test, namely RC-PoliTO-03, was performed on a dry sample of dense Perth sand. After an initial consolidation up to the first testing confining pressure, the sample is excited with small-amplitude input torques, in order to not exceed the linearity threshold. The small-strain dynamic parameters can then be obtained without any change in the structure of the sample. Subsequently, a new stage starts by increasing the confining pressure up to the desired value. The procedure allows defining thoroughly the G_0 and D_0 distributions versus p'_0. When the maximum desired p'_0 is reached, a full RC test is carried out up the medium-large strain range. The confining pressure is then progressively decreased in further stages and for each stage, the MRD curves of the sample are obtained by performing a full RC test.

A summary of all the tests is given in Table 4.5. The results are presented in Figure 4.26-Figure 4.29 in terms of dynamic properties versus cyclic shear strain amplitudes. The tests investigated cyclic shear strains ranging from 10^{-4} to 10^{-1} %. As regards the undrained tests, the pore water pressure build-up is also presented as normalized excess pore pressure $\Delta u_w / p'_0$.

Table 4.5: Summary of the Resonant Column tests carried out at the Politecnico di Torino (confining pressures and void ratios refer to the starting instant of each i-th stage).

Test name	Nr. of stages	Drainage	Shear strain range	$p'_{0,i}$ [kPa]	$e_{0,i}$
RC-PoliTO-01	4	Undrained	Small-to-large	25, 50, 100, 200	0.60 - 0.59
RC-PoliTO-02	5	Undrained	Small-to-large	25, 50, 100, 200, 400	0.57 - 0.56
RC-PoliTO-03A	10	Drained	Small strains	25, 50, 100, 200, 300, 400, 500, 600, 700, 800	0.55 - 0.54
RC-PoliTO-03B	6	Drained	Small-to-large	800, 400, 200, 100, 50, 25	0.54 - 0.55

The first two tests were performed on saturated samples characterized by e_0 (before the first stage) of 0.60 and 0.57, respectively for test RC-PoliTO-01 and -02. Test RC-PoliTO-01 comprises 4 stages carried out at p'_0 ranging from 25 kPa up to 200 kPa. Conversely, 5 stages were carried out in test RC-PoliTO-02, with a maximum p'_0 of 400 kPa. The third test was carried out on a dense sample (i.e. e_0 of 0.55) and it comprises 16 stages in total. The first 10 stages (identified as RC-PoliTO-03-A) were performed at low amplitudes to define the small-strain parameters at p'_0 ranging from 25 to 800 kPa. Conversely, the last 6 stages (identified as RC-PoliTO-03-B) investigated the small-to-medium strain range.

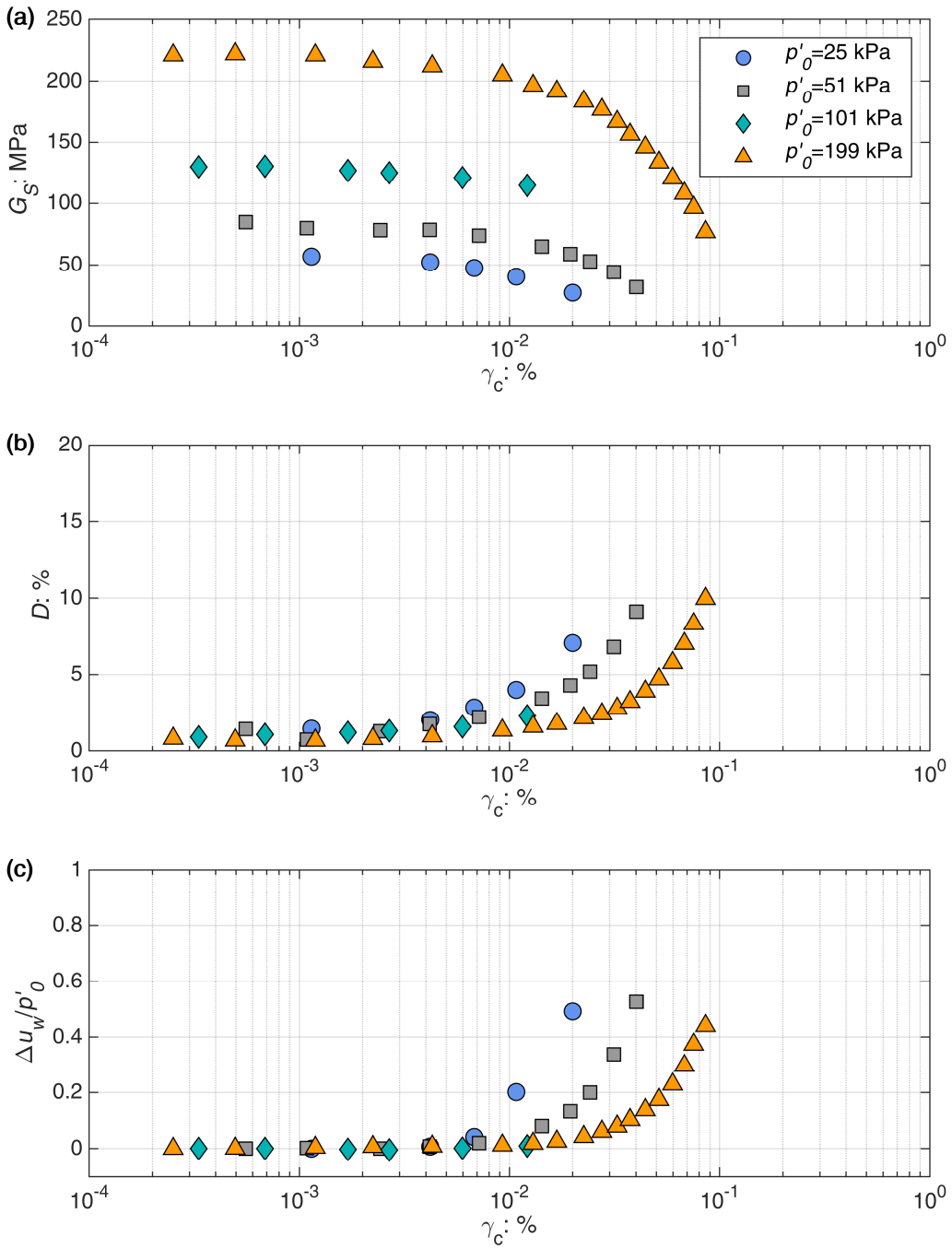

Figure 4.26: Undrained multistage test RC-PoliTO-01: (a) secant shear modulus vs cyclic shear strain amplitude; (b) damping ratio vs cyclic shear strain amplitude; (c) normalized pore water pressure build-up vs cyclic shear strain amplitude.

The influence of the confining pressure is clear on the small-strain properties and the MRD curves. The G_0 significantly increases from one stage to another, while lower values are obtained at the end of each stage due to the pore pressure build-up. On the other side, D_0 slightly decreases with p'_0 although its influence is not so clear. A wider almost linear visco-elastic range is also observed at larger p'_0. The linearity threshold seems to increase with p'_0, shifting the MRD curves towards larger γ_c amplitudes.

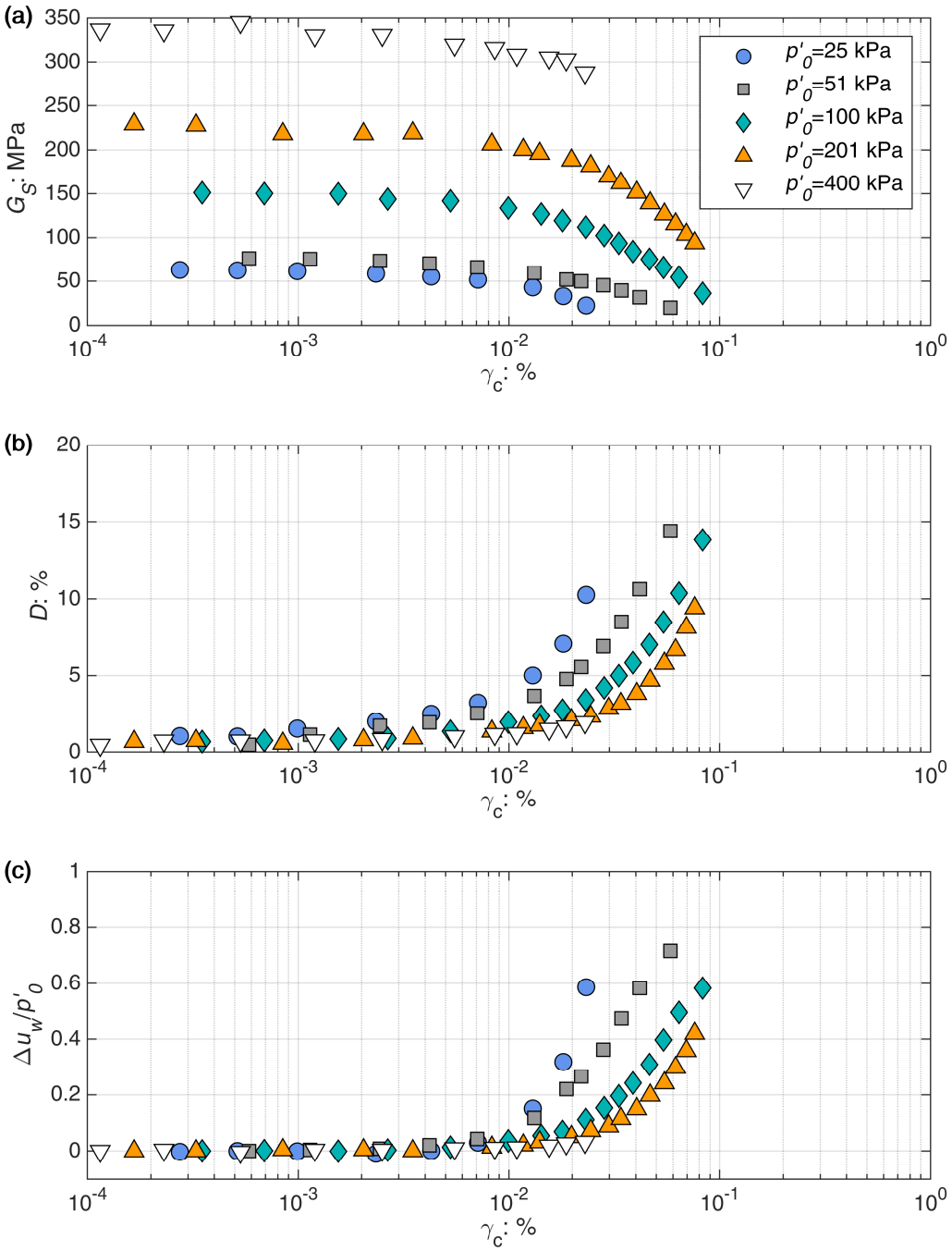

Figure 4.27: Undrained multistage test RC-PoliTO-02: (a) secant shear modulus vs cyclic shear strain amplitude; (b) damping ratio vs cyclic shear strain amplitude; (c) normalized pore water pressure build-up vs cyclic shear strain amplitude.

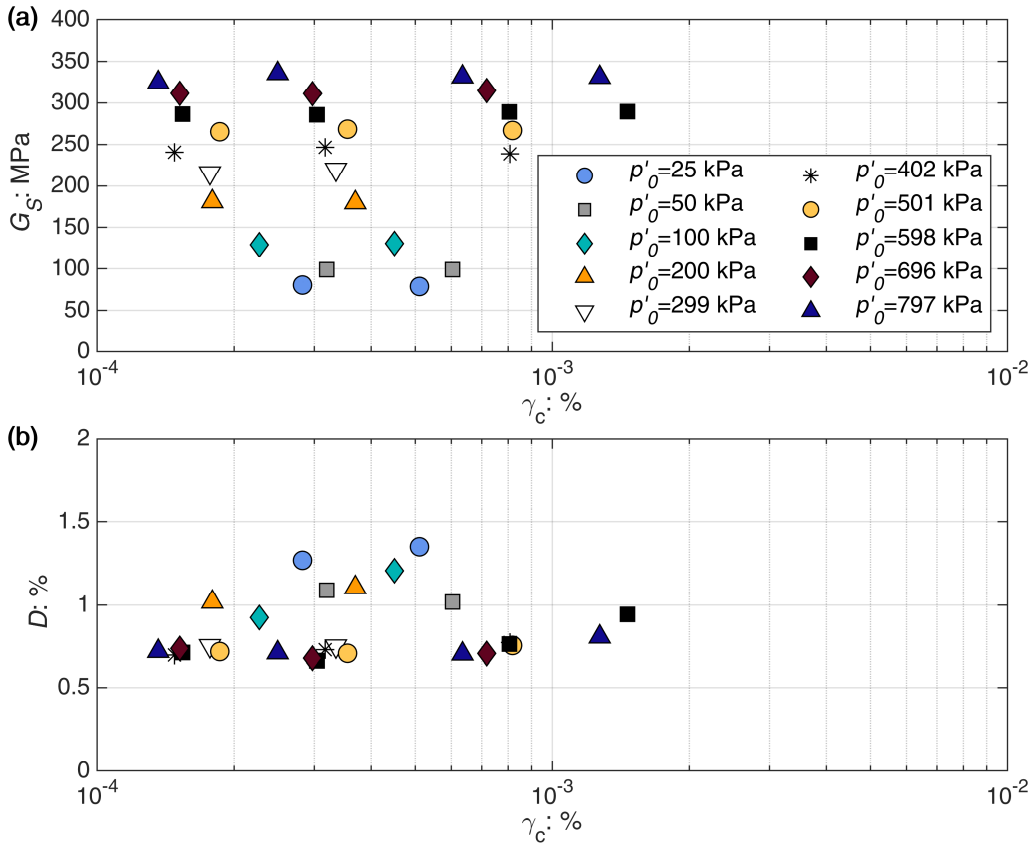

Figure 4.28: Drained multistage test RC-PoliTO-03A: (a) secant shear modulus vs cyclic shear strain amplitude; (b) damping ratio vs cyclic shear strain amplitude.

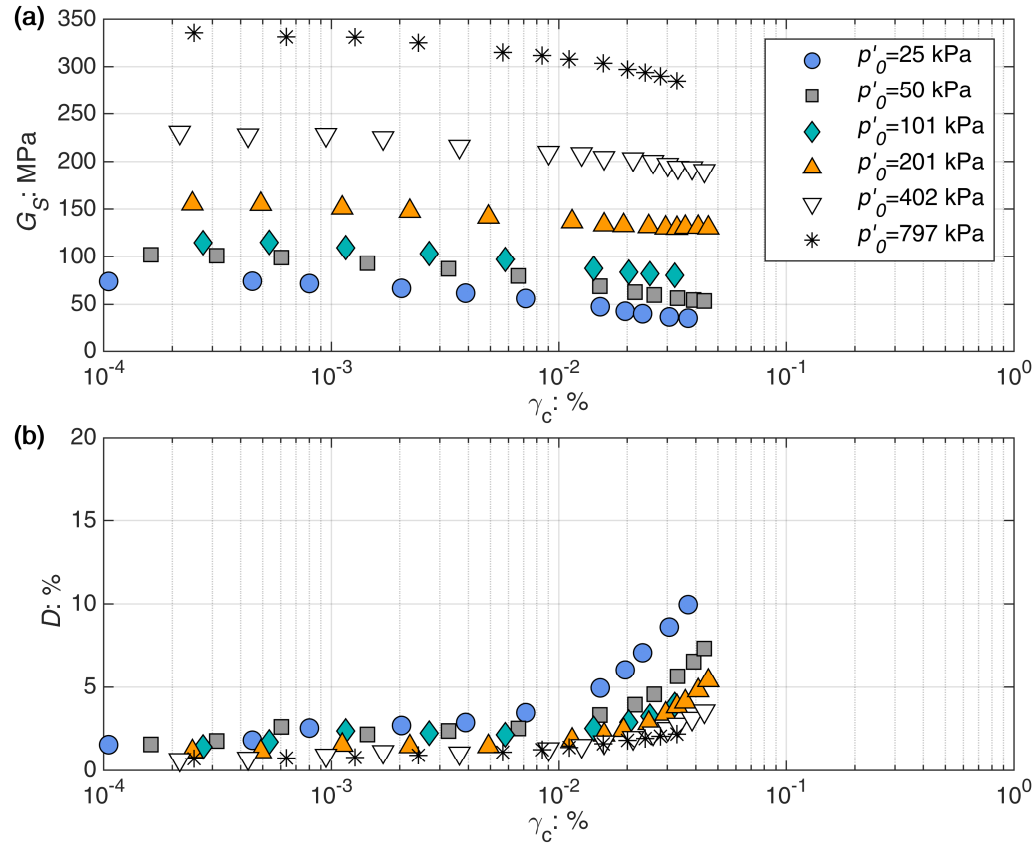

Figure 4.29: Drained multistage test RC-PoliTO-03B: (a) secant shear modulus vs cyclic shear strain amplitude; (b) damping ratio vs cyclic shear strain amplitude.

4.3.4 Cyclic threshold shear strains

The dynamic behaviour of granular materials is highly nonlinear outside the very small-strain range. The almost linear range is observed just for shear strains lower than the linear cyclic threshold shear strain, γ_{tl}. The latter can be defined as γ_c corresponding to G_S / G_0 of about 0.98 (Ni, 1987; Kim, 1991; Menq, 2003). At larger γ_c, the soil behaves nonlinearly, but no significant changes are observed in the microstructure until the volumetric threshold shear strain, γ_{tv}, is reached. After the volumetric threshold, a soil in undrained conditions exhibits pore water pressure build-up. The γ_{tv} can thus be defined as γ_c corresponding to the onset of the pore pressure build-up (Vucetic, 1994). The cyclic thresholds obtained according to the abovementioned criteria are reported in Table 4.6 for each stage of the two RC tests performed under undrained conditions.

The results are plotted in Figure 4.30 as a function of p'_0. The experimental γ_{tl} are compared to the formulation for the threshold implicitly assumed by Menq (2003) in its empirical model, according to D_{50} and C_u of the Perth sand (Table 4.1). Conversely, the γ_{tv} values are compared with the band and average line proposed by Vucetic (1994) for sandy soils (i.e. PI equal to 0). The

The γ_{tl} slowly increases with increasing p'_0, widening the almost linear viscoelastic strain range, following previous findings (e.g., Seed et al., 1986; Ishibashi and Zhang, 1993; Menq, 2003). A large scattering of the data is observed, probably due to the difficulties in defining straightforwardly the threshold. In the very small-strain range, small variations of G_S / G_0 are associated with significant variations of γ_c. The data are anyway quite consistent with the trend proposed by Menq (2003), although its model seems to slightly underestimate the threshold. The latter is probably due also to the modified hyperbolic relationship adopted by the Author to model the MR curves (see Ciancimino et al., 2019, for further references). In the final analysis, the γ_{tl} of Perth sand is thought to be somewhere between 0.0005 and 0.002%.

Table 4.6: Cyclic threshold shear strains obtained from the RC tests.

Test name	p'_0 [kPa]	e_0	γ_{tl} [%]	γ_{tv} [%]
RC-PoliTO-01	25	0.60	0.0016	0.0068
	51	0.59	0.0007	0.0072
	101	0.59	0.0015	0.0121
	199	0.59	0.0021	0.0093
RC-PoliTO-02	25	0.57	0.0011	0.0071
	51	0.57	0.0016	0.0071
	100	0.57	0.0018	0.0053
	201	0.57	0.0004	0.0083
	400	0.56	0.0026	0.0055

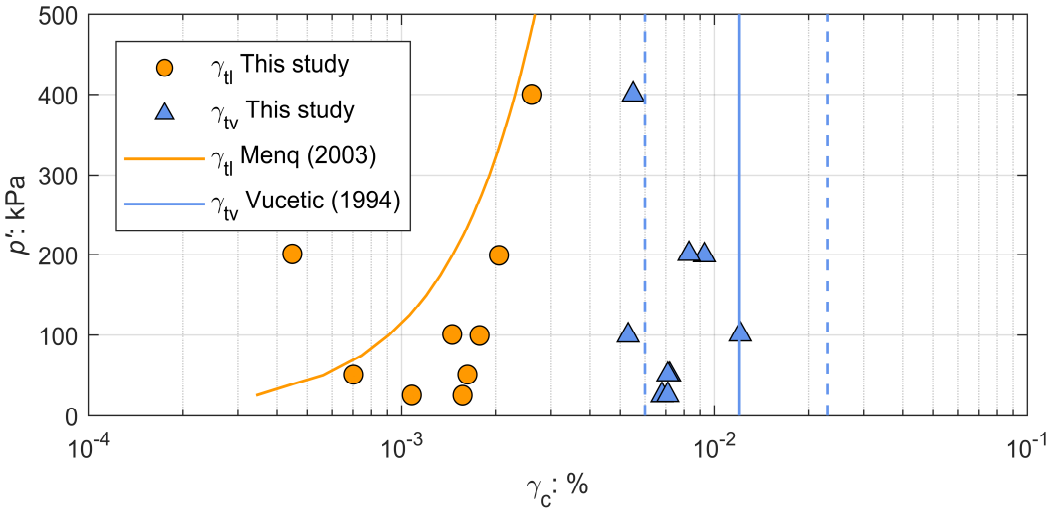

Figure 4.30: Cyclic threshold shear strains of the Perth sand.

On the other side the experimental γ_{tv} fall between the lower limit and the average value proposed by Vucetic (1994), revealing for the Perth sand a tendency in developing excess pore pressure also at relatively small shear strains. The onset of the pore pressure build-up took place in each stage for shear strains in the range between 0.005 and 0.012%, regardless of p'_0. Conversely, its rate of increase depends on p'_0 (see Figure 4.26.c and Figure 4.27.c). As an example, a $\Delta u_w / p'_0$ of about 0.5/0.6 was reached for γ_c equal to 0.02 % in the stages performed at a p'_0 of 25 kPa. The same $\Delta u_w / p'_0$ was reached for a γ_c of 0.08 % in the stages characterized by a p'_0 of 200 kPa. The results are consistent with the findings of previous studies, suggesting that for sandy soils p'_0 strongly influences the cyclic pore water pressure patterns and rates but it has practically no effect on γ_{tv} (e.g., Silver and Seed, 1971; Youd, 1972; Dobry et al., 1982; Hsu and Vucetic, 2004).

It should be pointed out that the influence of e_0 on the cyclic threshold shear strains was here not investigated because of the small differences between the e_0 of the two samples. The aforementioned considerations are thus valid just for Perth sand in a dense state (i.e. e_0 of about 0.55/0.60). Previous studies, however, highlighted that the influence of the relative density is practically negligible on the cyclic thresholds of sands (e.g., Silver and Seed, 1971; Youd, 1972; Dobry et al., 1982; Menq, 2003; Hsu and Vucetic, 2004).

4.3.5 Small-strain dynamic properties

The small-strain dynamic properties of granular soils depend mainly on the state of the material in terms of confining pressure and void ratio. The influence of the two variables on G_0 was first pointed out by Hardin and Richart (1963) and Hardin and Black (1966). The Authors also suggested a relationship to model this dependency based on a void ratio function, $F(e)$, and two calibration parameters, namely A_G and n_G (Eq. (4.22), see Section 4.3.2).

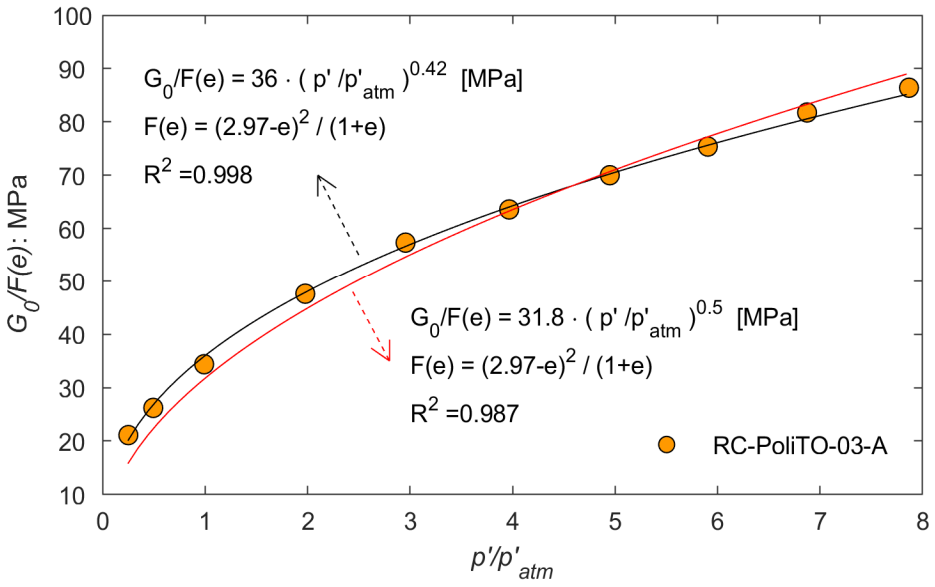

Figure 4.31: Small-strain shear modulus of the Perth sand as a function of the normalized confining pressure: calibration of the Hardin and Richart (1963) equation.

The results of the low-amplitude test (RC-PoliTO-03A) were used to calibrate the coefficients of the Hardin and Black (1966) equation for the Perth sand. Specifically, an average value of G_0 was computed for each step of the low-amplitudes test. Figure 4.31 reports the experimental data as a function of the normalized confining pressure p'/p_{atm}. The calibrated relationship is then the following:

$$G_0 = 36 \cdot F(e) \cdot \left(\frac{p'}{p_{atm}} \right)^{0.42} \tag{4.36}$$

where G_0 is expressed in MPa, while the void ratio function is assumed to be equal to the widely adopted one suggested by Hardin and Black (1966):

$$F(e) = \frac{(2.97 - e)^2}{1 + e} \tag{4.37}$$

It is worth mentioning that the data cover a narrow range of void ratios (from 0.56 to 0.60). As a consequence, the consistency of Eq. (4.36) is verified just for Perth sand in a dense state and care should be exercised when the relationships are adopted outside the range of the experimental data. For instance, an exponent n_G lower than 0.5 is typical of sands in a dense state, while it could significantly increase for looser sands (Santamarina et al., 2005).

Very frequently, the influence of the sand state on the actual exponent n_G is neglected and an average value of 0.5 is adopted for the sake of simplicity. This is for example the case of the constitutive model adopted in the present thesis to reproduce the sand stress-strain behaviour (see Section 6.1.5 for further details). It is then useful to provide also a further calibration of the Hardin and Black (1966) equation assuming a constant n_G of 0.5:

$$G_0 = 31.8 \cdot F(e) \cdot \left(\frac{p'}{p_{atm}} \right)^{0.5} \tag{4.38}$$

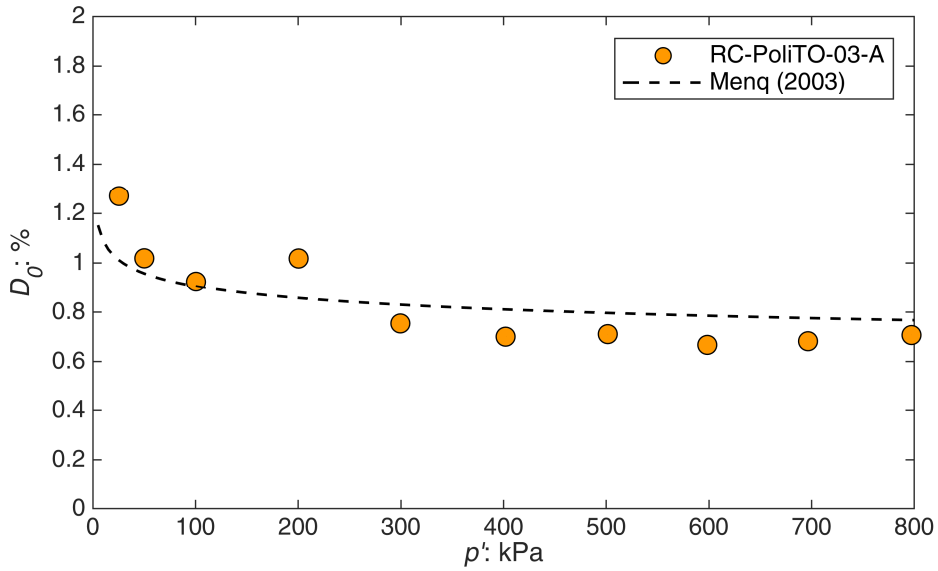

Figure 4.32: Small-strain damping ratio of the Perth sand as a function of the confining pressure.

As it can be observed in Figure 4.31 such an approximation does not result in a significant error, for instance the R^2 decreases from 0.998 to 0.987. Consequently, the prediction of the small-strain shear modulus provided by Eq. (4.38) is again considered reliable.

As far as the small-strain damping is concerned, Figure 4.32 presents the experimental data as a function of p'. The plot also reports the prediction proposed by Menq (2003) (Eq. (4.25), see Section 4.3.2), based on D_{50} and C_u of the Perth sand (Table 4.1). The D_0 of the Perth sand ranges from 0.7 to 1.3%, with a mean value of 0.8%. The comparison with the Menq (2003) equation is quite satisfying, D_0 slightly decreases with increasing p'. The trend is evident especially for p' lower than 50 kPa. As a matter of fact, the variability that usually affects the definition of D_0 overcomes somehow the influence of p' here observed. As a consequence, it appears to be reasonable to adopt an average value of 0.8% D_0, for p' larger than 50 kPa.

4.3.6 MRD curves

The nonlinear behaviour of soils in the small-to-large strain range is usually represented through the Modulus Reduction and Damping curves (Seed and Idriss, 1970). The latter exploit the dependency of G_S/G_0 and D from the γ_c amplitude. As a consequence of the influence of p' on G_S and D, the curves are usually defined for a reference p'_0, corresponding to the initial value measured at the end of the consolidation phase. Nevertheless, p' can significantly change throughout a RC test performed under undrained conditions due to the pore pressure build-up.

It is worth noticing that for a sand sample in a given initial state, the amount of excess pore pressure that build-up during a RC test depends not only on the shear strain amplitude but also on the testing procedure. For instance, in the RC tests here presented, for a given loading amplitude, a range of 400 frequencies is investigated

to define the resonance frequency. For each frequency, 20 cycles of forced vibrations are applied to the sample. The pore pressure build-up anyway takes place also for frequencies different from the resonance one. Therefore, it is not straightforward to define the number of cycles that produced the observed excess pore pressure. Moreover, changing the testing procedures (e.g. by changing the range of frequencies investigated) would result in a different excess pore pressure build-up. The issue is particularly relevant for sandy soils, characterized by a small almost linear range of shear strains. It is then crucial to associate every single point of the MRD curves with the actual p'_i measured at resonance, in such a way to consistently compare results from different tests.

Figure 4.33.a reports the results of the RC tests in terms of G_S/G_0 curves. The data are plotted as a function of the actual p'_i of each point of the curves. It is evident from the plot that the range described by the experimental data is quite wide. Moreover, the trend described by the tests performed under undrained conditions seems to considerably differ from the one obtained from the drained test. The curves obtained from undrained tests seem to decay too fast with respect to the drained ones, even considering the actual p'_i.

These differences can be explained by analysing the normalization procedure of G_S to its small-strain value, G_0. The G_0 is measured at shear strain amplitudes which are, by definition, below the linearity threshold. It is then associated with the initial effective confining pressure, p'_0. Normalizing G_S (obtained at a particular confining pressure, p'_i, smaller than p'_0) to $G_0(p'_0)$ would result in an excessive decay of the modulus due mainly to the variation of the effective confining pressure rather than to the increase of the shear strain amplitude. A procedure is then proposed in the following to overcome the issue.

The normalized shear modulus for a particular p'_i can be expressed as:

$$G_S/G_0(p'_i) = \frac{G_S(p'_i)}{G_0(p'_0)} \cdot \frac{G_0(p'_0)}{G_0(p'_i)} \tag{4.39}$$

where $G_S(p'_i)/G_0(p'_0)$ is the secant shear modulus normalized to G_0 measured at the first amplitude of each stage (as reported in Figure 4.33.a).

According to Eq. (4.22), the second part of Eq. (4.39) can be written as:

$$\frac{G_0(p'_0)}{G_0(p'_i)} = \frac{A_G \cdot F(e) \cdot (p'_0/p_{atm})^{n_G}}{A_G \cdot F(e) \cdot (p'_i/p_{atm})^{n_G}} = \left(\frac{p'_0}{p'_i}\right)^{n_G} \tag{4.40}$$

The *actual* normalized shear modulus can thus be obtained by combining Eqs. (4.39) and (4.40):

$$G_S/G_0(p'_i) = \frac{G_S(p'_i)}{G_0(p'_0)} \cdot \left(\frac{p'_0}{p'_i}\right)^{n_G} \tag{4.41}$$

where n_G is equal to 0.42 (see Section 4.3.5 for further details).

The effectiveness of the procedure is represented in Figure 4.33.b, which reports, the MR curves after the correction procedure. It can be observed that the experimental data after the correction cover a narrower range, flatting the differences between data measured under drained or undrained conditions.

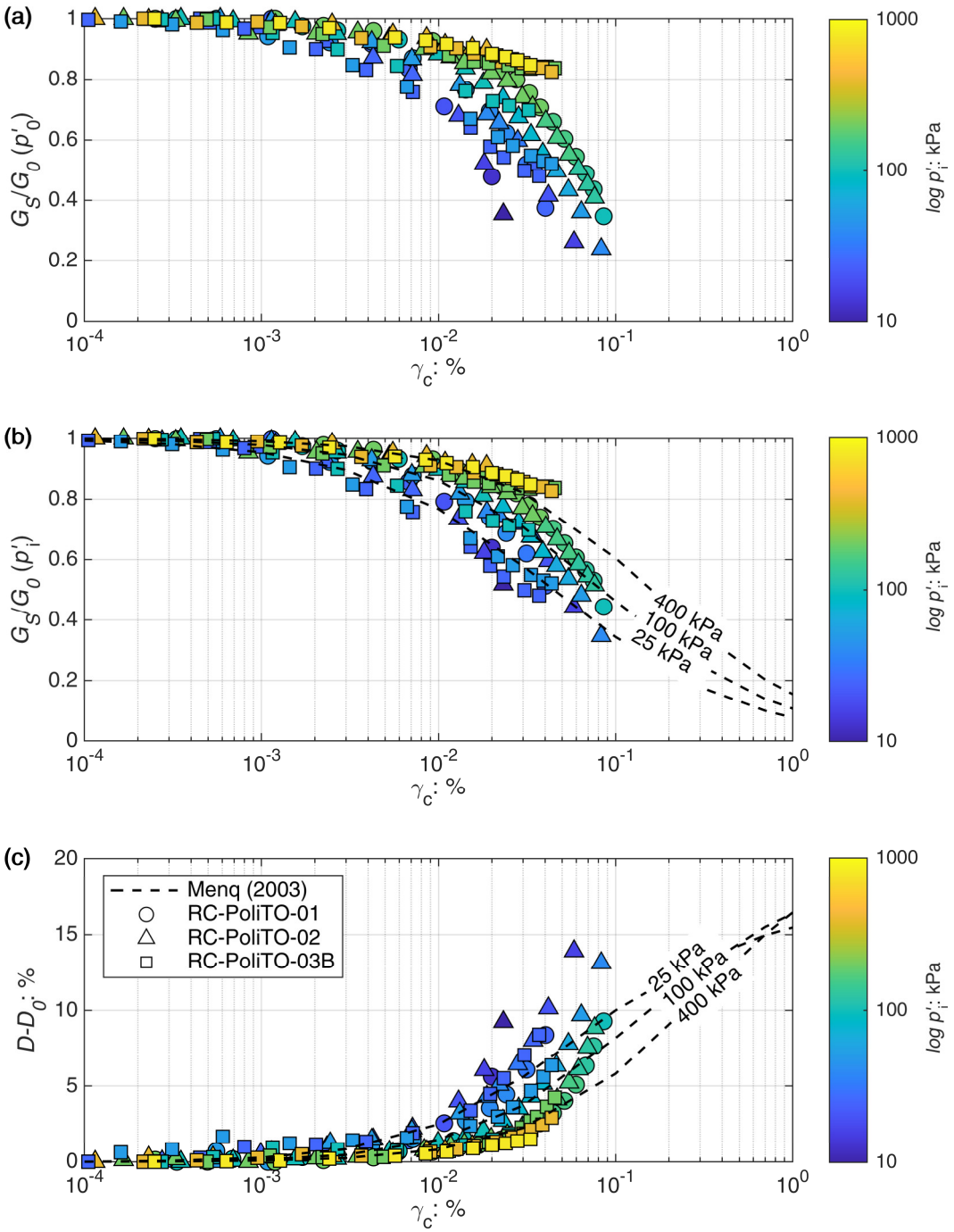

Figure 4.33: MRD curves of the Perth sand: (a) modulus reduction curves (before the correction of G_0); (b) modulus reduction curves (after the correction of G_0) (c) damping curves.

The experimental curves can now be directly compared to the predictions of the Menq (2003) model, as reported in Figure 4.33.b for three different p', namely 25, 100, and 400 kPa. By increasing p'_0 shifts the MR curve on the right, widening the almost linear range. The influence of p'_i is relevant especially for pressures less than 100 kPa while it becomes less relevant at higher pressures, consistently with previous findings (e.g. Seed et al., 1986).

For shear strains above the volumetric threshold, the reduction of p'_i implies a faster decay of the shear modulus and then steeper MR curves than the one

proposed by Menq (2003). This effect is visible also after the correction procedure and it can be explained by looking at the actual p'_i. By reducing the effective confining pressure, the experimental data "jump" from the initial MR curve (representative of the nonlinear behaviour of the soil at p'_0) to a new one, corresponding to a confining pressure of p'_i. The range identified by Menq (2003) is anyway fully consistent with the experimental data obtained for the Perth sand.

Figure 4.33.c reports the comparison between the experimental hysteretic damping ratios, i.e. the experimental D reduced by its small-strain value D_0, and the ones predicted by the Menq (2003) model, again as a function of the actual p'_i of each point. The data reveal a significant increase of $D - D_0$ just after the linearity threshold. The hysteretic damping increases faster with respect to the predictions of the Menq (2003) model, reaching rapidly a value of 15% in the range of γ_c between 0.01 and 0.1%. The results are anyway consistent with the findings of previous studies, which suggest much steeper hysteretic damping curves for sands (e.g., Seed et al., 1986; Vucetic and Dobry, 1991). Finally, the effect of the confining pressure is again quite evident, lower $D - D_0$ values are observed for a given γ_c with increasing p'_i. Its influence anyway decreases above values of about 100 kPa.

Chapter 5

Experimental assessment of the performance of a scoured bridge pier

Local scour phenomena have been extensively studied from a hydraulic point of view, leading to several empirical approaches for predicting the maximum scour depth (e.g., Breusers and Raudkivi, 1991; Melville and Coleman, 2000; Arneson et al., 2012; Sheppard et al., 2014). In contrast, only a few experimental studies have focused on the effects of scouring on the mechanical response of the foundation (e.g., Qi et al., 2016b; Zhang et al., 2019; Chortis et al., 2020).

The two aspects of the problem (*hydraulics* and *mechanics*) are analysed separately, and the assessment of the performance of scoured piers is performed without considering a well-defined water flow scenario. The hydraulics predictive equations are used to estimate the maximum scour depth, and the local scour hole is modelled crudely: either by removing a constant thickness soil layer (no distinction between general and local scour) or by considering an idealized scour hole geometry (a cone sloping at the critical state friction angle) (e.g., Alipour and Shafei, 2012; Wang et al., 2014b; Klinga and Alipour, 2015). However, recent studies (Foti and Sabia, 2010; Qi et al., 2016b; Chortis et al., 2020; Kariyawasam et al., 2020) suggest that the scour hole geometry may have a significant effect on the mechanical response of the soil-structure system.

A major objective of this thesis was to carry out an experimental study on the influence of scouring on the mechanical response of bridge piers. This chapter reports the results of a series of experimental tests conducted on a model representing a single-column bridge pier founded on a cylindrical embedded foundation. A 2-step methodology is developed to study the *hydraulic* and the *mechanical* part of the problem. In the first step, a novel experimental apparatus is employed to conduct hydraulic 1*g* physical model tests, to simulate the development of the local scour

hole as a consequence of a well-defined hydraulic scenario. In the second step, the results of hydraulic 1*g* tests are used to reproduce the actual geometry of the scour hole in *Ng* physical models tested in a geotechnical centrifuge, to study the mechanical response of the scoured foundation. The influence of local scour on foundation performance is investigated through monotonic vertical and lateral pushover tests, and slow-cyclic lateral push tests. Although the study focuses mainly on local scour, the effects of general scour (i.e., erosion of a constant thickness soil layer) are also investigated to reveal and quantify the differences between these two distinct processes.

The main findings of this chapter have been already accepted for publication in Ciancimino et al. (2021).

5.1 Problem definition and experimental methodology

An idealized single degree of freedom (SDOF) system is considered, representing a prototype bridge pier of height h = 6.9 m, supported on a cylindrical foundation of diameter D_f = 2 m and embedment depth d = 2 m, founded on dense sand (Figure 5.1). Since the focus of the study is on foundation performance, a rigid pier is considered. The bridge deck is represented by a concentrated mass m_1, adjusted to achieve a factor of safety against vertical loading $FS_v \approx 8$ before scouring (including the pier and foundation masses, m_2 and m_3, respectively). The selected FS_v, which corresponds to a moderately loaded structure, is calculated based on the vertical bearing capacity of the foundation, experimentally measured through a vertical push test conducted in the geotechnical centrifuge.

A novel hybrid approach is developed to study the mechanical behaviour of the foundation subjected to flood-induced scour due to a well-defined hydraulic scenario. A 2-step methodology is employed, decoupling the *hydraulic* (i.e. the scour process around the bridge pier) and the *mechanical* part of the problem, as summarized in Figure 5.2.

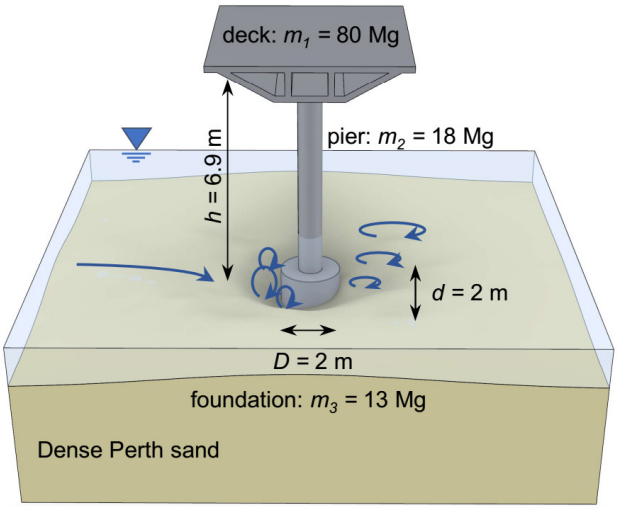

Figure 5.1: Problem definition: SDOF bridge pier subjected to flood-induced scour.

The first step simulates the *hydraulic* process through small-scale (1:50) 1***g*** physical model tests under clear-water conditions (Figure 5.2.a). The experiments are conducted employing a Miniaturised Tidal Generator (MTG; Jones and Anastasopoulos, 2020), recently developed at ETH Zurich (ETHZ). As discussed in more detail later on, the MTG allows proper simulation of the scour process under realistic and well-defined hydraulic scenarios. The results of these tests can be used to define the scour depth and, most importantly, the morphology of the scour hole, acquired through a 3D scanner.

After digital processing, the inverse of the scour hole surface is 3D printed to produce a mould of the scour hole (Figure 5.2.b). The 3D-printed mould is used to reproduce the measured geometry of the scour hole (from Step 1) in a centrifuge model (Figure 5.2.c), which is subsequently tested (Step 2) in the ETHZ drum centrifuge (Springman et al., 2001). The second step addresses the mechanical part of the problem, using 1:*N* scaled models tested at *N****g***, thus achieving correct scaling of the in-situ stresses.

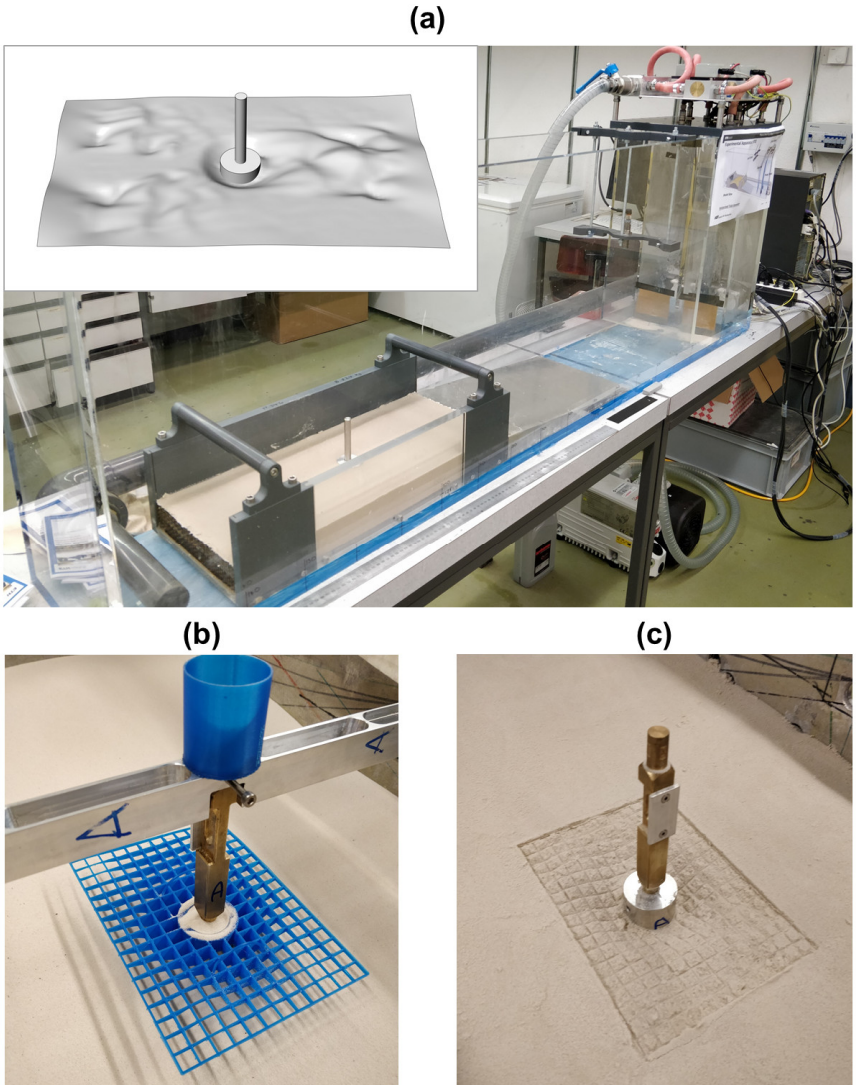

Figure 5.2: Methodology: (a) development of the scour hole through the MTG and 3D scan of the surface; (b) 3D printed mould of the scour hole; and (c) reproduction of the geometry to prepare models suitable in the geotechnical drum centrifuge.

The performance of the bridge pier is studied through vertical push tests, monotonic lateral pushover tests and lateral slow-cyclic tests. Table 5.1 summarizes the relevant scaling laws for both 1***g*** and *N**g*** physical model tests.

The underlying assumptions of the hybrid two-step methodology are: (1) 1***g*** experiments are appropriate to reproduce the *hydraulic* scouring process; and (2) the scouring process does not strongly influence the void ratio of the remaining (unscoured) soil (i.e., the void ratio at the end of the scouring process is still uniform in the model). The first hypothesis is widely adopted in hydraulic experiments, where small and medium scale tests are conducted to study the scour phenomenon and the results are analyzed according to dimensionless quantities (e.g., Melville and Raudkivi, 1996; Coleman, 2005; Moreno et al., 2016). Furthermore, the effectiveness of the *hydraulic* 1***g*** tests is verified by comparing the results with predictions given by widely used empirical models. The second hypothesis is considered reasonable, especially in clear-water conditions, where no sediments are transported by the river or the material is transported in suspension (Melville and Coleman, 2000). No interaction takes place between the transported material and the scour process, and the soil is progressively eroded until the equilibrium scour depth is reached. The only part of the model where this hypothesis may not be verified is the depositional mound which forms at the exit slope from the scour hole (Arneson et al., 2012). This is, however, a relatively small zone downstream of the bridge, where the scour hole is shallower, which should not significantly influence the *mechanical* response of the structure. Finally, the overconsolidation effects due to the erosive process are not expected to be very relevant on dense sand, also in the light of the small amount of soil that is going to be removed (i.e. about 1 m at the prototype scale, corresponding to a maximum load of about 10 kPa).

The direct (fully coupled) physical modelling of both the *hydraulic* and the *mechanical* part of the problem in a geotechnical centrifuge would be the best option to simulate the entire process as realistically as possible, provided that proper scaling of the water flow can be achieved. However, this would require a MTG mounted in the geotechnical centrifuge, which is not currently feasible. The developed decoupled approach represents a good balance between the reliability of the results and feasibility of physical model tests.

Table 5.1: Scaling laws for 1g and Ng centrifuge model tests (Muir Wood, 2004; Madabhushi, 2014).

Quantity	Scaling factors (model/prototype)	
	1*g*	*Ng* (centrifuge)
Acceleration	1	N
Length	N^{-1}	N^{-1}
Mass	N^{-3}	N^{-3}
Force	N^{-3}	N^{-2}
Stress	N^{-1}	1
Strain	1	1
Time (diffusion)	N^{-1} *	N^{-2} *
Time (dynamic)	$N^{-0.5}$	N^{-1}

* assuming same fluid viscosity used in model and prototype

5.2 1*g* physical modelling of local scour

A series of 1:50 scale 1***g*** experiments is conducted to study the development of the local scour hole around the idealized bridge pier. The foundation-structure model consists of a cylindrical aluminium foundation of 40 mm diameter and height (D_f = 2 m in prototype scale), attached to a cylindrical aluminium pier of 12 mm diameter (D_p = 0.6 m in prototype scale).

The experiments were conducted employing the ETHZ MTG (Figure 5.2.a), which can produce arbitrary waves or pseudo-steady flows through a system of pressure-controlled water tanks (Jones and Anastasopoulos, 2020). Specifically, a target waveform is sent in real-time to high-performance digital valves. The waveform corresponds to the static air pressure required to hold a column of water of height, $h_{t,i}$, in the *i-th* pump-tank at time *t*. The air pressure is then released in a controlled way to produce the desired flow. The apparatus is equipped with re-circulation pumps to reduce the amount of water needed and to keep constant the height of the water flow. In the present study, the tanks are configured to act as a pumping system, which draws water from one side of the apparatus and discharges it at the opposite end. The removable model box is placed in the main channel and subjected to a long pseudo-steady flow. High precision ultrasonic sensors are used to measure the water level in the tank(s) $h_{t,i}$, and the flow depth y_0 directly upstream of the pier (Figure 5.3). By knowing the geometry of the two tanks and $h_{t,i}$, it is possible to compute the total volume of water V_w, discharged in a time $\bar{t}$. Consequently, the mean flow rate $\bar{Q}$ is computed as $V_w / \bar{t}$. The mean velocity, $\bar{v}$, of the water flow is thus obtained as the ratio of $\bar{Q}$ to the flow area, given by the mean flow depth $\bar{y}_0$ times the width of the model.

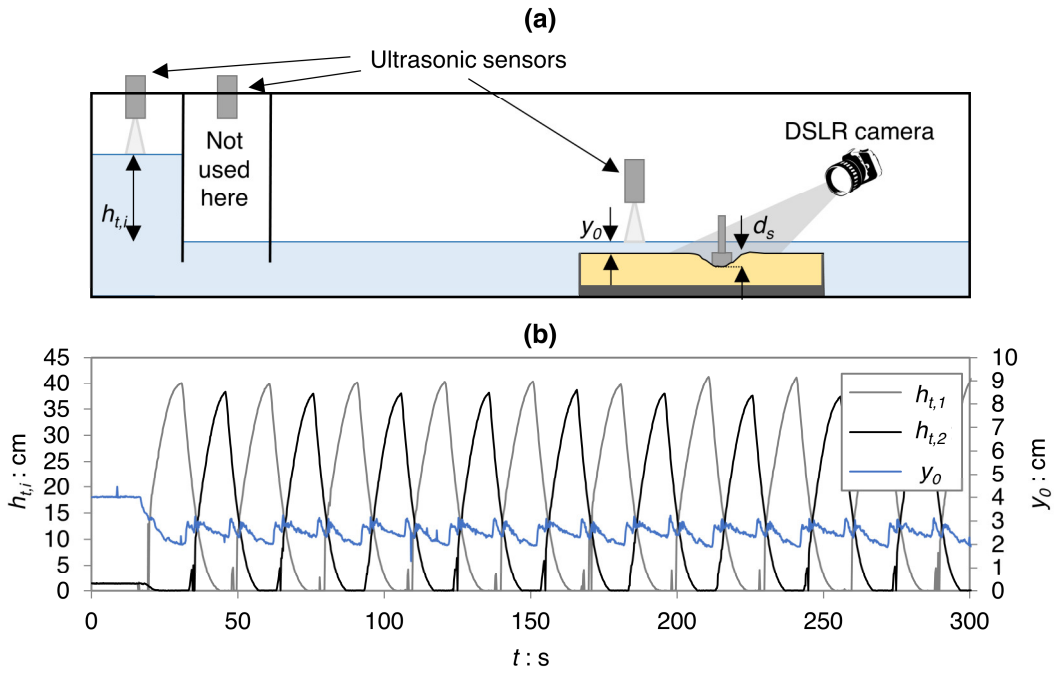

Figure 5.3: 1g physical modelling of local scour: (a) MTG experimental set-up; (b) tank height $h_{t,i}$ and flow depth y_0 recorded by ultrasonic sensors (modified from Jones and Anastasopoulos, 2018).

The time evolution of the scour hole around the pier is monitored through still images taken by a Digital Single-Lens Reflex (DSLR) camera at evenly spaced time intervals of 10 s. A series of circles with a spacing of 1 mm was engraved on the lateral surface of the foundation to allow effective tracking of the scour depth.

The shape of the scour hole is acquired through a high precision 3D scan (3D Systems Corporation, Sense 2, Figure 5.4) with a spatial resolution of 0.9 mm and a depth resolution of 1 mm (i.e., about 5 cm in prototype scale). Scans are taken at different instants and at the end of the scour process when the equilibrium scour depth is reached.

5.2.1 Model preparation and test programme

The 1***g*** local scour tests, as well as the subsequent centrifuge tests, were conducted using fine Perth silica sand (see Chapter 4 for further details). The models are prepared outside the MTG, using a removable container of 50 cm length and 26 cm width (Figure 5.2.a), encompassing permeable lateral boundaries to allow for equilibration of pore water pressures inside the channel.

The model structure is firstly placed inside the box, then the sand is layered through a dry sand-raining system. The desired relative void ratio, e, of the sand (i.e. 0.56±0.02) is obtained by adjusting the pluviation height and the opening of the diffuser at the bottom of the sand container. Pots placed outside the model box are simultaneously filled to directly measure the achieved dry unit weight of the soil.

A full description of the sand-raining system, along with the results of calibration tests, is reported in Morales (2015). The soil is then carefully layered at the top to obtain an almost flat initial surface. The procedure adopted to prepare the models is fully consistent with the one subsequently used for the centrifuge tests.

Figure 5.4: 3D scan used to acquire the shape of the scour hole (3D Systems Corporation, Sense 2).

Table 5.2: Main characteristics of the conducted 1g scour tests (data in model scale).

Test	Mean flow rate, $\overline{Q}: cm^3/s$	Normalized flow velocity, $\overline{v}/U_c$	Mean flow depth, $\overline{y}_0 : mm$	Void ratio, e	Relative density, D_R
S1	780	0.70	27.5	0.55	0.86
S2	702	0.63	27.4	0.55	0.86
S3	566	0.40	34.6	0.55	0.86

As summarized in Table 5.2, three *hydraulic* 1***g*** tests were conducted with mean water flow velocities: $\overline{v} =$ 109.1 mm/s, 98.6 mm/s, and 62.9 mm/s. The water flow velocity is normalized to the critical velocity U_c, obtained from Neill's (1967) equation, as a function of the mean grain size of the sand d_{50} (see Section 2.2.2.2 for further details). The critical velocity defines the beginning of sediment motion and, therefore, of live-bed scour conditions (Melville and Coleman, 2000). A value of $\overline{v}/U_c < 1$ suggested that scouring will develop under clear-water regime, as required for the tests conducted herein. The three water flow velocities were thus selected to cover a wide range of $\overline{v}/U_c$, being sure of not exceeding the critical velocity.

At this point, a crucial issue requires clarification. When dealing with the mechanics of soil-structure interaction (as is the case for the centrifuge tests of Step 2), assuming that the soil behaves as a continuum, the d_{50} of the sand does not need to be scaled (i.e., the same sand can be used to model the prototype) – provided that some basic requirements are met. In contrast, when modelling a scour process, the actual particle size distribution influences the development of the scour hole. The value of U_c at prototype scale cannot be obtained by applying the usual 1***g*** scaling laws to the corresponding value computed at model scale. Hence, the $\overline{v}/U_c$ ratio has to be computed at model scale, adopting the actual d_{50} of the sand. This ratio is the key parameter defining the scour regime (i.e., clear-water or live-bed local scour), and consequently the expected scour depth. Therefore, the results of the scour tests are considered representative of prototype problems with $\overline{v}/U_c$ ratios consistent with the ones obtained at model scale (Table 5.2).

5.2.2 Test results

The key results of the scour tests are presented and discussed in prototype scale. depicts the evolution of scouring in terms of average scour depth d_s (i.e., the scour depth measured along the longitudinal direction of the bridge) as a function of normalized time t^*:

$$t^* = \frac{t \cdot \overline{v}}{D_p} \tag{5.1}$$

where D_p is the pier diameter. The plot also shows the maximum scour depth $d_{s,max}$ observed at the end of each test along the upstream side. The difference between $d_{s,max}$ and d_s increases with time, due to the developing asymmetry of the scour hole.

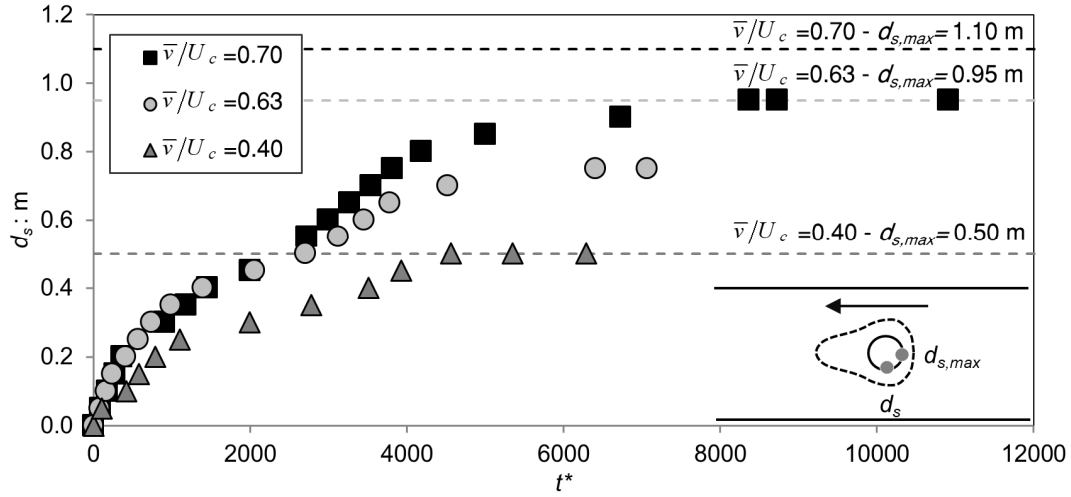

Figure 5.5: Evolution of scour depth d_s with dimensionless time t^*, along with the maximum scour depth $d_{s,\max}$ (measured along the upstream side) as a function of water flow scenario.

After an initial phase in which a rapid increase is observed, the scour depth keeps increasing with a reduced pace, until asymptotically reaching its maximum value, in accord with the expected trends for local scour in clear-water conditions (e.g. Arneson et al., 2012). A maximum scour depth of about 1.1 m is observed for Test S1 ($\overline{v}/U_c$ = 0.7). The decrease of the $\overline{v}/U_c$ ratio leads to a decrease of the maximum scour depth, reaching a value of 0.5 m for test S3 ($\overline{v}/U_c$ = 0.4). The maximum scour depths are of the same order of magnitude of the water depth, as expected for wide piers in relatively shallow flows (Arneson et al., 2012).

In theory, a longer time would be required to ensure that the equilibrium scour depth is reached for a specific *hydraulic* scenario (Melville and Chiew, 1999). However, in the conducted tests no significant changes were observed after $t^* \approx 6000 \div 8000$, which was defined as the reference final condition. In principle, some minor changes could affect the scour depth if the water flow was kept constant for a much longer time. This is not anyway within the scope of this study, which aims at quantifying the mechanical consequences of scouring for a defined hydraulic scenario of a specified water flow lasting for a specified time.

Figure 5.6 presents the progression of the scour hole with dimensionless time for test S1 $\left(\overline{v}/U_c = 0.7\right)$, in terms of contour plots of bed elevation (Figure 5.6.a) and transverse (with respect to the bridge axis) cross-sections at the foundation centreline (Figure 5.6.b).

Initially, for t^*=1090, the scour hole starts developing along the foundation flanks and the eroded soil is deposited downstream. The scour hole progressively extends around the foundation, and the initial gentle slope becomes steeper (t^*=2730). For t^*>4380, the maximum scour depth $d_{s,max} \approx 1.1$ m is reached, upstream. However, the scour hole is not yet fully developed, especially along the sides of the foundation, where it reaches a depth of 0.7 m.

The final configuration (t^*=8730), corresponding to the equilibrium scour depth, is characterized by a scour hole with a maximum upstream slope of about

30°, which is equal to the critical state friction angle, φ'_{CS}, of Perth sand (see Section 4.2.4). Downstream, the depositional zone is reduced, and a gentle slope can be observed, connecting the scour depth of about 0.5 m to the original ground surface. Along the longitudinal direction (with respect to the bridge axis, i.e., perpendicular to the flow direction), the scour hole is reasonably symmetric, with a scour depth slightly lower than the maximum. The final shape of the scour hole is totally consistent with widely accepted guidelines (e.g., Melville and Coleman, 2000; Arneson et al., 2012).

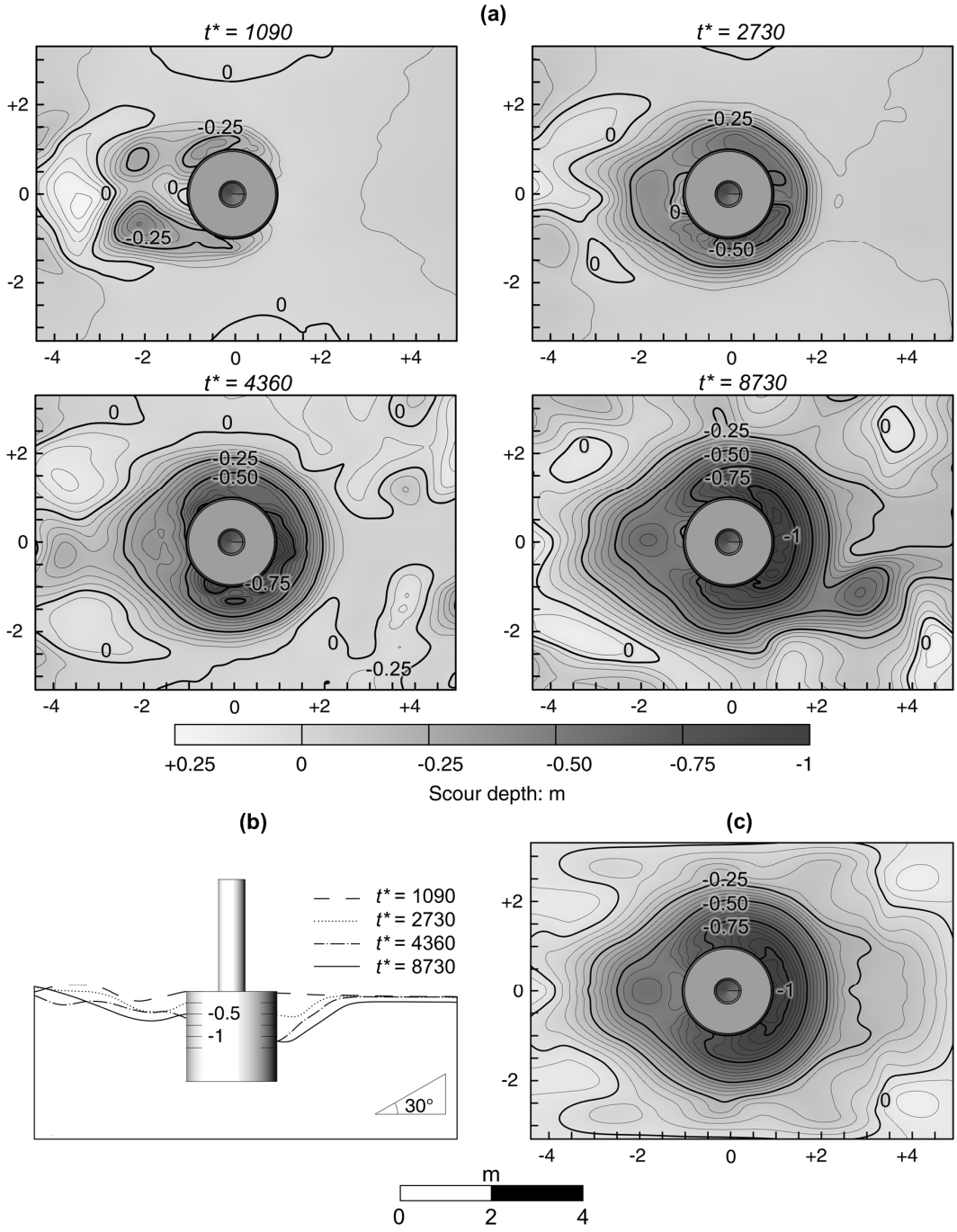

Figure 5.6: Time evolution of the scour hole for test S1 $\bar{v}/U_c = 0.7$: (a) scanned contour plots of bed elevation; (b) cross-sections at the foundation centreline; and (c) contour plot of the regularized surface used for the 3D printed mould.

The final scour hole ($t^* = 8730$) obtained from Test S1 is used as a reference for the centrifuge model tests of Step 2 (mechanical problem), aiming to investigate a scenario where the effects of scouring on the behaviour of the foundation are maximized. The 3D-scanned geometry is initially regularized to obtain a symmetric shape in the transverse direction, which converges to the initial flat surface at the side boundaries (Figure 5.6.c). Then, moulds of the scour hole were 3D printed (using a Dremel 3D40 printer with a resolution of 0.3 mm), appropriately scaled to match the scale of the centrifuge model tests of Step 2 (Figure 5.7).

5.2.3 Verification against existing empirical models

In this section, the experimental results are validated against the maximum scour depth predicted by two widely adopted empirical models for local scour around complex piers (i.e., piers supported by a larger diameter caisson or a caisson-pile foundation) under clear-water conditions. The comparisons are presented and discussed in prototype scale. It should be mentioned that, in the predictive models, the scour depth is always expressed as a function of dimensionless groups. Therefore, it is straightforward to apply the 1$\boldsymbol{g}$ scaling laws of Table 5.1 to convert the scour depth from model to prototype scale.

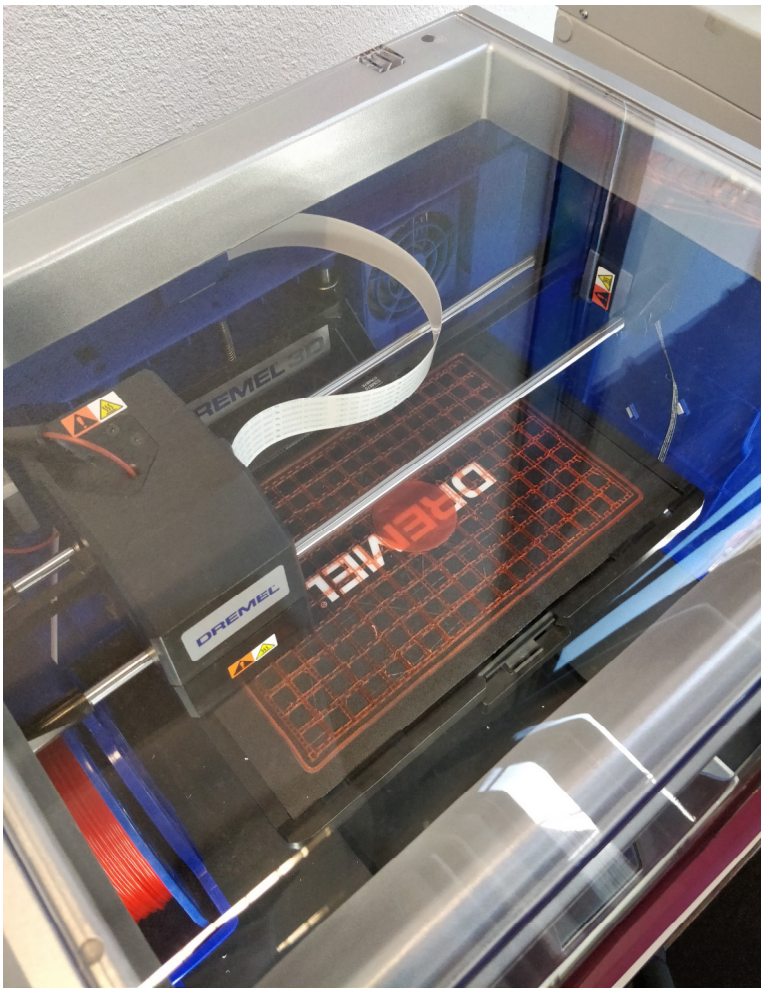

Figure 5.7: Dremel 3D40 printer used to produce moulds of the scour hole.

The first empirical method is the one proposed in the Hydraulic Engineering Circular Nr.18, HEC-18, of the Federal Highway Administration (Arneson et al., 2012). It is based on the hypothesis of superposition, according to which the maximum equilibrium scour depth can be computed separately for the pier ($d_{s,p}$) and the foundation ($d_{s,f}$), and the total maximum scour depth of the complex pier is obtained by the sum of the two components. A correction for wide piers in shallow flows (as suggested by Johnson and Torrico, 1994) is also applied.

The second empirical method is the one proposed by Coleman (2005), which is based on the concept of an equivalent pier diameter D_e, as the diameter of a single column that would produce the same scour depth with the complex system. Different equations are proposed to compute D_e, according to the distance of the bed elevation to the top of the foundation before scouring (equal to 0 in our case). The scour depth is then computed through the Melville and Coleman (2000) equation, applying the correction suggested by Parola et al. (1996) to account for the foundation shielding effect.

The two empirical methods are applied to estimate the (maximum) equilibrium scour depth for the conditions of the three laboratory tests. The details about the calculation are provided in Table 5.3 and Table 5.4. A full description of the two methods can be found in Section 2.3.3.

Both methods provide almost the same predictions of $d_{s,max}$, namely 1.2 m, 1.1 m, and 0.7 m for Test S1, S2, and S3, respectively. The empirical estimates are in good agreement with the experimental results (1.1 m, 0.95 m, and 0.5 m, respectively), slightly overestimating the scour depth by 0.1 m to 0.2 m. Bearing in mind that the empirical predictive methods are supposed to be conservative, the comparison is quite acceptable. Moreover, the shape of the scour hole (as previously discussed) is consistent with results reported in the literature (e.g., Melville and Coleman, 2000; Arneson et al., 2012). It may, therefore, be concluded that the 1***g*** tests are adequate to model the scour process and the results can be used to study the mechanics part of the problem in the geotechnical centrifuge.

Table 5.3: Equilibrium scour depth predictions from the HEC-18 method (Arneson et al., 2012).

Test	$K_{h,p}$	$d_{s,c}$: m	K_w	$d_{s,f}$: m	$d_{s,\max}$: m
S1	0.33	0.30	0.77	0.91	1.21
S2	0.33	0.28	0.72	0.81	1.10
S3	0.33	0.24	0.55	0.49	0.74

Table 5.4: Equilibrium scour depth predictions from the Coleman (2005) method.

Test	D_e : m	K_{yb} : m	K_1	$d_s(f=0)$: m	$d_{s,\max}$: m
S1	0.84	2.02	0.70	1.41	1.23
S2	0.84	2.02	0.63	1.28	1.12
S3	0.84	2.02	0.39	0.80	0.70

5.3 Centrifuge modelling

In the second step, a series of centrifuge model tests were performed in the ETHZ geotechnical drum centrifuge manufactured by Broadbent & Sons Ltd (Figure 5.8). The centrifuge has an outer diameter of 2.2 m and a channel width of 0.7 m and is capable of 440***g*** centrifugal acceleration carrying a payload of 2 t (Springman et al., 2001).

It is mainly composed of the drum channel and the tool platform. The tool platform includes most of the instrumentation together with the acquisition system, while the drum channel is the model space (Figure 5.9). The platform can either rotate with the channel or not accordingly with the desired experimental setup.

The vertical push tests were performed at 100***g***, while the horizontal ones at 50***g***. Given the dependence of the ***g***-level from the radius, a reference position has to be defined. An effective radius corresponding to two-thirds of the model depth of interest was chosen to minimize the error in the stress profile (Madabhushi, 2014). The model depth of interest was chosen equal to the embedment depth plus two times the diameter of the foundation, with a resulting maximum error in the stress profile of the soil of 2 %.

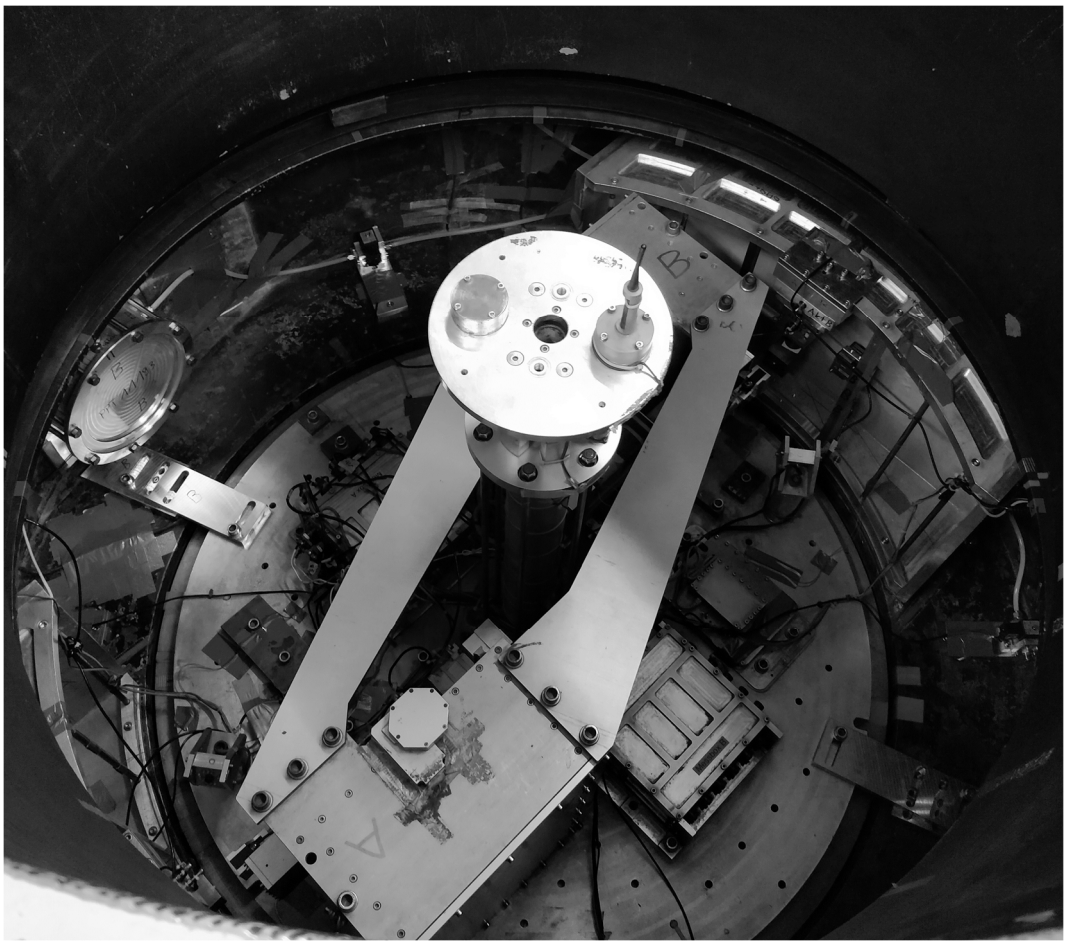

Figure 5.8: ETHZ drum geotechnical centrifuge.

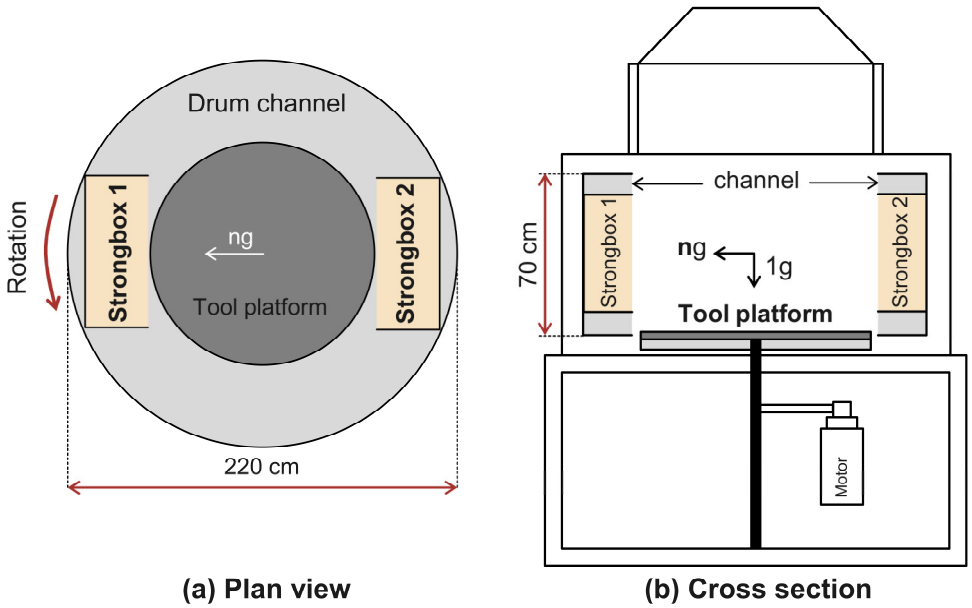

Figure 5.9: Schematic representation of the ETHZ geotechnical drum centrifuge: (a) plan view; (b) cross-section.

5.3.1 Experimental Setup

5.3.1.1 Model preparation

The models are prepared outside the centrifuge in strongboxes and subsequently installed in the drum channel, following the procedure suggested by Laue et al. (2002). Two models with the same instrumentation (models A and B) are placed symmetrically in the centrifuge and tested simultaneously to maintain channel balance (Figure 5.9).

Sand pluviation is conducted following the same procedure as for the scour tests. Once the foundation level is reached, the model structure is placed on the soil along with the 3D printed mould of the scour hole (Figure 5.2.b). The sand is then pluviated through the mesh of the mould around the foundation. Preliminary tests conducted filling pots placed just below the mould showed that such procedure does not influence the relative density of the sand, providing that the dimensions of the mesh are sufficiently larger than openings of the sand-raining system. The regularized scour hole geometry obtained in equilibrium conditions during Test S1 (Figure 5.6.c) is adopted as a reference scenario to study the effects of local scour on foundation performance.

Once the target ground level is reached, the soil is saturated and then partially de-saturated (using porous stones, placed at the bottom of the strongboxes), leading to an unsaturated specimen with an apparent cohesion. This process allows the strongbox to be rotated by 90° to be mounted on the drum channel, keeping the model stable until the centrifuge starts spinning. At the end of the de-saturation process, the mould is removed reproducing the shape of the scour hole (Figure 5.2.c). Subsequently, the strongboxes are installed in the channel and the sensors and actuators are connected. The centrifuge is spun to the desired ***g***-level and the tests are conducted.

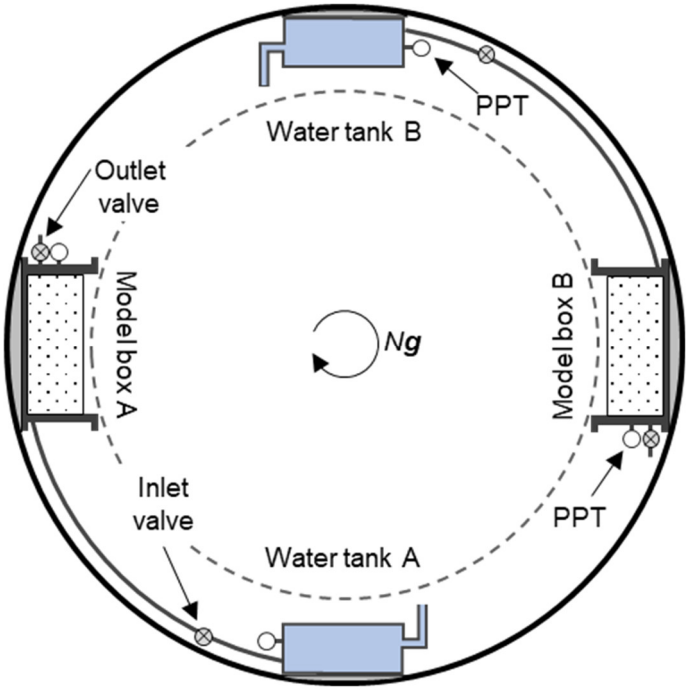

Figure 5.10: Schematic plan view of the model boxes and the saturation systems.

During the spinning up phase, the models are again saturated using two water tanks connected via check valves to the strongboxes (Figure 5.10). The valves are initially closed, and the water tanks are filled up to the desired level of the water table defined by a couple of standpipes, providing water from outside to the channel. The inlet valves are then opened to saturate the model boxes. As the hydraulic head difference between the standpipes and the boxes is reduced, the saturation process slows down, avoiding undesired changes of the scour hole morphology (as also confirmed by the onboard cameras).

The choice of using water as saturation fluid implies the well-known discrepancy between the scaling laws for diffusion and dynamic time (see Table 5.1). However, the present study focuses on the behaviour of the foundation under drained conditions, and therefore this discrepancy is not of relevance. The whole process is monitored by Pore-water Pressure Transducers (PPTs). The latter showed a hydrostatic distribution of the water pressure, ensuring a high degree of saturation. Once the models are saturated, the loading is applied to the structures. At the end of the test, the water is drained through the outlet valves to keep the models stable when the centrifuge stops spinning.

5.3.1.2 Foundation-structure modelling

In the case of the vertical push tests, carried out at 100***g***, only the footing is necessary: an aluminium cylinder of 20 mm diameter and height. Aluminium was chosen given its similarity with reinforced concrete in terms of unit weight. For the horizontal pushover tests, conducted at 50***g***, the physical model (Figure 5.11) also includes the pier, which corresponds to the idealized SDOF prototype system (Figure 5.1).

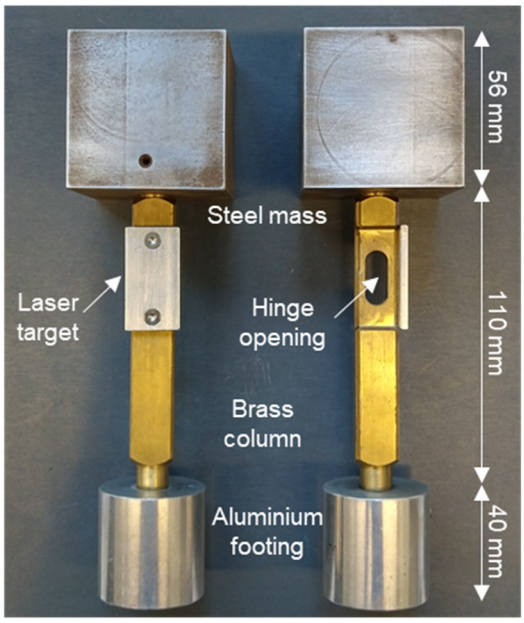

Figure 5.11: Model SDOF structures used for the lateral pushover centrifuge tests.

The foundation is an aluminium cylinder of 40 mm diameter and height, while the pier of 110 mm height is made of brass to ensure adequate stiffness and strength. A small aluminium plate was added to serve as a target for the laser transducers used to measure the horizontal displacements. The steel mass representing the deck is defined based on the desired vertical safety factor of the foundation, as previously discussed.

It is worth mentioning that due to the height of the SDOF system compared to the radius of the drum centrifuge, when the corresponding masses are converted from model to prototype scale, the radial error (Madabhushi, 2014) is not negligible. To that end, the actual radial distance of the mass is used to determine the mass scaling factor *N,* rather than the reference radius (2/3 of the model depth of interest).

Concerning particle size effects, the ratio of the foundation diameter to d_{50} is equal to 87 and 174 at 100***g*** and 50***g***, respectively. Ovesen (1979) suggested a minimum ratio of 35 for shallow circular footings, while Remaud (1999) reported a ratio of 60 to study the lateral response of piles (see Garnier et al., 2007 for further details). Therefore, the obtained ratios are considered sufficiently large to neglect particle size effects.

5.3.1.3 Vertical push tests

The vertical push tests are conducted in cylindrical strongboxes of 400 mm diameter and 200 mm height. The boxes are filled with sand up to 140 mm, ensuring a distance between the foundation base and the bottom boundary of $6D_f$, while the sidewalls are far away from the foundation (>$9D_f$), thus minimising undesired boundary effects. The experimental setup is presented in Figure 5.12. The tests are conducted under displacement-controlled loading, using a screw jack actuator installed on the tool platform. The actuator is equipped with a load cell and is initially disconnected from the footing (Figure 5.12.b).

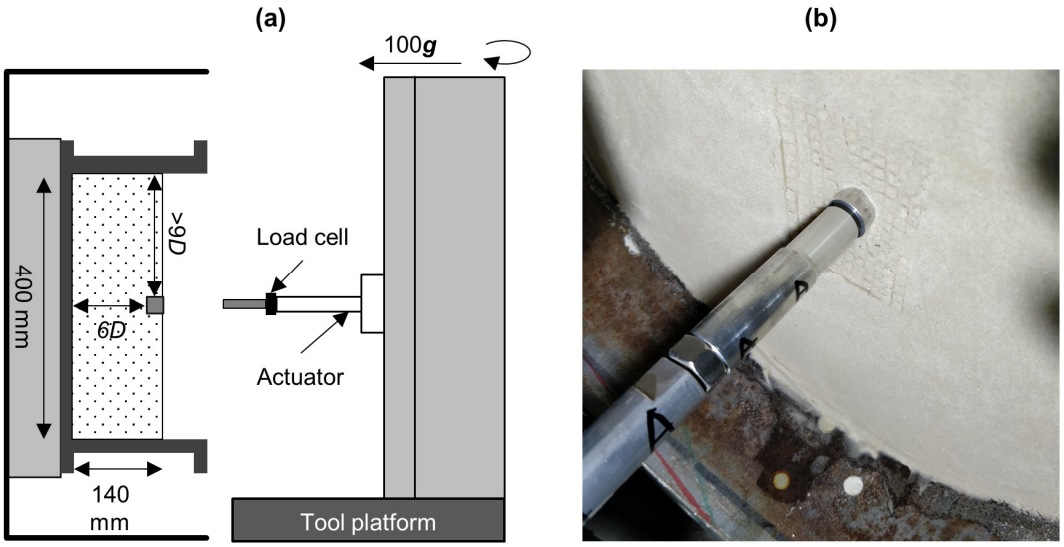

Figure 5.12: Experimental setup for the vertical push tests: (a) schematic cross-section; and (b) photo taken just before a test.

After spinning, the foundation is pushed with a constant velocity of 0.02 mm/s to a maximum displacement of 20 mm to obtain the vertical load-settlement $V-w$ response. The normalized velocity $vD_f/c_v = 8\cdot10^{-4} < 10^{-2}$ is considered sufficient to ensure drained conditions according to Randolph and Hope (2004), assuming the consolidation coefficient of fine silica sand c_v = 500 mm^2/s (Qi et al., 2016b).

5.3.1.4 Monotonic and cyclic lateral pushover tests

The lateral pushover tests are also displacement-controlled, employing electric screw-jack actuators (Concens, 35) rigidly attached to the semi-circular strongboxes of 320 mm height and 1050 mm length (Figure 5.13.a). The actuators are connected to the models through sliding hinges, with pins free to move in the vertical direction (Figure 5.13.b). This connection is essential to apply the desired horizontal displacement while allowing the structure to freely settle (or uplift) and rotate.

The distance between the foundation and the bottom boundary is larger than $3D_f$, while the distances of the foundation to the lateral sidewalls are larger than $4D_f$ and $12D_f$, in the transverse and longitudinal direction, respectively, to minimise undesired boundary effects. The actuators are connected outside the drum centrifuge, and then the strongboxes are installed in the channel. During this phase, an external support is used to hold in position the pier, rigidly connected to the foundation. After installation, the support is removed, and the steel mass is connected to the pier. An electromagnetic system holds in-place the mass during the initial spin-up phase (Figure 5.13.b). When a centrifugal acceleration of 10g is reached, the system is released.

For each strongbox, a high-resolution load cell of 2kN capacity (MTS, Type 8523) is installed on the actuator to measure the horizontal force H applied to the structure. Three laser sensors (Micro-Epsilon, optoNCDT 1402) are used to measure the in-plane displacements of the structure: L_1 and L_2 measure horizontal displacements and L_3 vertical displacements (Figure 5.13).

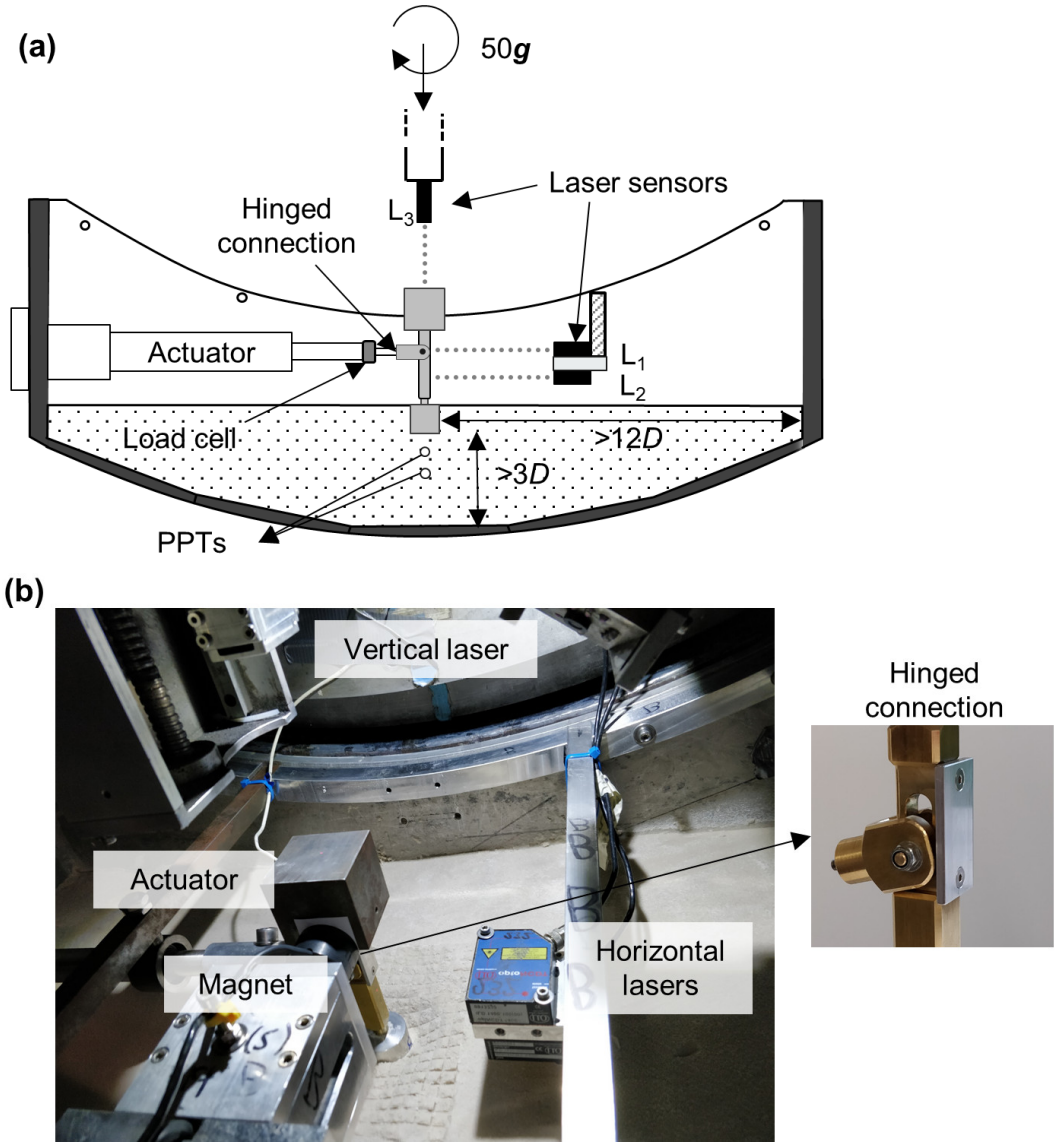

Figure 5.13: Experimental setup for the lateral pushover tests: (a) schematic cross-section (modified from Taeseri et al., 2018); and (b) photo taken just before one of the tests.

As shown in Figure 5.14, the rotation, θ, of the structure can be computed as:

$$\theta = \frac{u_{L_1} - u_{L_2}}{h_L} \tag{5.2}$$

where u_{L_1} and u_{L_2} are the displacements measured by the horizontal lasers, while h_L is the distance between the laser sensors. The settlement w of the structure (using the centre of the bottom of the footing as a reference) can instead be calculated, after geometrical considerations, as follows:

$$w = w_{L_3} + \left(\frac{h_{tot}}{\cos\theta} - h_{tot} + \left(u_{L_1} - h_{act} \cdot \tan\theta \right) \cdot \tan\theta \right) \tag{5.3}$$

where w_{L_3} is the vertical displacement measured by laser L_3, while h_{act} is the distance between the actuator (and also the laser L_1) and the bottom of the footing.

The overturning moment can be computed as:

$$M = H \cdot h_{act} \tag{5.4}$$

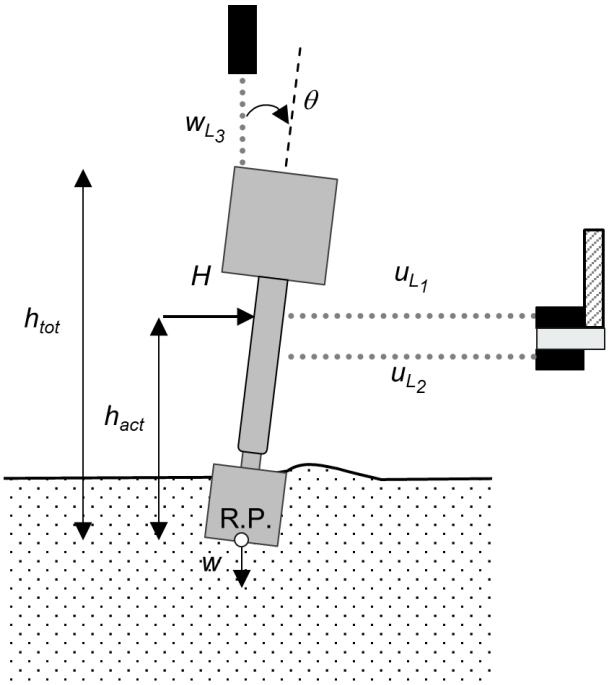

Figure 5.14: Reference scheme adopted to study the rocking response of the pier.

The model structures, considering scoured and unscoured conditions, are subjected to monotonic and slow-cyclic pushover loading. The monotonic tests are performed with a constant velocity of 0.5 mm/s up to a maximum displacement of 8 mm, which is adequate to measure the entire moment–rotation ($M-\theta$) response, all the way up to toppling. The slow-cyclic tests are performed according to a protocol that consists of 10 load cycles for 8 different increasing amplitudes.

Two PPTs are embedded in the soil below the foundation (at 0.5D and 1D) to detect a potential undesired pore-water pressure build-up (Figure 5.13.a). The PPTs, however, measured just small, stable in time, increments of pore-water pressure.

For instance, Figure 5.15 plots the increments of pore water pressure Δu_w as measured by the two PPTs during a cyclic test (test CH1), compared to the hydrostatic increment $\gamma_w w$ due to the settlement of the foundation. It is evident that the PPTs measured just the changes due to the vertical movement of the sensors, confirming the fully drained hypothesis of the tests.

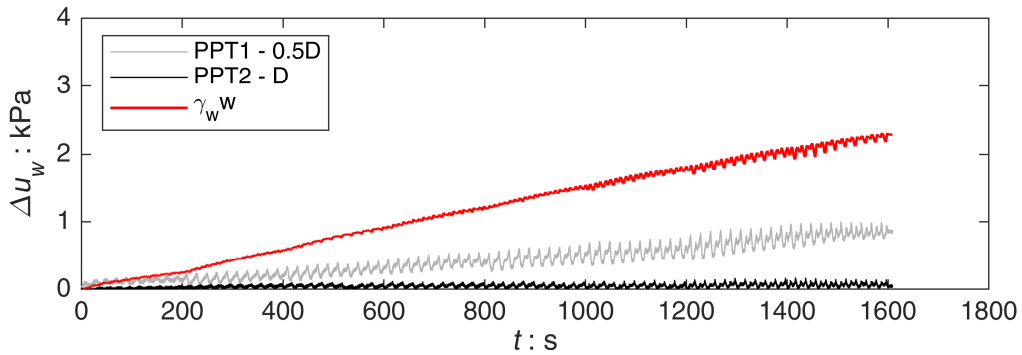

Figure 5.15: Pore water pressure build-up measured during a cyclic horizontal test (test CH1).

In the following sections, the results are presented in prototype scale, according to the scaling laws of Table 5.1. The data were acquired with a sampling frequency of 100 Hz. A smoothing procedure was applied to the raw data through a 3rd order Savitzky-Golay filter using a built-in Matlab routine (MathWorks, 2020), where each value is defined through a local polynomial least-squares fitting.

As an example, Figure 5.16 reports the comparison between raw and filtered data for a montonic horizontal test (test MH1). The filtering procedure is able to filter out the high-frequency noise but still preserving the actual experimental trends.

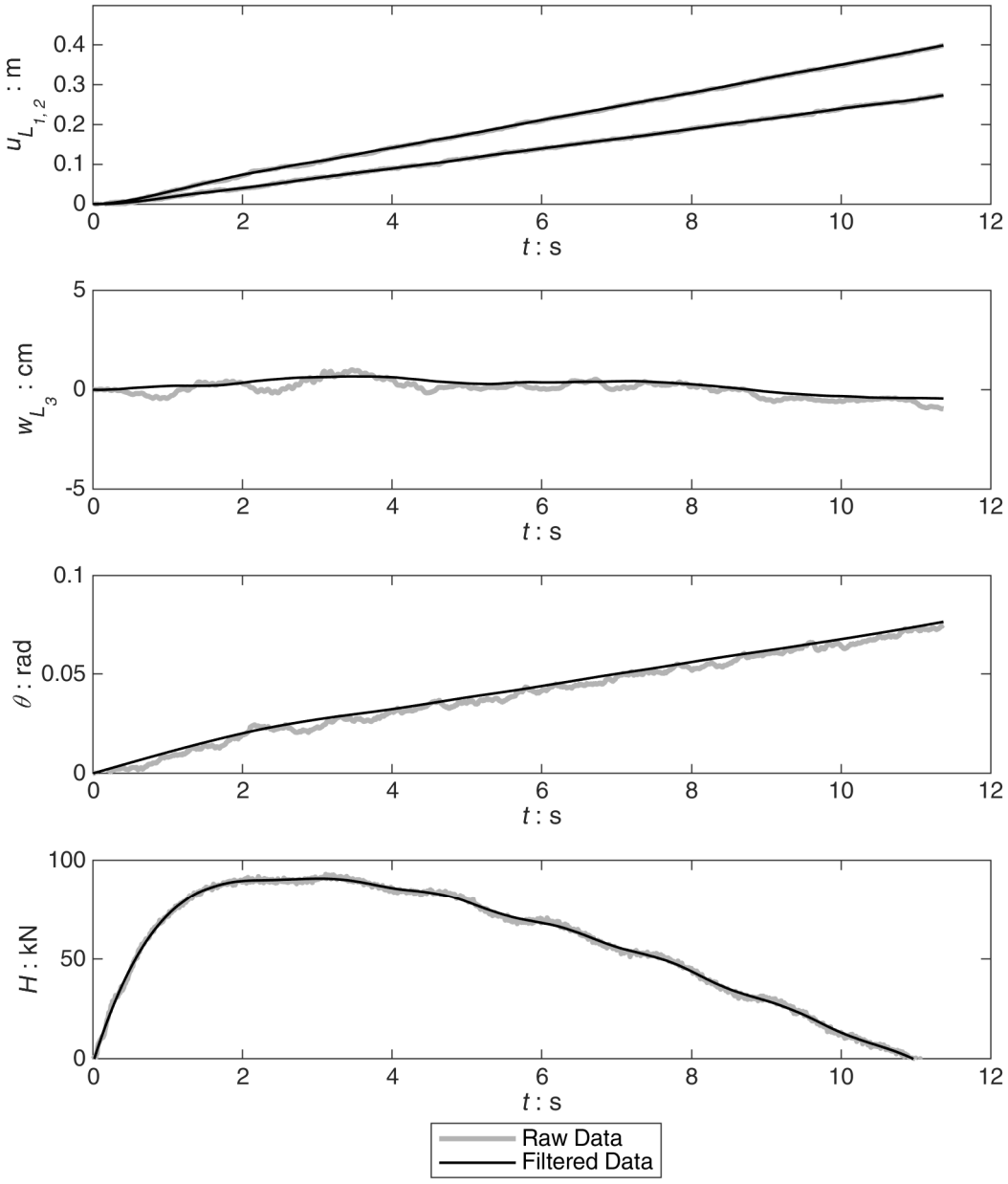

Figure 5.16: Effectiveness of the filtering procedure (test MH1).

5.3.2 Vertical loading

The bearing capacity of the foundation subjected to purely vertical loading is investigated for unscoured and scoured conditions. As summarized in Table 5.5, four vertical push tests ($V1_{A,B}$ and $V2_{A,B}$) were conducted, checking also the repeatability of the experimental process. Figure 5.17 presents the key results in terms of tangent vertical stiffness–settlement $(K_v - w)$, and vertical load – settlement $(V - w)$ response. The repeatability of the testing process is demonstrated by the comparison of the $K_v - w$ curves (Figure 5.17.a). Comparing each pair of tests for scoured and unscoured conditions, small discrepancies are observed but the results are consistent. For each case, the bearing capacity is estimated considering the average of the two tests.

Table 5.5: Summary of the vertical push tests.

Test	Condition	Void ratio, e	Settlement at failure, w_{ult}: m	Vertical bearing capacity, V_{ult}: MN	Average	Vertical safety factor, FS_v
$V1_A$	Unscoured	0.55	0.45	8.91	8.93	8.60
$V1_B$	Unscoured	0.54	0.47	8.96		
$V2_A$	Scoured	0.55	0.49	8.14	8.24	7.95
$V2_B$	Scoured	0.54	0.46	8.33		

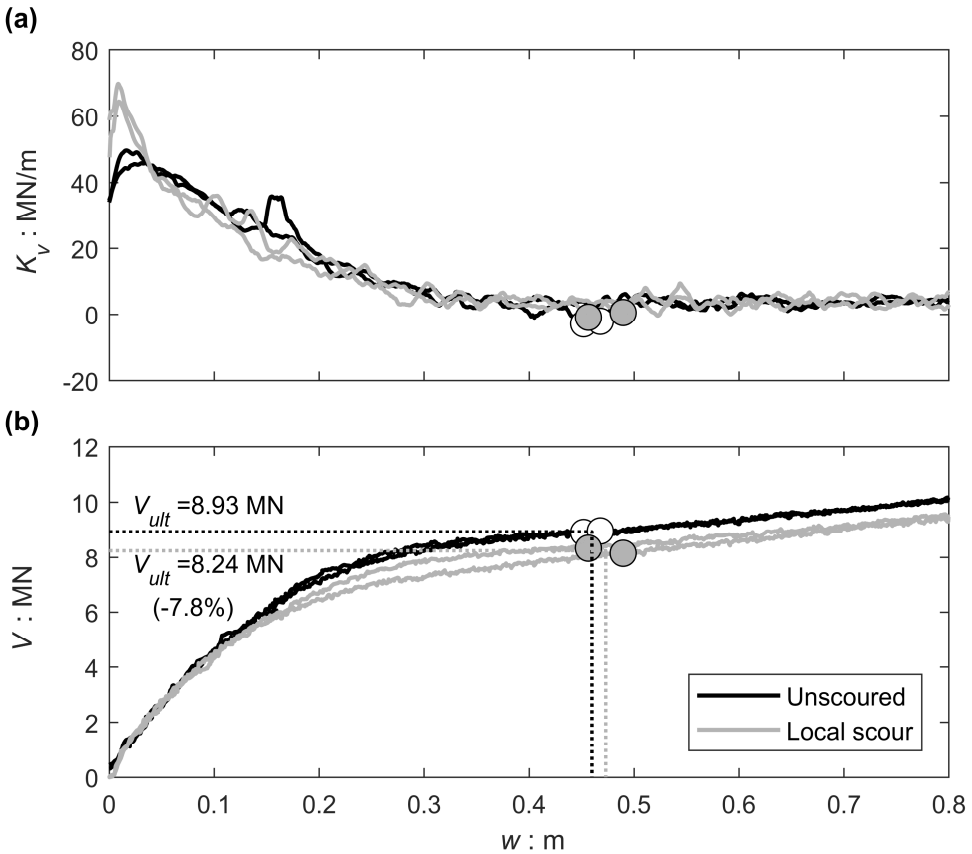

Figure 5.17: Vertical response of the footing before and after local scouring: (a) tangent vertical stiffness–settlement $K_v - w$ and (b) load–settlement $V - w$ response.

Regarding the failure mode, a local shear mechanism was observed rather than a general one, as it should be expected for a relatively shallow footing on dense sand (Vesic, 1973, 1975). The $K_v - w$ curves (Figure 5.17.a) are slightly nonlinear up to a settlement w = 0.15 m. Then, the failure mechanism starts developing, and the response becomes highly nonlinear. Once the failure mechanism is fully developed, the curves exhibit an almost linear hardening response. The latter is partially due to the progressive increase of foundation embedment.

Since no clear plateau can be identified in the V-w curves, the bearing capacity V_{ult} cannot be directly inferred. Following the procedure suggested by Anastasopoulos et al. (2012), V_{ult} is defined as the load at the initiation of the hardening regime (i.e. the point at which the $K_v - w$ curves become horizontal), which corresponds to settlement w_{ult} (Figure 5.17). Using this definition, V_{ult} = 8.93 MN in unscoured conditions. When considering scoured conditions, V_{ult} = 8.24 MN (i.e., a reduction of 7.8 %). This limited reduction is mainly due to the decrease of the effective overburden pressure in the soil below the foundation; the size of the local scour hole is not sufficient to intersect the failure surface.

The measured V_{ult} is used as a reference to determine the deck mass required to achieve a factor of safety under purely vertical loading FS_v of about 8, which corresponds to a moderately loaded bridge system. Specifically, FS_v is computed as:

$$FS_v = \frac{V_{ult} + W_3'}{W_3' + W_2 + W_1} \tag{5.5}$$

where W_3', W_2, and W_1 are, respectively, the weight of the footing under buoyancy, the weight of the column, and the weight of the deck. In the unscoured case, the achieved FS_v is 8.6, reducing to 7.95 with scouring.

5.3.3 Lateral pushover loading

The lateral response is investigated through displacement-controlled monotonic pushover tests. The problem is symmetric in the longitudinal direction (y), and therefore a single test is adequate. In the transverse direction (x), given the asymmetry of the scour hole, two tests were necessary: one downstream and one upstream (Figure 5.18). An additional model was realized by removing a uniform soil layer of 1 m thickness (i.e., the average scour depth due to local scour) to compare the effect of general (i.e., uniform) to local scour.

The idealized SDOF structure can be considered representative for relatively long multi-span bridges loaded in the transverse direction. In the longitudinal direction, such a system can be representative provided that the deck is not monolithically connected to the piers (i.e., supported on bearings).

Table 5.6 summarizes the conduced pushover tests (MH1-5), along with the measured moment capacity M_{ult} and the rotation angle at incipient overturning of the structure θ_{ult}.

Table 5.6. Summary of monotonic lateral pushover tests.

Test	Condition	Loading direction	Void ratio, e	Moment capacity, M_{ult} : kNm	Percentage decrease	Overturning rotation, θ_{ult} : rad
MH1	Unscoured	–	0.56	554	–	0.072
MH2	Local Scour	Transverse Downstream	0.55	447	-19.3%	0.064
MH3	Local Scour	Transverse Upstream	0.56	406	-26.7%	0.067
MH4	Local Scour	Longitudinal	0.56	342	-38.3%	0.051
MH5	Gen. Scour	–	0.57	289	-47.8%	0.048

Figure 5.19 reports the results of the tests in terms of the moment-rotation $(M-\theta)$ response. The response of the scoured structure is compared to the reference case of unscoured conditions. The $M-\theta$ response exhibits an initial quasi-elastic branch, followed by strongly nonlinear response until full mobilization of the ultimate moment capacity M_{ult}, and a final descending branch (due to $P-\delta$, second-order, effects) until reaching the overturning rotation θ_{ult}. In all cases examined, the scouring leads to a substantial decrease of M_{ult}. In the case of local scour and loading in the transverse direction (Figure 5.19.a,b), M_{ult} decreases from 19% to 27%, when loaded towards the downstream or the upstream side, respectively. The overturning rotation θ_{ult} is also reduced to 0.064 rad (downstream loading) and 0.067 rad (upstream loading), compared to 0.072 rad of the unscoured reference case. These differences, attributed to the larger volume of eroded soil along the upstream side (Figure 5.18), are non-negligible, but also not excessive.

A much more significant reduction (38%) of M_{ult} is observed in the longitudinal direction (Figure 5.19.c), where a larger volume of soil is eroded from the sides of the foundation. The reduction of θ_{ult} is also more significant, decreasing from 0.072 rad (unscoured case) to 0.051 rad.

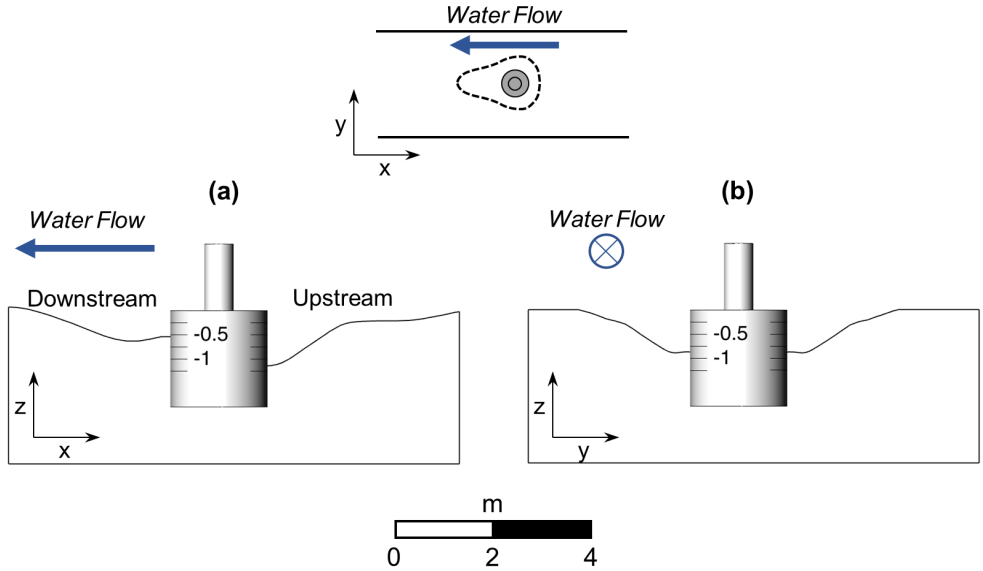

Figure 5.18: Cross-sections of the scour hole: (a) transverse direction; and (b) longitudinal direction (referring to the bridge axis).

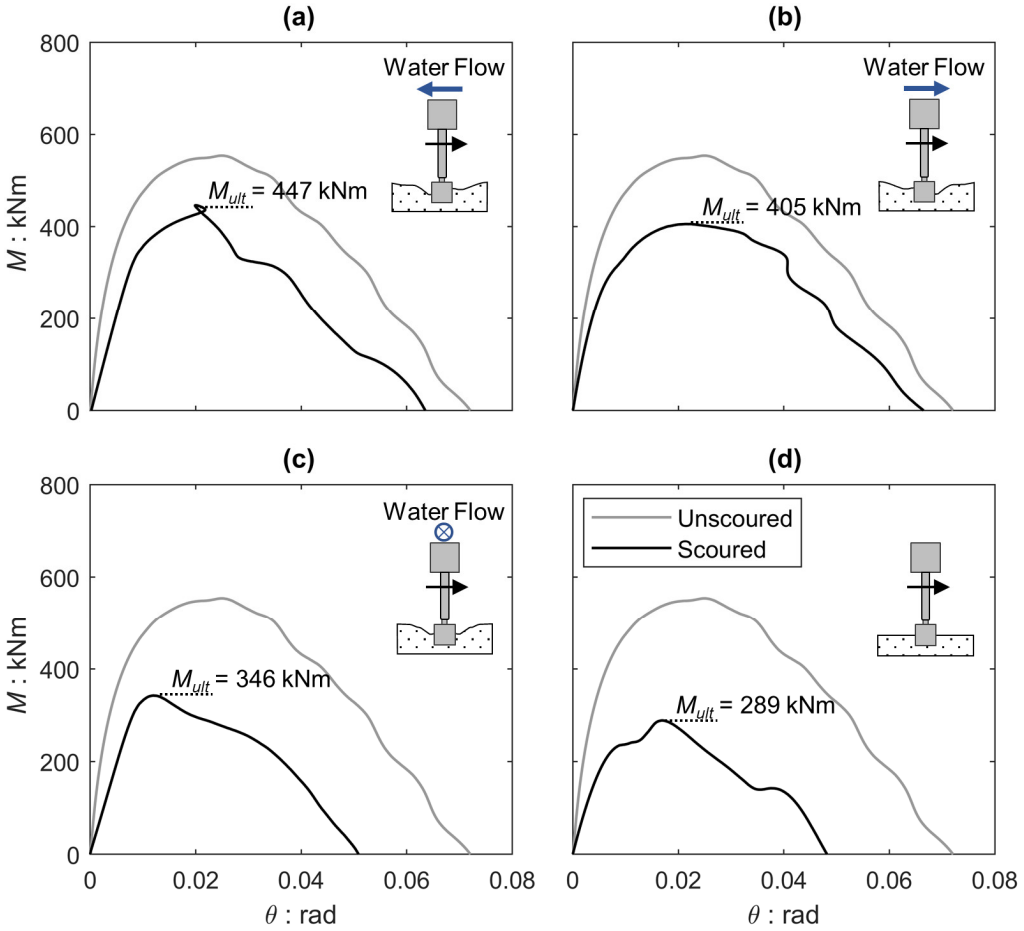

Figure 5.19: Moment-rotation $M-\theta$ response before and after the scouring for loading in: (a) transverse-downstream direction; (b) transverse-upstream direction; (c) longitudinal direction; and (d) general (uniform) scour assumption.

As expected, the maximum reduction of M_{ult} (48%) and θ_{ult} (0.048 rad) is observed in the case of general scour (Figure 5.19.d). In this case, the foundation embedment is simply reduced to d = 1 m (as opposed to 2 m before scouring). The results indicate that the simplified assumption of uniform scour can be excessively conservative, especially when considering the transverse direction of loading (which is usually critical). It may therefore be concluded that modelling the actual geometry of the scour hole, due to local scour processes, may have a significant effect on the conclusions and the decision regarding retrofit.

5.3.4 Slow-cyclic lateral loading

According to Gajan and Kutter (2008) and Anastasopoulos et al. (2012), the results of slow-cyclic lateral pushover tests can be considered representative of the seismic performance of a foundation system. Three displacement-controlled slow-cyclic centrifuge model tests (CH1-3) are conducted to explore the effects of scouring on foundation performance. As summarized in Table 5.7, three cases were examined: unscoured (reference) condition; after local scour along the transverse direction of the bridge (which is usually critical); and after general scour.

Table 5.7: Summary of the slow-cyclic horizontal tests.

Test	Condition	Loading direction	Void ratio, e
CH1	Unscoured	–	0.55
CH2	Local Scour	Transverse	0.56
CH3	General Scour	–	0.56

As shown in Figure 5.20, the displacement protocol consists of 8 packages of increasing displacement amplitude (2.5, 5, 7.5, 10, 15, 20, 30, and 40 cm in prototype scale), each one containing 10 load cycles. This allowed studying the slow-cyclic response of the foundation from small to large range of rotation.

The load is applied at a sufficiently slow rate, maintaining a model frequency of 0.05 Hz (0.001 Hz in prototype scale), avoid possible dynamic effects that would further complicate the response.

Figure 5.21 compares the moment–rotation $(M-\theta)$ and the settlement–rotation $(w-\theta)$ response for the three cases examined. The monotonic response is also included to allows for comparison.

Especially in Test CH3 (general scour), a non-negligible asymmetry in the $M-\theta$ response was observed during the last two packages (30 and 40 cm amplitude), which is attributed to excessive deformation. To allow for comparison, the last two packages are excluded from Test CH3.

Consistently with the monotonic tests, the unscoured foundation exhibits the largest M_{ult} (Figure 5.21.a), followed by the one subjected to local scour (Figure 5.21.b), and general scour (Figure 5.21.c). Despite the previously discussed geometric asymmetry of the local scour hole, no significant asymmetries are observed in the $M-\theta$ loops.

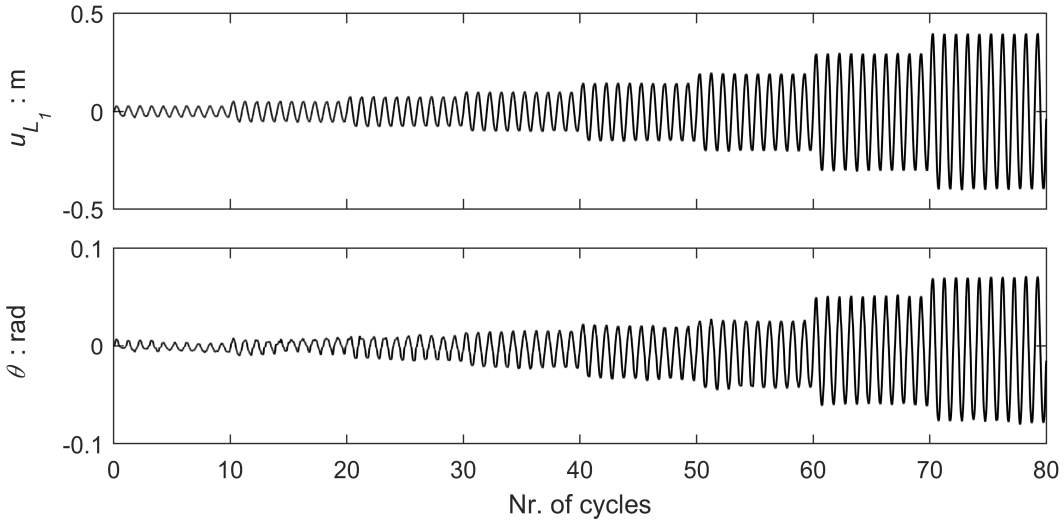

Figure 5.20: Displacement protocol used for the slow-cyclic horizontal tests and the corresponding cyclic rotations.

Interestingly (but not surprisingly), the cyclic $M-\theta$ loops exhibit an overstrength compared to the monotonic backbone curve for all cases examined. The overstrength ratio r_M, can be defined as the increase in the cyclic moment capacity over the monotonic moment capacity (Kokkali et al., 2015). The r_M reaches 120% for the unscoured foundation, becoming even higher (135%) in the case of local scour, and going to an astonishing 210% under general scour conditions. Kokkali et al. (2015) suggested that the cyclic overstrength is mainly due to progressive soil densification, and to the increase of foundation embedment due to settlement accumulation. The increase of embedment is more substantial for the scoured systems, leading to the larger r_M. In the case of general scour, settlement accumulation leads to a very pronounced increase of the embedment ratio from 0.5 to 1.

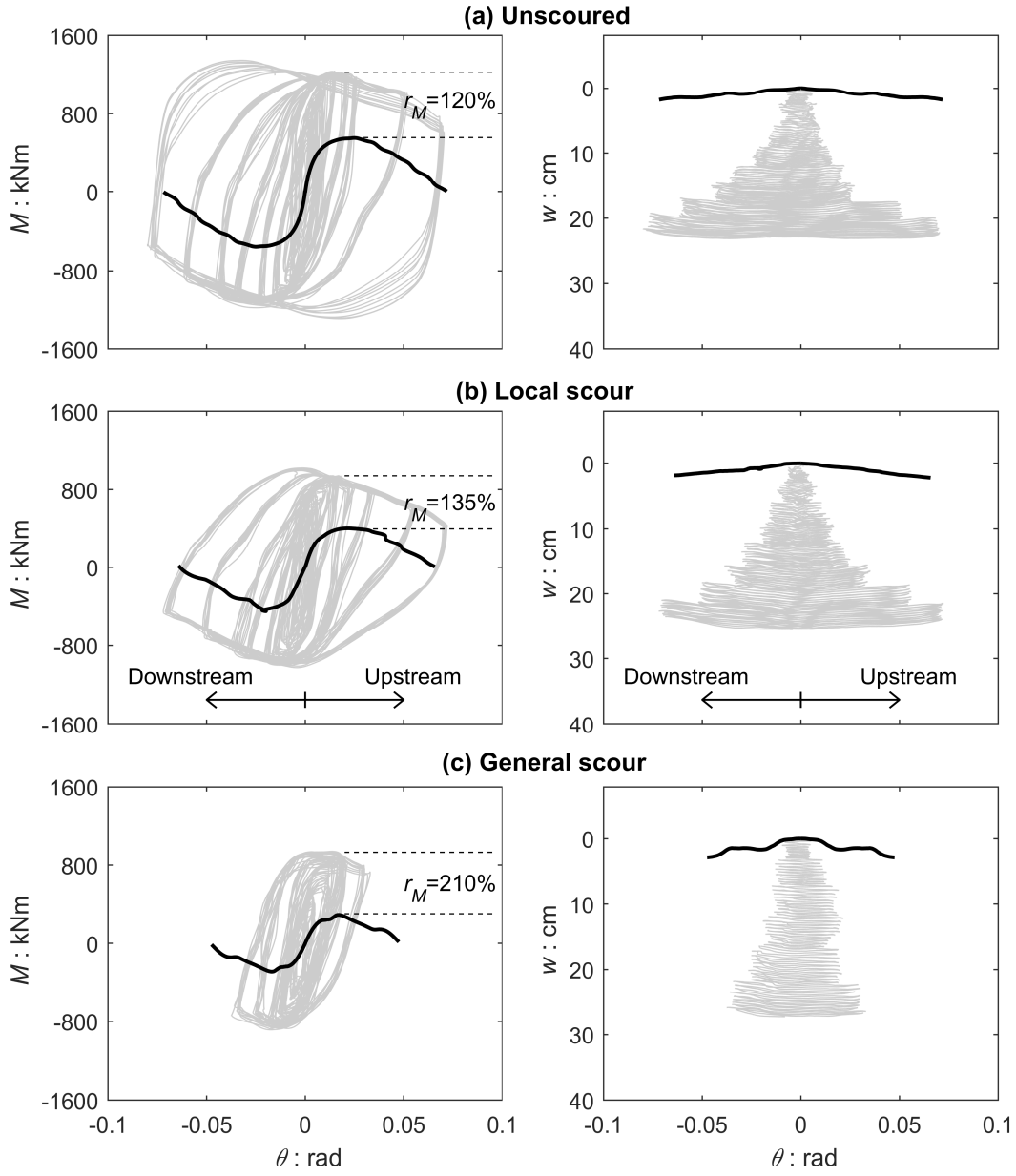

Figure 5.21: Slow-cyclic moment-rotation $M-\theta$ and settlement-rotation $w-\theta$ response for: (a) unscoured conditions; (b) local scour; and (c) general scour.

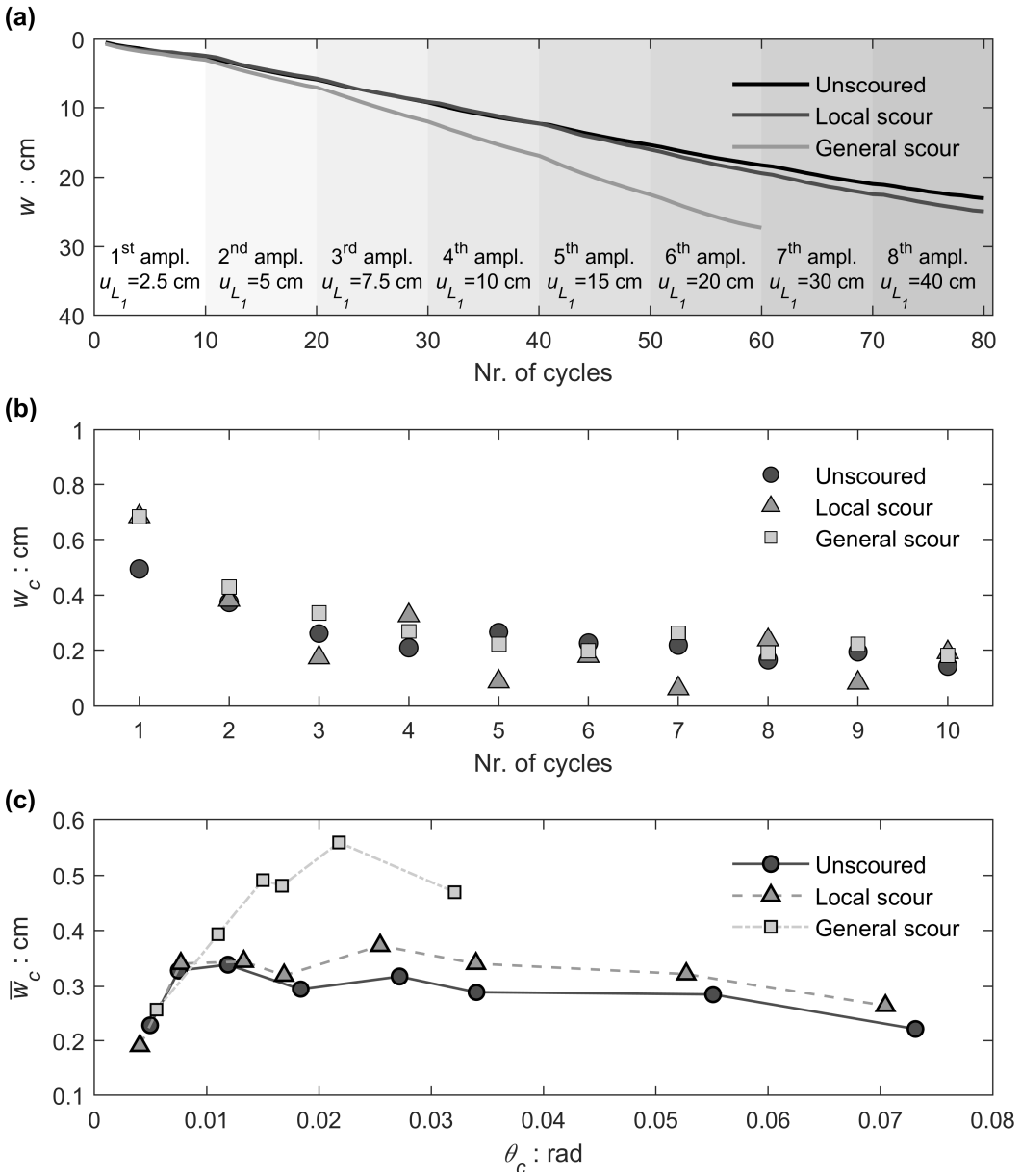

Figure 5.22: Settlement accumulation during cyclic loading: (a) settlement w in function of number of cycles; (b) settlement per cycle w_c in function of number of cycles (1st package); and (c) mean settlement per cycle $\overline{w}_c$ in function of cyclic rotation θ_c.

The observed overstrength can be better explained by looking into the settlement accumulation during cyclic loading (Figure 5.22). The settlement *w* at the end of each cycle is plotted against the number of cycles in Figure 5.22.a. In contrast to local scour, which does not affect the rate of settlement accumulation considerably, general scour leads to a very pronounced increase. Figure 5.22.b depicts the evolution of cyclic settlement w_c (due to one cycle of loading) for the first 10-cycle package (of smallest amplitude), also in function of the number of cycles. In all cases examined, w_c decreases with the number of (constant amplitude) cycles. This reveals that (at least for small displacement amplitudes), cyclic sand densification is the controlling parameter: sand densification leads to the observed decrease of settlement accumulated per cycle w_c.

The rate of settlement increases with the initiation of the following larger amplitude package. Figure 5.22.c plots the average settlement per cycle $\overline{w}_c$ for each 10-cycle package, as a function of cyclic rotation θ_c. For relatively small θ_c (< 0.01 rad), the accumulated settlement is mainly due to sand densification under the foundation, and hence the results are insensitive to scouring. The effect of scour becomes evident for larger θ_c (> 0.02 rad), where the moment capacity is fully mobilized and the rate of settlement is mainly controlled by soil plastification. General scour leads to a pronounced decrease of embedment, leading to a much shallower failure mechanism, leading to the observed drastic increase of $\overline{w}_c$. Local scour leads to a loss of side resistance, but not to such a pronounced decrease of embedment. As a result, the failure mechanism is not affected to the same extent, and hence its effect on $\overline{w}_c$ is less significant. For even larger θ_c, the dilative response of sand starts to compensate the plasticity-induced settlements, leading to progressive stabilization and even decrease of the rate of settlement, especially in the general scour case.

5.3.5 Effects of scouring on the rocking stiffness degradation and damping ratio curves

As shown in Gazetas et al. (2013), the degradation of secant rocking stiffness with rotation θ and the corresponding hysteretic damping ratio offer a convenient way to quantify nonlinear foundation response, and can also be used to assess dynamic performance based on equivalent-linear analyses. In this context, this section investigates the effects of scouring on the cyclic secant rocking stiffness $K_{r,c}$ and the hysteretic damping ratio $\xi_{r,h}$, as a function of θ.

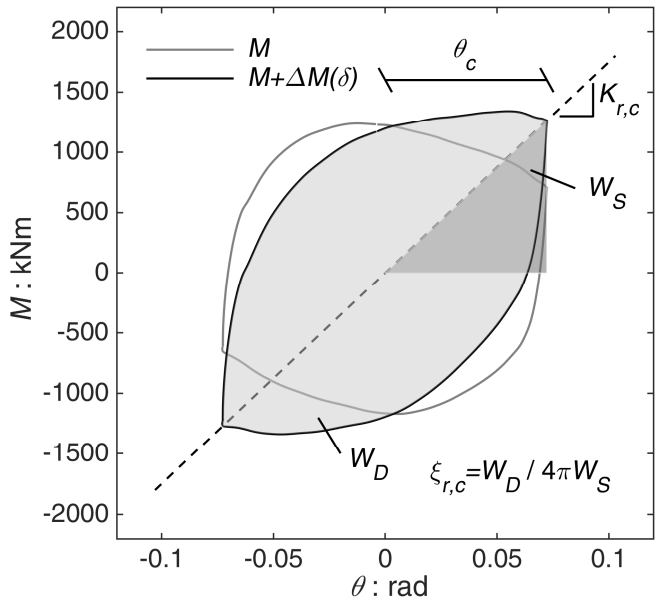

Figure 5.23: Calculation of secant rocking stiffness $K_{r,c}$ and hysteretic damping ratio $\xi_{r,h}$ on the basis of cyclic $M-\theta$ loops.

Their calculation is performed using the $M-\theta$ loops of the cyclic pushover tests, as shown in Figure 5.23. The moment $\Delta M(\delta)$ caused by second-order $(P-\delta)$ effects is added to the external applied moment. During loading, $\Delta M(\delta)$ reduces the moment capacity leading to an additional *apparent* stiffness degradation. Conversely, as shown by Panagiotidou et al. (2012), during unloading $\Delta M(\delta)$ is opposed to the motion leading to an *apparent* overstrength. The latter also leads to enlargement of the $M-\theta$ loops, increasing hysteretic damping. Hence, $K_{r,c}$ is defined as the slope of the line connecting the edges of the $(M+\Delta M)-\theta$ loops, and the $\xi_{r,h}$ as a function of the energy W_D dissipated within one such loop over the corresponding elastic strain energy W_S.

Figure 5.24 plots the $K_{r,c}$ and $\xi_{r,h}$ curves obtained from the cyclic pushover tests. The average cyclic rocking stiffness of each load package (i.e., the average $K_{r,c}$ obtained for the 10 cycles of equal imposed displacement) is compared to the monotonic secant stiffness $K_{r,m}$ computed from the monotonic pushover tests, again correcting for $P-\delta$ effects. Due to measurement accuracy, the estimated $K_{r,m}$ for very small rotations is not considered reliable. Hence, the results are plotted for $\theta > 0.008$ rad, and curve-fitting is performed to roughly estimate the small-strain rocking stiffness (shown with dashed lines).

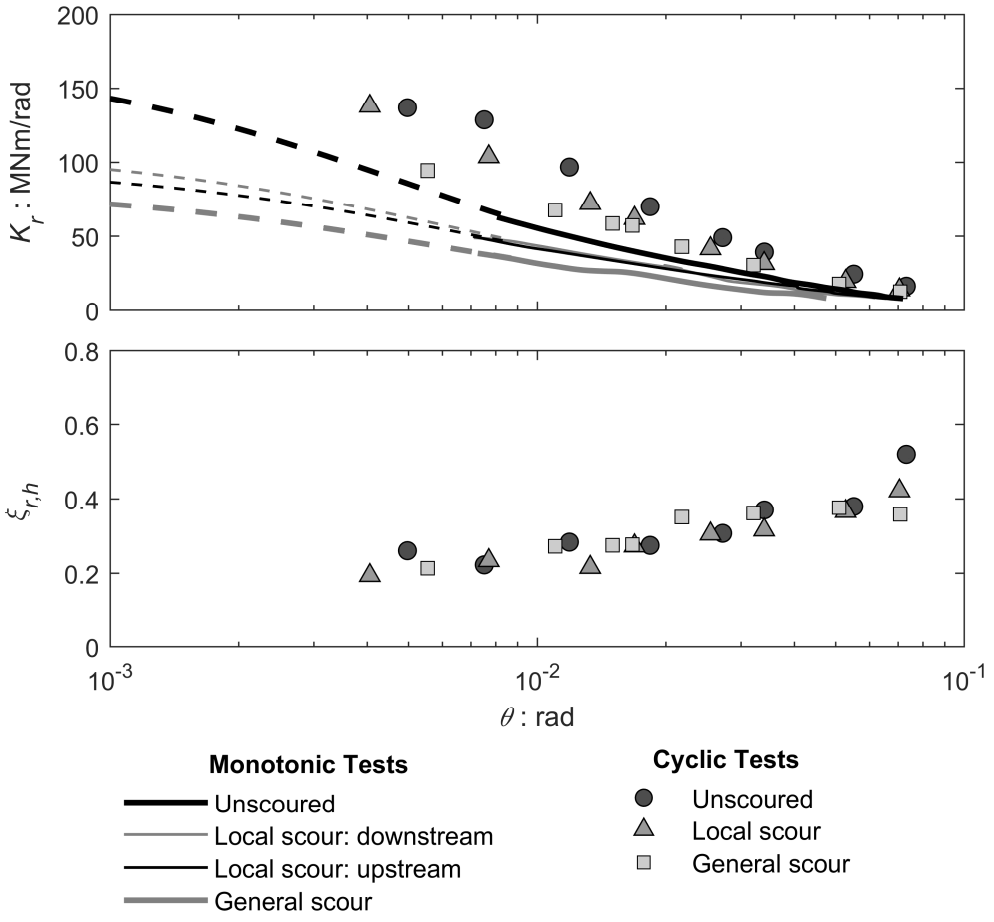

Figure 5.24: Effects of scour on rocking stiffness degradation $K_{r,c}$ and damping ratio $\xi_{r,h}$ as a function of rotation θ. The cyclic secant rotational stiffness is compared to secant monotonic stiffness (the dashed part of the curves is estimated by fitting).

The previously discussed overstrength (Figure 5.21) leads to a significant increase of $K_{r,c}$ in comparison to $K_{r,m}$. Nevertheless, the trends are consistent between cyclic and monotonic tests. General scour leads to a pronounced reduction of the secant rocking stiffness for the entire range of θ; the effect of local scour is moderate. Despite the geometric asymmetry of the scour hole, the direction of loading (upstream or downstream) does not significantly affect the $K_{r,m}$ curves. This is consistent with the shape of the $M-\theta$ loops, which are only slightly skewed (Figure 5.21.b). The hysteretic damping ratio $\xi_{r,h}$ increases with rotation θ, reaching a maximum of 0.4 to 0.5. Despite the difference in secant stiffness, the damping ratio is insensitive to the degree of scouring.

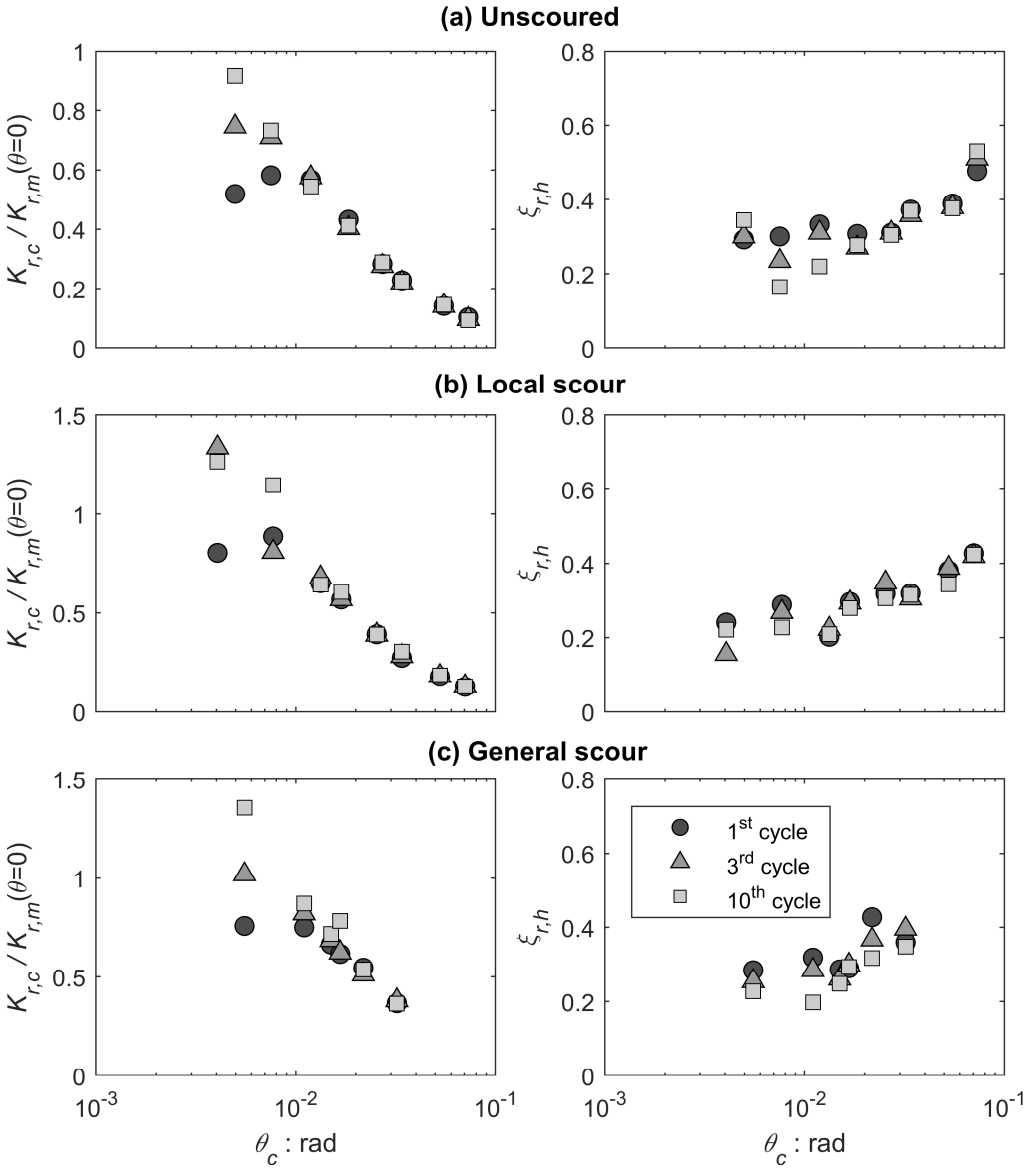

Figure 5.25: Influence of the number of cycles on normalized cyclic secant rocking stiffness $K_{r,c}/K_{r,m}(\theta=0)$ and damping ratio $\xi_{r,h}$ in function of cyclic rotation θ_c for: (a) unscoured reference case; (b) local scour; and (c) general scour.

Figure 5.25 offers direct visualization of the effect of the number of cycles on nonlinear rocking response. The cyclic secant rocking stiffness $K_{r,c}$, normalized to the estimated small-strain monotonic rocking stiffness $K_{r,m}(\theta = 0)$, is plotted for the 1st, 3rd and 10th cycle of each θ_c amplitude (from the corresponding load packages); the same is applied to the hysteretic damping ratio $\xi_{r,h}$. For all cases examined, the normalized secant rocking stiffness $K_{r,c}/K_{r,m}(\theta = 0)$ increases during the first two packages, tending to stabilize during the ensuing larger amplitude packages. This tendency is present in the unscoured case (Figure 5.25.a), but is more pronounced when the foundation is subjected to local (Figure 5.25.b) and general scouring (Figure 5.25.c), where sand densification is accompanied by an increase of embedment (due to the progressive accumulation of settlement). The increase of embedment, as previously discussed, leads to a significant overstrength when the cyclic response is compared to the monotonic one, which reflects in $K_{r,c}$ values at small rotations even larger than $K_{r,m}(\theta = 0)$. In stark contrast, $\xi_{r,h}$ is insensitive to the number of cycles. However, it should be pointed out the experimental estimation of hysteretic damping is characterized by larger uncertainties for low rotational amplitudes, which may have partially concealed such effects. At very small rotations it is challenging to define very precisely the shape of the hysteresis loops due to the accuracy of the instrumentation. Therefore, minor differences between $\xi_{r,h}$ measured at different small amplitude cycles may not have been detected.

5.4 Discussion and conclusions

This chapter has reported an experimental study on the response of a moderately loaded bridge pier, supported on a cylindrical embedded foundation, subjected to flood-induced scour. A hybrid 2-step methodology was developed for this purpose. In the first step, the hydraulic problem of local scour around a pier is modelled in 1***g***. The scour hole morphology is 3D-scanned and a mould is 3D-printed to reproduce the geometry in an *N****g*** model, subsequently tested in the ETHZ drum centrifuge to study its mechanical response.

The methodology was applied to investigate the performance of the soil-structure system prior to and after local scour through vertical, lateral monotonic, and lateral slow-cyclic pushover tests. An additional test series was conducted to study the effects of general scour, removing a layer of constant thickness equal to the maximum measured local scour depth. The key conclusions of the experimental study are summarized as follows:

1. Local scour has a limited effect on the vertical response of the foundation. In stark contrast, the lateral response is significantly affected, with the foundation moment capacity being reduced by 19% to 38%, depending on the direction of loading. General scour has an even more pronounced effect, leading to 48% reduction of M_{ult}. It may therefore be concluded that accounting for the scour hole geometry is essential to address the effects of

local scour. Assuming general scour conditions can be largely over-conservative.

2. For all the investigated configurations, the slow-cyclic pushover tests reveal a significant overstrength compared to the monotonic backbone curve and the corresponding M_{ult}. These differences, quantified through the moment overstrength ratio r_M, are attributed to progressive sand densification, and the increase of embedment due to settlement accumulation. While local scour leads to a small increase of r_M, the effect of general scour is pronounced. This is mainly attributed to the drastic increase of the embedment ratio from 0.5 to 1, due to the accumulation of settlement.
3. The rate of settlement accumulation during cyclic loading is not affected significantly by local scour. In contrast, general scour leads to a pronounced increase. For small cyclic rotation ($\theta_c < 0.01$ rad), the accumulated settlement is mainly due to sand densification, and hence the response is insensitive to scouring. The rate of settlement is affected by scour for larger θ_c (> 0.02 rad), where M_{ult} is fully mobilized and soil plastic response becomes the controlling factor. General scour leads to a pronounced increase of the settlement rate is observed due to general scour. The increase is mainly attributed to the significant loss of embedment that leads to a shallower failure mechanism and a substantial decrease of FS_v. This is not the case for local scour, which only leads to a small decrease of FS_v, thus not significantly affecting the failure mechanism and the rate of settlement accumulation.
4. In contrast to general scour, which leads to a pronounced reduction of the secant cyclic rocking stiffness $K_{r,c}$ for the entire range of θ, local scour has a moderate effect. Despite the observed asymmetry of the scour hole, the secant rocking stiffness is insensitive to the loading direction. The hysteretic damping ratio $\xi_{r,h}$ increases with rotation θ, but seems to be insensitive to scouring.

The above-discussed conclusions are clearly valid for the specific condition investigated in the experimental tests, i.e. a moderately loaded bridge pier constituted by a slender column supported on a cylindrical caisson foundation with a embedment-to-diameter ratio of 1. Nevertheless, the experimental tests represent an important basis that can be used to define an accurate numerical model able to reproduce the changes in the performance of caisson foundations induced by foundation scour.

Chapter 6

Soil constitutive model

The results of the experimental tests presented in Chapter 5 have shown the significant effects of scouring on the performance of caisson foundations. As previously discussed, both local and general scour can have a major impact on the horizontal performance of caissons, although the two conditions may lead to different outcomes.

However, two main issues spring to mind when the experimental results are analyzed in the light of the differences between local and general scour: (i) is it possible to predict the main mechanisms affecting the two phenomena and, in turn, their mechanical consequences? (ii) which is the impact of local and general scour on bridge piers with different characteristics from the specific case here analyzed?

Numerical models can help to answer these questions. However, it is first necessary to calibrate a constitutive model able to reproduce the stress-strain behaviour of the Perth sand at an element level. Subsequently, the constitutive model can be used to simulate the response of the soil in a boundary value problem, such as the ones analyzed in the centrifuge tests. If the validation against the centrifuge tests is considered satisfactory, the numerical model can be used to predict, in a reasonable way, the response of the soil-structure system also under different loading conditions.

This chapter presents the main features of the soil constitutive model adopted in this study, namely the Severn-Trent model (Gajo and Muir Wood, 1999a, b; Gajo, 2010). The model has proved to be effective in predicting the sand behaviour for a wide range of boundary value problems (e.g., Abate et al., 2008; Abate et al., 2010; Rotisciani and Miliziano, 2014; Kowalczyk and Gajo, 2020). The constitutive parameters are derived for the Perth sand considering the element tests introduced in Chapter 4, with a particular focus on the drained triaxial tests carried out on dense sand samples. The calibration procedure is initially performed by comparing the results of the triaxial tests to the predictions of the constitutive model, obtained by imposing a “true” triaxial stress-state on a single finite element. Then, the

calibration is refined by treating the triaxial tests as boundary value problems, thus including also the effects of the end restraints. Finally, the cyclic response of the sand as predicted by the model is compared to the results of the resonant column tests.

6.1 The Severn-Trent sand model

The Severn-Trent sand model, as in the version proposed by Gajo (2010), is adopted to simulate the soil response in this study. The original model (Gajo and Muir Wood, 1999a, b) is based on the bounding-surface approach and a hyperbolic degradation of plastic stiffness. It has been shown to be effective in describing the stress-strain response of sands for a wide range of soil densities and confining pressures, adopting a single set of constitutive parameters with a clear physical meaning (Gajo and Muir Wood, 1999a, b). Although equivalent to the original one, the version here employed (Gajo, 2010) is based on the framework of the classical kinematic-hardening plasticity and it adopts a hyperelastic formulation. Such a hyperelastic formulation can simulate the evolution of the elastic anisotropy of the material due to both stress and strain changes. Besides, it takes into account the dependence of the elastic stiffness on mean stress. It is worth to mention that, for the sake of simplicity, the intial inherent elastic anisotropy and the plastic strain induced evolution of the fabric tensor are neglected in this study.

The main features of the Severn-Trent model as is in the version here adopted are presented in the following sections. For a detailed description of the constitutive model, the interested reader can refer to Gajo and Muir Wood (1999a, 1999b) and Gajo (2010).

6.1.1 Basic concepts

The mechanical behaviour of sands is known to be both pressure- and density-dependent (see also Section 4.2.1). As a consequence, the current strength of the sand is not constant, but it depends on the current specific volume and mean stress. The Severn-Trent model adopts the state parameter Ψ, as proposed by Been and Jefferies (1985), to account for pressure and density dependency (Gajo and Muir Wood, 1999b). The parameter is an indicator of the distance between the current state and the critical state, and it can be expressed as:

$$\Psi = v_0 - v_\lambda + \lambda \ln p' \tag{6.1}$$

where v_0 is the current void ratio, while v_λ and λ are the constitutive parameters defining the position of the Critical State Line in the $v - \log p'$ plane (see also Figure 4.5). The sizes of both the strength and the yield surfaces are related to the size of the critical state surface through a ratio r defined as:

$$r = 1 - k\Psi \tag{6.2}$$

where k is a constitutive parameter.

A sand at an initial state denser than critical experiences a dilative behaviour under shearing and, consequently, a progressive softening towards the critical state condition. Conversely, if the initial state is looser than critical the sand tends to densify, experiencing a progressive hardening. Consequently, in the *true* stress space, the sand may undergo both hardening and softening at shearing and the yield and strength surfaces can, in turn, expand or shrink.

As discussed by Gajo and Muir Wood (1999a, 1999b), it is convenient to formulate the model by referring to a *normalized* stress $\bar{\boldsymbol{\sigma}}$ space, in which the deviatoric component of the *true* stress $\boldsymbol{\sigma}$ is divided by the ratio r:

$$\bar{\boldsymbol{\sigma}} = \frac{1}{1 - k\Psi}\,\mathrm{dev}\boldsymbol{\sigma} - p\mathbf{I} \tag{6.3}$$

where $\mathbf{I}$ is the second-order unity tensor. In such a space, the *normalized* strength and yield surfaces are constant in size and the *normalized* stress $\bar{\boldsymbol{\sigma}}$ can only experience a progressive kinematic hardening, reaching the critical state condition at infinite strains. Besides, in the *true* stress space, the axis and the boundaries of the yield surface are curved due to its change in size induced by the dependence on the state parameter. Conversely, in the *normalized* stress space, the yield surface is characterized by straight boundaries and a straight axis and its current position is totally defined by a second-order symmetric tensor $\boldsymbol{\alpha}$ (Figure 6.1).

It is worth noting that the model is formulated in terms of effective stresses. However, the symbol p is adopted rather than p' in Eq. (6.3) and hereafter in the description of the model to indicate the *effective* confining pressure, for consistency with the reference publications (Gajo and Muir Wood, 1999b, a; Gajo, 2010).

In the following, reference is made to the formulation of the model in the *normalized* stress space. Once the *normalized* stress $\bar{\boldsymbol{\sigma}}$ is obtained, the *true* stress $\boldsymbol{\sigma}$ can be straightforwardly computed from Eq. (6.3).

6.1.2 Yield and strength surfaces

The shapes of both the yield and the strength surfaces are defined through the Argyris criterion (Argyris et al., 1974), which provides the best numerical prediction of the sand behaviour along non-triaxial stress-paths (Gajo and Muir Wood, 1999a).

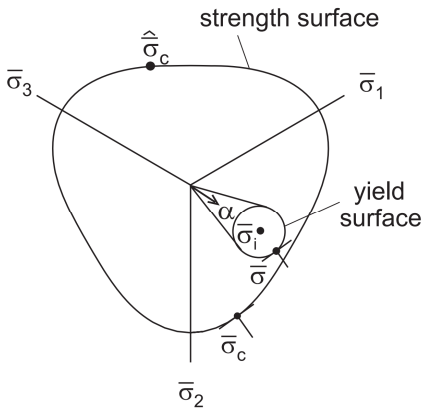

Figure 6.1: Schematic illustration of the position of the yield and strength surfaces and the conjugate stresses in the normalized deviatoric plane (from Gajo, 2010).

According to the abovementioned criterion, the strength surface, in the *normalized* stress space, can be expressed as follows (Gajo, 2010):

$$\bar{F}\left(\bar{\boldsymbol{\sigma}}\right)=\sqrt{\frac{3}{2}\mathrm{tr}\left(\mathrm{dev}\,\bar{\boldsymbol{\sigma}}\right)^{2}}-M_{CS}\,g\left(\theta_{\sigma}\right)p \tag{6.4}$$

where M_{CS} is a constitutive parameter representing the slope of the CSL in the $q-p$ plane, equal to $\left(6\sin\varphi'_{CS}\right)/\left(3-\sin\varphi'_{CS}\right)$, and $g\left(\theta_{\sigma}\right)$ is a function of the Lode angle θ_{σ} which describes the shape of the deviatoric section of the strength surface (Argyris et al., 1974):

$$g\left(\theta_{\sigma}\right)=\frac{2m}{1+m+\left(1-m\right)\cdot\cos\left(3\theta_{\sigma}\right)} \tag{6.5}$$

being m a further constitutive parameter, typically chosen to ensure the convexity of the surface.

The yield surface is defined as a fraction of the strength surface according to a ratio $R<1$ (Gajo, 2010):

$$\bar{f}\left(\bar{\boldsymbol{\sigma}},\boldsymbol{\alpha}\right)=\sqrt{\frac{3}{2}\mathrm{tr}\left(\mathrm{dev}\,\bar{\boldsymbol{\sigma}}-\frac{\mathrm{tr}\,\bar{\boldsymbol{\sigma}}}{\mathrm{tr}\,\boldsymbol{\alpha}}\mathrm{dev}\,\boldsymbol{\alpha}\right)^{2}}-RM_{CS}\,g\left(\theta_{\sigma}\right)p \tag{6.6}$$

In the *true* stress space, the mathematical formulation of both the yield and the strength surface is much more complicated, being the surfaces dependent on the current state of the material through the state parameter Ψ. The latter depends in turn on the current specific volume v and, thus, on the plastic volumetric strains $\mathrm{tr}\,\boldsymbol{\varepsilon}^{p}$. Consequently, the strength surface undergoes isotropic hardening in the *true* stress space, while it is constant in the *normalized* space. On the other side, the yield surface can undergo both isotropic and kinematic hardening in the *true* stress space, while it is only subjected to kinematic hardening in the *normalized* space (Gajo and Muir Wood, 1999a, b).

6.1.3 Hardening rule

As proposed by Gajo and Muir Wood (1999a, 1999b), the concept of conjugate stresses is adopted to introduce the hardening rule which defines the kinematic hardening of the yield surface. The conjugate stress $\boldsymbol{\sigma}_{c}$ is defined as the *image* stress of $\boldsymbol{\sigma}$ on the strength surface. In the *normalized* stress space, the position of $\bar{\boldsymbol{\sigma}}_{c}$ is defined such that the deviatoric component of the normal to the strength surface is proportional to the deviatoric component of the yield surface (Figure 6.1).

The translation rule describes the movement of the yield surface (i.e. the change of the tensor $\boldsymbol{\alpha}$ which defines its position) towards the strength surface. By referring to the increment $\dot{\boldsymbol{\alpha}}$, it can be expressed as (Gajo, 2010):

$$\dot{\boldsymbol{\alpha}}=\tau\mathrm{T}_{\alpha}\left[\bar{\boldsymbol{\sigma}}_{c}-\bar{\boldsymbol{\sigma}}\right] \tag{6.7}$$

where T_{α} is a fourth-order projection tensor, and τ is a scalar quantity dependent on the plastic strain rate $\dot{\boldsymbol{\varepsilon}}^{p}$.

In the original Severn-Trent model, a hyperbolic relationship is adopted to model the relationship between $\dot{\boldsymbol{\varepsilon}}^{p}$ and $\bar{q}$ within the framework of bounding surface plasticity (Gajo and Muir Wood, 1999a, b). Conversely, in the version here adopted

(Gajo, 2010) the same response is obtained based on the kinematic hardening plasticity, assuming τ as follows:

$$\tau = -\frac{\beta}{\beta_{\max} B}\left\{\frac{\mathbf{Q}\cdot(\bar{\boldsymbol{\sigma}}_c - \bar{\boldsymbol{\sigma}}_i)}{\mathbf{Q}\cdot(\bar{\boldsymbol{\sigma}} - \bar{\boldsymbol{\sigma}}_i)}\right\}^{\alpha}\left((\bar{\boldsymbol{\sigma}}_c - \bar{\boldsymbol{\sigma}})\cdot\dot{\boldsymbol{\varepsilon}}^p\right)\left\{\frac{\partial f}{\partial \boldsymbol{\alpha}}\cdot \mathrm{T}_{\alpha}\left[\bar{\boldsymbol{\sigma}}_c - \bar{\boldsymbol{\sigma}}\right]\right\}^{-1} \qquad (6.8)$$

where: $\bar{\boldsymbol{\sigma}}_i$ is the initial stress state when yielding starts, which is fixed until a loading reversal takes place; $\mathbf{Q} = \partial f / \partial \boldsymbol{\sigma}$ is the gradient of the yield function; β is the distance of $\bar{\boldsymbol{\sigma}}$ from its conjugate stress $\bar{\boldsymbol{\sigma}}_c$, equal to $\mathbf{Q}\cdot(\bar{\boldsymbol{\sigma}}_c - \bar{\boldsymbol{\sigma}})$; $\beta_{\max}$ is the maximum value that β can assume and it is equal to $(1-R)\mathbf{Q}\cdot(\hat{\bar{\boldsymbol{\sigma}}}_c - \bar{\boldsymbol{\sigma}}_c)$, being $\hat{\bar{\boldsymbol{\sigma}}}_c$ the stress state lying on the strength surface at a position diametrically opposite to $\bar{\boldsymbol{\sigma}}_c$ (see Figure 6.1); B and α are constitutive parameters governing basically the evolution of the plastic modulus with plastic strains.

If α is set equal to 0, Eq. (6.8) produces a relationship between $\dot{\boldsymbol{\varepsilon}}^p$ and $\bar{q}$ completely equivalent to the hyperbolic one initially proposed by Gajo and Muir Wood (1999a, 1999b). Conversely, for $\alpha \geq 1$ the stress-strain response is smoothed in the transition from the elastic to the elastoplastic zone (Gajo, 2010).

6.1.4 Flow rule

The definition of a flow rule is needed to link the volumetric and the distortional strain increments. In the model here adopted, the deviatoric associativity is assumed, and the flow rule is described by the following relationship (Gajo, 2010):

$$\frac{\operatorname{tr}\mathbf{P}}{\|\operatorname{dev}\mathbf{P}\|} = -\frac{\sqrt{3}}{\sqrt{2}}A\frac{1}{g\left(\theta_{(Q)}\right)p}\left[\left(1+k_d\Psi\right)\operatorname{dev}\bar{\boldsymbol{\sigma}}_c - \operatorname{dev}\bar{\boldsymbol{\sigma}}\right]\cdot\frac{\operatorname{dev}\mathbf{Q}}{\|\operatorname{dev}\mathbf{Q}\|} \qquad (6.9)$$

where $\mathbf{P}$ is the plastic flow direction, and A and k_d are constitutive parameters.

6.1.5 Hyperelastic formulation

The elasticity model adopted in the present version of the Severn-Trent model is based on a hyperelastic formulation as presented by Gajo and Bigoni (2008). The stress state $\boldsymbol{\sigma}$ is directly obtained from the elastic potential, defined as follows:

$$\varphi\left(\boldsymbol{\varepsilon}^e, \boldsymbol{\varepsilon}^p\right) = \gamma d(\boldsymbol{\varepsilon}^p)\left(-\operatorname{tr}\left(\mathbf{B}\boldsymbol{\varepsilon}^e\right)\right)^{\eta} + \zeta d(\boldsymbol{\varepsilon}^p)\left(\operatorname{tr}\left(\mathbf{B}\boldsymbol{\varepsilon}^e\right)^2\right)^{\lambda} \qquad (6.10)$$

where: $\mathbf{B}$ is a symmetric, second-order, positive-definite fabric tensor which describes the fabric anisotropy; $d(\boldsymbol{\varepsilon}^p)$ is a scalar function which describes the void ratio dependency; and γ, η, ζ and λ are constitutive parameters.

In the Severn-Trent model as proposed by Gajo (2010), the initial fabric tensor $\mathbf{B}_0$ evolves with plastic strains. However, for the sake of simplicity, the tensor $\mathbf{B}$ is assumed to be constant (i.e. $\mathbf{B} = \mathbf{B}_0$) in this study. Consequently, the laws defining the plastic-induced evolution of the fabric tensor are here not discussed.

Under the assumption of linear isotropic elasticity, the fabric tensor $\mathbf{B}_0$ is equal to the second-order unity tensor $\mathbf{I}$. By assuming a given value for the Poisson's ratio ν, the constitutive parameters of Eq. (6.10) can be calibrated to obtain a tangent stiffness which follows the empirical relationship as proposed by Hardin and Black (1966):

$$G_0 = 3230 \cdot p_r \cdot \frac{\left(3.97 - v\right)^2}{v} \cdot \left(\frac{p}{p_r}\right)^{0.5} \tag{6.11}$$

where p_r is the reference pressure (1 kPa), as in the model proposed by Gajo (2010). In the present study a slightly modified version of Eq. (6.11) is considered, by assuming a value for G_0 totally consistent with the one measured for the Perth sand (see Section 4.3.5 for further details):

$$G_0 = 3159 \cdot p_r \cdot \frac{\left(3.97 - v\right)^2}{v} \cdot \left(\frac{p}{p_r}\right)^{0.5} \tag{6.12}$$

In addition, the initial inherent anisotropy due to soil deposition is also neglected (i.e. $\mathbf{B}_0 = \mathbf{I}$).

It is worth mentioning that an effective elastic shear modulus can be adopted instead of the small-strain shear modulus. Such an effective value, computed as a fraction E_R of the shear modulus predicted by Eq. (6.11), can be used to improve the calibration of the constitutive model under undrained conditions.

Finally, from the elastic potential as expressed in Eq. (6.10), the stress $\boldsymbol{\sigma}$ can be obtained as follows (Gajo, 2010):

$$\begin{aligned} \boldsymbol{\sigma} &= \frac{\partial \varphi\left(\boldsymbol{\varepsilon}^e, \boldsymbol{\varepsilon}^p\right)}{\partial \boldsymbol{\varepsilon}^e} = \\ &= -\gamma\, d(\boldsymbol{\varepsilon}^p)\eta\left(-\operatorname{tr}\left(\mathbf{B}\boldsymbol{\varepsilon}^e\right)\right)^{\eta-1}\mathbf{B} + 2\zeta d(\boldsymbol{\varepsilon}^p)\lambda\left(\operatorname{tr}\left(\mathbf{B}\boldsymbol{\varepsilon}^e\right)^2\right)^{\lambda-1}\mathbf{B}\boldsymbol{\varepsilon}^e\mathbf{B} \end{aligned} \tag{6.13}$$

6.1.6 Summary

In the previous sections, the main features of the Severn-Trent model have been presented. The constitutive model has been implemented by Gajo (2017) in a Fortran subroutine as a user-defined material (UMAT) for the Finite Element software ABAQUS/Standard (Systèmes Dassault, 2020).

The constitutive model, as in the version used in the present study, is completely defined after that the thirteen constitutive parameters are calibrated. The parameters are summarized in Table 6.1.

The first three parameters - namely: v_λ, λ, and φ'_{CS} - define the Critical State Line in both the volumetric and the deviatoric planes. The size of the yield surface is defined as a fraction R of the size of the strength surface, while its shape (as well as the shape of the strength surface) is controlled by the parameter m. Moreover, the sizes of both the strength and the yield surfaces depend on the current state of the material Ψ, as a function of the parameter k.

Inside the yield surface, the small-strain elastic stiffness is computed as a fraction E_R of the G_0, obtained through the expression proposed by Hardin and Black (1966). In the present study, the inherent elastic anisotropy of the material (and its evolution) is neglected, so the tensor $\mathbf{B}_0$ is assumed to be constant and equal to $\mathbf{I}$. The remaining parameters controlling the elastic behaviour are obtained as a function of the Poisson's ratio ν.

Table 6.1: Constitutive parameters of the Severn-Trent model (after Gajo, 2010).

Parameter	Description
v_λ	Intercept for the CSL in the $v - \ln p'$ plane at $p' = 1$ Pa
λ	Slope of the CSL in the $v - \ln p'$ plane
φ'_{CS}	Critical state friction angle
m	Parameter controlling the deviatoric section of the yield surface
k	Link between changes in state parameter Ψ and the current size of the yield surface
A	Multiplier in the flow rule
k_d	State parameter contribution in the flow rule
B	Parameter controlling the hyperbolic stiffness relationship
α	Exponent controlling the hyperbolic stiffness relationship
R	Size of the yield surface with respect to the size of the strength surface
E_R	Fraction of G_0 used in computations
ν	Poisson's ratio
$\mathbf{B}_0$	Tensor controlling the inherent anisotropy (here neglected, i.e. $\mathbf{B}_0 = \mathbf{I}$)

At yielding, the plastic modulus follows a hyperbolic stiffness relationship based on B and α. B controls the rate at which the plastic modulus decays with plastic strains, while α smooths the stress-strain response in the transition from the elastic to the elastoplastic zone.

Finally, the flow rule is controlled by A and k_d. A is the multiplier of the flow rule, while k_d is the state parameter contribution.

6.2 Calibration of the constitutive model

6.2.1 Constitutive parameters

The constitutive parameters defining the sand stress-strain response as predicted by the Severn-Trent model are calibrated against the experimental tests performed on Perth sand and presented in Chapter 4. The parameters defining the position of the CSL are firstly discussed.

As already pointed out in Section 4.2.4, the definition of the position of the CSL in the volumetric plane is not a trivial task, mainly due to the tendency of the sand to localise shear strains (especially when dense samples are considered) and to the limitations associated to the experimental measurements at very high axial strains (e.g. Desrues et al., 1996; Verdugo and Ishihara, 1996). However, a reasonable estimation of the CSL for the Perth sand was obtained based on the triaxial tests performed on samples with an initial state looser than critical (see Figure 4.19). By expressing the confining pressure in Pa (as required in the constitutive model), the intercept v_λ and the slope λ of the CSL of the Perth sand here assumed are equal

to 2.027 and 0.019, respectively. Although more experimental data would be needed, in principle, to properly define the CSL, the parameters here adopted have shown the be effective in describing the behaviour of the Perth sand, at least for the ranges of confining pressures and void ratios here considered.

For the critical state friction angle φ'_{CS}, a value of 30.6° was obtained according to the triaxial tests (see Figure 4.18). The value is also quite consistent with the one obtained by Buchheister (2009), so a critical state friction angle φ'_{CS} of 30° is adopted.

The elastic parameters are derived adopting a Poisson's ratio ν of 0.2 a fraction E_R equal to 1, thus assuming the full small-strain shear stiffness G_0 as obtained from the resonant column tests. Consistently, a very small size of the yield surface is adopted ($R = 0.01$, i.e. the size of the yield surface is 1/100th of the strength surface). Finally, for the parameter m a typical value of 0.8 is adopted, to ensure the convexity of the yield and the strength surfaces.

The remaining parameters are calibrated through a trial and error procedure based on the experimental tests reported in Chapter 4. In particular, for the calibration of A, B, k and k_d reference is made mainly to the results of the drained triaxial tests, consistently with the drained state achieved in the centrifuge tests. The resulting values are: A=0.65; B=0.007; k=2.6; and k_d=1.8. Conversely, the parameter
α=1.2 is defined considering the Modulus Reduction and Damping curves as obtained from the resonant column tests.

In the following, the simulations of the element tests are presented to show the capacity of the soil constitutive model in predicting the stress-strain response of the Perth sand.

6.2.2 Simulation of drained triaxial tests on Perth sand

The soil-structure model analyzed in the centrifuge tests is characterized by a layer of Perth sand in a dense state, loaded under drained conditions. Consequently, the calibration of the Severn-Trent model was carried out mainly focusing on the results of the drained triaxial tests performed on dense samples of Perth sand.

Soil constitutive models are usually calibrated by referring to the results of laboratory tests performed on soil samples, typically loaded under triaxial conditions. The samples are assumed to be subjected to uniform stresses and strains and the experimental data are analyzed under the hypothesis of cylindrical deformation of the specimen, i.e. global stresses and strains are computed as a function of average external measurements (see Section 4.2.2.4 for further details). The results of the tests are considered representative of the *true* soil behaviour at an element level.

Nevertheless, the effects of the external boundary conditions – e.g. end-restraint, insufficient drainage, membrane effects – imposed on the samples can have a significant impact on the measured response. In particular, the rough end plates usually adopted in triaxial standard tests are known to be responsible for non-uniform stress and strain fields within the sample, which lead to a barrel-shape

deformation of the specimen and localization of shear strains, especially in the case of dense sand samples (Desrues et al., 1996).

This important issue has been analyzed by many studies in the past, both from an experimental and a numerical point of view (e.g., Taylor, 1941; Sheng et al., 1997; Kodaka et al., 2007; Muraro and Jommi, 2019). Some researchers state that such an effect can be minimized by adopting height-to-diameter ratios of samples larger than 1.5 (e.g. Olson et al., 1964; Bishop and Green, 1965). However, Kirkpatrick and Belshaw (1968) showed that significant non-uniformities can be observed on sand samples even for larger ratios. On the one hand, the presence of the rough end plates leads to an *apparent* increase in the shear strength of the material (e.g. Kodaka et al., 2007). On the other hand, the restraint effect prevents the full development of volumetric strains at the top and the bottom of the sample, reducing the dilation tendency of dense samples at shearing (e.g. Shockley and Ahlvin, 1960; Rowe and Barden, 1964). As discussed by Sheng et al. (1997), boundary effects should be taken into account for proper calibration of a constitutive model. Triaxial tests should then be treated as boundary value problems, rather than tests representative of the actual soil behaviour.

The typical barrel-shape deformation was observed also in the triaxial tests performed on Perth sand samples. Figure 6.2 reports the comparison between the shapes at failure of a sample initially looser (Figure 6.2.a) and one initially denser (Figure 6.2.b) than critical. As expected, both the samples are characterized by non-cylindrical deformations. Also, for the sample initially denser than critical a clear strain localization can be observed. The latter implies the formation of a local shear band, leading to questions relating to the interpretation of the tests at high axial strains in terms of global average quantities.

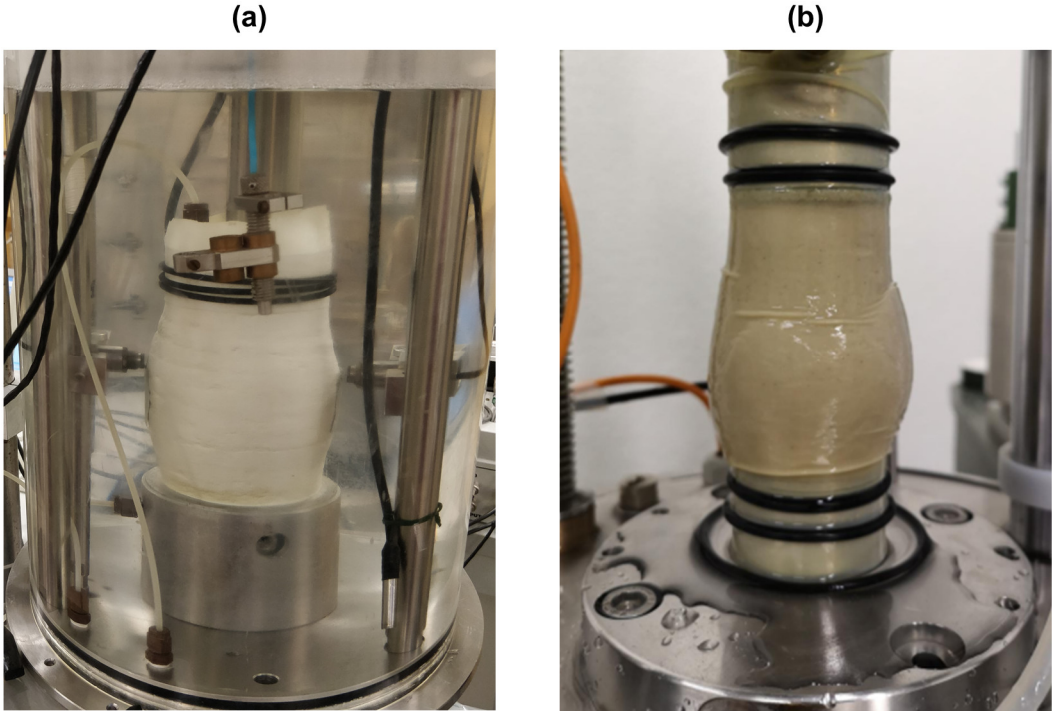

Figure 6.2: Typical barrel-shape deformation observed on (a) loose and (b) dense (from Bühler et al., 2019) samples of Perth sand.

Following the notation introduced by Muraro and Jommi (2019), the drained triaxial tests are simulated considering both the *material soil behaviour* under true triaxial stresses and the *sample behaviour*, i.e. treating the tests as boundary value problems. The simulations are performed through the Finite Element software ABAQUS/Standard (Systèmes Dassault, 2020). To simulate the material behaviour as predicted by the Severn-Trent model, a single CAX8RP (i.e. 8-node axisymmetric quadrilateral, biquadratic displacement, bilinear pore pressure, reduced integration) element, subjected to an initial isotropic triaxial state, is sheared under drained conditions (Figure 6.3.a).

Conversely, the sample behaviour is simulated by imposing the external boundary conditions to a quarter of the soil sample modelled in axisymmetric conditions (Figure 6.3.b). Specifically, the numerical model includes both the soil sample and the steel top plate, for which a Linear Elastic constitutive model is adopted with Young's Modulus $E_S = 210$ GPa and Poisson's ratio $\nu = 0.3$. A rough interface (infinitely rigid in the normal direction) with a friction coefficient $\mu = \tan\varphi'_{CS}$ is introduced between soil and the top plate. It is worth mentioning that such an assumption for the friction coefficient is not very relevant, as will be discussed more in detail later on. After an initial isotropic consolidation up to the desired confining pressure p'_0, an axial displacement is applied to the top plate up to the desired level of the global axial strain of the sample. The shearing takes place under drained conditions (i.e. imposing $\Delta u_w = 0$).

In the following, the results of the simulations of both the material soil behaviour and the sample behaviour are discussed and compared to the experimental results.

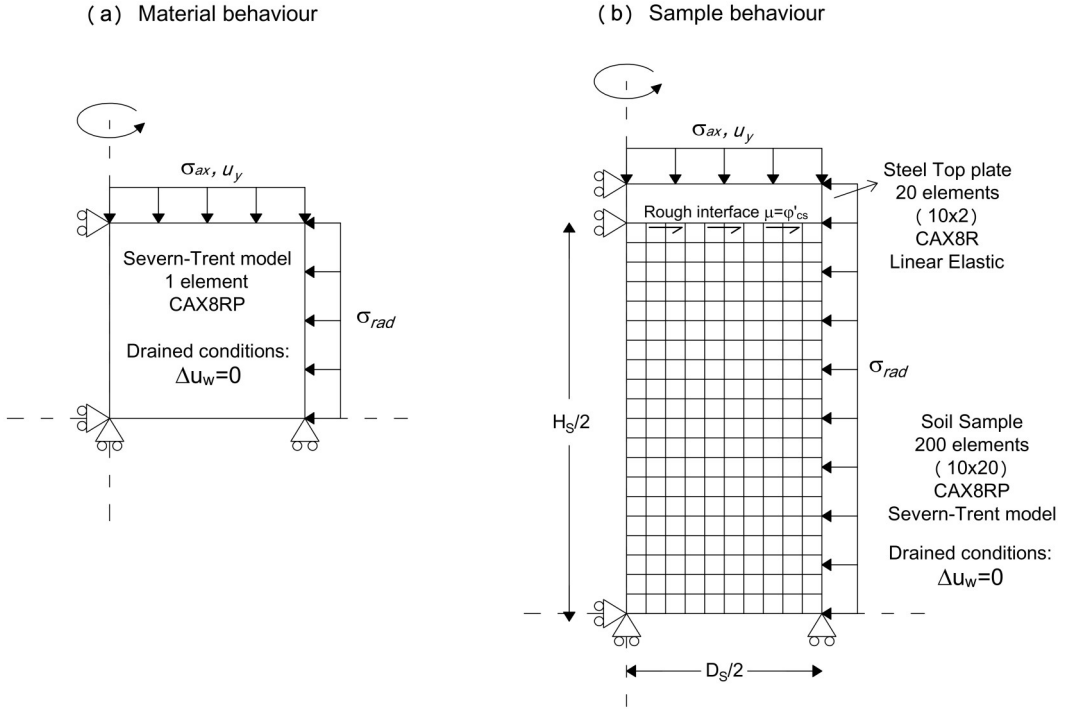

Figure 6.3: Schematic illustration of the FEM models used to simulate (a) the material soil behaviour and (b) the sample behaviour.

6.2.2.1 *Material behaviour*

Five tests performed on samples of Perth sand sheared under drained conditions are selected for the calibration. Specifically, reference is made to four tests carried out at different confining pressures on samples at almost the same dense initial state – namely: tests TX-ETH-03-06 – and to one test carried out on an initially loose sample – namely test TX-PoliTO-04.

In the simulations performed to obtain the material behaviour as predicted by the Severn-Trent model, stresses and strains are uniform throughout the element. The quantities can thus be directly extracted from a single integration point of the finite element.

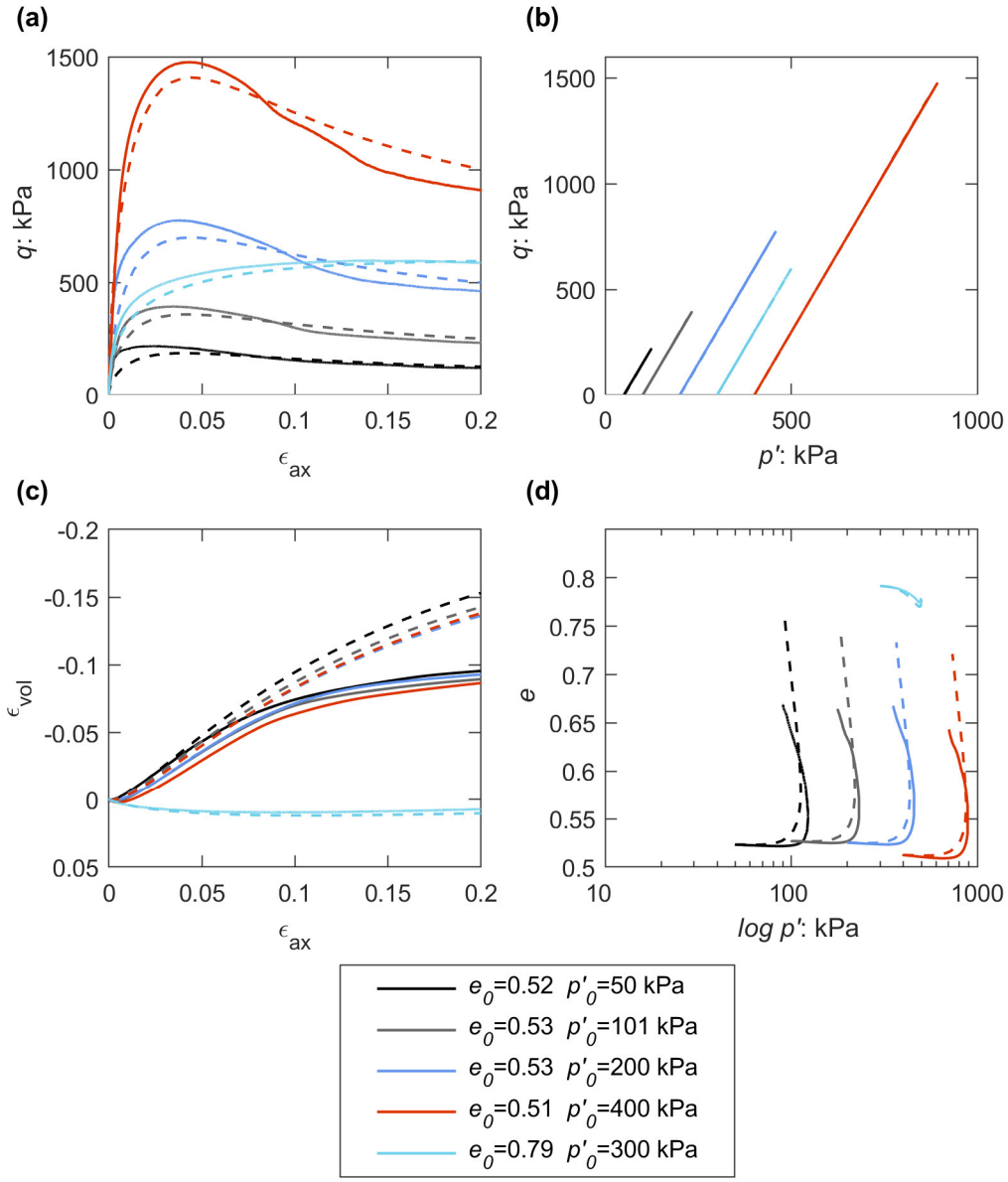

Figure 6.4: Comparison between the experimental data (solid lines) and the material behaviour (dashed lines) as predicted by the Severn-Trent model under drained conditions: (a) deviatoric stress vs axial strain; (b) effective stress paths; (c) volumetric strain vs axial strain; (d) void ratio vs mean effective confining stress.

Figure 6.4 reports the comparison between the experimental data and the numerical predictions. As it can be observed by Figure 6.4.a, the comparison in terms of deviatoric response for the dense samples is quite satisfactory in the whole range of axial strains. The calibration was in fact performed in such a way that both the peak strength and the post-peak softening are well predicted. In the centrifuge tests, the soil close to the foundation was brought to the failure, so it is important to properly simulate its behaviour up to high strain levels. Conversely, in terms of volumetric strains, the comparison is satisfying up to axial strains of about 0.1. Hereafter, strain localization is thought to be originated in the triaxial tests, leading to an apparent decrease of the volumetric strains computed globally throughout the samples. This issue is reflected also in the volumetric $e - \log p'$ plane, where the lower dilation observed in the triaxial tests results in lower void ratios with respect to the predicted ones.

Many attempts were made to improve the calibration of the model both in terms of deviatoric and volumetric response. However, it was not possible to improve at the same time both the responses, that are linked by the flow rule. For instance, assuming a larger value for the flow rule multiplier A would result in the best fitting of the post-peak softening but also a in further increase of the volumetric strains. On the other hand, larger values of the parameter k imply the best fitting of the peak strength, but again an increase of the volumetric strains.

As regards the prediction of the drained response of Perth sand in a loose initial state, the comparison is very satisfying for the whole range of axial strains, both in terms of deviatoric and volumetric responses. The model well predicts the progressive hardening of the material towards the critical state, which is almost reached for a void ratio slightly lower than the initial one. In contrast to the experimental tests performed on dense samples, no significant strain localizations were observed on initially loose samples (Figure 6.2.a). Consequently, also the interpretation of the tests in terms of global quantities is reliable even at higher axial strains.

6.2.2.2 Sample behaviour

The sample global behaviour is simulated for the same drained tests chosen in the previous section. The global stresses and strains of the samples are computed through a procedure analogous to the one employed for the interpretation of the experimental data (see Section 4.2.2.4) to allow for a direct comparison between the numerical simulations and the experimental tests.

An increasing vertical displacement is imposed on the top plate, and the corresponding nodal forces are recorded and summed up to obtain the total axial force F. The volume of the sample (measured in the experimental tests through the volume gauge) is computed step-by-step from the updated nodal coordinates obtained by extracting the nodal displacements. The cross-sectional area of the sample A_c is then computed from the global volumetric strain and the global axial strains, assuming a cylindrical deformation of the specimen. Finally, the deviatoric stress is computed as $q = F / A_c$.

A preliminary analysis was conducted to evaluate the influence of the value assumed for the friction interface coefficient μ and the mesh discretization on the results of the simulations. Figure 6.5 reports the logarithmic shear strain field in an initially dense sample of Perth sand (i.e. simulation of test TX-ETH-05) at an axial strain $\varepsilon_{ax} = 10\%$ for three different cases: (a) base case (Figure 6.3.b); (b) $\mu = \tan\varphi'_{CS} / 2$; (c) sample discretized with a finer mesh (elements length half of the base case).

No noticeable differences are observed by adopting a lower interface friction coefficient: in all the cases the top plate acts as fixed support, restraining the horizontal displacements at the interface. Such a constriction implies the development of a shear band that starts at a distance of about a quarter of the height of the sample from the top plate.

Conversely, the rate of development and the width of the shear band is influenced by the finite element mesh. If a finer discretization is adopted the localization develops fastly and in a narrower shear band. However, as it can be observed from Figure 6.5.c, the differences between the base case and the case with the finer mesh are not significant, even for a relatively large axial strain (i.e. 10%).

A direct comparison between the three cases is presented in Figure 6.6 in terms of global deviatoric and volumetric responses of the samples. No differences are observed assuming a much lower interface friction coefficient. As for the finite element mesh, small differences are observed for very high axial strains (i.e. >10%) in terms of deviatoric stress, while the global volumetric strain of the sample is not affected by the discretization. It can therefore be stated that the numerical model developed for the base case (Figure 6.3.b) is appropriate to simulate the sample behaviour, especially when reference is made to global stresses and strains computed averaging the results to the whole sample.

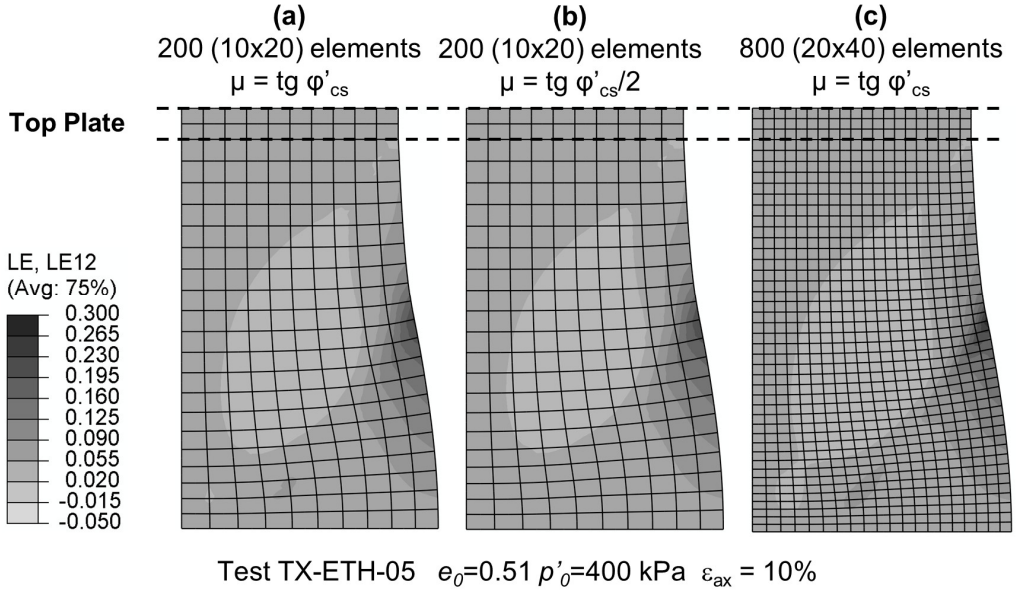

Figure 6.5: Logarithmic shear strain field in a dense sample sheared under drained conditions at $\varepsilon_{ax} = 10\%$: (a) base case; (b) friction coefficient $\mu = \tan\varphi'_{CS} / 2$; (c) finer mesh.

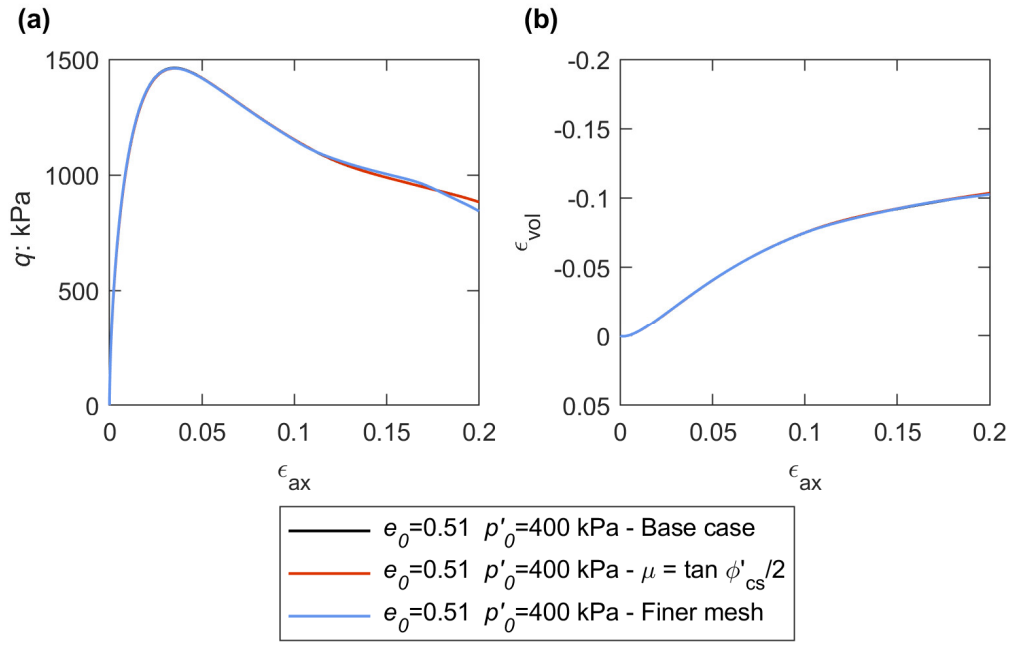

Figure 6.6: Comparison between the sample behaviour under drained conditions as predicted by the three preliminary numerical models: (a) global deviatoric stress vs global axial strain; (b) global volumetric strain vs global axial strain.

Figure 6.7 reports the comparison between the logarithmic shear strain field which develops within an initially dense sample (Figure 6.7.a) and an initially loose sample (Figure 6.7.b) for three different global axial strains, namely: $\varepsilon_{ax} = 5$, 10 and 15%. Soon after the application of the global axial strain ($\varepsilon_{ax} = 5\%$), a parasite shear strain develops from the edge at the top of the sample, at the interface with the top plate. Such a shear strain localization develops throughout the sample in both cases but it is much more evident for the dense sample.

For increasing global axial strain levels ($\varepsilon_{ax} = 10\%$), the deformed shape of the two samples starts to be different. The confining effect induced by the top plate results in a pronounced bulging of the initially dense sample, while the loose sample presents a smoother barrel-shape.

Finally, at very high axial strains ($\varepsilon_{ax} = 15\%$), the dense sample presents a very clear localization of shear strains which starts from a distance of about a quarter of the height of the sample from the top plate and develops towards the middle of the sample.

As observed by previous studies both experimentally and numerically, at very high global axial strains, the X-shape localization of shear deformations results in the formation of shear bands throughout the entire specimen (Lade, 1982; Desrues et al., 1996; Sheng et al., 1997). Conversely, not significant shear bands are observed in the loose sample. The latter is consistent with the observed failure modes of the samples (Figure 6.2).

Figure 6.8 reports the comparison between the material and the sample behaviour for the two tests at different initial void ratios. The comparison is reported in terms of global stresses and strains.

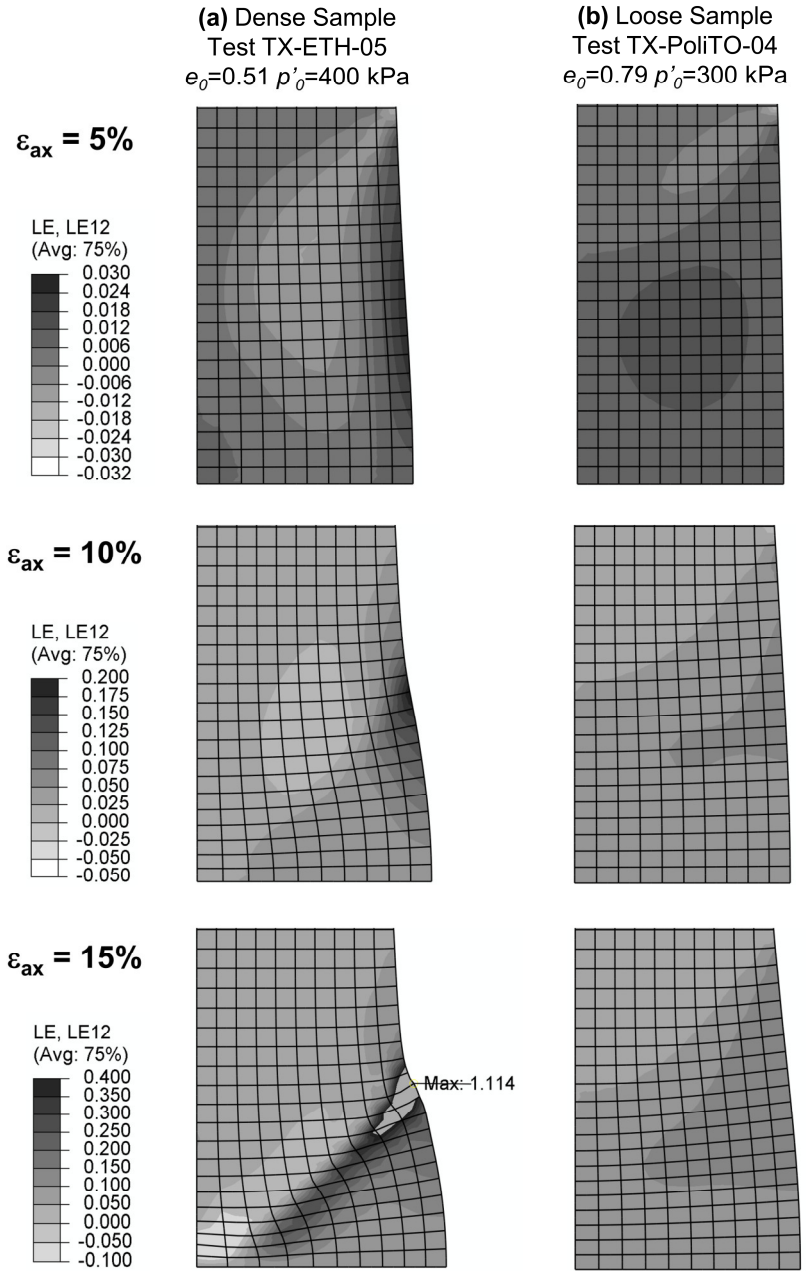

Figure 6.7: Simulation of the sample behaviour under drained conditions: logarithmic shear strain field in (a) an initially dense sample (test TX-ETH-05) and (b) an initially loose sample (test TX-PoliTO-04) of Perth sand at different global axial strains.

For the sample looser than critical, the differences between the two simulations are relatively small. The two volumetric responses are almost identical, and the deviatoric stress q starts to differ just for global axial strains ε_{ax} larger than 10% when the incorrect assumption of a cylindrical deformation of the sample for the computation of the cross-sectional area becomes relevant. Conversely, for the dense sample, the confining effect due to the top plate implies an increase of the deviatoric stress q and a consequent *apparent* larger shear strength at peak of the sample (Figure 6.8.a).

Direct visualization of the nonuniform stress field within the dense sample at the peak (ε_{ax}=2%) is given in Figure 6.9. Consistently with previous findings (Sheng et al., 1997), the highest internal axial stresses are concentrated at the end

edges and in the middle of the sample (Figure 6.9.a). On the other hand, the highest internal radial stresses are observed close to the plates due to its confining effect (Figure 6.9.b). The shear stresses along the interface imply a rotation of the principal stresses and the development of a parasite shear stress τ that would be null for a *true* triaxial stress state (Figure 6.9.c).

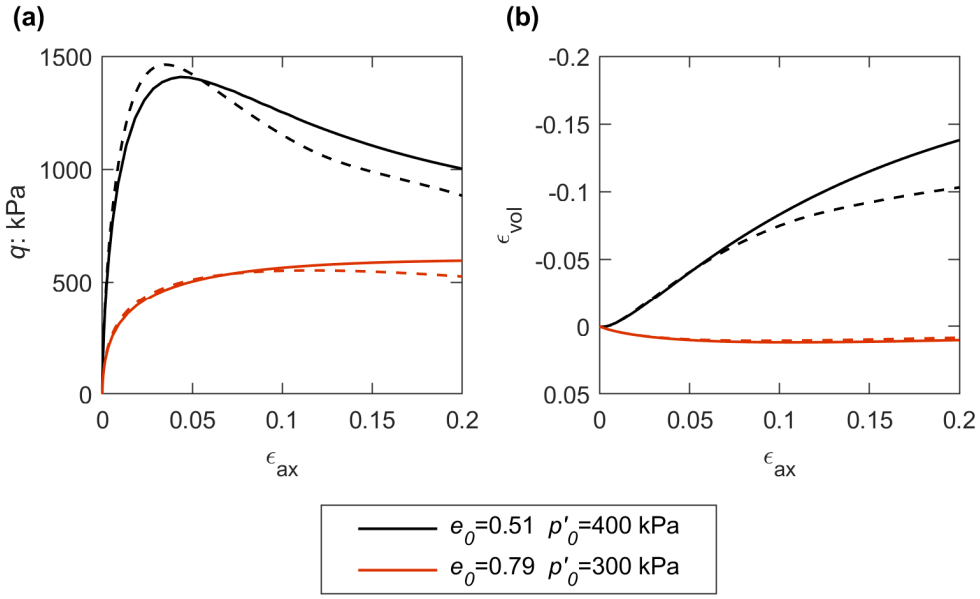

Figure 6.8: Comparison between material (solid lines) and sample (dashed lines) behaviour for two specimens sheared under drained conditions at different initial void ratios: (a) global deviatoric stress vs global axial strain; (b) global volumetric strain vs global axial strain.

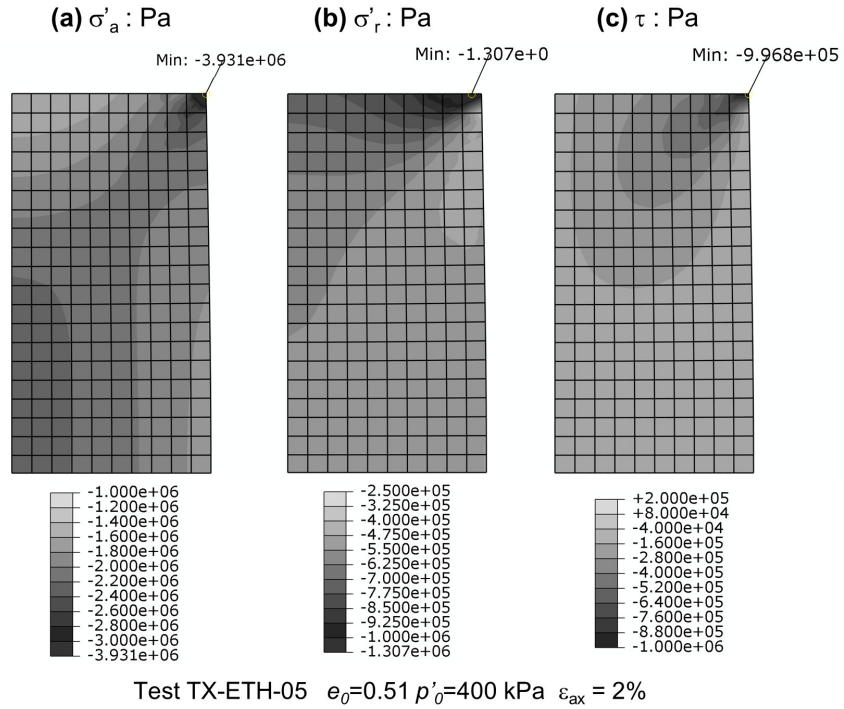

Figure 6.9: Distribution of effective stresses in an initially dense sample sheared under drained conditions at a global axial strain of 2%: (a) effective axial stress; (b) effective radial stress; (c) shear stress.

As previously discussed, such shear stress is responsible for the formation of shear bands. After the peak, a more pronounced softening is observed for the sample behaviour when compared to the material behaviour (Figure 6.8). On the one side, the formation of the shear bands implies a concentration of shear stresses and then a faster softening of the global deviatoric response. On the other side, it induces an *apparent* final plateau in the global volumetric strain response. The latter has to be interpreted as the manifestation of strain localization, rather than the approach to the critical state condition in terms of dilation (Desrues et al., 1996). An approach to the critical state condition can instead be observed locally, inside the shear band. Figure 6.10 plots the void ratio distribution in the sample for a global axial strain of 15%. In the elements located inside the shear band, the void ratio reaches a quite high value (i.e. about 0.81). As opposite, inside the so-called "dead zone" close to the top (and the bottom) of the sample, the void ratio is slightly higher than the initial one (i.e. 0.51).

Figure 6.11 reports the comparison between the experimental results and the sample behaviour for the five tests previously introduced (namely: tests TX-ETH-03-06 and test TX-PoliTO-04). The comparison is again reported in terms of global variables. The experimental results are captured very well by the numerical simulations for the entire range of axial strains (i.e. up to ε_{ax}=20%). In particular, the higher peaks in terms of deviatoric stress q observed in the experimental results in comparison to the material behaviour are now well-reproduced by the numerical simulations of the sample behaviour (Figure 6.11.a). As previously discussed, these differences are due to the confining effect exerted by the top (and the bottom) plate, and cannot thus be captured by the simulations at an element level.

Also, the *apparent* final plateaux observed in the volumetric responses is well-captured by the numerical simulations, which now provide just a slight overprediction of the volumetric strains ε_{vol} for very high axial strains (Figure 6.11.c). As a consequence, the predictions of the numerical simulations in terms of the evolution of the soil state in the volumetric plane $e - \log p'$ are also substantially improved (Figure 6.11.d).

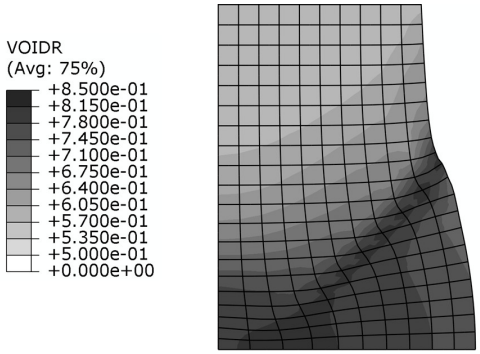

Figure 6.10: Void ratio distribution in an initially dense sample sheared under drained conditions at a global axial strain of 15%.

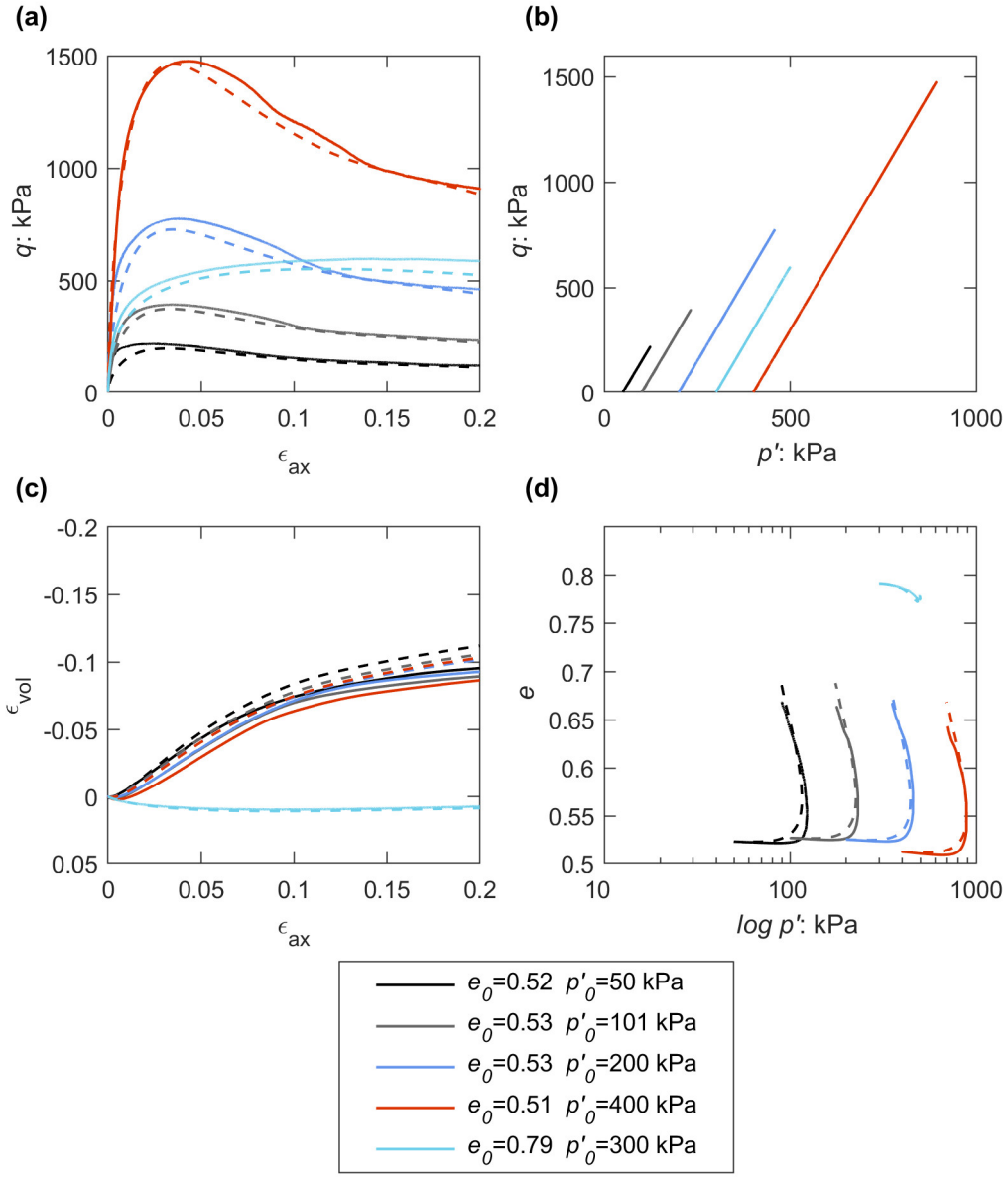

Figure 6.11: Comparison between the experimental data (solid lines) and the sample behaviour (dashed lines) as predicted by the Severn-Trent model under drained conditions: (a) deviatoric stress vs axial strain; (b) effective stress paths; (c) volumetric strain vs axial strain; (d) void ratio vs mean effective confining stress.

6.2.3 Simulation of undrained triaxial tests on Perth sand

As previously discussed, the calibration of the constitutive model was performed focusing on the drained response of the Perth sand. Nevertheless, in this section, the results of the undrained triaxial tests are compared to the numerical predictions to show the response of the calibrated Severn-Trent model under undrained conditions. In particular, reference is made to the two tests performed on loose samples of Perth sand (namely: test TX-PoliTO-03 and -04), given that for the tests performed on medium dense samples cavitation of the saturation fluid and, in turn, partially drained conditions probably developed within the samples (see Section 4.2.2.5 for further details).

The comparisons are here presented considering exclusively the material behaviour. Preliminary analyses showed that no significant differences are observed between material and sample behaviour for undrained triaxial tests performed on initially loose samples, providing that the permeability of the soil is sufficiently high to avoid nonuniformities within the sample in terms of pore pressure. This is consistent with the simulations of drained triaxial tests on loose samples, where the only slight difference observed between material and sample behaviour is due to the barrel-shape deformation of the sample at high axial strains (Figure 6.8).

Figure 6.12 reports the comparison between the numerical simulations and the experimental data. As it can be observed, although the overall behaviour of the sand predicted by the numerical simulations is consistent with the experimental results, the constitutive model predicts a much higher excess pore pressure Δu_w than the measured values (Figure 6.12.c). The latter results in a faster decrease of the confining pressure p' and, in turn, in lower peak values of the deviatoric stress q (Figure 6.12.a-b).

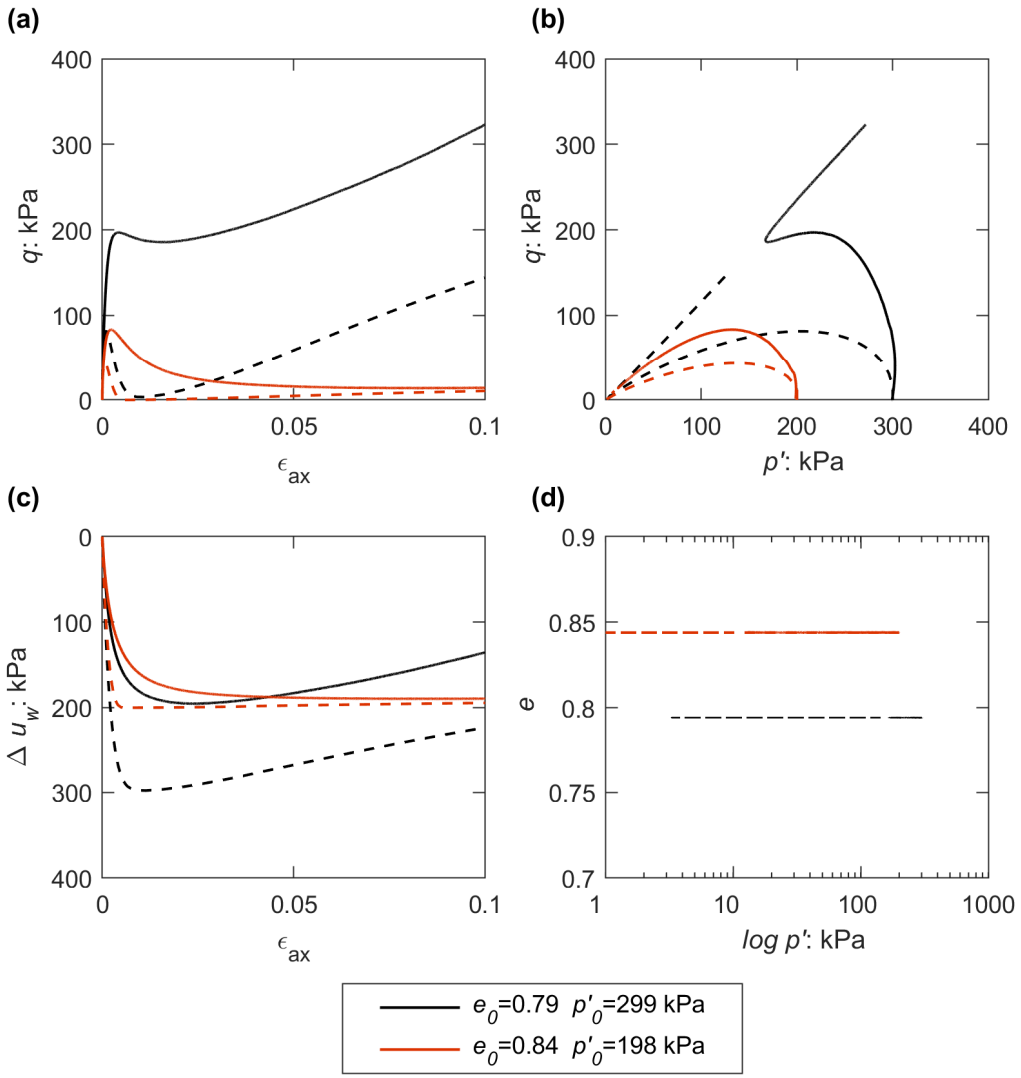

Figure 6.12: Comparison between the experimental data (solid lines) and the material behaviour (dashed lines) as predicted by the Severn-Trent model under undrained conditions: (a) deviatoric stress vs axial strain; (b) effective stress paths; (c) excess pore pressure vs axial strain; (d) void ratio vs mean effective confining stress.

As discussed in detail by Gajo and Muir Wood (1999b), the choice of the elastic parameters strongly affects the simulations of undrained triaxial tests performed on loose sand samples. The calibration of the Severn-Trent model under undrained conditions can be substantially improved by considering an initial inherent anisotropy of the sample (i.e. $\mathbf{B}_0 \neq \mathbf{I}$) and its evolution with plastic strains (Gajo, 2010).

Alternatively, Gajo and Muir Wood (1999b) suggested that a fraction E_R of the small-strain shear modulus should be used and it should be defined, together with the Poisson's ratio ν, to avoid an excessively large bulk modulus for the soil. The same strategy has been subsequently adopted also by other studies (e.g., Abate et al., 2010; Kowalczyk and Gajo, 2020).

Figure 6.13 reports, as an example, the material behaviour as predicted by the constitutive model adopting an effective shear modulus G equal to 1/3 of the small-strain shear modulus G_0, and assuming a Poisson's ratio ν of 0.1.

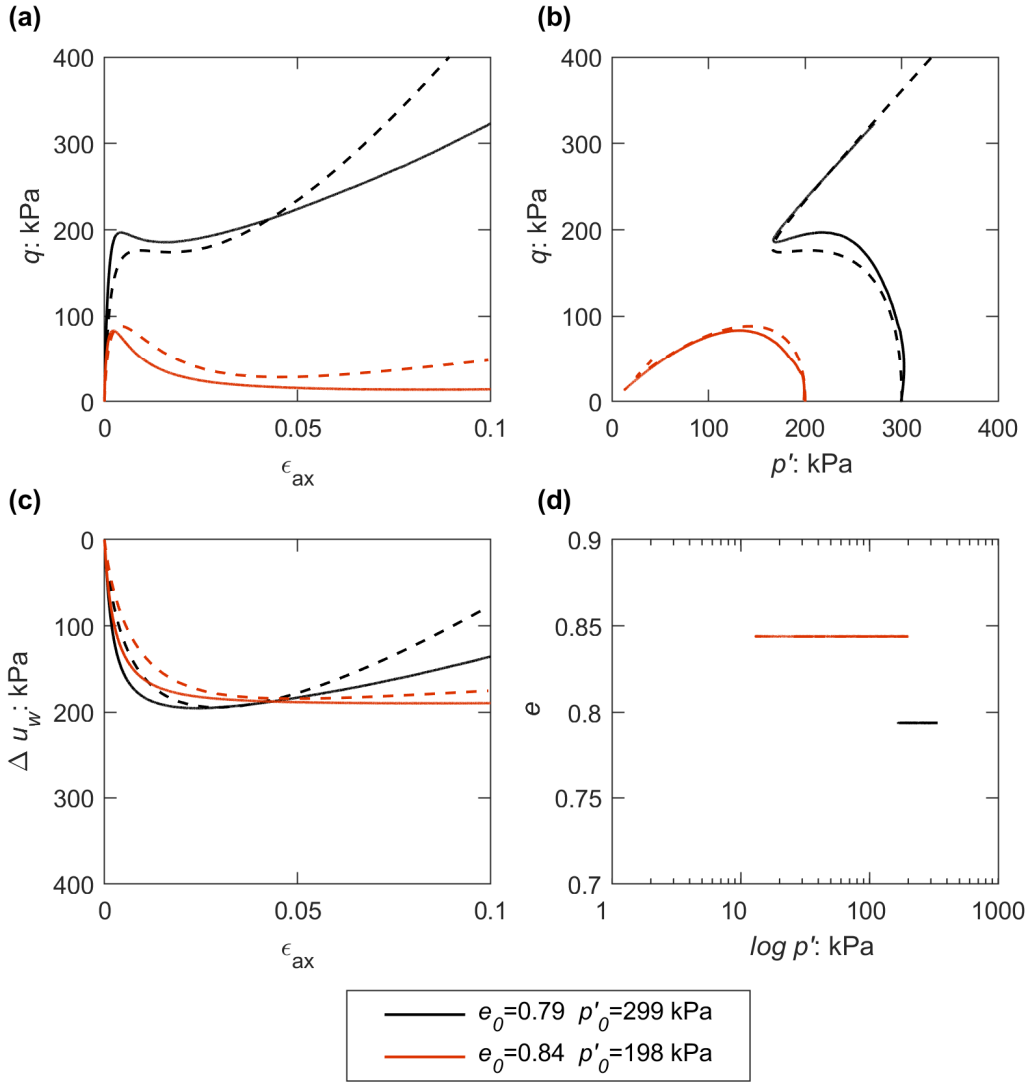

Figure 6.13: Comparison between the experimental data (solid lines) and the material behaviour (dashed lines) as predicted by the Severn-Trent model (with E_R=1/3 and ν =0.1) under undrained conditions: (a) deviatoric stress vs axial strain; (b) effective stress paths; (c) excess pore pressure vs axial strain; (d) void ratio vs mean effective confining stress.

The response of the soil under undrained conditions is now well-captured, especially in terms of effective stress-paths $q - p'$ (Figure 6.13.b). The pore pressure build-up is in fact better predicted by the model (Figure 6.13.c) and, in turn, also the peak values of the deviatoric stress q are consistent with the ones experimentally measured (Figure 6.13.a).

The drawback of assuming a fraction E_R of the small-strain shear modulus less than 1 is that, obviously, the small-strain shear modulus distribution does not match the prediction given by Eq. (6.12). Consequently, the drained behaviour of the sand in the very small-strain field, basically the strain range investigated by the Resonant Column tests, could not be adequately reproduced. Conversely, the drained response, as observed in the triaxial tests at medium-to-large strains, would not be substantially modified.

Bearing in mind that the target of the study is to investigate the response of the soil-foundation system under drained conditions over a wide range of rotations, it was decided to assume the full small-strain shear modulus, neglecting the differences observed in the undrained behaviour.

6.2.4 Simulation of the cyclic behaviour of the Perth sand

The cyclic behaviour of the Perth sand was experimentally investigated through a set of Resonant Column tests. In the tests, a sample isotropically consolidated is loaded by applying a cyclic torsional moment to the top of the specimen. For a given loading amplitude, a wide range of frequencies is analyzed to clearly identify the resonance condition of the first torsional mode of the specimen and, thus, to define the secant shear modulus G. The procedure is repeated for several amplitudes, in order to describe the sand response in a wide range of shear strains (for further details regarding the experimental procedure see Section 4.3.3.3).

The tests can be performed under drained or undrained conditions, but the results in terms of Modulus Reduction and Damping (MRD) are consistent, providing that the obtained G are normalized to a proper value of G_0 (see Section 4.3.6).

The experimental procedure previously described is difficult to simulate as all the details regarding the experimental apparatus should be accurately modelled to obtain an accurate simulation of the dynamic response of the system. Moreover, the procedure comprises several cyclic loadings (i.e. about 8,000) for each loading amplitude. Consequently, it was decided to study the cyclic response of the soil as predicted by the constitutive model simulating a set of Cyclic Direct Simple Shear (C-DSS) tests.

The simulations are performed on a single C3D8P (i.e. 8-node trilinear displacement and pore pressure) element. The element is firstly initialized under geostatic conditions. Then, it is consolidated up to the desired confining pressure p'_0 by increasing the vertical effective stress σ'_z under oedometric conditions. Such a consolidation phase is intended to model the real stress path that would take place in a C-DSS test.

At the end of the consolidation phase, a cyclic horizontal displacement is applied at the top nodes. The loading protocol consists of 10 cycles applied for 13 increasing displacement amplitudes. The displacement amplitudes are chosen to obtain 13 equally spaced (in logarithmic scale) cyclic shear strain amplitudes, which completely describe the range of shear strains investigated by the RC tests (i.e. from 10^{-6} to $2 \cdot 10^{-3}$). All the simulations are performed under drained conditions.

Figure 6.14 reports the results of the numerical simulation of a C-DSS performed on a sample with an initial void ratio $e_0 = 0.57$, consolidated up to a confining pressure $p'_0 = 800\,\text{kPa}$. The hysteresis $\tau - \gamma$ loops are plotted in Figure 6.14.a, while Figure 6.14.b presents the progressive accumulation of volumetric strains (due to the vertical settlement of the top nodes) with increasing loading cycles.

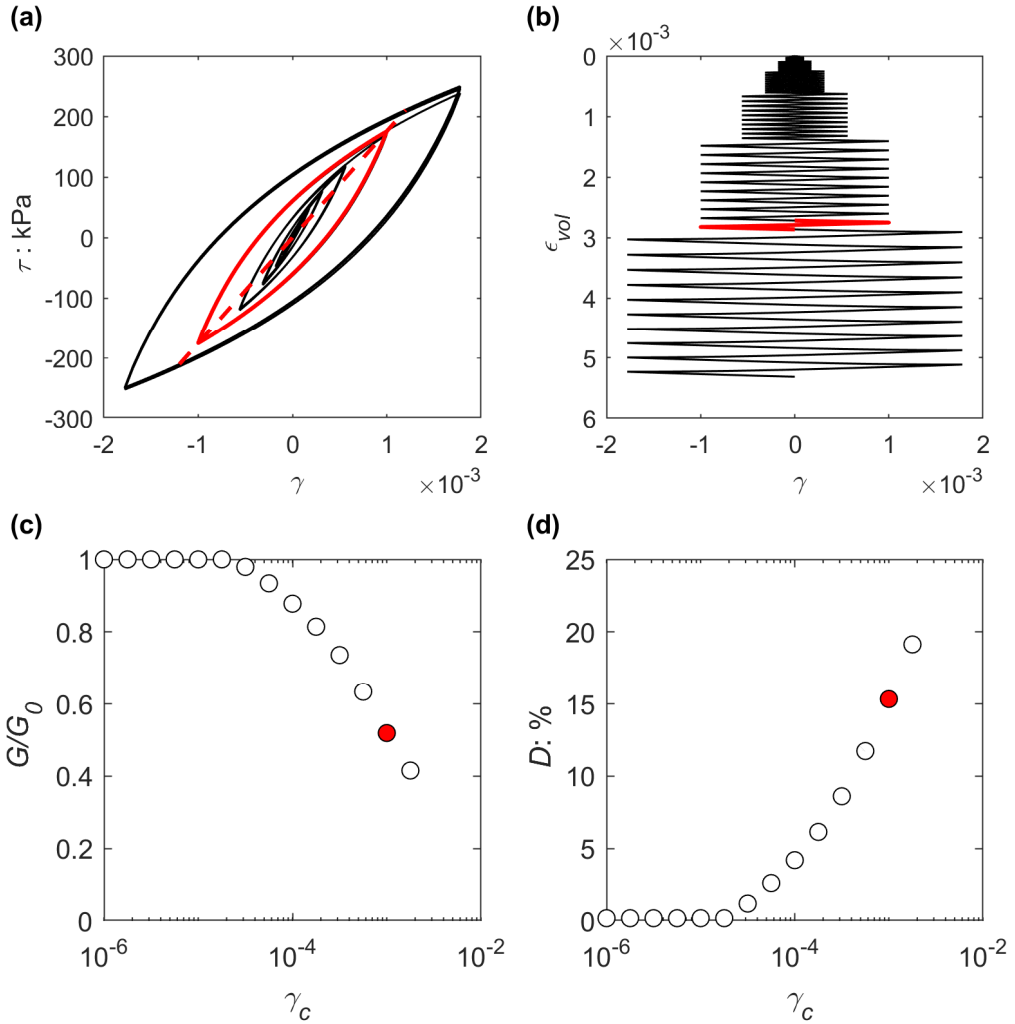

Figure 6.14: Results of the numerical simulation of a C-DSS ($e_0 = 0.57$, $p'_0 = 800\,kPa$): (a) shear stress vs shear strain hysteresis loops; (b) volumetric strain accumulation; (c) Modulus Reduction curve; (d) Damping curve.

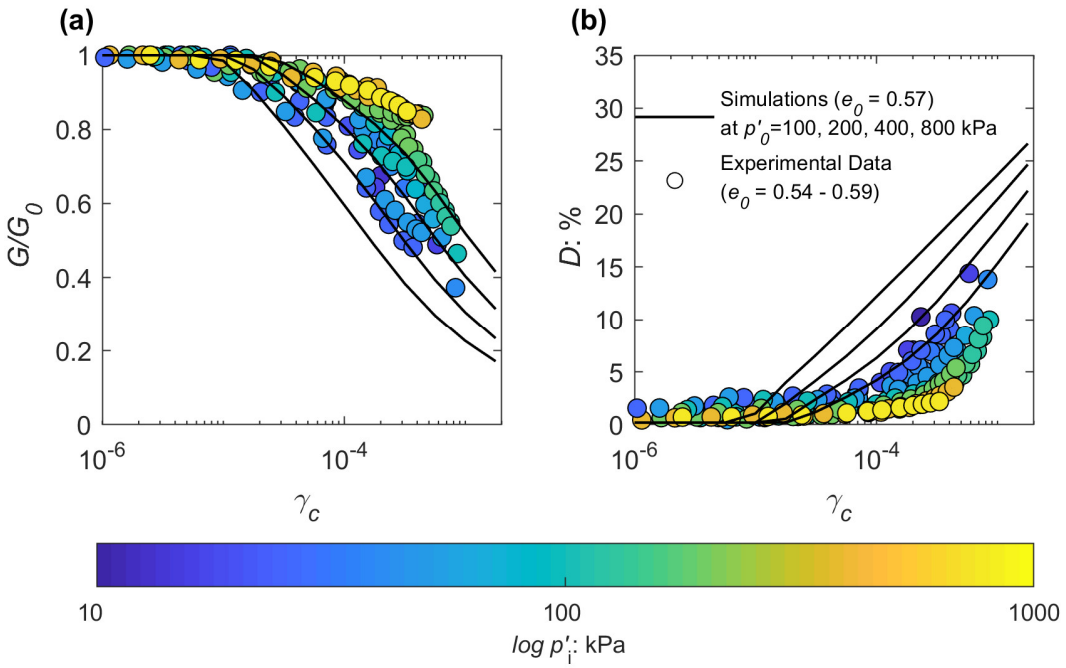

Figure 6.15: Comparison between simulations and experiments: Modulus Reduction (a) and Damping (b) curves vs cyclic shear strain amplitude.

The results of the simulated C-DSS tests are interpreted in terms of equivalent linear parameters (i.e. the MRD curves) to allow for a direct comparison with the RC tests. In particular, for a given displacement amplitude the secant shear modulus G is obtained as the slope of the tenth cycle, while the corresponding damping ratio is computed as a function of the ratio between the area enclosed inside the loop and the elastic shear strain energy. The procedure is then repeated for each cyclic shear strain amplitude γ_c to obtain the MRD curves (Figure 6.14.c-d).

The comparison between the simulated and the measured MRD curves is presented in Figure 6.15. The model predicts a slightly larger decay of the normalized secant shear modulus G/G_0 for γ_c ranging from 10^{-5} to 10^{-4}. However, the smoothed degradation of G/G_0 with increasing γ_c is overall well-simulated by the model as well as the dependency of the response from the confining pressure p'_0 (Figure 6.15.a). Besides, it should be noted that the G_0 simulated by the model is totally consistent with the small-strain modulus predicted by Eq. (6.12). As regards the damping ratio D, the model slightly overestimates its increase with increasing γ_c, especially for low confining pressures. The general trend is however consistent with the measured one.

6.3 Summary

This chapter has presented the soil constitutive model adopted to simulate the stress-strain behaviour of the Perth sand. After an initial, general, presentation of the Severn-Trent model, the calibration procedure carried out to define the constitutive parameters is presented. A summary of the model parameters calibrated for the Perth sand is given in Table 6.2.

Table 6.2: Constitutive parameters of the Severn-Trent model calibrated for the Perth sand.

Parameter	Calibrated value
v_λ	2.027
λ	0.019
φ'_{CS}	30°
m	0.8
k	2.6
A	0.65
k_d	1.8
B	0.007
α	1.2
R	0.01
E_R	1
ν	0.2
$\mathbf{B}_0$	$\mathbf{I}$

The Severn-Trent model, as here calibrated, has proved to be effective in predicting the Perth sand behaviour for a wide range of confining pressures and relative densities. In particular, the model simulates very well the results of the experimental triaxial tests performed on dense and loose samples of Perth sand under drained conditions. Conversely, some adjustments should be implemented to simulate the response of the sand under undrained conditions, which are anyway not relevant for the subsequent numerical simulations. As for the drained cyclic response of the sand, the predictions of the model are consistent with the measured data both in terms of small strain shear modulus G_0 and MRD curves.

This calibration procedure, performed exclusively on laboratory element tests, provides a reliable constitutive model for the numerical simulations of boundary value problems. The set of constitutive parameters can then be used to simulate the centrifuge tests, as reported in the next chapter.

Chapter 7

Numerical simulations versus centrifuge tests

The influence of scouring on the performance of a caisson foundation was investigated through a series of centrifuge tests, as reported in Chapter 5. Although the tests provided relevant information regarding the phenomenon, some aspects require additional investigation. In particular, the main failure mechanisms that affect the foundation subjected to general and local scour have to be carefully identified.

This chapter presents the comparison between the experimental centrifuge tests and the numerical simulations. The simulations are performed at the prototype scale adopting the Severn-Trent sand constitutive model, calibrated independently on the results of soil element tests, as reported in Chapter 6.

The purpose of this comparison is twofold: on the one hand, it can provide insights regarding the failure mechanisms; on the other hand, it serves as a validation of the numerical model. Moreover, if the numerical model can simulate the experimental results, it can be reasonably used also to predict the effects of scouring on structures with different characteristics and subjected to different loading conditions.

Firstly, the main aspects of the numerical model are presented. The chapter then compares the pure vertical and the monotonic pushover tests with the corresponding numerical simulations. Finally, the effects of scouring on the cyclic behaviour of the footing are analyzed by adopting two different loading protocols.

7.1 Numerical modelling

The numerical simulations are carried out using the Finite Element software ABAQUS (Systèmes Dassault, 2020). The constitutive model employed to predict the soil stress-strain behaviour is the Severn-Trent sand model (Gajo and Muir Wood, 1999b, a; Gajo, 2010), as calibrated in Chapter 6. Consistently with the target relative density of the study (i.e. $D_R = 80\%$), the model is initialized adopting a constant void ratio equal to 0.575, regardless of the minor differences in the measured void ratios achieved in the centrifuge tests. Such differences are anyway in the range of about ±0.02 with respect to the target one, thus practically negligible.

Consistently with the centrifuge tests, the analyses are performed under drained conditions. The soil stress-state is initially computed under hydrostatic conditions considering a water table corresponding to the soil surface. In the subsequent steps, a null pore water pressure build-up is imposed throughout the soil.

The vertical stress field σ'_v in the model is initialized as:

$$\sigma'_v = \gamma' z \tag{7.1}$$

where the weight under buoyancy of the soil γ' is defined according to Eq. (7.2):

$$\gamma' = \rho g - \gamma_w \tag{7.2}$$

being ρ the soil density, computed under the hypothesis of full saturation of the porous medium as follows:

$$\rho = \frac{\rho_s}{1+e} + \frac{e \cdot \rho_w}{1+e} \tag{7.3}$$

where ρ_s is the density of the grains. The horizontal stress σ'_h is then obtained as a function of σ'_v:

$$\sigma'_h = \sigma'_v \cdot K_0 \tag{7.4}$$

where K_0 is the coefficient of earth pressure at rest, for which a value 0.35 is computed by applying Jaky's (1944) equation with a peak friction angle for the dense sand $\varphi'_{peak} = 40°$.

For consistency with the experimental tests, the parameters of the foundation are defined based on typical values expected for aluminium. An isotropic linear elastic constitutive law is then adopted for the caisson material considering a Young's Modulus $E_a = 70\,\text{GPa}$ and a Poisson's ratio of 0.33, while a material density of 2750 kg/m^3 is selected. Nevertheless, it should be noted that the foundation behaves practically as an infinitely rigid body, so the parameters are not expected to influence the outcomes of the simulations.

As regards the soil-caisson interface, a pure frictional contact algorithm is adopted, thus allowing sliding and detachment of the elements. Specifically, the default "hard" pressure-overclosure relation is used in the normal direction, while in the tangential direction the interface response is modelled through a "penalty" algorithm with a friction coefficient $\mu = 0.23$. The latter was defined based on a series of direct shear interface tests carried out by Schwerzmann (2019). In those tests, the coefficient has been measured using Perth sand in a dense state and aluminium

plates, manufactured consistently with the caisson foundation model employed in the centrifuge tests of this study.

All the numerical simulations are performed by taking into account the nonlinearity induced by the changes in the geometry during the analysis. On one side, this is crucial to properly model the response of the soil elements placed close to the foundation. Such elements undergo very high stresses and strains going towards the failure of the soil-structure system, especially in the pure vertical tests. Consequently, true stresses and strains have to be considered rather than nominal values. On the other side, in the horizontal tests, the additional moment $\Delta M(\delta)$ given by second-order (i.e. $P-\delta$) effects is relevant for high rotations. By considering the geometrical nonlinearity, the second-order effects are implicitly considered in the numerical simulations. However, since the soil constitutive model has been developed within the small-strain framework, the results for very large strains should be treated with caution. As a consequence of the geometric nonlinearity, although not explicitly specified in the text, reference is made in the following to logarithmic strains rather than the engineering ones.

7.2 Pure vertical loading

This section studies the mechanical problem of the vertical bearing capacity of a cylindrical caisson foundation subjected to local and general scour. As previously reported by many Authors (e.g. Gajan and Kutter, 2008; Anastasopoulos et al., 2012; Gazetas et al., 2013; Zafeirakos and Gerolymos, 2013), the horizontal response of a foundation is strongly dependent on its vertical loading condition (usually identified through the vertical safety factor, FS_v). Therefore, it is crucial to be able to capture the response of the footing also under pure vertical loading.

7.2.1 Problem definition

The problem here considered refers to the case study investigated through the centrifuge tests (see also Section 5.1). A rigid cylindrical caisson foundation with diameter D_f =2 m and embedment d =2 m is pushed vertically to obtain the vertical load-settlement ($V-w$) curve. The soil consists of a homogeneous half-space of Perth sand in a dense state (i.e. $D_R \approx 80\%$).

In the numerical models, the total height of the foundation is equal to 3 m rather than 2 m (i.e. 2 m of embedment d plus 1 m above the soil surface). The upper part of the foundation is included in the simulations to avoid the "collapse" of the soil along the sides of the structure, which would prevent the possibility to draw the entire $V-w$ curve up to failure. The additional frictional resistance offered by this part of the foundation is anyway almost negligible. Moreover, when the simulations are compared to the centrifuge tests, this small difference is partially balanced by the additional frictional resistance offered by the soil along the contact surface with the actuator arm (see Figure 5.12). The comparison is therefore considered consistent, providing that the upper part of the foundation is modelled weightless.

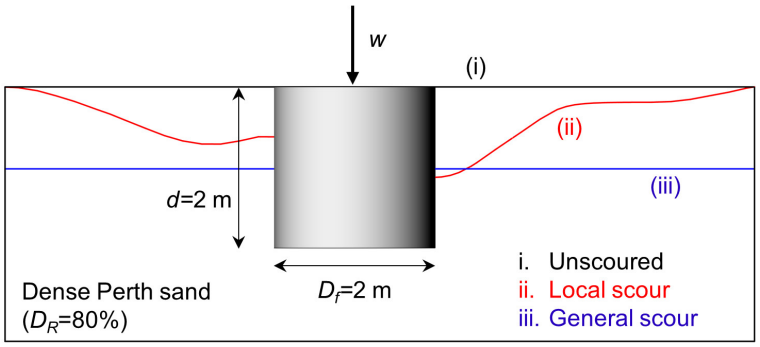

Figure 7.1: Problem definition for the pure vertical tests.

The analyses considered three different scouring conditions: (i) unscoured; (ii) local scour; (iii) general scour (Figure 7.1). Although not experimentally investigated in the vertical tests, the case of a foundation subjected to general scour (i.e. removal of a constant thickness soil layer) is also considered to better interpret the results of the horizontal tests performed under this specific condition.

7.2.2 Numerical steps and initial conditions

The vertical analyses consist of the following steps:

1. definition of the initial equilibrium through a geostatic numerical step by starting from an initial stress field obtained according to Eq. (7.1) and Eq. (7.4);
2. ideal ("wished in place") installation of the caisson foundation (the geometric nonlinearity is activated in this step);
3. vertical push of the top surface of the caisson under drained conditions. The numerical simulation is performed under displacement-control, so an increasing vertical displacement is applied on the top surface of the foundation up to failure, while the remaining degrees of freedom are fixed (i.e. neither rotations nor horizontal displacements of the foundation are allowed).

The caisson installation is modelled as "wished in place", so the construction phases (and the possible associated disturbance effect) are neglected, as also adopted in other studies (e.g. Zafeirakos and Gerolymos, 2013, 2014, 2016). A possible approach to model the installation phases of the foundation has been recently proposed by Gaudio and Rampello (2019, 2020). It consists of applying a volumetric contraction to the caisson volume to induce the disturbance effect in the soil due to the excavation process before the caisson construction. The Authors showed that such disturbance effect can modify the stress state field in the soil close to the foundation, attaining active limit conditions along the sides of the caisson.

Nevertheless, in this study, it was decided to neglect the installation phases to focus the attention on the effects of scouring. Moreover, it should be considered that a "wished in place" activation is consistent with the experimental procedure employed to build up the models. In the centrifuge tests, the soil is pluviated up to

the desired foundation level, the caisson is then placed on the surface and the sand is pluviated along the sides of the caisson without any disturbance effect.

The comparison between the stress field in the soil elements along the sides of the caisson before and after the activation of the foundation is reported in Figure 7.2 for the "benchmark" (unscoured) model. After the installation of the caisson, the horizontal and vertical stresses, σ'_h and σ'_v, closely follow Eqs. (7.1) and (7.4) up to a depth z of about 1.6 m. For higher depths, the additional load given by the difference between the unit weight of the soil and the caisson starts to influence the stress field, leading to an increase of both σ'_v and σ'_h.

It is worth mentioning that for the scoured models, the loading-unloading process induced by the progressive erosion of the soil along the sides of the foundation is neglected. This choice was made to closely follow the loading path experienced in the soil during the experimental tests. The "decoupled" experimental methodology employed to study the effects of scouring indeed does not consider the influence of the erosive process on the remaining soil (see Section 5.3.1.1 for further details). However, this influence is thought to be almost negligible for sand in dense state, considering that the maximum thickness of soil removed is 1 m, corresponding to about 10 kPa of additional initial σ'_v.

7.2.3 Finite element mesh and boundary conditions

Four numerical models are developed to study the problem (Figure 7.3), namely: (a) 2D axisymmetric unscoured model; (b) 2D axisymmetric model subjected to general scour; (c) 3D unscoured model; (d) 3D model subjected to local scour.

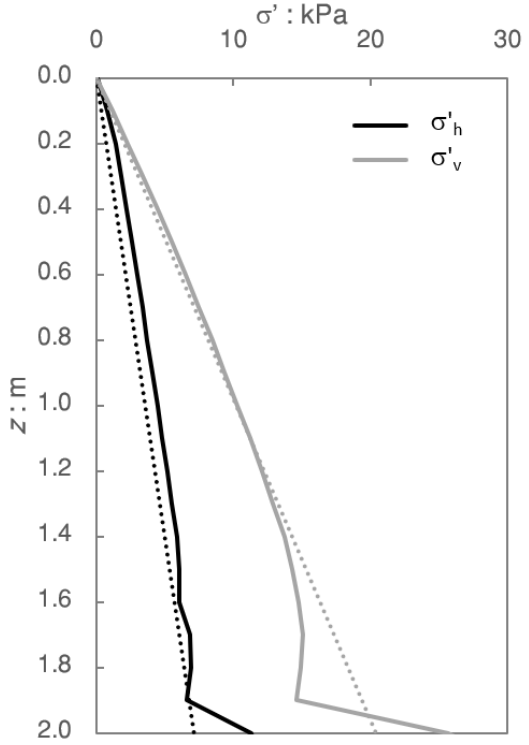

Figure 7.2: Comparison between the stress field in the soil elements along the sides of the caisson before (dotted lines) and after (solid lines) the installation of the footing.

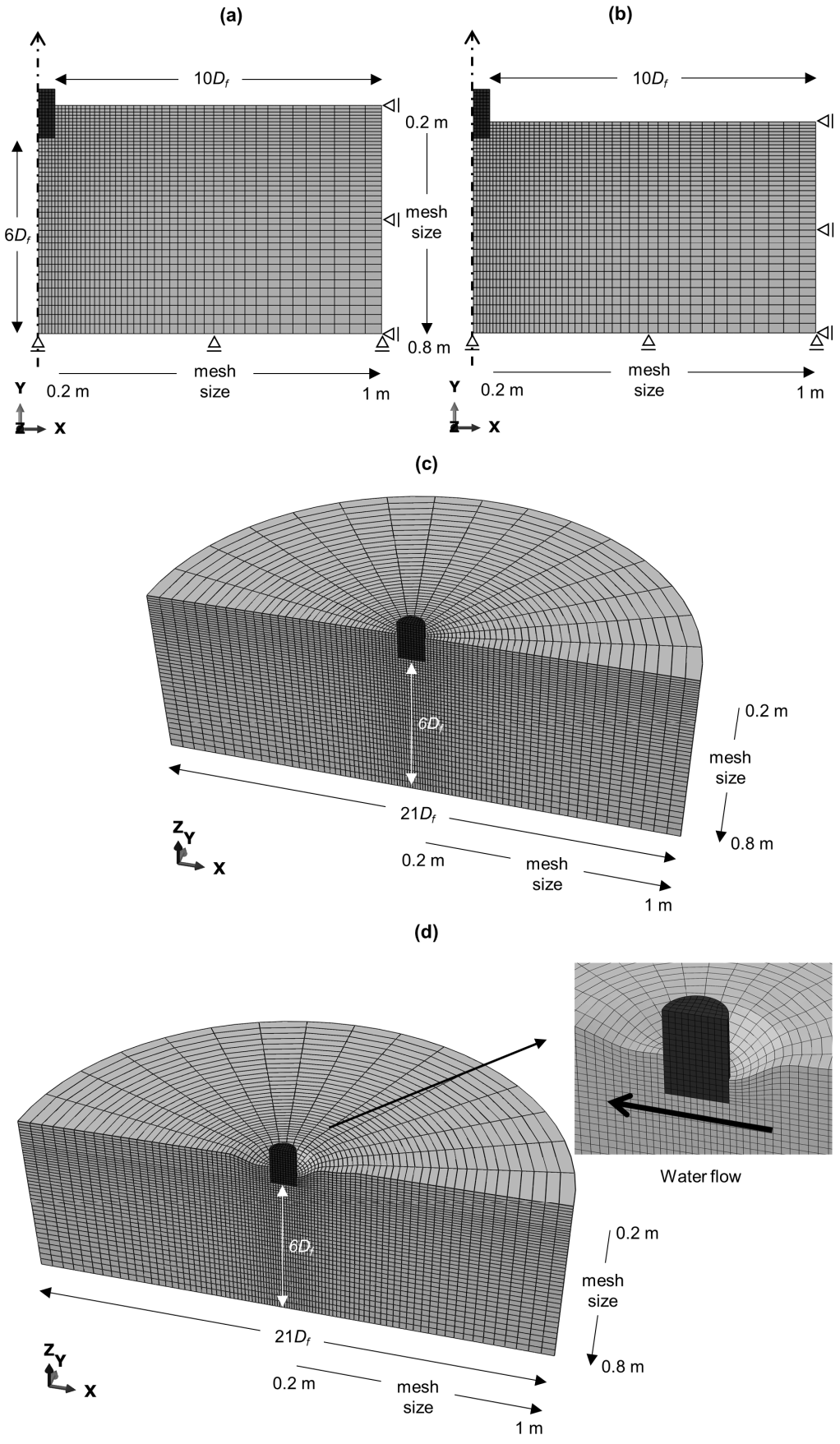

Figure 7.3: Finite element mesh for the vertical push tests: (a) 2D axisymmetric unscoured model; (b) 2D axisymmetric model subjected to general scour; (c) 3D unscoured model; (d) 3D model subjected to local scour.

The numerical elements used to model the soil are the CAX8RP (i.e. 8-node axisymmetric quadrilateral, biquadratic displacement, bilinear pore pressure, reduced integration) elements for the axisymmetric models and the C3D20RP (i.e. 20-node brick, triquadratic displacement, trilinear pore pressure, reduced integration) elements for the 3D models. Conversely, for the foundation, the corresponding elements without the pore pressure degrees of freedom (i.e. CAX8R and C3D20R) are adopted. The choice of the numerical elements is guided by the need to reach very high-stress gradients in the soil close to the foundation, avoiding anyway the typical numerical issues related to volumetric and shear locking of the elements. It is worth mentioning that given that the load is applied under drained conditions, the pore pressure degrees of freedom are fixed during the loading phase.

The 2D axisymmetric unscoured model (Figure 7.3.a) was firstly used to conduct a sensitivity study on the effects related to the mesh discretization and the size of the model. With due consideration to the computational cost, preliminary analyses were carried out in an attempt of reducing the horizontal extent of the FE discretized field down to 5 times the diameter of the foundation D_f. The analyses, however, showed that the dimensions of the FE field play a role for very large displacements. In particular, the displacement field (and the corresponding pressure bulb) starts to be influenced by the "elementary" lateral boundary conditions for imposed vertical settlements $w > 0.1\,\text{m}$. It was therefore decided to adopt for all the vertical simulations a FE element discretized field with the same dimensions of the strongboxes used in the centrifuge tests (see Figure 5.12), namely a soil cylinder with a total height of $7\,D_f$ (i.e. $6\,D_f$ below the base of the foundation) and a radius of $10.5\,D_f$ (i.e. a distance of $10\,D_f$ from the sides of the foundation).

As regards the mesh size, a sensitivity study was conducted on the 2D axisymmetric unscoured model by varying the size of the elements. Figure 7.4 reports the comparison between the $V-w$ curves obtained by adopting uniform meshes with sizes varying from 15 to 30 cm. A further reduction of the mesh size would not produce significant changes in the results. As can be observed from the plot, the mesh size is not very relevant in the first branch of the curve (up to about 10 cm of settlement). Conversely, for larger w, the results are slightly influenced by the mesh. As expected, a coarser mesh implies a slightly larger failure surface and a "slower" progressive failure of the soil, providing as a consequence a higher maximum limit load. The results are however not significantly influenced by the mesh size for settlements smaller than 0.25 m (i.e. 1/8 of D_f). By considering also the computational costs (especially for the 3D models) it was therefore decided to adopt for the following simulations an element size of 20 cm.

Once the size of the elements close to the foundation was selected, a further simulation was carried out by adopting a mesh size varying from 20 cm to 80 cm/1 m, respectively in the vertical and horizontal directions, in an attempt of reducing the number of elements included in the analyses. The comparison, reported in Figure 7.5, revealed that the differences between the results of the two models are barely visible, so the reduced mesh is considered appropriate to model the problem. The final mesh, reported in Figure 7.3.a, consists of about 1,900 CAX8RP soil

elements and 75 CAX8R foundation elements. Concerning the foundation subjected to general scour, a 2D axisymmetric model was developed by using the same mesh discretization rules adopted for the unscoured situation (Figure 7.3.b).

The results of the simulations performed under axisymmetric (unscoured) conditions were subsequently used as a "benchmark" to verify the suitability of the 3D (unscoured) model. The discretized field includes just half of the model, thanks to the symmetry conditions. The 3D mesh consists of about 28,000 C3D20RP soil elements and it is built by revolving the 2D mesh around the axis of symmetry of the model (Figure 7.3.c). The foundation is modelled using 480 C3D20R elements. The comparison between the 2D and the 3D simulations is presented in Figure 7.5. Again the differences between the results of the two simulations are practically negligible, so the 3D mesh is considered appropriate to model the problem.

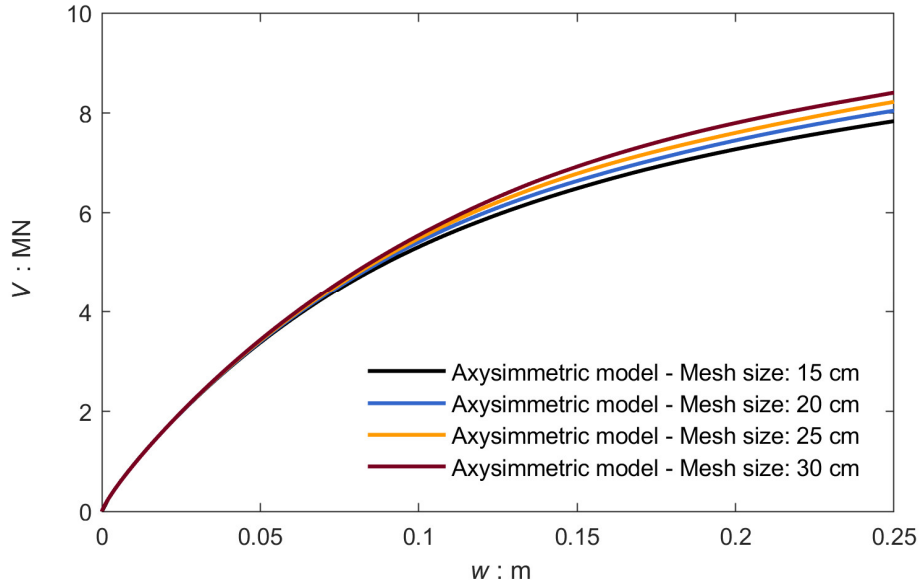

Figure 7.4: Mesh sensitivity study on the axisymmetric 2D unscoured model.

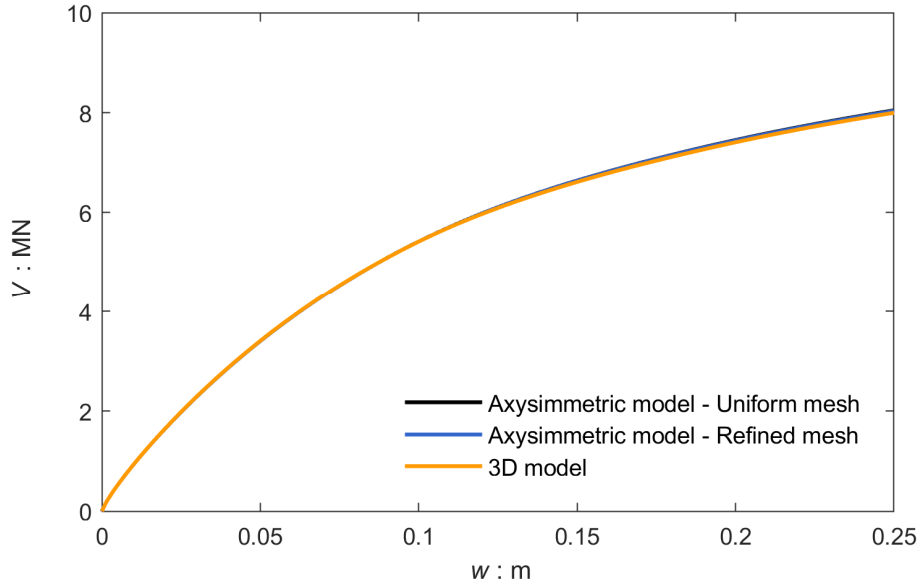

Figure 7.5: Comparison between the results of the uniform (and non-uniform) axisymmetric 2D model and the 3D model in unscoured conditions.

The verification of the 3D model under unscoured conditions was performed to ensure the consistency between the axisymmetric models (suitable for the unscoured and the general scoured foundations) and the 3D model of the caisson subjected to local scour. For such a condition, a 3D model is necessary due to the irregular shape of the scour hole. The local scour model includes again just half of the domain, thanks to the vertical symmetry plane placed along the direction of the water flow (Figure 7.3.c).

The 3D mesh is completely equivalent to the one adopted for the unscoured case for the soil from the base of the model up to the bottom surface of the caisson. The actual shape of the scour hole, as acquired in the experimental hydraulic tests through the 3D scan (see Section 5.2.2), is imported in ABAQUS to model the soil surface. The finite element mesh around the foundation is developed through a specific bottom-up procedure to avoid the formation of distorted finite elements. Such a procedure divides the soil layer into 8 sub-layers, projecting the base mesh (as discretized in correspondence of the base level of the caisson) on the top scoured surface. The final mesh is reported in Figure 7.3.d and it consists of approximately 28,000 C3D20RP soil elements and 480 C3D20R foundation elements.

7.2.4 Results

The results of the numerical simulations are reported in the following. Firstly, the numerical model is validated against the experimental results. The failure mechanisms are then analyzed in detail for the three scouring conditions. Finally, the pure vertical bearing capacity of the caisson is estimated considering the performance of the foundation system.

For the sake of simplicity, for the unscoured condition reference is made to the 2D axisymmetric model. The results obtained from the 3D model are totally equivalent to the axisymmetric ones.

7.2.4.1 Validation against the centrifuge tests

Figure 7.6 reports the results of the vertical push tests performed on the caisson foundation before and after local scouring. The comparison between the numerical simulations (solid lines) and the centrifuge tests (dotted lines) is presented in terms of tangent vertical stiffness-settlement ($K_v - w$) and load-settlement ($V - w$) responses. In particular, the experimental curves refer to the tests $V1_A$ and $V2_A$ (see Table 5.5). The curves obtained for the other two tests are not reported in the plot for clarity, the results are anyway almost equivalent (see Figure 5.17).

The 3D numerical simulation of the foundation under local scour reaches a maximum settlement w of about 0.25 m. After this point, it is not possible to keep pushing the foundation due to numerical convergency issues. Consequently, the last part (dashed line in the plot) of the numerical curves is estimated through a curve-fitting and extrapolation procedure.

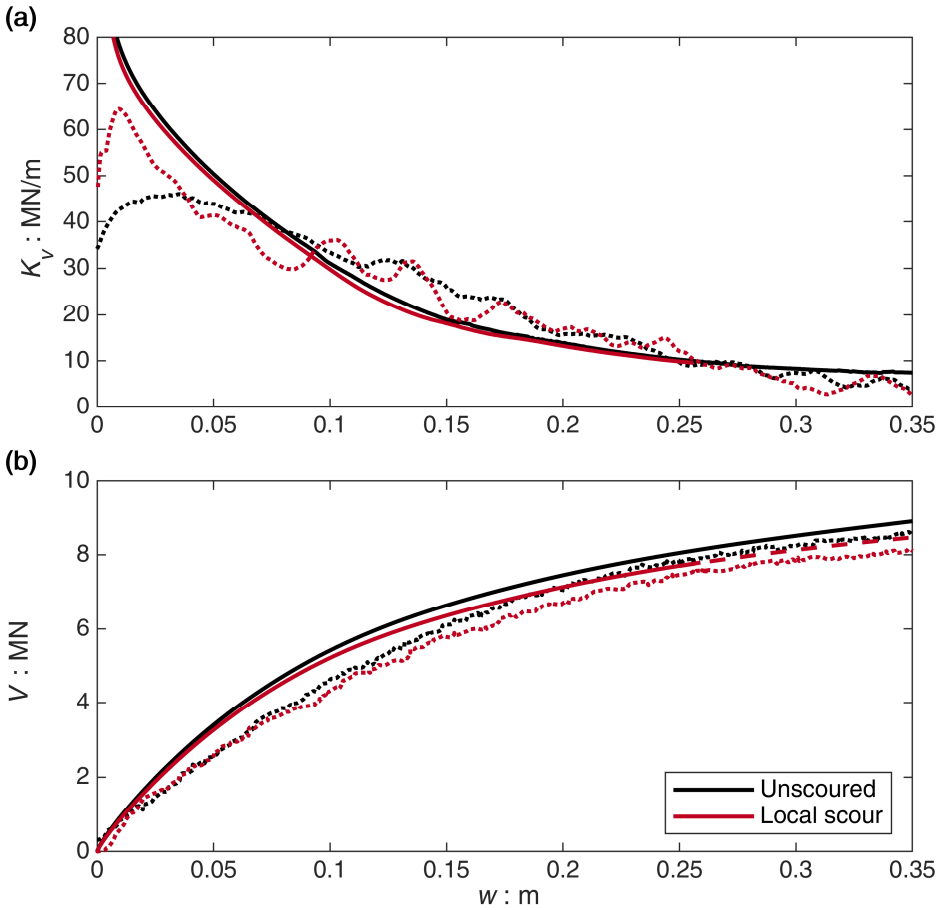

Figure 7.6: Numerical simulations (solid lines) versus centrifuge tests (dotted lines): vertical response of the caisson foundation before and after local scour in terms of (a) tangent vertical stiffness-settlement $K_v - w$ curves and (b) load-settlement $V - w$ response.

As it can be observed from Figure 7.6.a, the numerical model predicts very well the evolution of the tangent vertical stiffness K_v with an increasing settlement w, especially for $w > 0.05\,\text{m}$. The only significant difference between the numerical simulations and the experimental results can be observed in the first branch of the curves. The experimental tests show initially lower values of K_v, which increase for the first 0.02-0.03 m of settlement. The K_v tends then to decrease again, showing a trend consistent with the one predicted by the numerical model. A possible explanation for this slight discrepancy lies in the experimental procedure adopted for the tests. In the centrifuge tests, the actuator arm is not initially in contact with the foundation, to allow the caisson to freely settle during the spinning up phase. Subsequently, during the loading phase, the arm is pushed down with a constant velocity and the contact is established. It is then possible that during the very first part of the vertical push test, the contact is not yet perfect made, leading to a slight underprediction of the initial stiffness K_v due to a "seating" effect. Nevertheless, soon after the contact is established, the issue is overcome.

Similar considerations can be made by observing the $V - w$ curves (Figure 7.6.b). The first branch of the experimental curves presents a slower increase in the vertical load V when compared to the numerical ones. However, the trends of the two pairs of curves become very similar for larger w.

The numerical model seems able to properly predict the behaviour of the caisson foundation under pure vertical loading. Most importantly, the effects of local scouring are very well captured by the simulations. As observed in the experimental tests, the response of the caisson foundation after local scour is, in fact, almost identical to the one observed before scouring, with just a slight decrease in terms of vertical load V for high settlement w. This is probably due to the decrease of the effective overburden pressure in the soil below the foundation, rather than a variation in the failure mechanism.

7.2.4.2 Vertical bearing capacity

The results obtained from the numerical simulations for the three cases here considered are reported in Figure 7.7. In stark contrast to local scour, general scour strongly affects the vertical response of the caisson foundation, both in terms of stiffness and bearing capacity. In particular, the caisson foundation after general scouring shows a significantly lower vertical stiffness K_v even in the small-strain field (Figure 7.7.a). This is also reflected in the $V-w$ curves: the foundation subjected to general scouring undergoes a significant increase of the settlement w for a given value of the vertical load V (Figure 7.7.b).

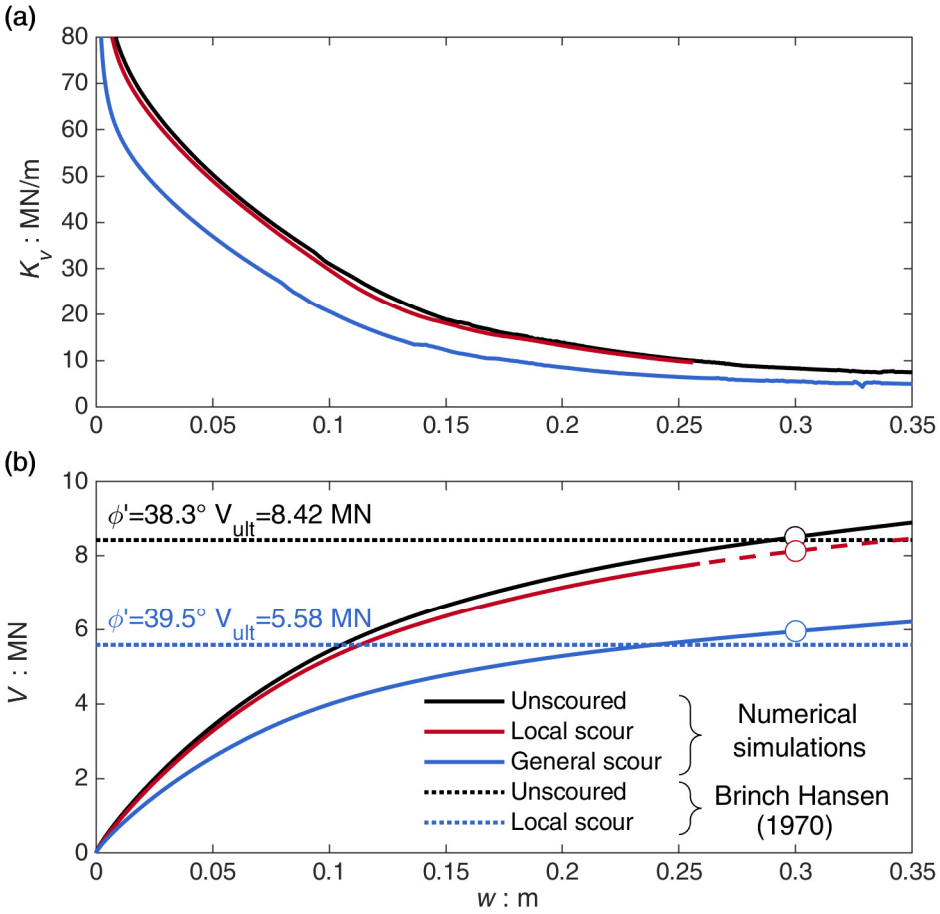

Figure 7.7: Numerical simulations: vertical response of the caisson foundation before and after local and general scouring in terms of (a) tangent vertical stiffness-settlement $K_v - w$ curves and (b) load-settlement $V - w$ response.

Such significant impact partially explains why bridges founded on relatively shallow foundations, under extreme scouring conditions, can experience a pure vertical failure due to just the dead load of the structure (see also Section 3.1.3.1).

As also observed in the centrifuge tests, a clear plateau can not be identified in the $V-w$ curves (Figure 7.7.b). The first branch of the curves presents a slightly nonlinear response, up to a settlement w of about 0.1 m. Then, the response becomes strongly nonlinear and the failure mechanism starts developing. After the failure mechanism is fully developed, the vertical tangent stiffness K_v tends to a residual (low, but non-zero) value (Figure 7.7.a). Consequently, the $V-w$ curves show a progressive hardening regime, suggesting that a local shear failure mechanism would take place rather than a general one (Vesic, 1973, 1975). This can be partially explained by the progressive increase of foundation embedment, as also noticed in previous experimental studies (e.g. Taeseri et al., 2018).

The evolution of the failure mechanism can be analyzed by looking at the void ratio distribution in the soil during the vertical push of the foundation. Figure 7.8 plots the deformed mesh with superimposed void ratio contours at increasing vertical settlement (i.e. w equal to 0.05, 0.15 and 0.30 m) for the foundation before (Figure 7.8.a) and after (Figure 7.8.b) general scour. The results for the foundation subjected to local scour are almost equivalent to the ones presented for the unscoured caisson. For an imposed settlement w of 0.05 m (i.e. within the slightly nonlinear branch of the $V-w$ curves), just the soil below the edges of the foundation shows significant dilation. For increasing settlements (w = 0.15 m), the failure soil edge starts developing below the foundation. Finally, for very large settlements (w = 0.30 m) a large portion of the soil below the foundation shows a significant increase in the void ratio e. The latter highlights the transition towards the critical state of the soil.

The failure surface, especially in the case of the unscoured foundation, develops just locally below the caisson, without reaching the soil surface. Moreover, no bulging is observed at the surface. Conversely, for the foundation subjected to general scour, the failure surface seems to reach, at least partially, the soil surface explaining why for such a condition a significant reduction of the capacity of the caisson is observed.

As previously discussed, it is not possible to identify a clear ultimate value V_{ult} for the vertical load. A possible strategy to estimate the vertical bearing capacity of the foundation was suggested by Anastasopoulos et al. (2012): V_{ult} is defined as the load at the initiation of the hardening regime (i.e. the point at which the K_v-w curves become practically horizontal), which corresponds to settlement w_{ult}. This strategy was applied also in the first part of this study to define the experimental capacity of the foundation (see Section 5.3.2 for further details). However, a slightly different approach is here adopted to allow for direct comparison among the different cases.

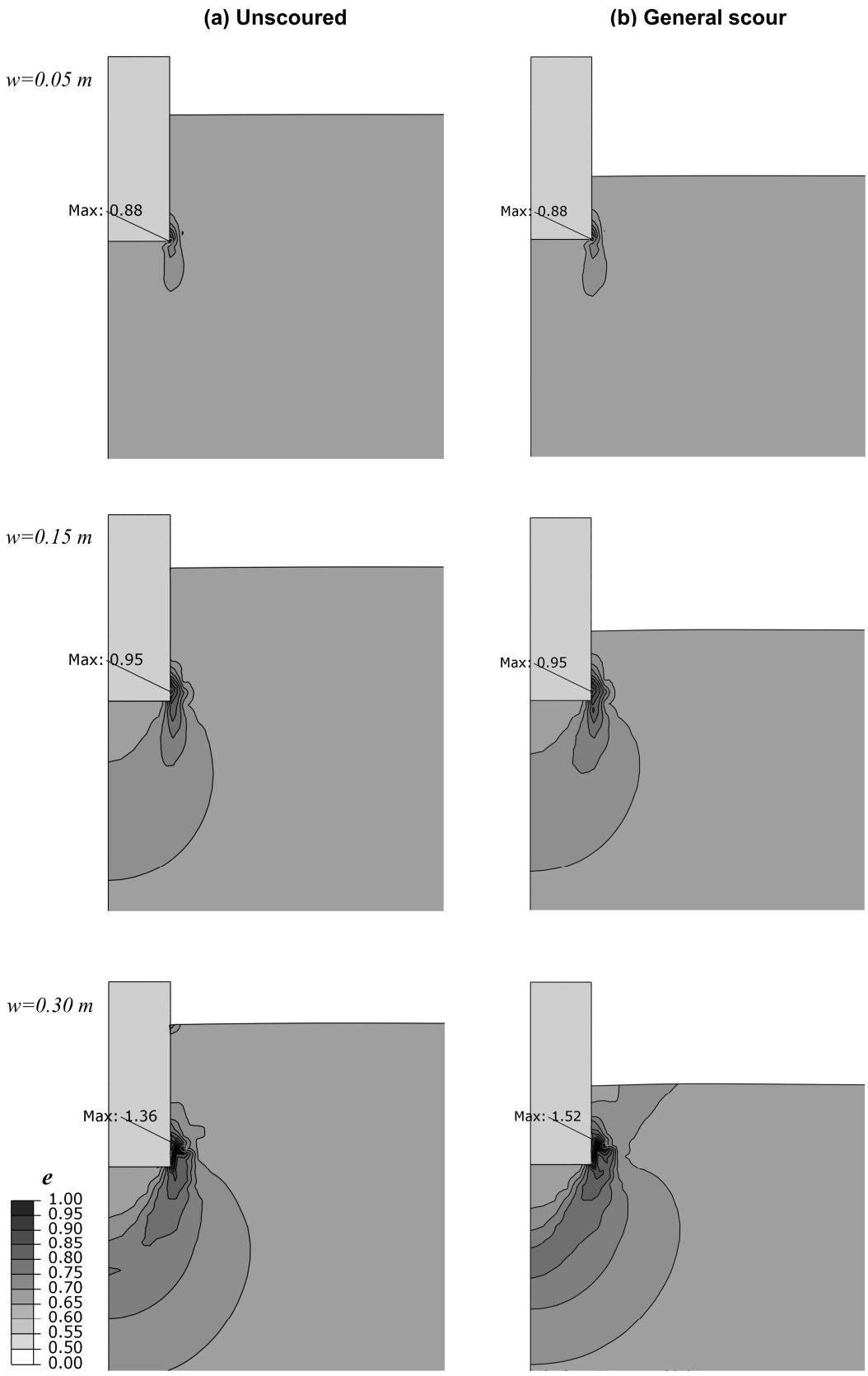

Figure 7.8: Deformed mesh with superimposed void ratio contours during a vertical push test: (a) unscoured foundation; (b) foundation subjected to general scour.

When a foundation exhibits a hardening regime, what effectively limits its capacity is the amount of settlement accumulated rather than the maximum allowable load. As a consequence, to analyze the performance of the caisson, it was decided to identify the ultimate vertical load V_{ult} as the load necessary to produce a settlement w_{ult} of 0.3 m. This value corresponds to a fairly large normalized settlement (i.e. w_{ult} / D_f equal to 15%), and it coincides approximately with the initiation point of the hardening regime (Figure 7.7.a).

Table 4.2 reports the ultimate load V_{ult} obtained from the numerical simulations and the centrifuge tests, computed according to the abovementioned criterion. The table also reports, for comparison, the predictions given by the analytical solutions as proposed by Brinch Hansen (1970). The analytical solution is applied considering the corrective factors proposed by Vesic (1973, 1975) for the unscoured and the general scour conditions. It should be noted that an operative peak friction angle φ'_{peak} has to be defined to compute the bearing capacity of a foundation resting on dense sand. The iterative procedure proposed by De Beer (1970) is here adopted according to Bolton's (1986) dilatancy relationship (see Appendix A.1 for further details). Direct visualization of the limit loads is also given in Figure 7.7.b, where the numerical limit loads $V_{ult}{}^{num}$ are identified with the circles while the analytical results are reported as dotted horizontal lines.

In the Table the differences between numerical and experimental (or analytical) results are also quantified as:

$$Diff\,(\%) = \frac{V_{ult}{}^{num} - V_{ult}{}^{exp,\,BH}}{V_{ult}{}^{exp,\,BH}} \tag{7.5}$$

being $V_{ult}{}^{num}$, $V_{ult}{}^{exp}$ and $V_{ult}{}^{BH}$ the ultimate vertical loads as obtained, respectively, from the numerical simulations, the centrifuge tests and the Brinch Hansen (1970) analytical solution.

The comparison between the numerical simulations and the centrifuge tests is very satisfying, with a maximum difference of 3.5% for the local scour condition. This confirms the ability of the numerical model in capturing the vertical response of the foundation. As regards the analytical solutions, it should be noted that it is difficult to perform a fully consistent comparison due to the conventional nature of the definition of V_{ult}. Nevertheless, the observed differences are quite reasonable, with a maximum value of 6.6% for the general scour condition.

Table 7.1: Results of the numerical simulations of the vertical push tests compared to experimental results and analytical solutions (Brinch Hansen, 1970).

Condition	Ultimate vertical load (for w_{ult} =0.3 m) V_{ult} : MN			Difference: %	
	Numerical simulations	Centrifuge tests	Brinch Hansen (1970)	$\frac{V_{ult}{}^{num} - V_{ult}{}^{exp}}{V_{ult}{}^{exp}}$	$\frac{V_{ult}{}^{num} - V_{ult}{}^{BH}}{V_{ult}{}^{BH}}$
Unscoured	8.50	8.23	8.42	+3.3	+0.95
Local scour	8.13	7.85	-	+3.5	-
General scour	5.95	-	5.58	-	+6.6

Overall, what emerges from the numerical simulations is that while local scour just slightly affects the vertical response of the caisson foundation (i.e. V_{ult} decreases from 8.50 to 8.13 MN), general scour can severely reduce the vertical performance of the foundation. After general scouring, the failure seems to shift from a local failure mechanism to a general one, with a substantial reduction of V_{ult} from 8.50 to 5.95 MN (i.e. about 30%).

The abovementioned conclusions are valid for this specific condition, i.e. an embedded foundation with d / D_f equal to 1, affected by scouring up to about half of the embedment depth d. As also observed in the past (see for instance the case history of the Schoharie Creek Bridge, Section 3.1.1), foundations subjected to extreme events can also experience a pure vertical failure due to local scour. This is however a fairly rare condition, usually associated with shallow foundations when the soil is eroded up to undermining the base of the footing.

7.3 Lateral pushover loading

One key element to consider when dealing with tall-slender structures (such as bridge piers) is the evaluation of the horizontal (and rotational) performance of the system. For these structures, the horizontal force and, in turn, the overturning moment transmitted by the superstructure can be indeed substantial. If the moment is such to induce the uplifting of one edge of the footing from the supporting soil, the corresponding stress concentration that will take place below the other edge may lead to the development of a bearing capacity failure mechanism.

In addition to the base resistance, the sides resistance has also to be considered for a caisson foundation. The rotation of the structure induces, in fact, an increase in the soil thrust acting along the pushing side of the foundation and a decrease along the opposite side. The corresponding resisting moment M_{sides} is then the consequence of passive- and active-like thrust failure mechanisms developing along the sides of the footing (see also Appendix A.2).

As a result of the abovementioned mechanisms, the system subjected to horizontal actions can experience severe nonlinearities, which may result in accumulation of permanent settlement and rotation of the structure and, ultimately, in its collapse. The issue is even more relevant if the foundation is subjected to general or local scour. The removal of soil around the sides of the footing implies a strong decay of the performance of the system.

These are the main aspects of the problem that emerged from the centrifuge tests, which have therefore to be reproduced by the numerical simulations. In the following, the horizontal monotonic tests are simulated to validate the numerical model. Furthermore, the failure mechanisms developing in the soil below, and along the sides, of the footing are analyzed to shed light on the main differences observed in the centrifuge tests between the effects of local and general scour.

7.3.1 Problem definition

The problem here considered refers to an idealized single degree of freedom (SDOF) system which represents the prototype bridge pier studied in the experimental part of this study (see Figure 5.1). According to the physical model, the numerical model consists of a rigid structure supported on a cylindrical caisson footing founded on dense Perth sand (Figure 7.9). In addition to the self-weight, the foundation is subjected to the vertical loads given by the deck and the pier mass. The latter are introduced as concentrated forces applied in correspondence with the centres of gravity of the two elements (Figure 7.9). It should be noted that these points are defined based on the actual shape of the two elements (for instance the centre of gravity of the pier does not coincide with its middle point) to allow for direct comparison with the experimental tests.

The numerical simulations consider again the three situations previously described: (i) unscoured; (ii) local scour; (iii) general scour (Figure 7.1). The three conditions are associated with different vertical safety factors FS_v. The latter can be computed as:

$$FS_v = \frac{V_{ult} + W_3'}{W_3' + W_2 + W_1} \tag{7.6}$$

where W_3', W_2, and W_1 are, respectively, the weight of the footing accounting for buoyancy, the weight of the column, and the weight of the deck. According to the results of the vertical push tests (see Section 7.2.4), FS_v in the reference condition is equal to 8, slightly reducing to 7.7 due to local scouring. The reduction is instead significant under general scour, where the FS_v is equal to 5.6.

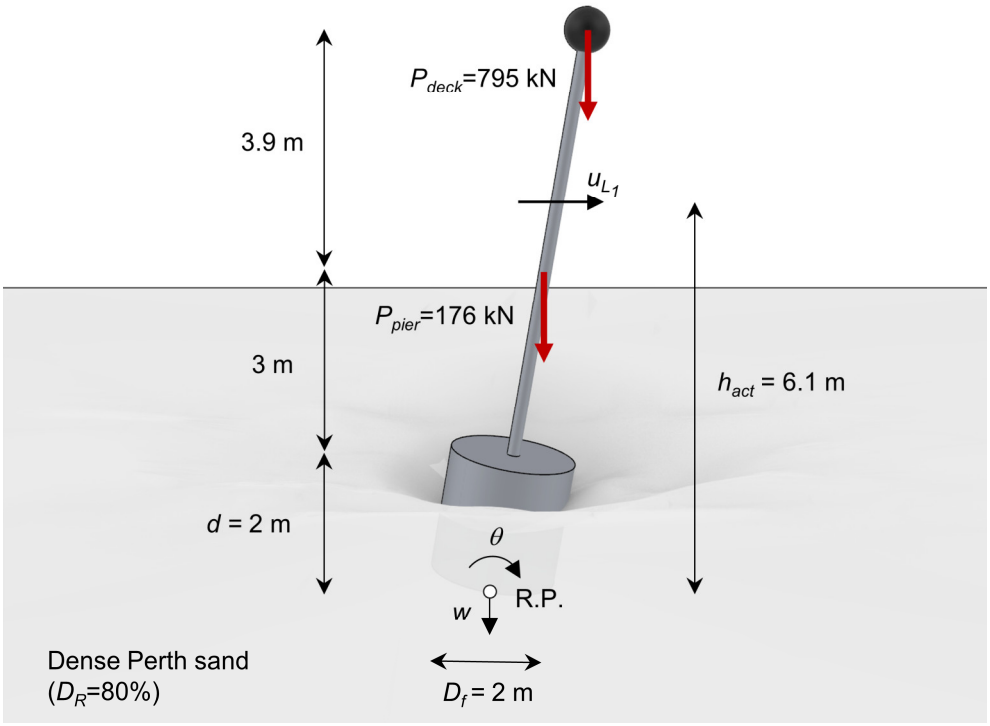

Figure 7.9: Problem definition: SDOF bridge pier under lateral pushover loading.

For the local scour condition, the attention is focused on the response of the foundation along the transverse direction of the bridge, which is usually critical. Along this direction, the response of the structure is different if the pier is pushed towards the upstream or the downstream side due to the asymmetry of the scour hole (see also Figure 5.6). Consequently, two different numerical simulations have to be performed to study the problem.

7.3.2 Numerical steps and initial conditions

The horizontal pushover analyses consist of the following steps:

1. definition of the initial equilibrium through a geostatic numerical step by starting from an initial stress field obtained according to Eq. (7.1) and Eq. (7.4);
2. ideal ("wished in place") installation of the caisson foundation (the geometric nonlinearity is activated in this step);
3. activation of the vertical loads (deck and pier masses);
4. horizontal pushover loading of the structure under drained conditions; the numerical simulation is performed under displacement-control, so an increasing horizontal displacement is applied on the rigid pier at an application point defined consistently with the experimental tests (Figure 7.9), while the remaining degrees of freedom are free (i.e. the structure is free to settle and rotate).

The 3D numerical models are developed considering half of the domain by virtue of the symmetry conditions along the vertical plane orientated along the direction of the flow. Consequently, during the third step, just half of the vertical forces (representing the deck and pier masses) are applied.

After the initial equilibrium is reached, the pushover loading is applied. During this step, the rigid motion of the structure is monitored considering: the horizontal, externally imposed, displacement u_{L1}; the in-plane rotation θ; and the vertical settlement w. Figure 7.9 reports the reference scheme adopted for the numerical simulations. It should be noted that the notations are chosen consistently with the experimental tests. The horizontal force necessary to produce the imposed horizontal displacement u_{L1} is recorded during the simulation. Such force is then doubled to obtain the total force H related to the full model (i.e. without considering the symmetry conditions). By knowing *H*, the external overturning moment *M* with respect to the reference point (i.e. the centre of the base of the caisson, Figure 7.9) is obtained as:

$$M = H \cdot h_{act} \tag{7.7}$$

The total moment M_{tot} acting on the structure is given by the sum of the overturning external moment M plus the additional moment $\Delta M(\delta)$ given by second-order (i.e. $P-\delta$) effects.

The initial stress conditions within the model are analyzed in Figure 7.10, which reports the comparison, for the "benchmark" (unscoured) model, between the stress field in the soil elements along the sides of the caisson before and after the installation of the foundation and at the end of the activation phase of the vertical loads.

The distributions of the horizontal and vertical stresses, σ'_h and σ'_v, in the first two steps are almost equivalent to the ones observed for the vertical tests (Figure 7.2). An increase of σ'_h is instead observed after the activation of the vertical loads. Conversely, σ'_v tends to slightly decrease with depth due to the yielding of the soil below the edges of the footing.

Figure 7.11 reports the comparison between the three conditions in terms of void ratio e (left pictures) and total displacement u_{tot} (right pictures) at the end of the activation phase of the vertical loads. As previously observed for the vertical tests, the response of the caisson foundation before and after local scour is very similar: the application of the loads implies a moderate yielding of the soil below the edges of the caisson as highlighted by the local increase of the void ratio e. Moreover, the induced displacement field is mainly concentrated below the footing, suggesting that for larger loads a local failure mechanism would take place.

The void ratio contours for the foundation subjected to general scour are similar, although slightly larger values of e are observed. Conversely, the induced displacements field seems to reach the soil surface, suggesting a transition towards a more fragile failure mechanism.

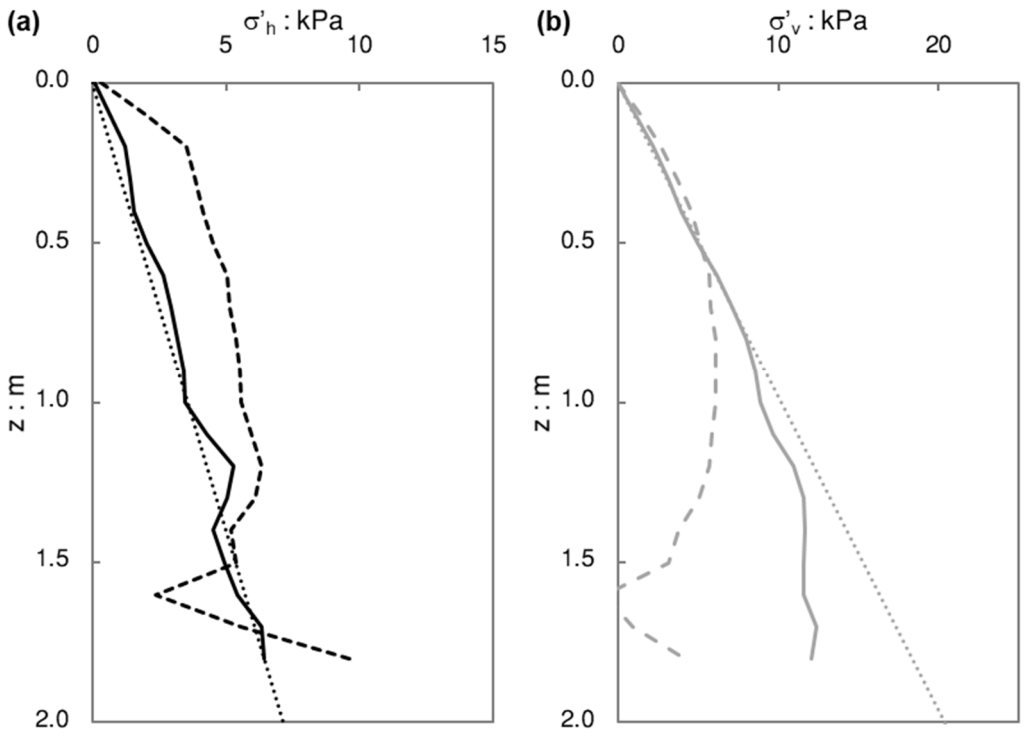

Figure 7.10: Comparison between the horizontal stress (a) and the vertical stress (b) in the soil elements along the sides of the caisson before (dotted lines) and after (solid lines) the installation of the footing and at the end of the activation phase of the vertical loads (dashed lines).

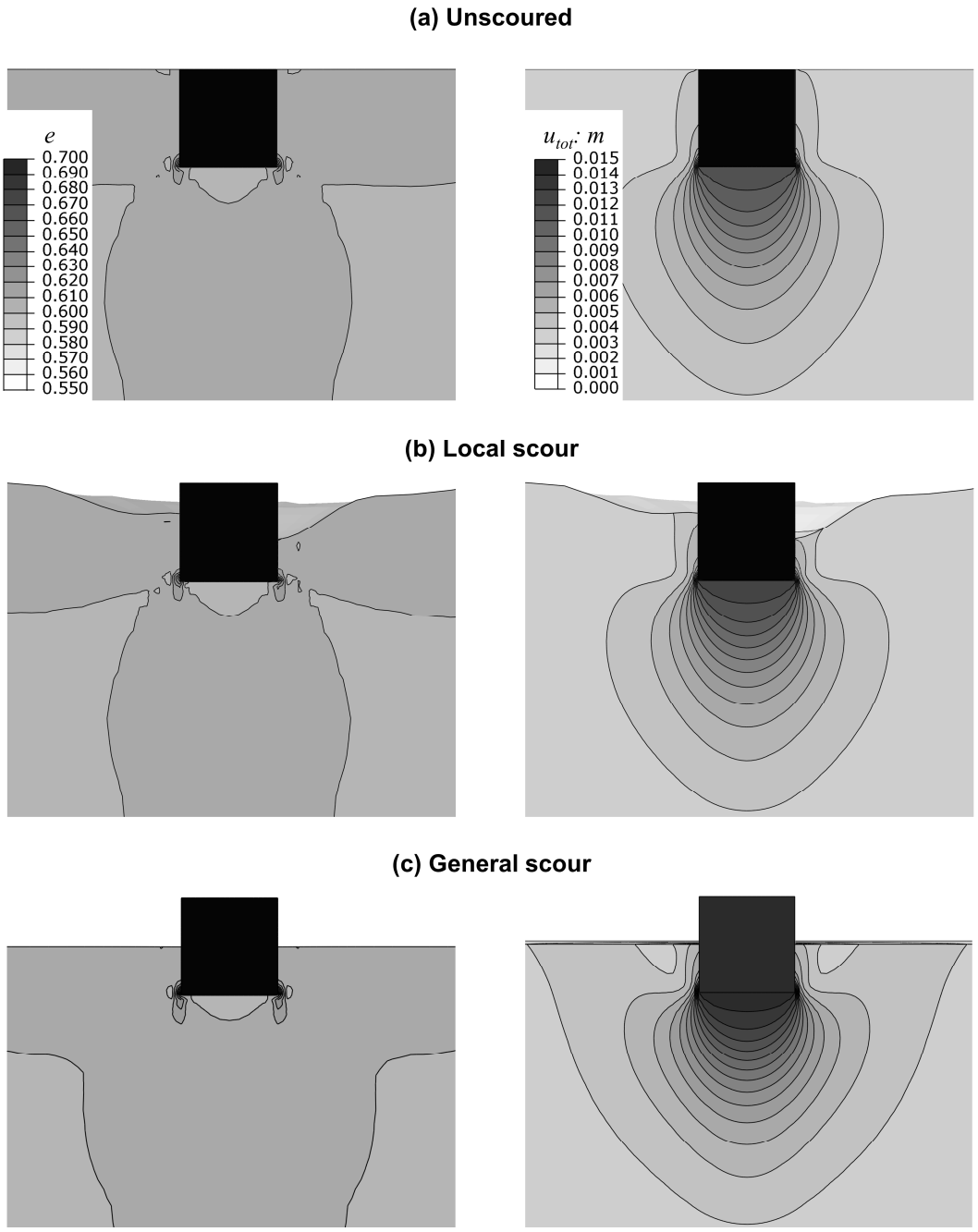

Figure 7.11: Deformed mesh with superimposed void ratio e (left) and total displacement u_{tot} (right) contours obtained at the end of the activation phase of the vertical loads: (a) unscoured foundation; (b) foundation subjected to local scour; (c) foundation subjected to general scour.

7.3.3 Finite element mesh and boundary conditions

The three finite element models developed to study the horizontal behaviour of the foundation are plotted in Figure 7.12. As previously discussed, the models consider just half of the domain, by exploiting the symmetry conditions. Consistently with the vertical simulations, the soil is discretized by using C3D20RP elements, while C3D20R elements are adopted for the foundation.

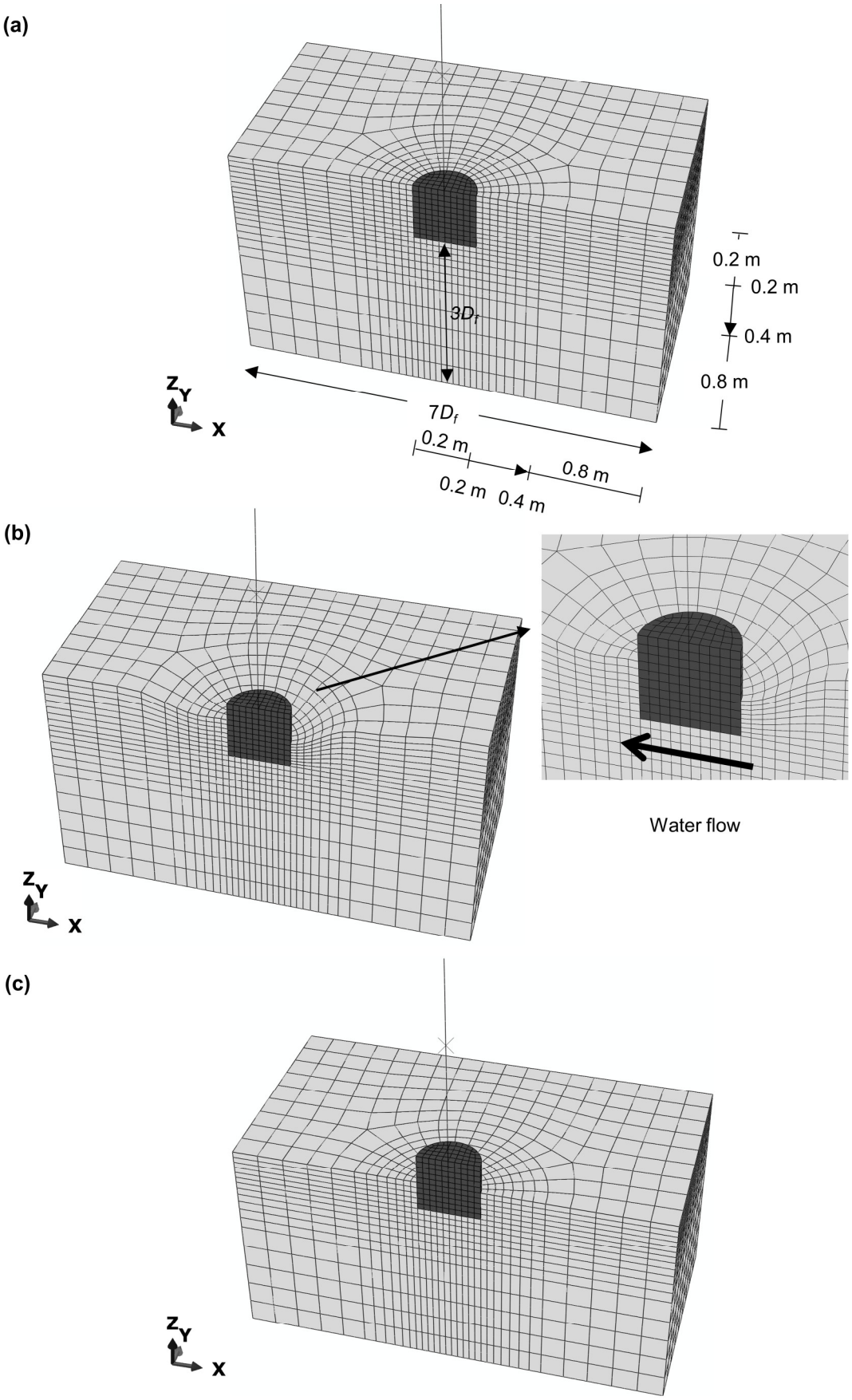

Figure 7.12: Finite element mesh for the horizontal pushover tests: (a) unscoured model; (b) model subjected to local scour; (c) model subjected to general scour.

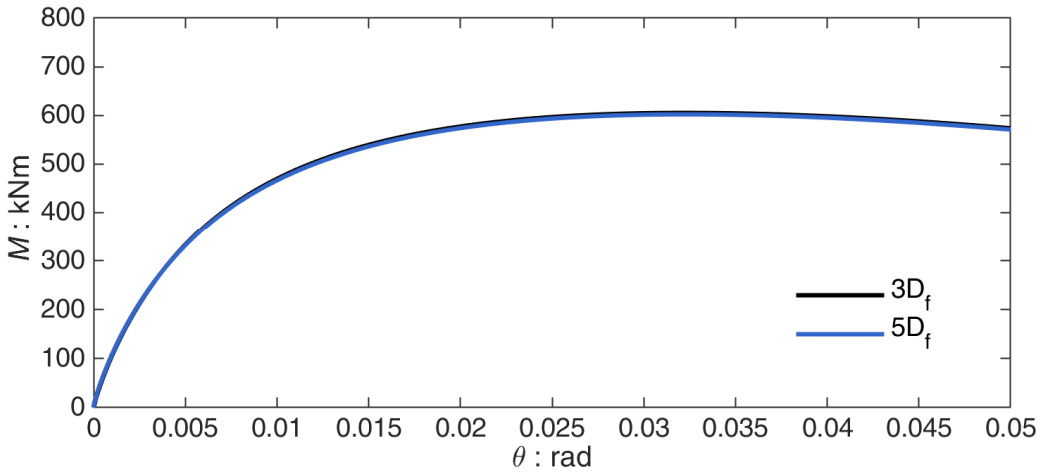

Figure 7.13: Verification of the finite element model size: comparison of $M-\theta$ curves obtained considering a distance between the foundation sides and the lateral boundaries equal to 3 and 5D_f (comparison reported for the unscoured model).

The pier is modelled as a discrete rigid beam by adopting RB3D2 (i.e. 2-node 3-D rigid beam) elements rigidly connected to the top surface of the foundation. The reference point chosen for the pier is the application point of the horizontal load, while the vertical forces representing the deck and pier masses are applied in correspondence with the centres of gravity of the two model parts (Figure 7.9).

Preliminary analyses were carried out in an attempt to reduce the size of the FE discretized field due to the computational costs. In particular, the vertical distance between the base of the caisson and the bottom of the model was kept constant and equal to $3D_f$ (i.e. as for the experimental tests, see Figure 5.12), while the horizontal distance between the sides of the foundation and the lateral boundaries was varied between $10D_f$ and $3D_f$.

Figure 7.13 reports the comparison between the $M-\theta$ curves obtained for the unscoured model, considering a lateral distance of $5D_f$ and $3D_f$. As it can be observed the curves are barely distinguishable, so a minimum distance of $3D_f$ is considered sufficient to avoid boundary effects. The results are consistent with several previous studies (e.g. Gazetas et al., 2013; Zafeirakos and Gerolymos, 2013, 2014, 2016), which suggest that a minimum distance of about three times the characteristic dimension of the foundation is sufficient to avoid any noticeable interaction between the ‘‘pressure bulb’’ and the boundary conditions for pushover analyses.

As regards the finite element mesh, the size of the elements close to the foundation was chosen equal to 20 cm, consistently with the models developed for the vertical simulations. In addition, preliminary analyses showed that the results of the pushover simulations are not substantially influenced by the size of the elements placed at a distance larger than $1D_f$ from the foundation. It was therefore decided to adopt a mesh size varying from 20 cm to 40 cm up to a distance of $1D_f$ from the foundation, and a mesh size of 80 cm outside.

Figure 7.12.a reports the finite element mesh adopted for the unscoured model, with the detail regarding the size of the elements. The mesh consists of about 6,300 C3D20RP soil elements and 480 C3D20R foundation elements. The model used for

the general scour condition is almost equal to the unscoured one where the elements corresponding to the first meter of soil are removed (Figure 7.12.c). It consists of about 5,000 C3D20RP soil elements and 480 C3D20R foundation elements. Figure 7.12.b plots the finite element mesh used to model the problem under local scour conditions. The mesh is obtained through a procedure similar to the one previously discussed for the vertical simulations (see Section 7.2.3) and it consists of about 5,800 C3D20RP soil elements and 480 C3D20R foundation elements.

7.3.4 Results

The results of the numerical simulations are validated in this section against the experimental findings from the centrifuge tests. In the following, reference is made to the rotational response of the pier, in terms of moment-, settlement- and stiffness-rotation curves. For slender structures (as the bridge pier here analyzed), the rocking response is in fact expected to be predominant under lateral loading conditions.

In the comparisons, a correction is applied to the experimental results to consider the effects of the radial gravity field on the second-order moment $\Delta M(\delta)$ due to the dead loads of the deck and the pier. The radial gravity field results in fact in a larger load arm δ' and, in turn, to an increase of $\Delta M(\delta)$ (Figure 7.14). A correction has then to be applied to the experimental results to allow for direct comparison with the numerical simulations. The correction is practically negligible for rotations lower than about 0.02 rad, while it becomes relevant for larger rotations.

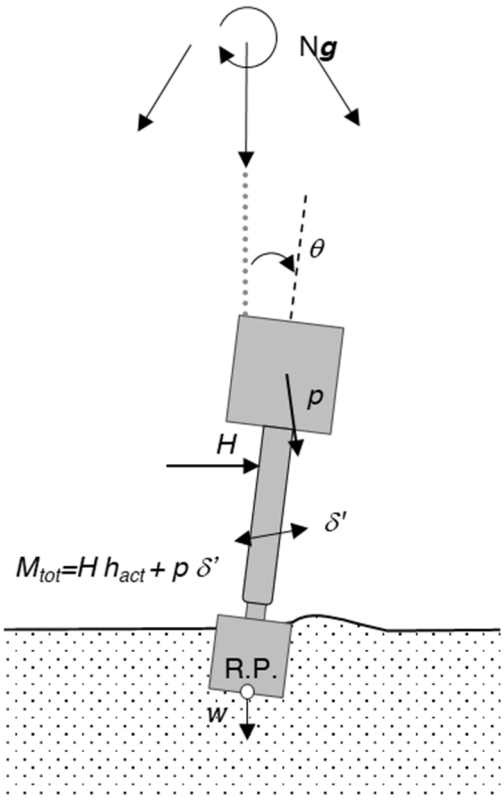

Figure 7.14: Correction for the radial gravity field acting on the deck and pier mass.

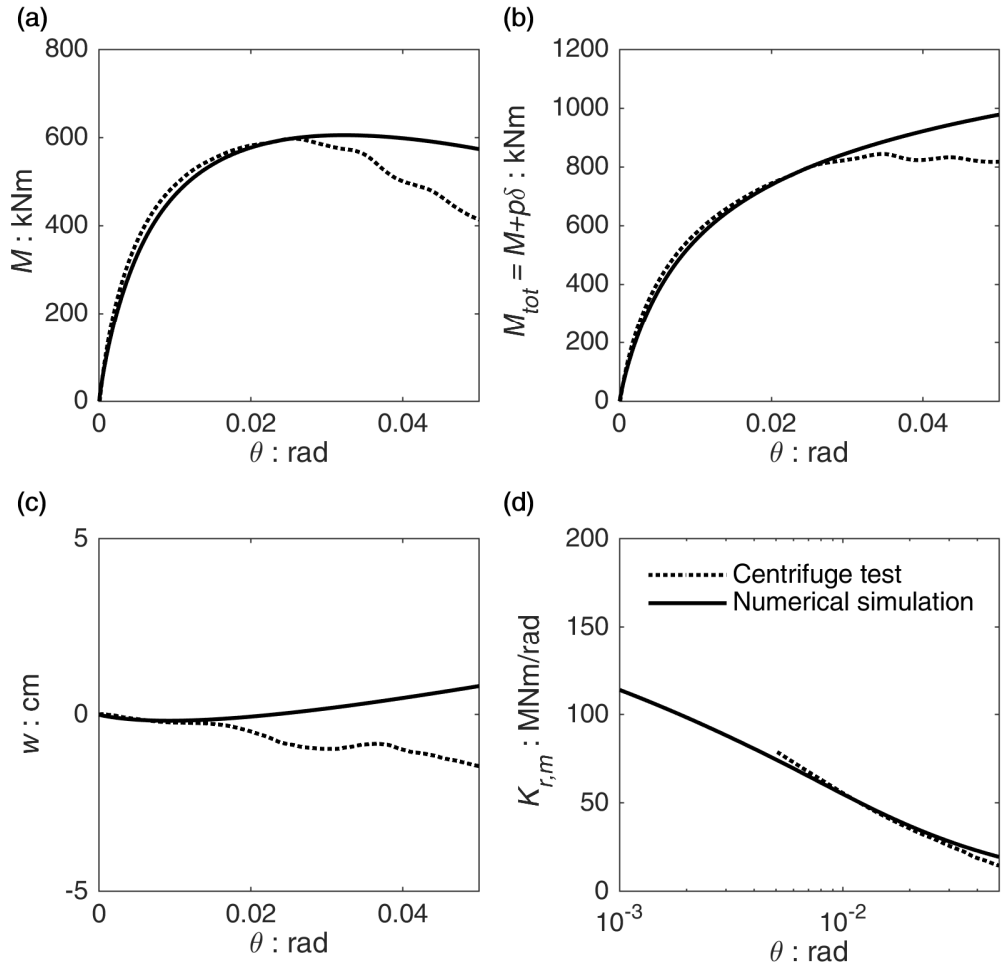

Figure 7.15: Numerical simulations (solid lines) versus centrifuge tests (dotted lines): rocking response of the unscoured caisson foundation in terms of (a) external overturning moment-rotation $M-\theta$ curves, (b) total moment-rotation $M_{tot}-\theta$ curves, (c) settlement-rotation $w-\theta$ curves, and (d) rocking monotonic stiffness-rotation $K_{r,m}-\theta$ curves.

7.3.4.1 Validation against the centrifuge tests

Figure 7.15 reports the comparison between the numerical simulation (solid lines) and the centrifuge test for the "benchmark" (unscoured) condition. By looking at the moment-rotation $M-\theta$ curves (Figure 7.15.a), it is quite evident that the response of the caisson foundation is very well-predicted by the numerical model up to fairly large rotations (i.e. $\theta \approx 0.03\,\text{rad}$). The comparison with the experimental results is satisfying both in terms of moment capacity M_{ult} and evolution of the rocking secant stiffness $K_{r,m}$ with θ (Figure 7.15.d).

For rotations $\theta > 0.03\,\text{rad}$, the experimental $M-\theta$ curve rapidly decreases due to second-order ($P-\delta$) effects. On the other side, the numerical model shows a slower decrease rate. By looking at the total moment (including $P-\delta$ effects) rotation curves $M_{tot}-\theta$, it is quite evident that while in the experimental tests the capacity of the foundation tends to stabilize for rotations larger than 0.03 rad, in the numerical simulations the capacity seems to monotonically increase after yielding without showing a clear plateau. This is thought to be caused by the resisting moment given by the soil along the sides of the foundation. The issue is specifically treated in the next section.

Regarding the settlement-rotation $w-\theta$ curves (Figure 7.15.c), the model seems to slightly overpredict the dilative response of the dense sand. As a consequence of such a dilative tendency, the plasticity-induced settlements are partially compensated, leading to a moderate uplift of the caisson foundation for high rotations (i.e. $\theta > 0.02\,\text{rad}$).

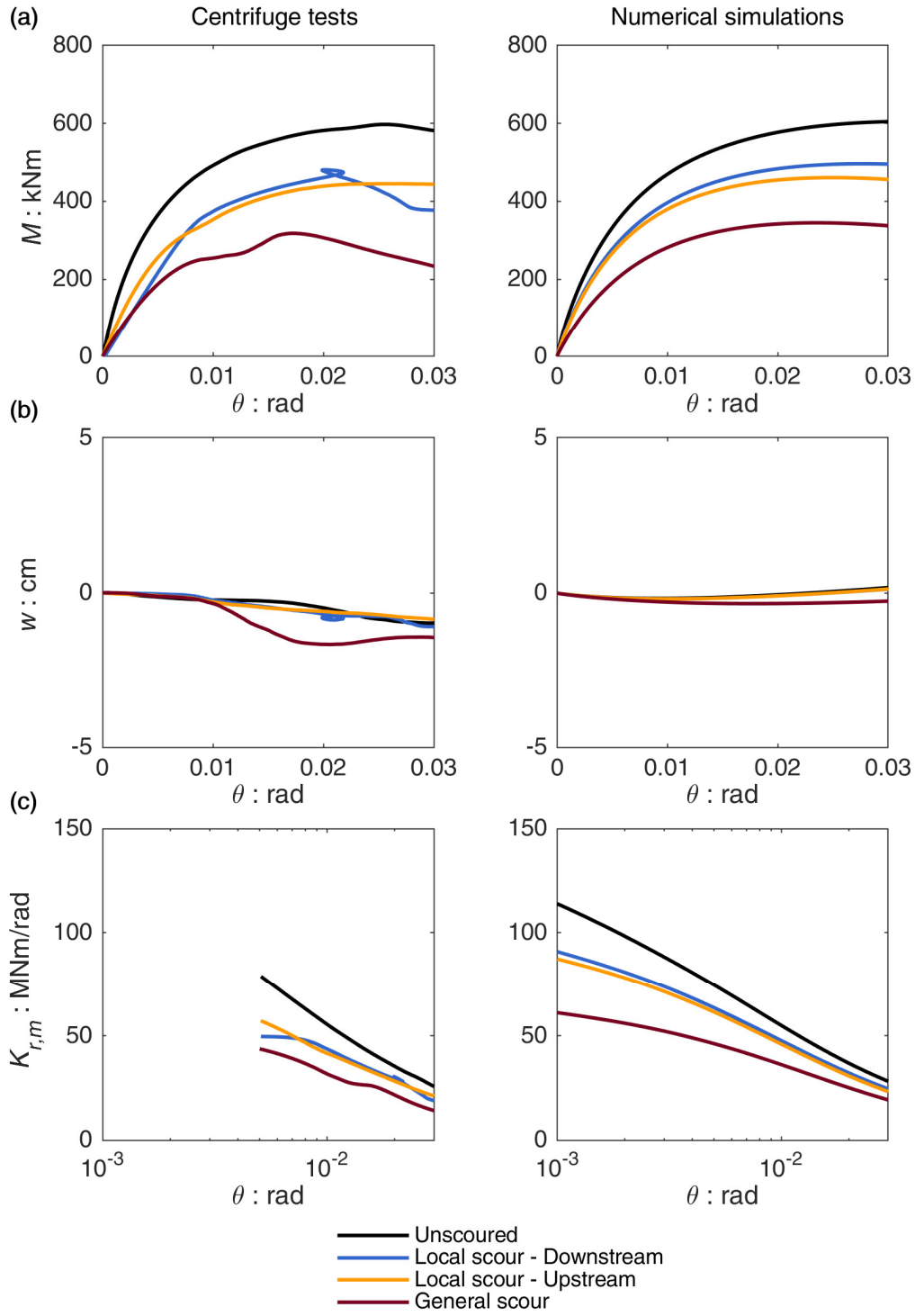

Figure 7.16: Numerical simulations (right pictures) versus centrifuge tests (left pictures): rocking response of the caisson foundation before and after scouring in terms of (a) external overturning moment-rotation $M-\theta$ curves, settlement-rotation $w-\theta$ curves, and (c) rocking monotonic stiffness-rotation $K_{r,m}-\theta$ curves.

However, it should be noted that the overall behaviour showed by the numerical simulations is consistent with the experimental results. Both in the numerical simulations and the centrifuge tests, the response is not dominated by sinking or uplifting. For instance, for a very large rotation $\theta = 0.05\,\text{rad}$, the numerical model predicts an uplift of about -0.8 cm (i.e. $w / D_f = -0.004$), while the model structure shows a settlement of 2 cm (i.e. $w / D_f = 0.0075$). So although it seems from the curves that the differences can be relevant, in practical terms the two models behave quite similarly.

This behaviour has been already observed in previous experimental studies (e.g. Anastasopoulos et al., 2012) and it is reasonable for a moderately loaded structure ($FS_V \approx 5 \div 10$) founded on dense sand, where the effects of the two mechanisms (namely: sand dilation and plasticity-induced settlements) are comparable.

Figure 7.16 reports the comparison between the numerical simulations and the centrifuge tests for the different conditions, namely: unscoured; local scour – upstream; local scour – downstream; general scour. The numerical model seems able to capture the effects of scouring on the $M - \theta$ curves in terms of reduction of the moment capacity of the foundation (Figure 7.16.a). As also observed experimentally, the effects of local scour can be significant, leading to a maximum reduction of the moment capacity of about 25% when the structure is pushed towards the upstream direction. The impact of general scour is even more pronounced, with a reduction of about 43%.

The comparison in terms of $w - \theta$ curves is presented in Figure 7.16.b. Local scour does not affect significantly the bearing capacity of the foundation, as pointed out in Section 7.2. The FS_v in fact slightly reduces from 8 to 7.7. Consequently, also the vertical response of the locally scoured structure during the pushover loading does not differ from the corresponding unscoured one. On the other side, FS_v decreases to 5.6 due to general scour conditions. The plasticity-induced settlements therefore slightly increase. Such an increase is not very relevant for monotonic loading conditions but can explain the pronounced accumulation of permanent settlement under cyclic conditions observed in the experimental tests (see Section 5.3.4).

Finally, Figure 7.16.c reports the comparison in terms of secant rocking stiffness evolution $K_{r,m} - \theta$. The numerical simulations are again consistent with the experimental results. General scour leads to a significant reduction of $K_{r,m}$ for the entire range of rotations. The reduction is less pronounced for local scour, but still significant.

By observing the numerical results, it is interesting to notice that such reduction becomes even more relevant for small rotations. For instance, for $\theta = 0.001\,\text{rad}$ $K_{r,m}$ is equal to about 115 MNm/rad before scouring, while it reduces to 90 and 60 MNm/rad due to local and general scouring, respectively. The result is qualitatively consistent with what has been observed from monitoring data of real scoured bridges (e.g. Foti and Sabia, 2010; Briaud et al., 2011; Kariyawasam et al., 2019). Scouring strongly affects the response of the structure, reducing the stiffness of the foundation system and, in turn, leading to a decrease of the pier natural vibration frequencies. The dynamic parameters of the soil-structure system can therefore be

used to infer the scour depth evolution (e.g. Prendergast and Gavin, 2014; Bao and Liu, 2017; Kariyawasam et al., 2020).

The $M-\theta$ curves are used to define the horizontal pushover capacity of the structures (Figure 7.15.a). It should be noted that, for a given rotation θ, the actual resisting moment is theoretically given by the total moment M_{tot} acting on the foundation, including the second-order effects. However, the capacity of a pier foundation is usually defined as the maximum external load that the structure can withstand before suffering damages which could compromise the safety of the bridge. The moment capacity M_{ult} is therefore defined according to the external moment-rotation $M-\theta$ curves, thus implicitly considering the second-order effects as also adopted by previous studies (e.g. Gazetas and Apostolou, 2004; Gajan et al., 2005; Panagiotidou et al., 2012).

In particular, it is here considered as M_{ult} the external moment necessary to produce a rotation $\theta = 0.02\,\text{rad}$, to allow for direct comparison among the different conditions. Such a fairly large value coincides approximately with the rotation after which the $M-\theta$ curves start to decrease due to $P-\delta$ effects (Figure 7.16).

The M_{ult} obtained from the numerical simulations and the centrifuge tests are reported in Table 7.2. In the table the differences between numerical and experimental results are also quantified as:

$$Diff\,(\%) = \frac{M_{ult}{}^{\text{num}} - M_{ult}{}^{\text{exp}}}{M_{ult}{}^{\text{exp}}} \tag{7.8}$$

being $M_{ult}{}^{\text{num}}$ and $M_{ult}{}^{\text{exp}}$ the ultimate moment capacities as obtained, respectively, from the numerical simulations and the centrifuge tests.

Due to the conventional nature of the definition of M_{ult} and to the presence of the second-order effects, it is not straightforward to compare the results of the monotonic pushovers to the analytical solutions. In addition, the analytical approaches are based on the definition of an "operative" friction angle φ' that is somehow an arbitrary value between the critical state and the peak friction angle (further details can be found in Appendix A). Therefore, no comparisons are here reported.

As already discussed, the M_{ult} unavoidably decreases due to scouring. The effects are more pronounced for the footing subjected to general scouring, but it is still important also for the local scouring condition.

Table 7.2: Results of the numerical simulations of the horizontal pushover tests compared to experimental results.

Condition	Moment capacity (for θ=0.02 rad) M_{ult} : kNm		Difference: %
	Numerical simulations	Centrifuge tests	$\frac{M_{ult}{}^{\text{num}} - M_{ult}{}^{\text{exp}}}{M_{ult}{}^{\text{exp}}}$
Unscoured	577	582	-0.9
Local scour - Downstream	484	461	+4.9
Local scour - Upstream	455	439	+3.6
General scour	342	307	+11.4

The numerical and experimental results are always in good agreement, with a percentage difference ranging from -0.9% for the unscoured case to a maximum value of +11.4% observed for the general scour case. Overall, the comparison between the numerical simulations and the centrifuge tests is very satisfying for a quite large range of rotations ($\theta < 0.03\,\text{rad}$). Most importantly, the effects of both local and general scouring on the behaviour of the foundation are well-predicted.

7.3.4.2 Failure mechanisms

The failure mechanisms of the caisson foundation are shown in Figure 7.17 for the structure before scouring (Figure 7.17.a), after local scouring (structure pushed towards the upstream direction, Figure 7.17.b) and after general scouring (Figure 7.17.c). The results are presented in terms of deformed mesh with superimposed void ratio (left pictures) and total displacement (right pictures) contours for an imposed rotation of 0.02 rad (i.e. equal to about the failure rotation).

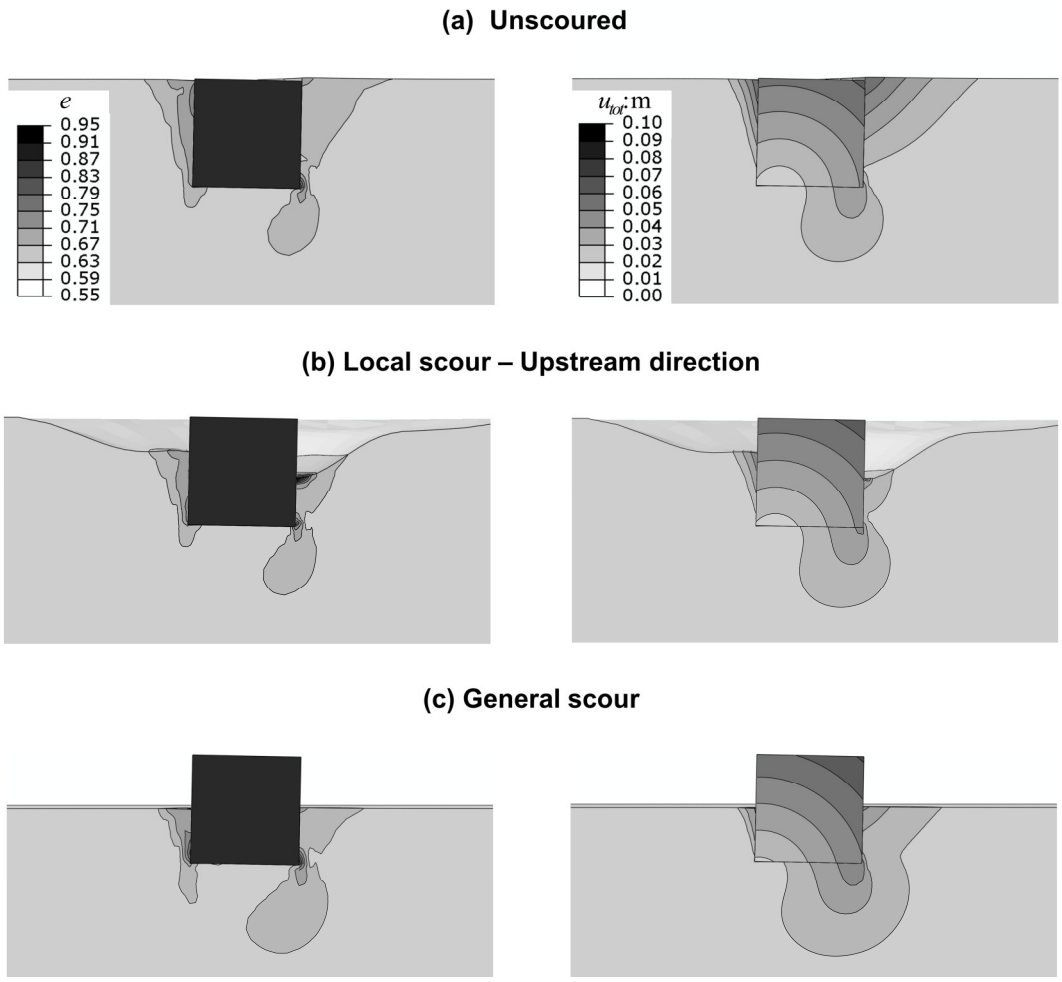

Figure 7.17: Deformed mesh with superimposed void ratio e (left pictures) and total displacement u_{tot} (right pictures) contours for an imposed rotation of 0.02 rad: (a) unscoured foundation; (b) foundation subjected to local scour pushed towards the upstream direction; (c) foundation subjected to general scour.

During a pushover test, the horizontal force and the corresponding overturning moment applied to the structure are always in phase. As the horizontal force increases, the moment applied to the structure increases as well. Moreover, the two loads are also proportional (i.e. the ratio between M and H is constant and equal to the loading arm h_{act}) as long as second-order effects are not predominant. For such a condition, the expected failure mechanism is a *scoop-slide* mechanism (Zafeirakos and Gerolymos, 2016), with one component (i.e. scoop or slide) prevailing to the other according to the length of the loading arm.

This hypothesis is confirmed for all the cases here examined by looking at the u_{tot} contours of Figure 7.17. In particular, the displacement field shows an almost pure rotation of the caisson, revealing that the failure is moving towards a *scoop* mechanism as it would take place for pure moment loading conditions when the motion is rocking-dominated.

The rotation of the caisson leads to the development of two distinct resisting mechanisms: a bearing capacity mechanism takes place below the base of the footing, while an additional resisting moment is given by the soil along the sides. The evolution of the two mechanisms is clearly visible in the void ratio contours reported in Figure 7.17. The soil yielding induced by the bearing capacity mechanism leads to the dilation, and the consequent increase in the void ratio, of the sand below the edge of the footing on the pushing side. This effect is more pronounced for the foundation subjected to general scour, as expected due to the reduction of the pure vertical safety factor FS_v (i.e. from 8 to 5.6). On the other side, active- and passive-like soil wedges develop along the sides of the footing. While the active-like wedge is well visible, it seems that the passive-like is not totally developed.

The resisting moment can be subdivided into two components to quantify the relative importance of the two mechanisms: the moment given by the soil below the base of the footing M_{base} and the moment given by the lateral soil thrusts M_{sides}.

The M_{base} is computed by multiplying the normal nodal contact forces acting at the base of the caisson for the corresponding loading arm (measured concerning the reference point at the middle of the base of the footing). The M_{sides} is then obtained for the difference between the total moment acting on the caisson M_{tot} (including second-order effects) and M_{base}.

The M_{base} and $M_{sides} - \theta$ curves are shown in Figure 7.18. The M_{base} rapidly increases up to a rotation of about 0.02 rad for all the cases examined, then the bearing capacity failure mechanism is almost fully developed and it tends to stabilize. Conversely, the M_{sides} seems to monotonically increase with θ, being responsible for the progressive hardening showed by the $M_{tot} - \theta$ curves (Figure 7.15).

Local scour does not affect significantly the bearing capacity of the caisson foundation. No significant differences are therefore observed between the $M_{base} - \theta$ curves of the structure before and after local scouring (Figure 7.18.a). On the other side, general scour leads to a reduction of FS_v from 8 to 5.6, affecting significantly also the moment bearing capacity. For a rotation of 0.02 rad (highlighted with the circles in the plot), M_{base} decreases from 560 to 480 kNm (i.e. about 14%).

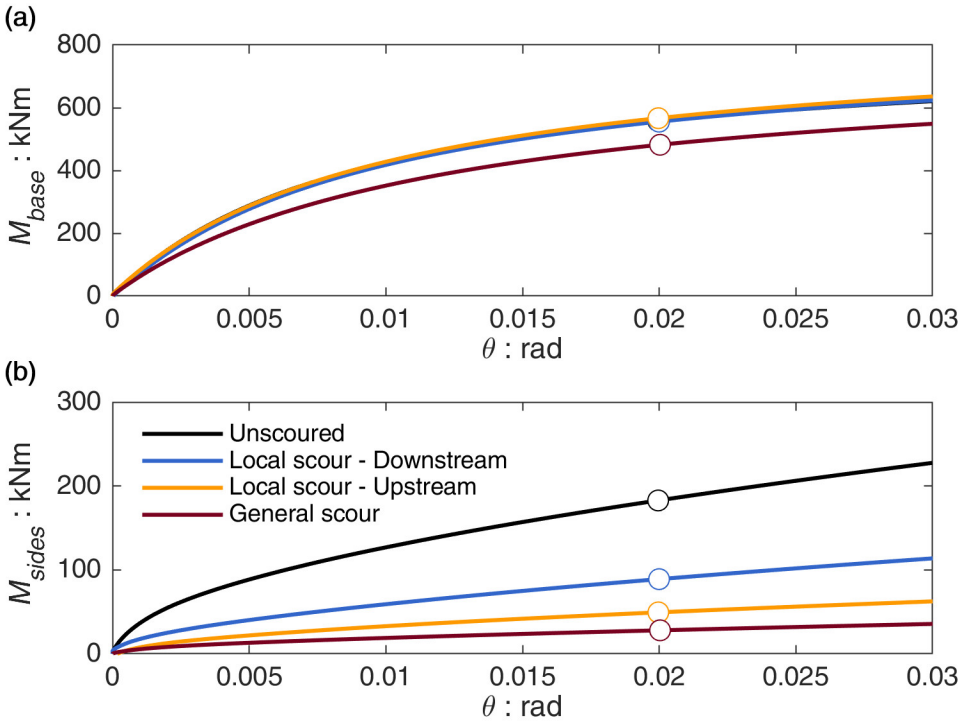

Figure 7.18: Rocking response of the caisson foundation before and after scouring in terms of (a) base resisting moment $M_{base} - \theta$ and (b) sides resisting moment $M_{sides} - \theta$ curves.

The resisting moment at the sides of the foundation is instead affected by both local and general scour (Figure 7.18.b). As expected, the maximum reduction is observed after general scouring with, M_{sides} (for a rotation of 0.02 rad) decreasing from 180 to 30 kNm (i.e. about 83%). Local scour affects M_{sides} to a lesser extent, but the reduction is still dramatic. M_{sides} is equal to 89 kNm when the structure is pushed towards the downstream direction (i.e. where the minimum amount of soil is removed), decreasing to 50 kNm towards the upstream direction. Such a decrease corresponds to a reduction of 51 and 72%.

The horizontal and vertical (σ'_h and σ'_v) stress distributions in the soil elements along the sides of the caisson are shown in Figures 7.19-21. The distributions are presented for increasing rotation to shed light on the evolution of the lateral resisting mechanism. By looking at σ'_h field for the unscoured foundation (Figure 7.19.a), it can be seen that the distribution along the pushing side assumes a parabolic shape, with a maximum approximately at the middle of the caisson decreasing to zero close to the foundation base. Conversely, the soil pressure rapidly decreases to zero along the opposite side.

The observed trends of the soil pressure distributions are consistent with the analytical solutions proposed by Fröhlich (1936) for a rigid caisson rotating around the centre of its base (see Appendix A.2 for further details). However, for increasing rotation, the soil pressure on the pushing side seems to continuously increase, in contrast to Fröhlich's (1936) solution where the maximum soil pressure is limited by the passive earth coefficient of the soil.

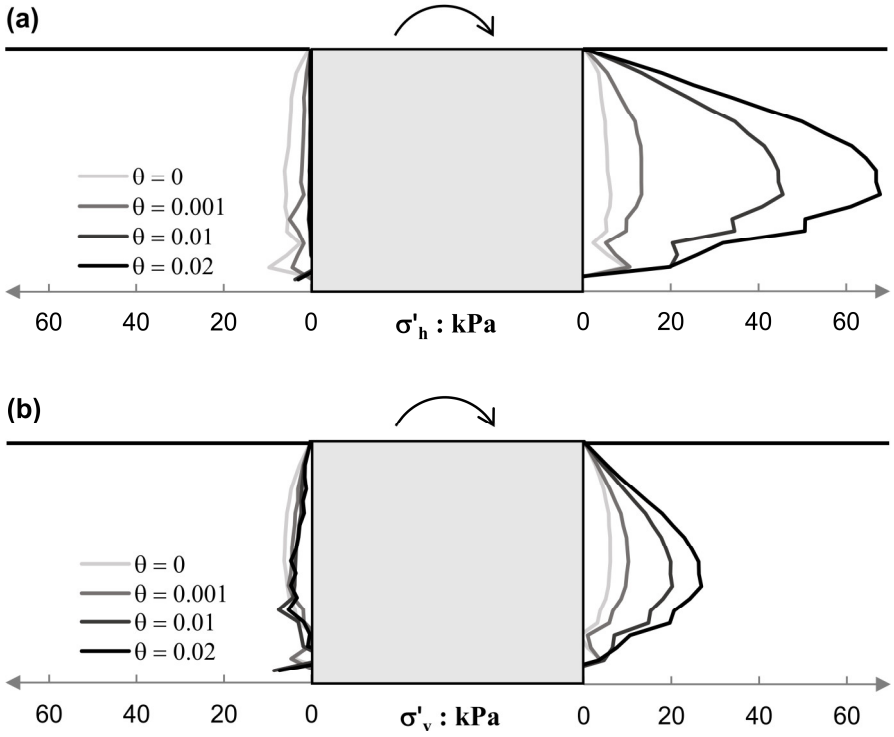

Figure 7.19: Horizontal (a) and the vertical (b) stress distribution in the soil elements along the sides of the unscoured foundation for increasing rotation.

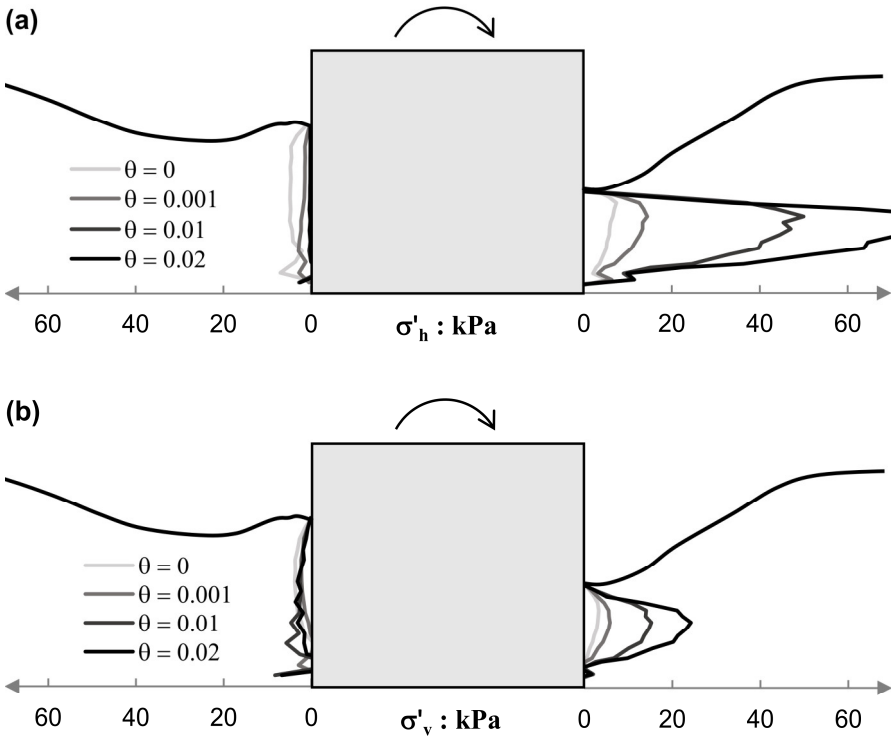

Figure 7.20: Horizontal (a) and the vertical (b) stress distribution in the soil elements along the sides of the foundation subjected to local scour (pushed towards the upstream direction) for increasing rotation.

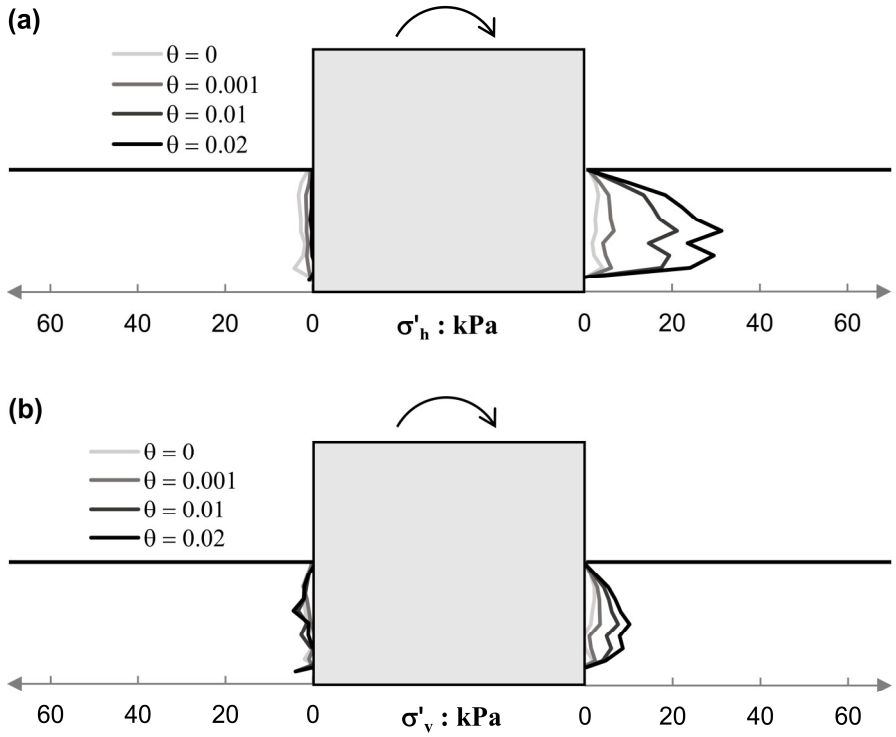

Figure 7.21: Horizontal (a) and the vertical (b) stress distribution in the soil elements along the sides of the foundation subjected to general scour for increasing rotation.

This difference can be explained by observing the σ'_v distributions (Figure 7.19.b). As the caisson rotation increases, the lateral surface of the caisson is no longer vertical. The contact pressure, which was initially perfectly horizontal, begins then to tilt, increasing with its vertical component the σ'_v distribution along the lateral surface of the caisson. As a consequence, the σ'_h distribution increases as well. Such a second-order effect, caused by the geometric nonlinearity of the problem, is obviously not considered by Fröhlich's (1936) solution which is valid for the small-strain field. Nevertheless, it can be relevant for large rotations (i.e. the rotations necessary to fully mobilize the passive earth resistance).

Similar trends can be observed for the foundations subjected to local and general scour (Figure 7.20 and Figure 7.21). Under both conditions, the soil erosion along the sides of the caisson leads to a substantial decrease of the soil pressure distribution (Figure 7.20.a and Figure 7.21.a) and, consequently, of M_{sides} (Figure 7.18.b).

However, some differences can be observed between the two situations. The σ'_v distribution rises with θ at a larger rate for the caisson subjected to local scour rather than the one subjected to general scour (Figure 7.20.b and Figure 7.21.b). The latter is due to the presence of the soil slopes of the scour hole. This explains the differences between the $M_{sides} - \theta$ curves obtained for the two conditions (Figure 7.18.b).

7.4 Slow-cyclic lateral loading

The effects of scouring on the cyclic response of the caisson foundation are analyzed by simulating the results of slow-cyclic (quasi-static) lateral pushover tests. The observed behaviour under slow-cyclic loadings can be considered representative of the seismic performance of the structure (Gajan and Kutter, 2008; Anastasopoulos et al., 2012).

The simulations are performed on the models previously introduced to simulate the response of the pier under lateral pushover loading for the three situations, namely: unscoured, local scour, general scour. For further details regards the numerical models reference can be made to Sections 7.3.1-7.3.3. It should be noted that just one simulation is necessary to investigate the cyclic response of the foundation after local scouring, given that the structure is loaded towards both directions (i.e. upstream and downstream).

7.4.1 Displacement protocols

The displacement protocol applied in the centrifuge tests consisted of 8 sets, each one containing 10 quasi-static loading cycles of increasing displacement amplitude (see also Figure 5.20). Therefore 80 cycles were in total applied to the structure, allowing to investigate the performance of the caisson under multiple loading cycles (of the same amplitude) for a wide range of rotations.

Such a displacement protocol however is not suitable for the numerical simulations. When the structure is loaded for a large number of cycles at relatively high rotations (i.e. close to the rotation corresponding at the moment capacity M_{ult}) a bearing capacity mechanism is mobilized and the caisson accumulates considerable settlements, as also observed in the experimental tests. The soil below and along the sides of the caisson is in fact subjected to very severe loading conditions. Preliminary analyses showed that, for this type of loading protocol, the soil starts to accumulate plastic strains in the order of magnitude of 100%, leading to convergency issues that prevent the possibility of accurate simulations of the problem.

In the light of these limitations, it was therefore decided to apply to the structure two different loading protocols for the numerical simulations. The first one is conceived to study the response of the structure under multiple loading cycles (Figure 7.22). It consists of 10 cycles with a constant displacement amplitude of 2.5 cm (i.e. the same amplitude applied in the 1st set of 10 cycles in the experimental tests). The second loading sequence consists of 9 loading cycles with increasing displacements to investigate the performance of the foundation from very small-to-large rotations (Figure 7.23). In particular, the displacement amplitudes are chosen such that the corresponding rotation amplitudes θ_c cover a range between 0.0001 and 0.01 rad with 9 almost equally spaced points in a logarithmic scale. The resulting rotation amplitudes are presented in Figure 7.23.c.

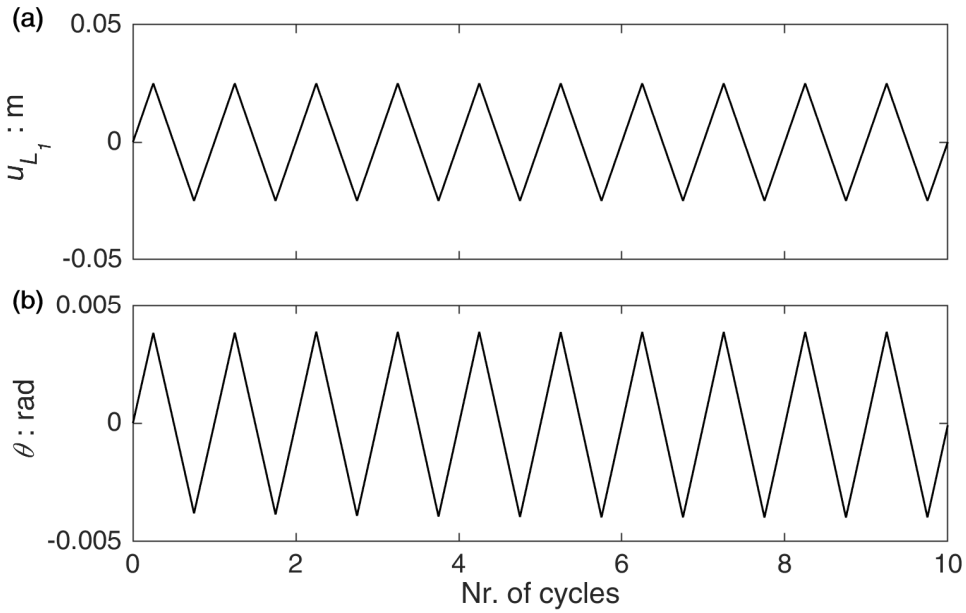

Figure 7.22: Displacement protocol (a) used to assess the performance of the foundation for multiple loading cycles and the corresponding cyclic rotations (b).

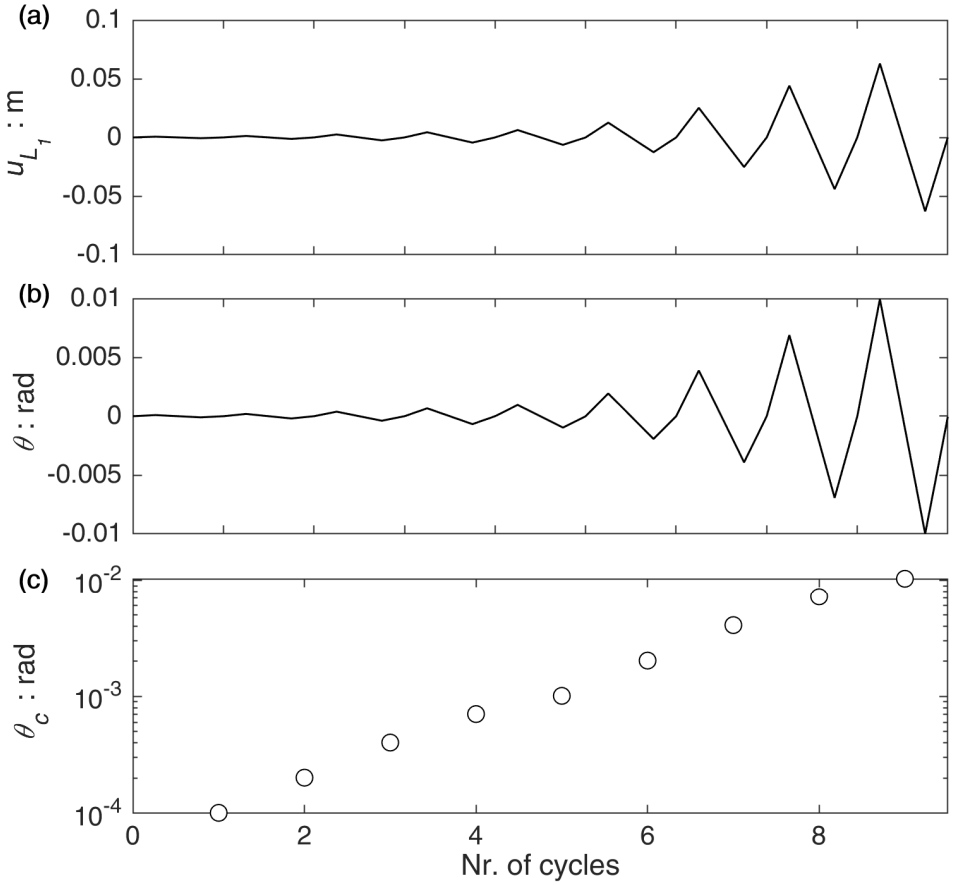

Figure 7.23: Displacement protocol (a) used to assess the performance of the foundation for increasing rotations and the corresponding cyclic rotations (b) and amplitudes (c).

7.4.2 Performance for multiple loading cycles

The results of the simulations performed to investigate the effects of multiple quasi-static loading cycles are presented in Figure 7.24 in terms of moment-rotation $M-\theta$ and settlement-rotation $w-\theta$ response. The monotonic responses (red lines) are also included for comparison. The unscoured foundation (Figure 7.24.a) exhibits the highest moment capacity, followed by the caisson subjected to local (Figure 7.24.b) and general scour (Figure 7.24.c).

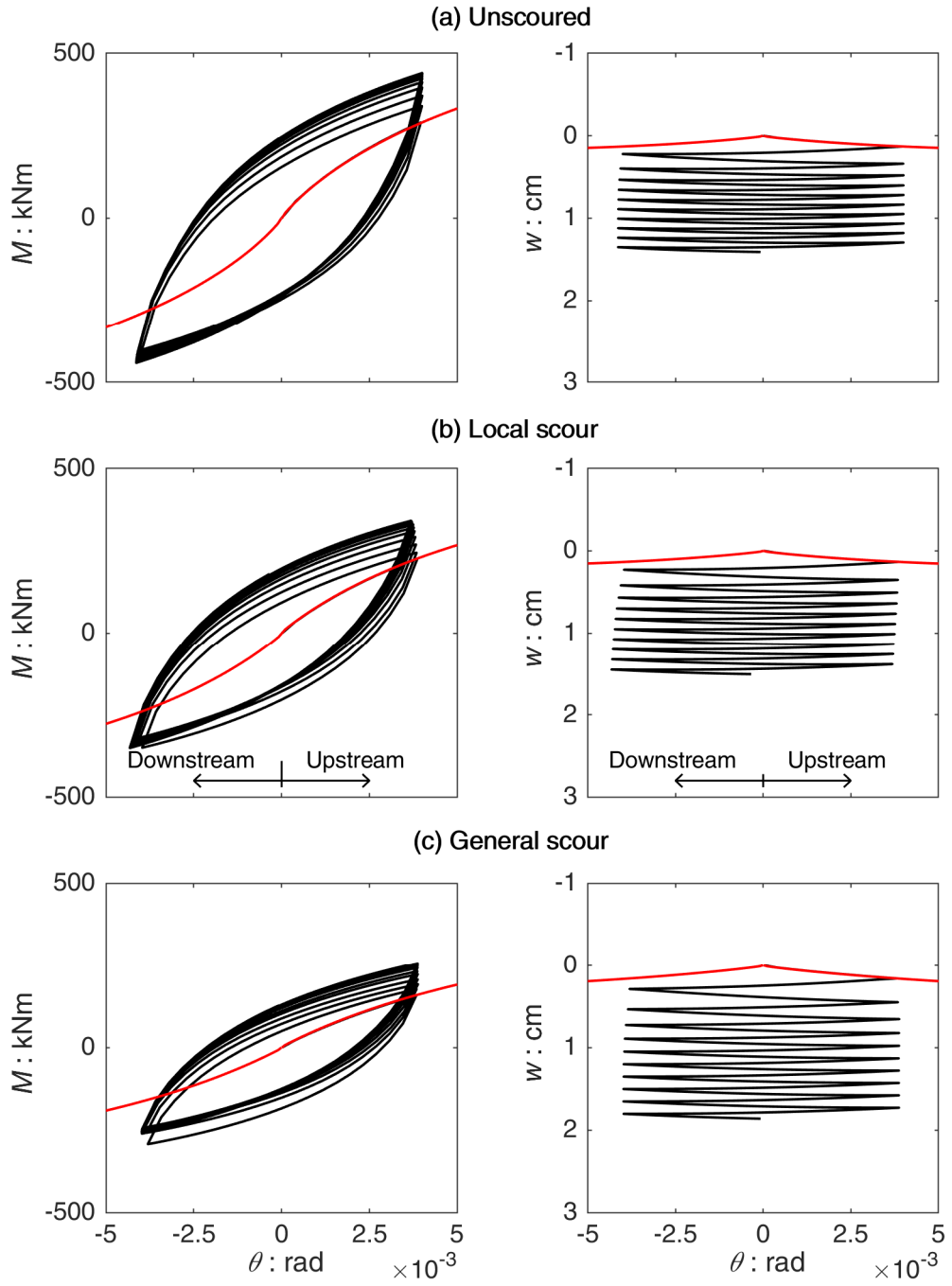

Figure 7.24: Slow-cyclic moment-rotation $M-\theta$ and settlement-rotation $w-\theta$ response for multiple loading cycles: (a) unscoured conditions; (b) local scour; and (c) general scour.

This is consistent with the monotonic responses obtained from the numerical simulations as well as the experimentally measured cyclic responses. Similarly, the amount of settlement accumulated by the caisson subjected to general scour (Figure 7.24.c) is significantly larger than the one obtained for the unscoured and the local scour condition (Figure 7.24.a-b).

The cyclic responses show a clear *overstrength* when compared to the monotonic backbone curves, as also experimentally observed in previous studies (e.g. Kokkali et al., 2015). Under fully drained conditions, the application of multiple loading cycles leads to progressive hardening of the soil and, consequently, an increase of the secant foundation stiffness. With increasing loading cycles, however, the soil tends to a steady-state and the volumetric strain accumulation, as well as the secant stiffness evolution, begins to level off. Such behaviour, usually termed as *elastic shakedown*, is responsible for the progressive increase in the foundation stiffness with multiple loading cycles and it is characteristic for sands (Zhu et al., 2013; Cox et al., 2014; Kokkali et al., 2015; Tasiopoulou et al., 2021).

The progressive hardening of the foundation response is presented in Figure 7.25 in terms of cyclic rocking stiffness $K_{r,c}$ (Figure 7.25.a), hysteretic damping ratio $\xi_{r,h}$ (Figure 7.25.b), and settlement per cycle w_c (Figure 7.25.c). The figures on the left depict the results of the centrifuge tests (for the 1st package of 10 cycles), while the results of the numerical simulations are plotted on the right. It should be noted that both $K_{r,c}$ and $\xi_{r,h}$ are computed referring to the $M+\Delta M\left(\delta\right)-\theta$ loops, consistently with the procedure adopted for the experimental tests (see Section 5.3.5).

For all the cases, the cyclic rocking stiffness $K_{r,c}$ progressively increases from its monotonic value with increasing loading cycles due to sand densification effects (Figure 7.25.a). Such a progressive hardening is more pronounced during the first cycles, while it tends to stabilize for the subsequent cycles. The downside is the accumulation of settlements due to sand densification and plasticization below the footing (Figure 7.25.c). Again for increasing cycles, the response tends to level off and w_c decreases due to the decreasing rate of volumetric strain accumulation.

The trends previously described can be identified in the results of both the numerical simulations and the centrifuge tests. However, some differences are observed, especially when comparing the evolution of the numerical and experimental $K_{r,c}$. The hardening rate of $K_{r,c}$ predicted by the numerical model rapidly decreases after the first 4 loading cycles, while in the centrifuge tests a more pronounced increase is observed, leading to substantially higher values of $K_{r,c}$.

To better explain these differences further clarifications are required regards the nature of the cyclic behaviour of the foundation. The progressive hardening shown by cyclically loaded foundations under drained conditions is usually attributed, quite generally, to *sand densification effects* (e.g. Cox et al., 2014; Kokkali et al., 2015; Tasiopoulou et al., 2021). More specifically, it is possible to identify two complementary phenomena contributing to the hardening of the foundation response. During the initial loading phase, the dilation tendency of the sand below the footing induces a geometrical rearrangement of the sand particle orientation

distribution (Nemat-Nasser, 1980; Nemat-Nasser and Tobita, 1982). Such *fabric* changes keep going on in the same sense until the foundation is monotonically loaded. However, when the loading reversal takes place, the sand particles, previously biased toward dilation, starts to be biased toward contraction. This phenomenon, as observed by Dafalias and Manzari (2004), enhances the contractive part following the loading reversal, inducing a "net" contractive effect and, in turn, a reduction of the void ratio. As a consequence, the foundation tends to accumulate, cycle upon cycle, permanent settlements.

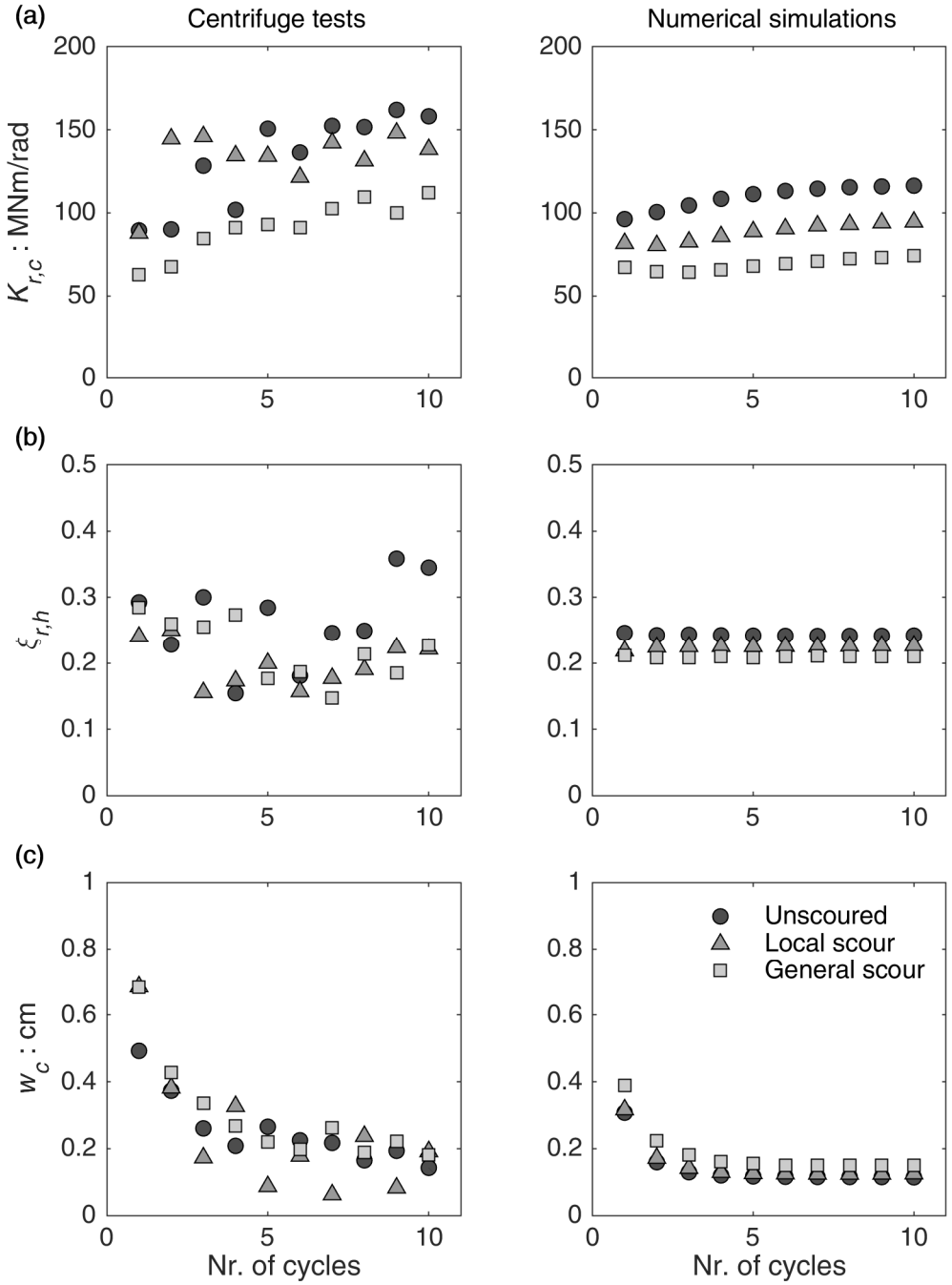

Figure 7.25: Numerical simulations (right pictures) versus centrifuge tests (left pictures, 1st package of 10 cycles): slow-cyclic response of the foundation before and after scouring for multiple loading cycles in terms of (a) cyclic rocking stiffness $K_{r,c}$, (b) hysteretic damping ratio $\xi_{r,h}$, and (c) settlement per cycle w_c.

The progressive hardening of the foundation response is therefore a consequence of both the actual sand densification (in terms of reduction of the void ratio) and the changes induced in the soil fabric. The soil constitutive model, as in the version adopted in this study, is only able to partially capture the hardening of the foundation response (basically the part induced by the void ratio reduction), as it lacks sufficient "memory" to reproduce the fabric effects. As previously discussed, the sand response in a given loading direction is strongly dependent on the number of loading cycles previously applied. As a consequence, to properly capture the sand fabric evolution it is necessary to "track" the modifications induced by multiple loading cycles applied in that specific direction. To this end, recent studies proposed to adopt an additional surface, termed as *memory surface*, to reproduce the effects of the fabric evolution (Corti et al., 2016; Liu et al., 2018).

A different approach was adopted by Tasiopoulou et al. (2021). The Authors proposed a modified version of the Ta-Ger model (Tasiopoulou and Gerolymos, 2016b, a) which can capture the stiffness evolution for a large number of cycles under drained, undrained and partially drained conditions. In their constitutive model, the hardening parameter (defining the degree of coupling between the elastic and plastic strains) evolves with the cumulative deviatoric shear strain increment, which contains the information regarding the loading history of the soil in that direction. Under fully drained conditions, the hardening parameter increases continuously up to a peak value, reproducing the experimentally observed hardening of the soil.

The abovementioned soil behaviour is very relevant when a large number of loading cycles of almost constant amplitude is applied to the structure. This is for example the case of foundations used to support offshore wind turbines, which are subjected to significant wind/wave loading (Zhu et al., 2013; Cox et al., 2014; Tasiopoulou et al., 2021). Tasiopoulou et al. (2021) for example successfully adopted the modified version of the Ta-Ger model to capture the experimental response of a single bucket foundation subjected to several loading cycles. However, when dealing with problems that mainly involve a small number of loading cycles of different amplitudes (for instance in the case of bridge foundations subjected to seismic loadings) the progressive hardening becomes less relevant.

As the hysteretic rocking damping ratio $\xi_{r,h}$ is regarded, it is difficult to identify clear trends in the experimental results due to the uncertainties in the definition of the hysteresis loops at small rotations. However, the comparison with the results of the centrifuge tests is quite satisfying in terms of average measured values (Figure 7.26.b). In the numerical simulations, the $\xi_{r,h}$ does not vary with the number of loading cycles. The $\xi_{r,h}$ seems instead to slightly decrease due to scouring. Specifically, it decreases from 0.25 to 0.23 due to local scouring, reducing down to 0.21 for the general scour condition. The reduced amount of soil in contact with the footing dissipate a smaller amount of energy, affecting the behaviour of the whole pier.

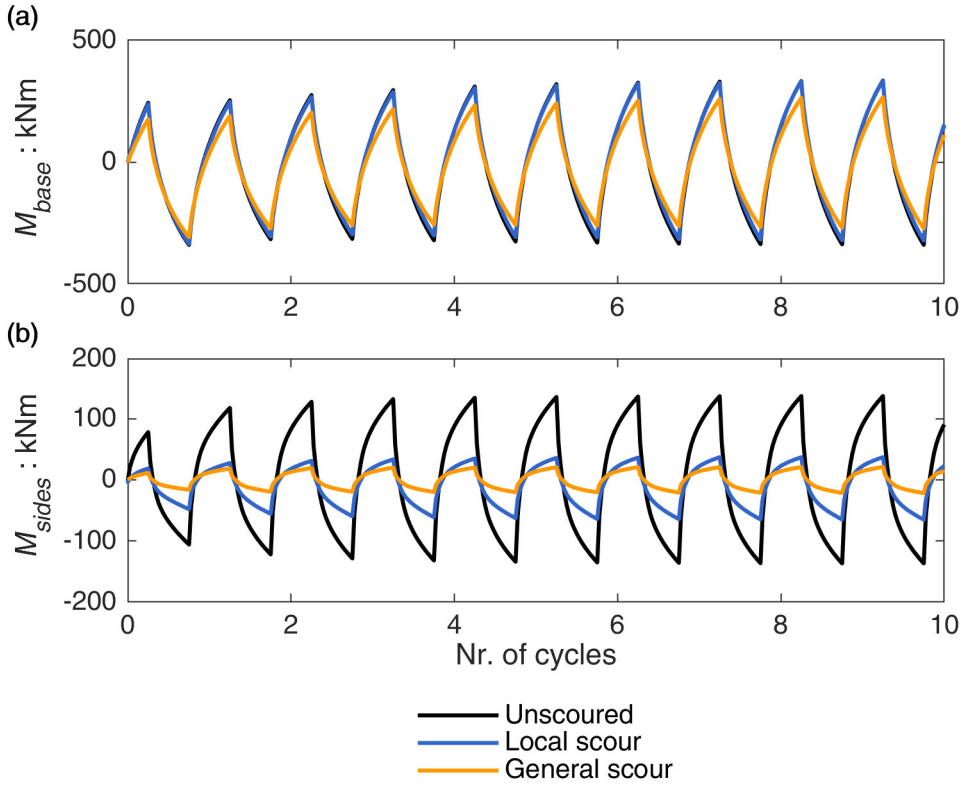

Figure 7.26: Slow-cyclic response of the foundation before and after scouring for multiple loading cycles in terms of (a) base resisting moment M_{base} and (b) sides resisting moment M_{sides}.

Figure 7.26 reports the cyclic response of the foundation in terms of base resisting moment-rotation ($M_{base}-\theta$) curves (Figure 7.26.a) and sides resisting moment-rotation ($M_{sides}-\theta$) curves (Figure 7.26.b). The effects of multiple loading cycles are visible on both the M_{base} and M_{sides} curves. However, while the resistance of the soil below the caisson seems to progressively increase for all the loading cycles applied to the structure (albeit its rate progressively decreases), the M_{sides} increases mainly in the first two loading cycles and then settles down. The increase of M_{sides} is mainly attributed to the reversal of the loading conditions applied to the soil along the sides of the foundation, while the sand densification takes place only below the footing.

As already observed for the monotonic responses, local scour does not affect the bearing capacity of the footing, so the $M_{base}-\theta$ curve is almost equivalent to the one obtained for the unscoured foundation. Conversely, general scour leads to a decrease of the FS_v from 8 to 5.6, affecting in turn also the $M_{base}-\theta$ response of the foundation (Figure 7.26.a). On the other side, both local and general scour have a strong impact on the $M_{sides}-\theta$ response (Figure 7.26.b). Interestingly, the geometric asymmetry of the local scour hole produces a strong asymmetric response of the foundation in terms of $M_{sides}-\theta$ curves. The maximum M_{sides} observed when the foundation is loaded towards the upstream direction (positive M_{sides} values in the plot) is quite close to the one observed for the general scour condition. Conversely, it is substantially larger in the other direction where the amount of soil eroded is minimized.

This difference however is not very relevant in the $M-\theta$ loops, where the two components are summed up. For instance, at the 10th cycle, the M_{sides} amplitudes are equal to 40 and 65 kNm, respectively towards the upstream and downstream direction. The total moment amplitude however is about 400 kNm. This explains why the experimental (and the numerical) $M-\theta$ loops do not show significant asymmetries (see also Figure 5.21).

7.4.3 Performance for increasing rotation amplitudes

The sand response is known to be highly nonlinear with increasing strain amplitude. It is then crucial the explore the effects of scouring on the performance of the pier for a wide range of rotation amplitudes θ_c. The second displacement loading protocol applied to the structure (Figure 7.23) allows for studying its response for rotations ranging from 0.0001 to 0.01 rad. The results are presented in Figure 7.27 in terms of moment-rotation $M-\theta$ and settlement-rotation $w-\theta$ response.

The monotonic curves (red lines) are again included for comparison. It should be noted that it is not possible to directly compare the results of the simulations with the centrifuge tests due to the differences between the experimental and the numerical loading protocol. Nevertheless, the overall behaviour of the foundation can be analyzed to validate, at least qualitatively, the evolution of the response as predicted by the numerical model.

The effects of local and general scour on the $M-\theta$ loops are relevant for the entire range of rotations. The moment capacity of the unscoured foundation is always substantially larger than the one observed under general and local scour. For all the conditions examined, the $M-\theta$ loops present again an overstrength when compared to the monotonic backbone curves. The overstrength is however less significant than for the case of the caisson subjected to multiple loading cycles (Figure 7.24). For this loading protocol, the hardening mechanism is less relevant, and the cyclic overstrength is mainly due to the loading reversal (and, thus, to the different stress path with respect to the monotonic pushovers).

The $w-\theta$ responses are quite similar for small rotation amplitudes. For larger rotations, the foundation exhibits quite similar behaviour before and after local scouring. Conversely, after local scouring, the foundation accumulates substantially larger permanent settlements.

Figure 7.28 reports the evolution of the cyclic response with increasing θ_c in terms of cyclic rocking stiffness $K_{r,c}$ (Figure 7.28.a), hysteretic damping ratio $\xi_{r,h}$ (Figure 7.28.b), and permanent settlement per cycle w_c (Figure 7.28.c). The trends observed for the $K_{r,c}$ curves are consistent with the ones shown by the experimental tests (Figure 5.24). The $K_{r,c}$ rapidly decreases for θ_c ranging from 0.0001 to 0.001 rad due to soil nonlinearity. For larger rotations, the foundation approaches its moment capacity and the rate of decrease tends to level off. The effects of scouring are significant in the entire range of rotations, consistently with what was observed in the monotonic tests.

As expected, the hysteretic damping ratio $\xi_{r,h}$ increases with increasing θ_c (Figure 7.28.b). Such an increase is more relevant for the unscoured foundation, leading to a $\xi_{r,h}$ of 0.3 for $\theta_c = 0.01\,\text{rad}$, while slightly lower values can be attained after local and general scouring. The soil erosion reduces the amount of energy dissipated (as also observed for multiple loading cycles) and the reduction is more significant with increasing rotation amplitudes.

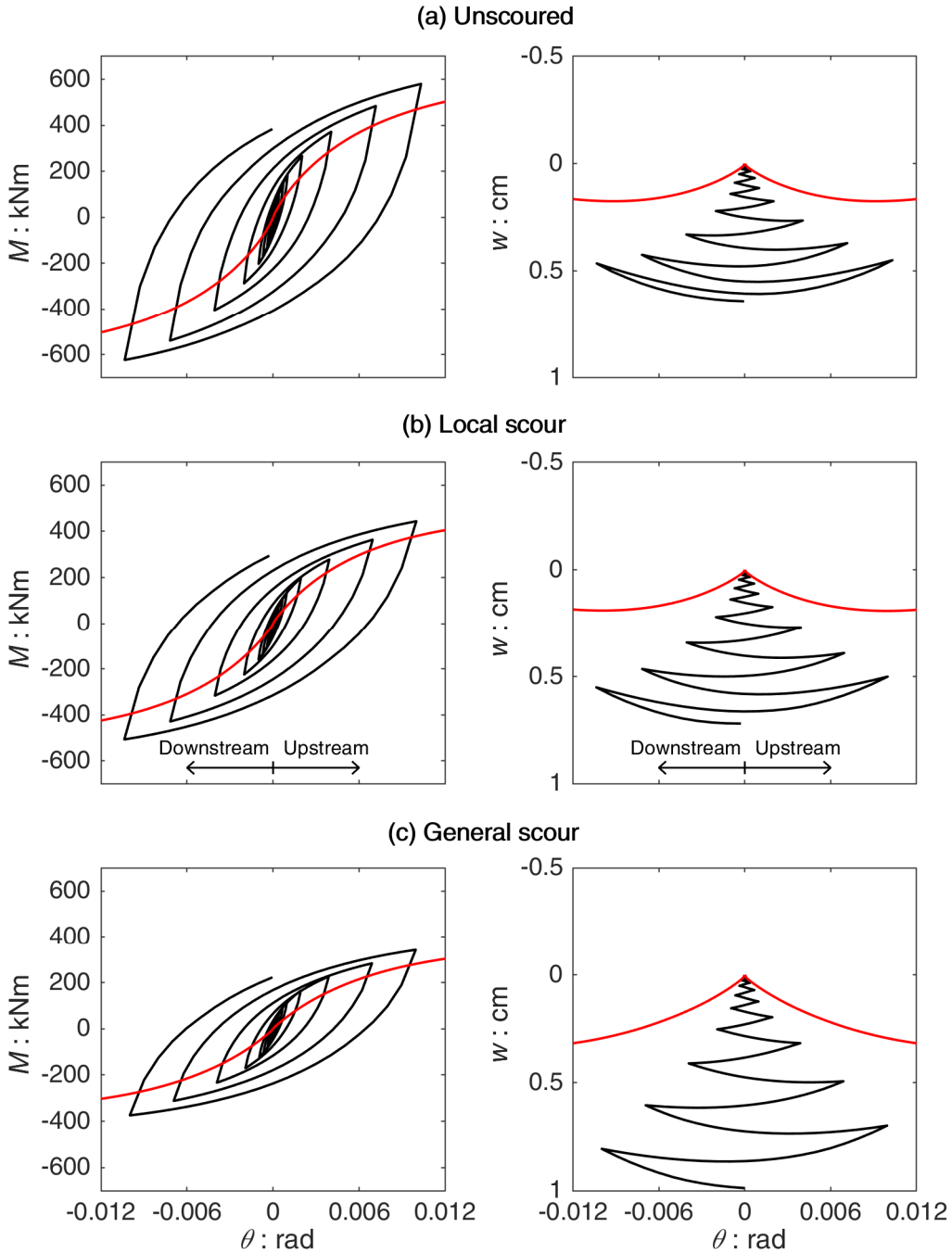

Figure 7.27: Slow-cyclic moment-rotation $M-\theta$ and settlement-rotation $w-\theta$ response for increasing rotation amplitudes: (a) unscoured conditions; (b) local scour; and (c) general scour.

Finally, the amount of settlement accumulated within each cycle w_c is presented in Figure 7.28.c. The w_c increases with θ_c for all the cases examined up to a rotation amplitude of about 0.008 rad. For larger amplitudes, the dilatant tendency of the soil starts to become predominant and w_c slightly decreases for both the unscoured and the locally scoured foundation. This is not the case of the foundation subjected to general scour, for which the plasticity-induced settlements are still predominant due to the reduction of its bearing capacity and, in turn, of its FS_v. The same general trends were observed also in the results of the experimental tests (see Figure 5.22) and explain the significant differences between the two cases in terms of permanent settlement accumulation.

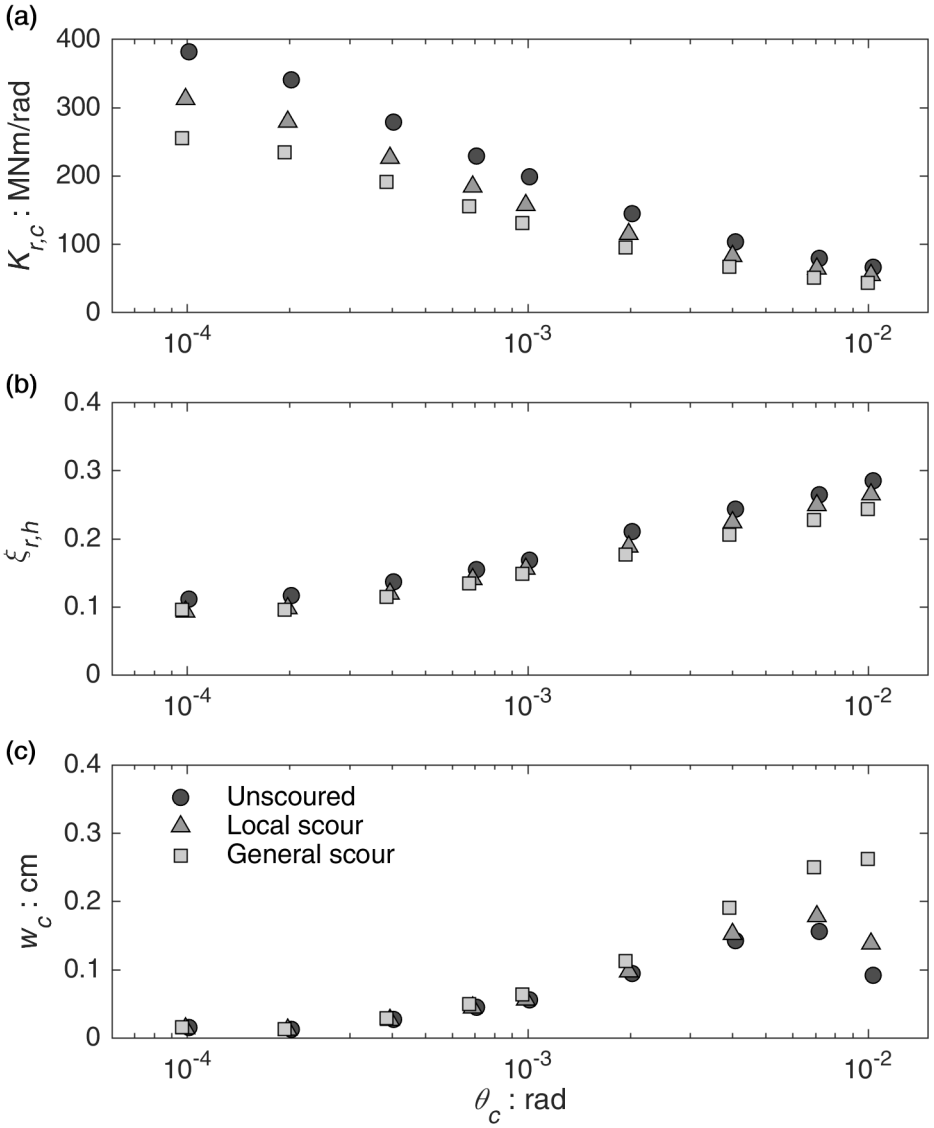

Figure 7.28: Slow-cyclic response of the foundation before and after scouring for increasing rotation amplitudes in terms of (a) cyclic rocking stiffness $K_{r,c}$, (b) hysteretic damping ratio $\xi_{r,h}$, and (c) settlement per cycle w_c.

7.5 Discussion

In this chapter, the results of the simulations carried out to validate the numerical model developed to study the performance of the foundation were reported. The model was developed based on the features of the prototype problem studied through the experimental tests reported in Chapter 5. The Severn-Trent sand model was employed to simulate the sand behaviour, by adopting the constitutive parameters calibrated independently on the results of soil element tests (see also Chapter 6).

The vertical response of the foundation before and after local scouring is consistent with the one observed in the centrifuge tests in terms of both vertical stiffness and pure vertical bearing capacity. Local scour does not significantly affect the bearing capacity of the caisson. The simulation performed after general scour revealed instead its strong impact on the vertical response of the foundation.

Such a reduction leads to a decrease of the vertical safety factor FS_v achieved in the monotonic pushover tests from 8 to 5.6, explaining the differences observed in the horizontal performance of the structure between the general and the local scour condition. While local scour mainly affects the resisting moments given by the soil at the sides of the footing M_{sides}, general scour reduces also the resistance exerted by the bearing capacity mechanism M_{base}. As a consequence, it affects also the amount of settlement accumulated by the foundation.

Similar conclusions can be drawn by looking at the cyclic performance of the structure. Local scour mainly affects the M_{sides}, reducing just partially the cyclic rocking stiffness $K_{r,c}$ of the foundation. Conversely, general scour affects the whole response of the caisson, leading to more significant decay of $K_{r,c}$ and a substantial increase of permanent settlements accumulated per cycle w_c. Besides, the removal of soil around the sides of the footing slightly reduces the amount of energy dissipated within each loading cycle $\xi_{r,h}$.

When the foundation is subjected to several loading cycles with the same rotation amplitude θ_c, a substantial increase of the moment capacity is observed due to the progressive sand densification. Such effect is just partially captured by the numerical model, which seems to lack of sufficient "memory" to track the effects of several loading cycles.

On the other hand, $K_{r,c}$ progressively decreases for increasing rotation amplitudes due to the soil nonlinear behaviour. At the same time, the amount of energy dissipated and, thus, $\xi_{r,h}$ progressively increases. As regards the settlements accumulated per cycle w_c, it continuously increases up to an amplitude of about 0.008 rad. For larger rotations, the dilative response of the soil becomes predominant and starts to compensate for the plasticity-induced settlements. This holds for the unscoured and the locally scoured foundation, whereas the reduction of FS_v caused by general scouring leads to a further increase of w_c and, thus, to a substantially larger accumulation of permanent settlements.

Overall, the comparison between the numerical simulations and the centrifuge tests have confirmed the ability of the soil constitutive model in predicting the main

aspects of the foundation response for a wide range of loading conditions. More importantly, the numerical model properly captures the effects of both general and local scour on the performance of the pier. It may therefore be concluded that the model can be used to infer the effects of scouring also on structures with different characteristics and subjected to different loading conditions.

Chapter 8

Parametric analysis of the monotonic lateral response of scoured caissons

In the previous chapters, the effects of local and general scour on the response of a bridge pier founded on a caisson supported on dense sand were analysed. The experimental and numerical analyses consider a moderately loaded caisson (i.e. $FS_{v,unsc} \approx 8$) with a slenderness ratio d/D_f of 1, a fairly common situation in practice. The results of the analyses revealed relevant insights on the influence of scouring on the resisting mechanisms exerted by the supporting soil. Such findings are anyway representative of the specific situation considered in the experimental tests. Caisson foundations characterized by different features could show different responses, leading in turn to different conclusions.

This chapter presents a parametric analysis of the monotonic lateral response of the pier. In particular, the study investigates the effects of scouring on bridge piers subjected to different vertical loading conditions (i.e. by varying the FS_v) and slenderness ratios d/D_f. The attention is focused on the lateral pushover response as it is usually the critical loading condition for scoured foundations.

The chapter initially presents an overview of the numerical simulations in the parametric study. The influence of the vertical load is then analyzed in Section 8.1, by comparing the responses of lightly, heavily, and very heavily loaded caisson foundations to the reference case characterized by $FS_v \approx 8$. Section 8.3 analyzes the influence of the slenderness ratio concerning two caissons with d/D_f equal to 2 and 4, respectively. The vertical responses of the foundations are preliminarily assessed to define the deck masses. The effects of scouring on the lateral monotonic pushovers are then presented. At the end of each section, the results are analyzed

and discussed with a view to extending the outcomes of the research to more general conclusions.

8.1 Overview

A parametric analysis is performed to analyze the influence of the slenderness ratio d/D_f and the vertical safety factor FS_v on the response of scoured caisson foundations. In particular, three scouring conditions are considered: (i) unscoured foundation, (ii) foundation subjected to local scour loaded in the transverse direction towards the upstream side (the critical condition), and (iii) foundation subjected to general scour.

The study is conducted by assuming as a reference case the prototype bridge pier investigated experimentally and numerically. The numerical model here adopted is equivalent to the one described in Section 7.3 in terms of constitutive models (for both the soil and the structure), initial conditions, soil-structure interfaces, numerical steps, model size and mesh discretization. The initial equilibrium condition is firstly established within the numerical model. The horizontal pushover loading is then carried out under drained conditions by progressively increasing the horizontal displacement applied on the rigid pier, at a constant height equal to 4.1 m from the top surface of the caisson foundation. Such a height is constant among the different models and it defines the ratio between the horizontal force *H* applied to the structure and the corresponding overturning moment *M.* Further details about the numerical modelling aspects can be found in Section 7.1 and Section 7.3.

The parametric analysis includes a total of 21 numerical simulations. The details of the numerical models can be found in the simulation matrix reported in Table 8.1. The influence of the vertical loading conditions is investigated by varying the deck mass (m_1) to cover a wide range of vertical safety factors $FS_{v,unsc}$ for the structure prior to scouring. The safety factors are computed through Eq. (7.6) based on the vertical capacity of the unscoured caisson $V_{ult,unsc}$, obtained from the numerical simulations of the vertical push tests.

For the sake of completeness, the Table also reports the actual vertical safety factor FS_v achieved for each condition, computed according to the vertical capacity V_{ult} of the foundation. The latter is equal to $V_{ult,unsc}$ for the unscoured caisson, while it reduces due to scouring.

As regards the slenderness ratio, the responses of two models with d/D_f equal to 2 and 4 are compared to the reference one (characterized by $d/D_f = 1$). The numerical models are developed adopting the same mesh discretization rules used for the base model, but a slightly larger mesh size for the elements close to the footing (i.e. 0.25 m rather than 0.2 m). Preliminary analyses showed that no significant differences can be observed in the results of the simulations, while at the same time the computation time is substantially reduced, especially for the foundation with $d/D_f = 4$. The external boundaries are placed at a distance of $3D_f$ from the caisson foundation for the model with d/D_f of 2, while the lateral distance is

increased up to $5D_f$ for the model with d/D_f of 4 to avoid any possible interaction between the displacement field induced in the soil and the boundary conditions. The resulting finite element meshes are reported in Figure 8.1 and Figure 8.2, together with the details regarding the number of elements used to discretize each model.

To allow for direct comparison among the different cases, the m_1 for these models are adjusted to achieve, along with the masses of the pier and the caisson, a vertical safety factor $FS_{v,unsc}$ approximately equal to 8 (i.e. as for the reference case identified as PO_1). Some additional vertical push simulations are then necessary to study the response of caissons characterized by d/D_f equal to 2 and 4. The simulations are carried out on numerical models equivalent to the ones described in Section 7.2, by progressively increasing the imposed vertical displacement up to failure. The foundation before and after general scour is analyzed using 2D axisymmetric models, while 3D models are used for the local scour condition. The results of the vertical simulations are analyzed in detail in Section 8.3.1, but for completeness, the vertical capacity V_{ult} (assumed as the vertical load necessary to produce a settlement of 0.3 m) for each condition is also reported in Table 8.1.

Table 8.1: Numerical simulation matrix of the lateral monotonic pushovers.

ID	Condition	d/D_f	m_1 : Mg	V_{ult} : MN	$FS_{v,unsc}$	FS_v
PO_1_a	Unscoured			8.5		8.0
PO_1_b	Local scour	1	81	8.1	8	7.7
PO_1_c	General scour			5.9		5.6
PO_2_a	Unscoured			8.5		14.3
PO_2_b	Local scour	1	33	8.1	14.3	13.7
PO_2_c	General scour			5.9		10.1
PO_3_a	Unscoured			8.5		3.8
PO_3_b	Local scour	1	205	8.1	3.8	3.6
PO_3_c	General scour			5.9		2.6
PO_4_a	Unscoured			8.5		3.0
PO_4_b	Local scour	1	264	8.1	3	2.9
PO_4_c	General scour			5.9		2.1
PO_5_a	Unscoured			8.5		2.0
PO_5_b	Local scour	1	410	8.1	2	1.9
PO_5_c	General scour			5.9		1.4
PO_6_a	Unscoured			13.3		8.0
PO_6_b	Local scour	2	132.5	13.1	8	7.9
PO_6_c	General scour			11.0		6.6
PO_7_a	Unscoured			21.7		8.0
PO_7_b	Local scour	4	219.8	21.5	8	7.9
PO_7_c	General scour			19.7		7.3

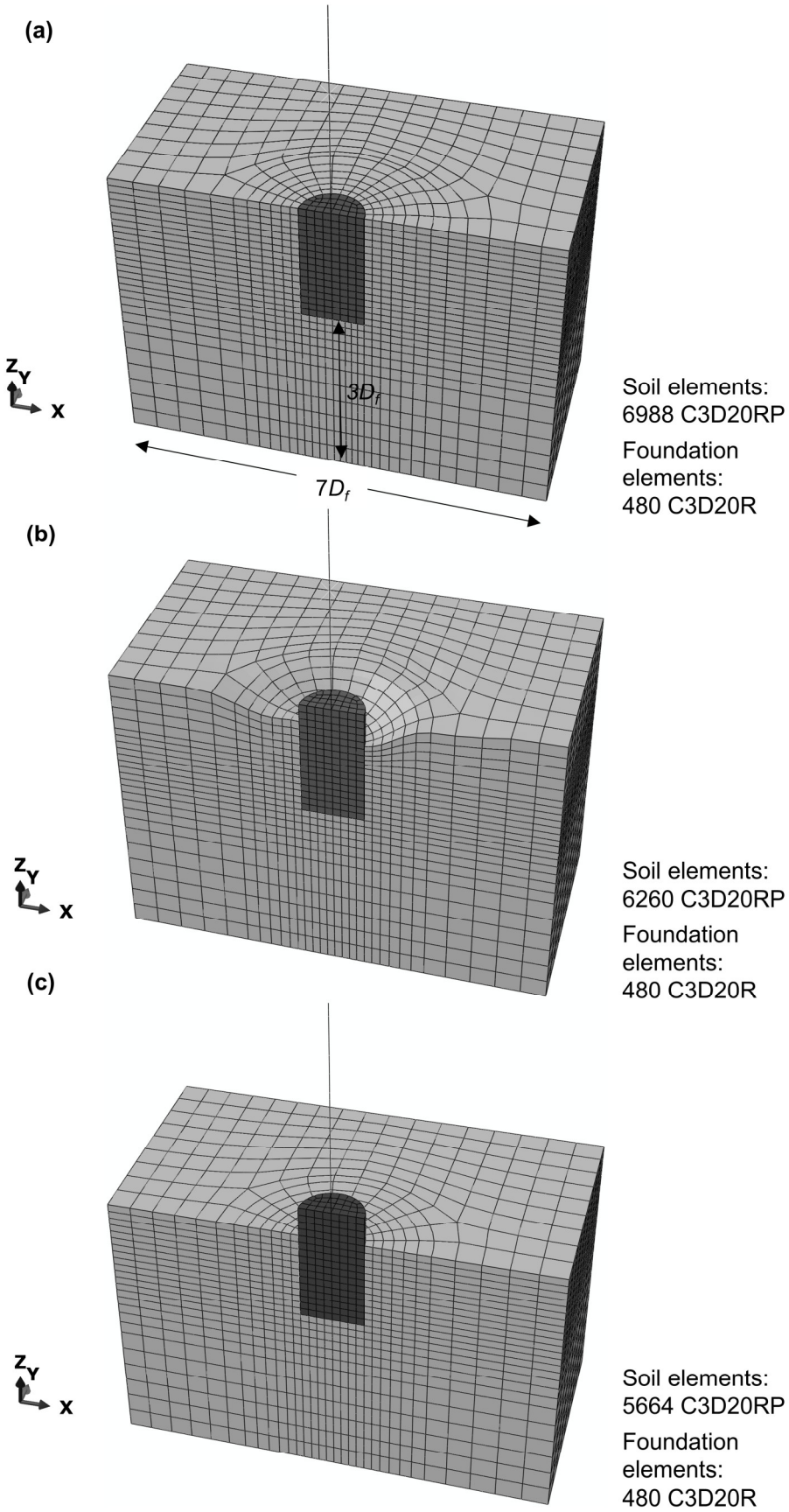

Figure 8.1: Finite element mesh for the horizontal pushover tests with slenderness ratio d/D_f =2: (a) unscoured model; (b) model subjected to local scour; (c) model subjected to general scour.

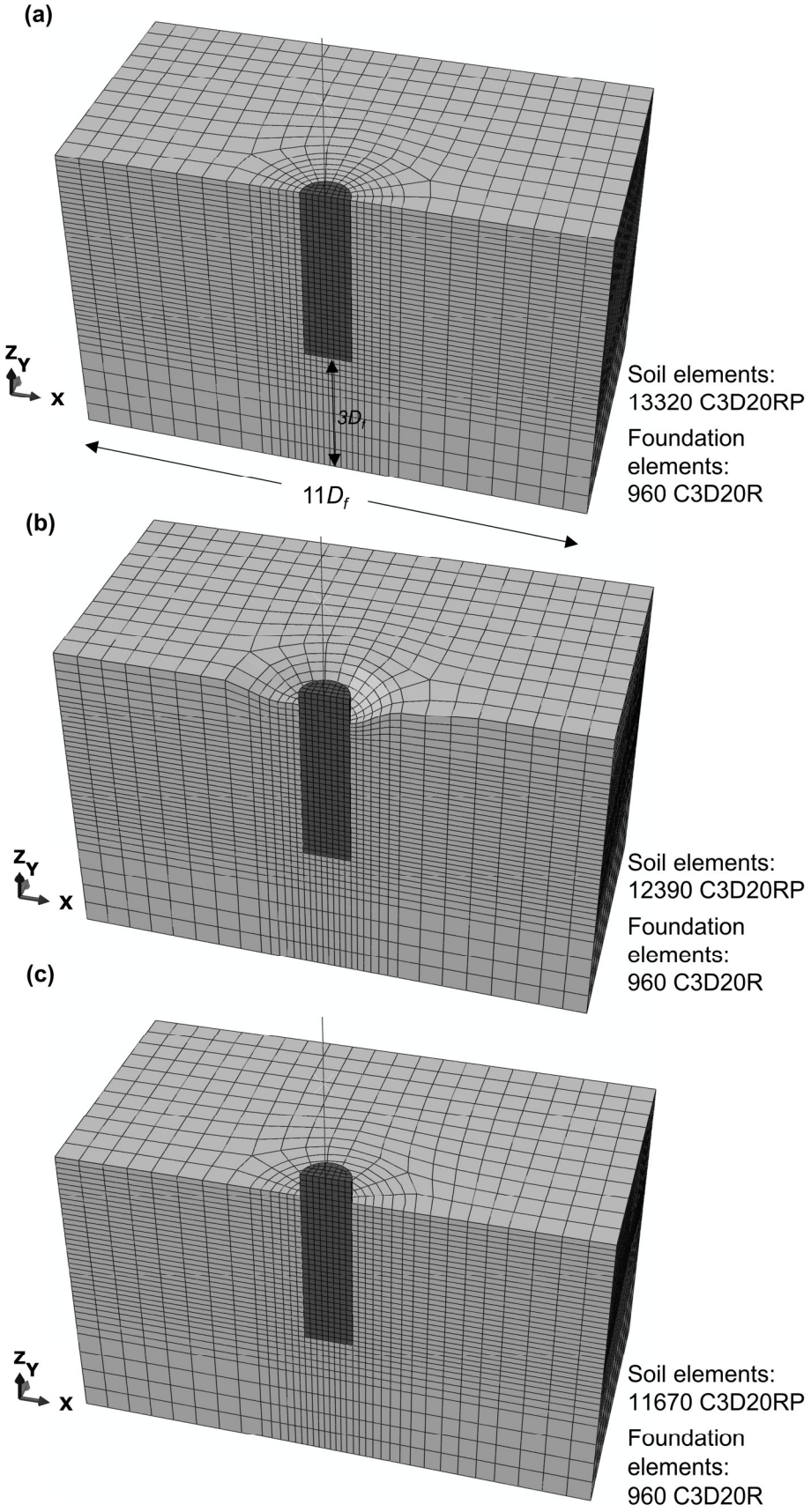

Figure 8.2: Finite element mesh for the horizontal pushover tests with slenderness ratio d/D_f =4: (a) unscoured model; (b) model subjected to local scour; (c) model subjected to general scour.

8.2 Influence of the vertical safety factor

The pure vertical safety factor FS_v of a bridge pier describes the initial loading conditions acting on the soil-foundation system. As already discussed in previous studies (e.g. Gajan et al., 2005; Gajan and Kutter, 2008; Anastasopoulos et al., 2012; Zafeirakos and Gerolymos, 2013), it influences the overall response of shallow and embedded foundations when subjected to lateral loadings.

Firstly, the FS_v strongly affects the moment capacity M_{ult} of the system (e.g. Gazetas and Apostolou, 2004; Gajan and Kutter, 2008; Zafeirakos and Gerolymos, 2016). For a given foundation (characterized by a specific purely vertical capacity V_{ult}), a larger FS_v implies a lower vertical load V acting on the footing. In general, the M_{ult} tends to increase with V for FS_v larger than 2, due to the reduction of the eccentricity of the load acting at the base of the footing. As the eccentricity is reduced, the contact area increases, increasing, in turn, the capacity of the footing. However, for $FS_v < 2$ soil plasticization becomes predominant due to the increases of the vertical load, and M_{ult} starts reducing.

The beneficial effect of the vertical load (for $FS_v > 2$) previously described is counterbalanced by second-order effects. The vertical load V is indeed responsible for the reduction in the moment-rotation $M-\theta$ curves usually observed for high rotations. The latter is due to the $P-\delta$ effects (e.g. Gazetas and Apostolou, 2004; Panagiotidou et al., 2012), which can be very relevant for slender structures such as bridge piers, leading to a substantial increase of the moment acting on the base of the footing.

The settlement response of the structure under lateral loadings is also defined by the FS_v (e.g. Gajan and Kutter, 2008; Anastasopoulos et al., 2012; Zafeirakos and Gerolymos, 2013). Foundations characterized by relatively high FS_v show an uplifting-dominated rocking response, without accumulation of settlements. A limited yielding is observed in the soil below the foundation, which is fully compensated by the dilative response of the sand. Conversely, extensive soil yielding is expected for heavily loaded footings characterized by lower FS_v values. For such foundations, the response is sinking-dominated, leading to accumulation (for instance under seismic loadings) of permanent settlements and rotations.

The above discussion makes it clear that the lateral behaviour of a scoured foundation has to be analyzed in light of its vertical safety factor FS_v. Indeed, the effects of scouring can be different if a lightly or a heavily loaded foundation is considered.

8.2.1 Lightly loaded foundations

The lateral pushover response of a lightly loaded foundation (numerical simulations PO_2 of Table 8.1, $FS_{v,unsc} \approx 14$) is compared to the reference case of a moderately loaded caisson (numerical simulations PO_1 of Table 8.1, $FS_{v,unsc} \approx 8$) in Figure 8.3. By observing the overturning moment-rotation $M-\theta$ curves (Figure 8.3.a), it is evident that the lower vertical load V applied to the foundation leads to a

reduction of the moment capacity of the structure for all the cases examined. This is not surprising, given that, for relatively high vertical safety factors, the beneficial effect of V related to the reduction of the load eccentricity is more relevant than the increase of the vertical action. The influence of the vertical load is also clearly visible on the vertical settlement-rotation $w-\theta$ curves (Figure 8.3.b). The lightly loaded structure shows, in fact, a clear uplifting-dominated rocking response. As V decreases, the dilative tendency of the dense sand becomes predominant to the vertical settlement due to soil yielding.

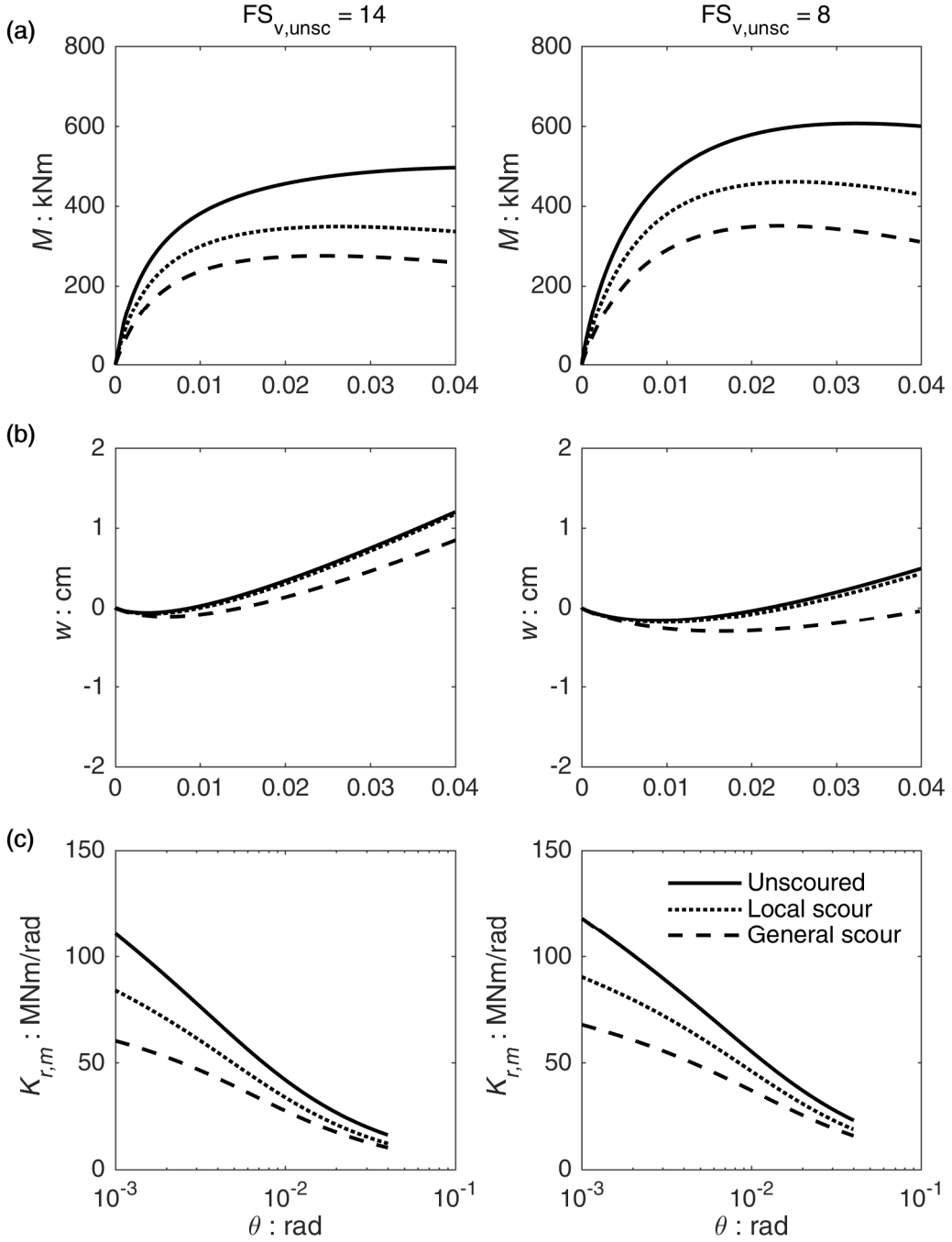

Figure 8.3: Comparison between the rocking response of a lightly loaded (left figures) and a moderately loaded (right figures) caisson foundation before and after scouring: (a) external overturning moment-rotation $M-\theta$ curves; settlement-rotation $w-\theta$ curves; (c) rocking monotonic stiffness-rotation $K_{r,m}-\theta$ curves.

This holds for all the cases examined, even in the case of the foundation subjected to general scour. For this condition, indeed, the actual vertical safety factor FS_v is equal to about 10, so it is sufficiently high to imply the uplifting of the caisson. Finally, a reduction in the rocking monotonic secant stiffness-rotation ($K_{r,m} - \theta$) curves is also observed for the entire range of rotations investigated (Figure 8.3.c).

Moreover, the $M - \theta$ responses after local and general scour are more similar for the lightly loaded structures (with $FS_{v,unsc} \approx 14$) with respect to the moderately loaded one (with $FS_{v,unsc} \approx 8$). This can be explained by decomposing the total moment M_{tot} (given by the sum of the external moment M plus the additional $\Delta M(\delta)$ due to $P - \delta$ effects) acting on the structure into the resisting moment given by the bearing capacity mechanism M_{base} and the one exerted by the soil along the sides of the caisson M_{sides} (see also Section 7.3.4.2).

Figure 8.4 compares the responses of the lightly and the moderately loaded structures in terms of M_{base} and $M_{sides} - \theta$ curves. For both the structures, the M_{base} rapidly increases up to rotations of about 0.02 rad, then it tends to an almost constant value (Figure 8.4.a). As previously speculated, such a value is strongly influenced by the vertical load V, being M_{base} lower for the lightly loaded footing due to the larger eccentricity.

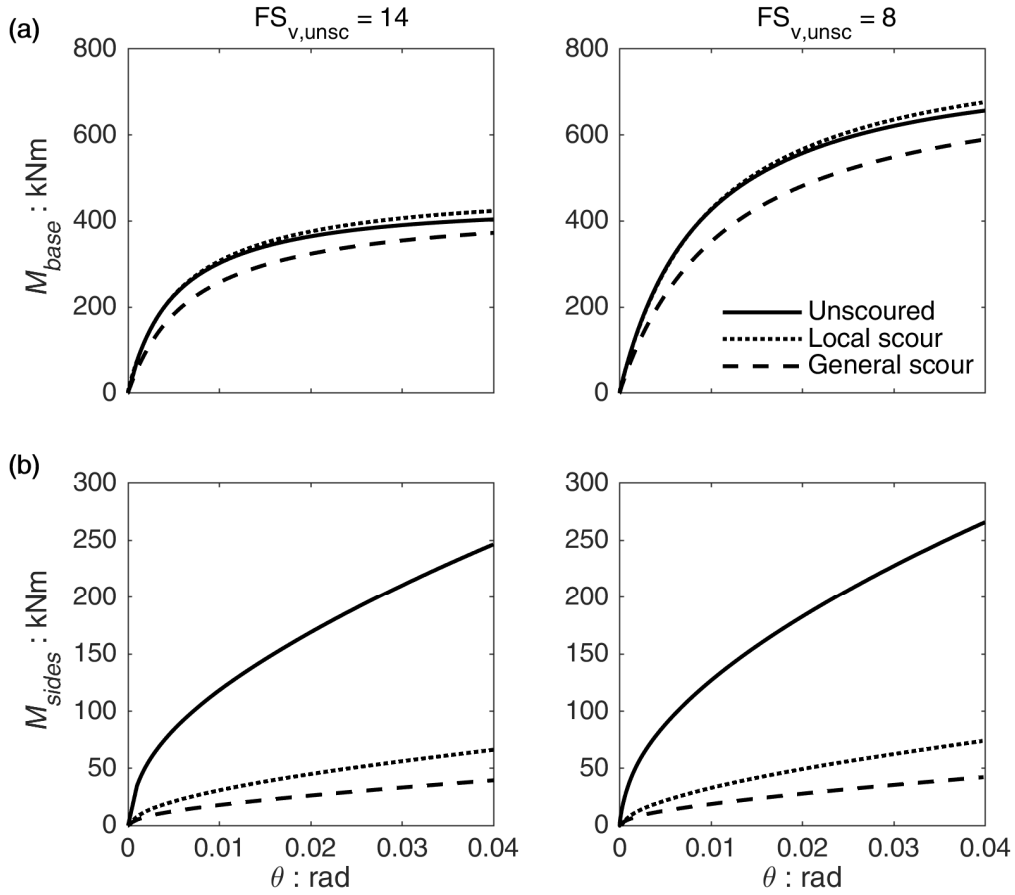

Figure 8.4: Comparison between the rocking response of a lightly loaded (left figures) and a moderately loaded (right figures) caisson foundation before and after scouring: (a) base resisting moment-rotation $M_{base} - \theta$ curves; (b) sides resisting moment-rotation $M_{sides} - \theta$ curves.

Conversely, the M_{sides} is almost not affected by the vertical load (Figure 8.4.b). For both the structures (lightly or moderately loaded) and under all the scouring conditions examined, it increases with a decreasing rate up to rotations of about 0.02 rad. Subsequently, it seems to level off, monotonically increasing at an almost constant rate. Such a behaviour can be explained with the progressive increase of the vertical stress acting on the soil along the pushing side due to second-order effects (Section 7.3.4.2 reports a detailed discussion on the issue).

General scour affects the bearing capacity mechanism of both structures, reducing M_{base}. However, for the moderately loaded structure, the base resisting mechanism is largely predominant, whereas this is not the case for the lightly loaded one where the contribution of the lateral mechanism is more relevant. As a consequence, the reduction of M_{base} has less impact on the $M-\theta$ response.

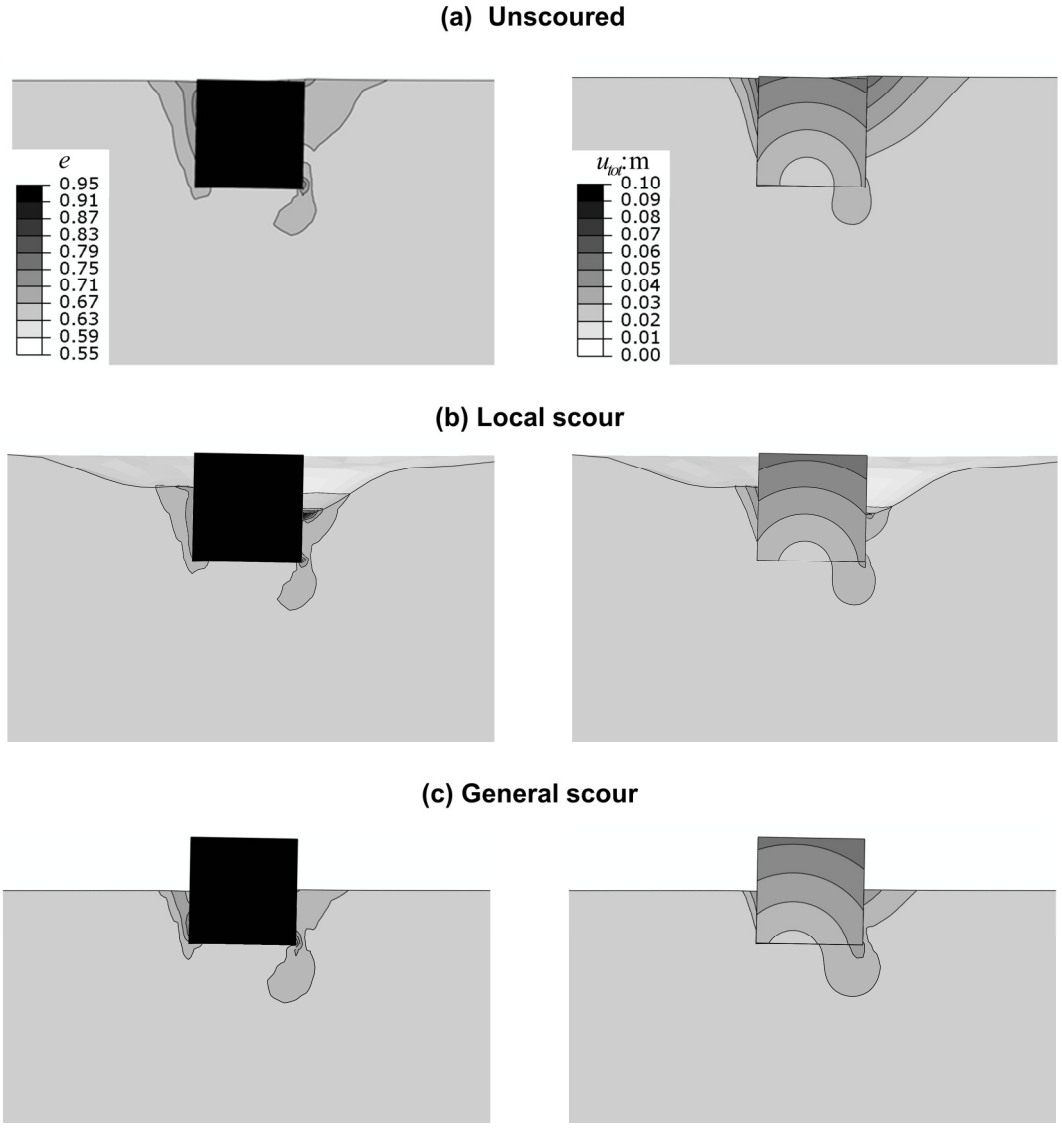

Figure 8.5: Deformed mesh with superimposed void ratio e (left figures) and total displacement u_{tot} (right figures) contours for an imposed rotation of 0.02 rad: (a) unscoured foundation; (b) foundation subjected to local scour; (c) foundation subjected to general scour. Lightly loaded foundation with $FS_{v,unsc}=14$ and $d/D_f=1$.

Likely, the lateral resisting mechanism would become predominant for structures characterized by very high $FS_{v,unsc}$, vanishing, in turn, the differences observed between local and general scour in terms of $M-\theta$ curves.

Figure 8.5 shows the failure mechanisms of the lightly loaded structure before scouring (Figure 8.5.a) and after local (Figure 8.5.b) and general (Figure 8.5.c) scour. The results are presented in terms of deformed mesh with superimposed void ratio (left figures) and total displacement (right figures) contours for an imposed rotation of 0.02 rad. By looking at the void ratio contours it is evident that for all the scouring conditions examined the soil plasticization is mainly located along the sides of the caisson and below the edge in correspondence of the pushing direction. Even for the general scour condition, the actual FS_v is sufficiently high to avoid extensive soil yielding. The u_{tot} contours reveal that the foundation is basically rotating around the centre of its base, without accumulation of settlements. As previously discussed, for larger rotations the dilatancy of the sand below the footing would become predominant leading to a translation of the rotation pole towards the pushing side and to an uplifting-dominated response (as shown in Figure 8.5.b).

8.2.2 Heavily loaded foundations

Figure 8.6 compares the response of a heavily loaded caisson (numerical simulations PO_3 of Table 8.1, $FS_{v,unsc} \approx 4$) to the reference case (numerical simulations PO_1 of Table 8.1, $FS_{v,unsc} \approx 8$). The increase of the vertical load V leads to a reduction of the eccentricity and, in turn, to a larger moment capacity of the foundation. This effect, although partially counterbalanced by $P-\delta$ effects, is visible in the $M-\theta$ responses of the heavily loaded unscoured and locally scoured structures (Figure 8.6.a). For both the conditions, the $M-\theta$ curves are larger than the corresponding ones obtained for the reference case up to rotations of about 0.04 rad. For larger θ values, the second-order effects become predominant reducing the capacity of the heavily loaded structures. The increase of the vertical load has however a different impact on the $M-\theta$ response of the caisson subjected to general scour. Indeed, the actual vertical safety factor FS_v of the structure for this condition reduces to 2.6. Such a reduction, in addition to the increase of second-order effects, leads to a lower moment capacity of the footing with respect to the reference case of a moderately loaded structure. Contrarily to the previous case, the differences between general and local scour appear then more pronounced for a heavily loaded structure.

Similar conclusions can be drawn from the $w-\theta$ curves (Figure 8.6.b). The response of the foundation before and after local scour is almost equivalent: the amount of settlement accumulated by the heavily loaded structure initially increases but its rate reduces with increasing rotation. For a rotation of about 0.04 rad, the response tends to a maximum settlement w of about 1 cm. On the other side, the response of the foundation after general scour is clearly sinking-dominated: the settlement increases almost monotonically for the entire range of θ. As also discussed by previous experimental studies (Gajan and Kutter, 2009; Anastasopoulos et al.,

2012), a critical value of FS_v defining the initiation of the sinking-dominated response exists somewhere between 2.6 and 5. For the specific condition here analyzed, it seems that this value is almost equal to the one achieved for the unscoured and the local scour conditions. Conversely, general scour brings the footing into the sinking-dominated regime.

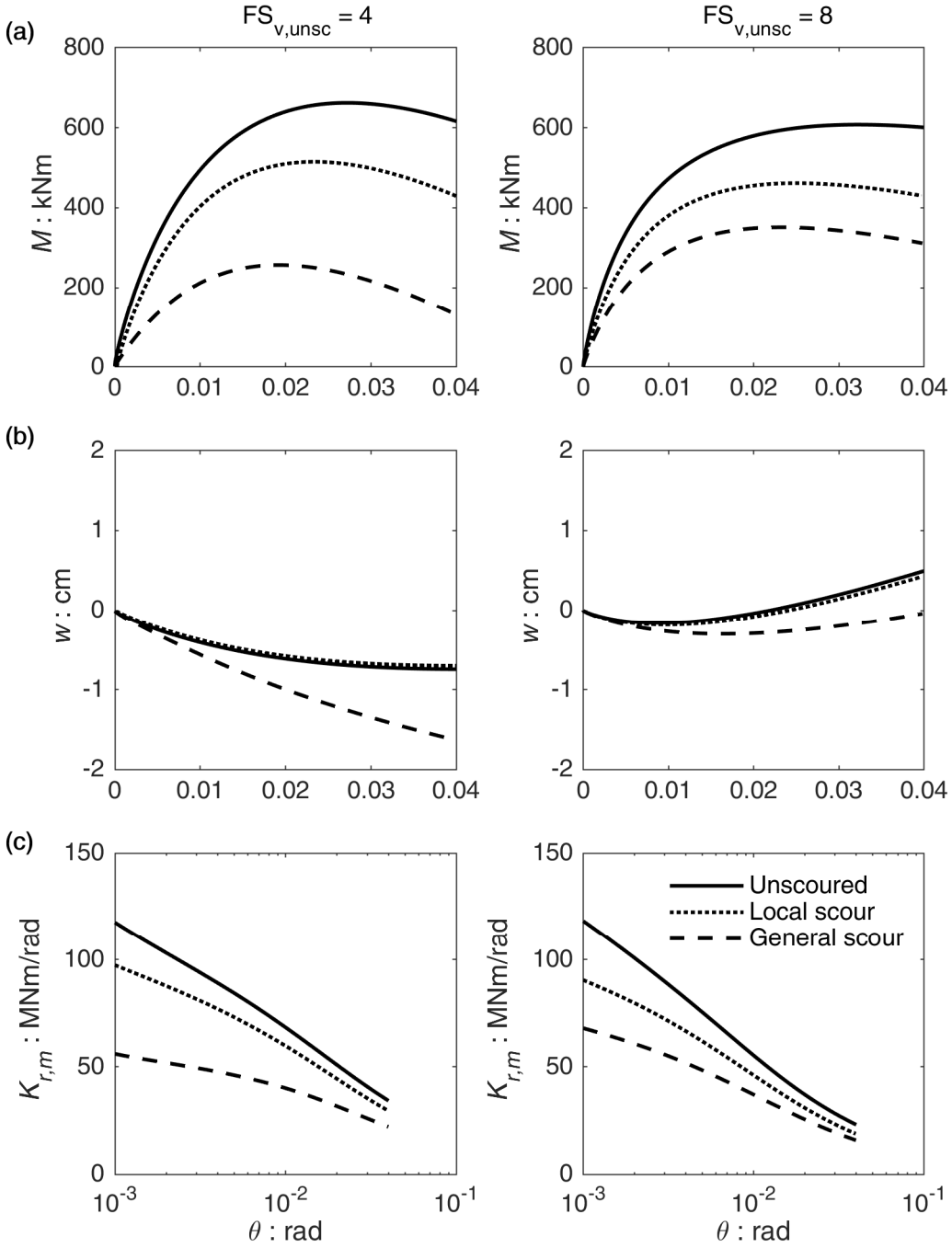

Figure 8.6: Comparison between the rocking response of a heavily loaded (left figures) and a moderately loaded (right figures) caisson foundation before and after scouring: (a) external overturning moment-rotation $M-\theta$ curves; settlement-rotation $w-\theta$ curves; (c) rocking monotonic stiffness-rotation $K_{r,m}-\theta$ curves.

Figure 8.6.c reports the comparison in terms of $K_{r,m} - \theta$ curves. It is worth noticing that the marked differences observed between local and general scour for the heavily loaded structure are also visible in the small-strain field. For instance, the $K_{r,m}$ for a rotation of 0.001 rad is equal to 120 MNm/rad for the unscoured condition, reducing to 100 MNm/rad (i.e. about 17%) due to local scour. Conversely, general scour leads to an impressive reduction of the 50% (down to about 60 MNm/rad) of $K_{r,m}$.

To better explain such differences between the responses of heavily and moderately loaded structures, it is possible to make again reference to the M_{base} and $M_{sides} - \theta$ curves, as shown in Figure 8.7. As opposed to the case of a lightly loaded structure, the capacity of a heavily loaded one is almost totally given by the resisting moment exerted by the bearing capacity mechanism. As expected, general scour significantly reduces the base capacity, affecting in turn the whole $M - \theta$ response. Conversely, the $M_{sides} - \theta$ curves are almost not affected by the vertical load, as previously discussed for the lightly loaded foundation.

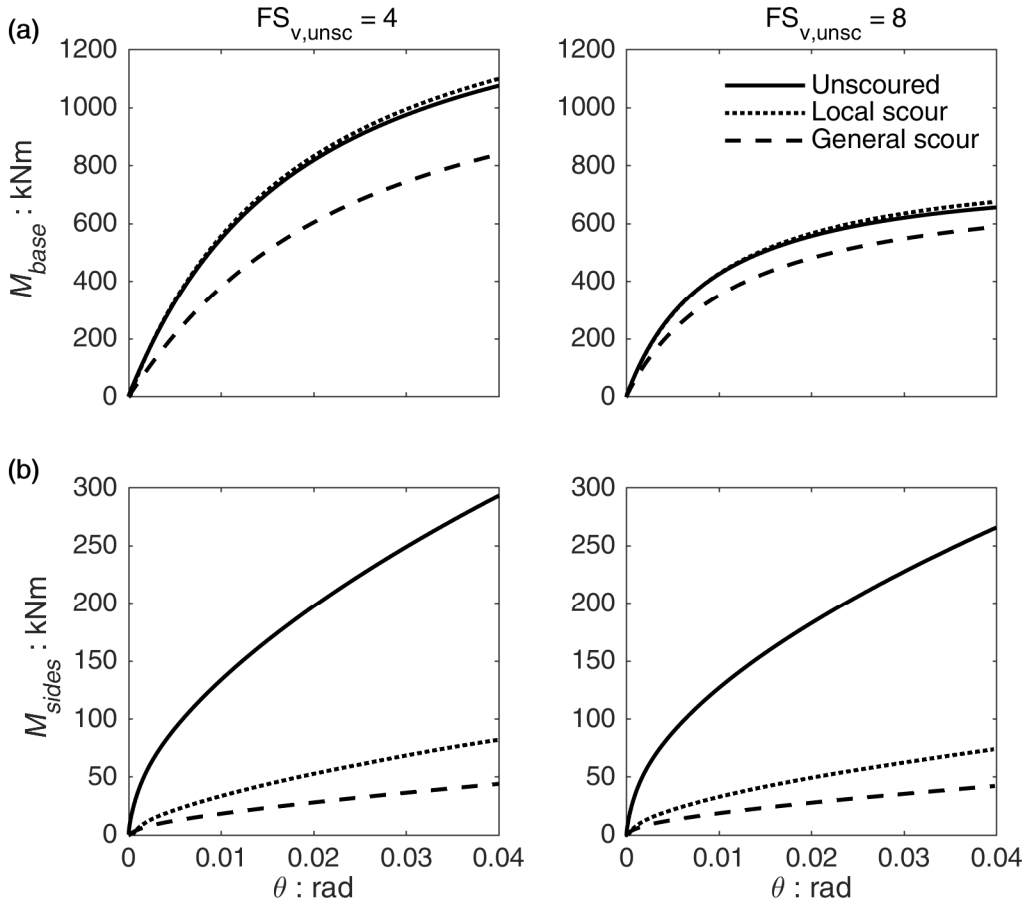

Figure 8.7: Comparison between the rocking response of a heavily loaded (left figures) and a moderately loaded (right figures) caisson foundation before and after scouring: (a) base resisting moment-rotation $M_{base} - \theta$ curves; (b) sides resisting moment-rotation $M_{sides} - \theta$ curves.

Finally, the void ratio and total displacement contours for a rotation of 0.02 rad are reported in Figure 8.8, superimposed on the deformed mesh. The void ratio field confirms that extensive soil yielding is taking place below the footing for all the scouring conditions examined. The failure mechanism starts from the soil below the edges of the footing, involving a large portion of sand down to a depth of about 1/1.5 times the diameter of the footing D_f. As showed by the u_{tot} contours, the rotation pole of the foundation is placed close to the left edge of the footing. The base of the foundation is in fact accumulating significant permanent settlements that will not be recovered even in the case of a loading reversal.

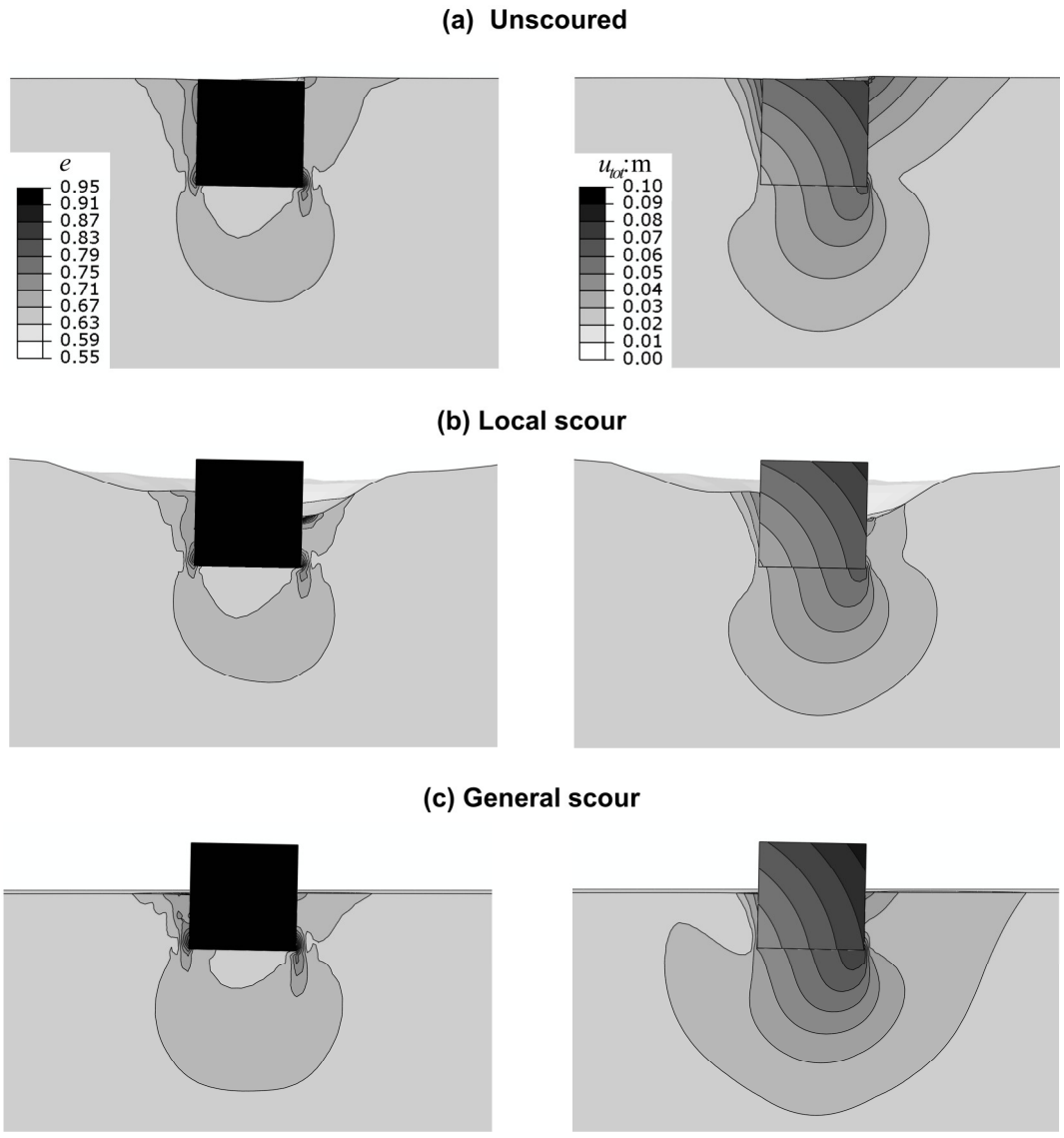

Figure 8.8: Deformed mesh with superimposed void ratio e (left figures) and total displacement u_{tot} (right figures) contours for an imposed rotation of 0.02 rad: (a) unscoured foundation; (b) foundation subjected to local scour; (c) foundation subjected to general scour. Heavily loaded foundation with $FS_{v,unsc} = 4$ and $d/D_f = 1$.

8.2.3 Very heavily loaded foundations

The two series of numerical simulations described in previous sections are characteristic of limit, but still possible, situations corresponding to lightly and heavily loaded caisson foundations. Two further series of analyses (i.e. PO_4 and PO_5 of Table 8.1) are performed to evaluate the effects of scouring on the performance of very heavily loaded foundations, characterized by $FS_{v,unsc}$ equal to 3 and 2, respectively. Clearly, such low $FS_{v,unsc}$ values are not usually adopted in the common practice, especially for slender structures as the bridge pier here analyzed. However, it is interesting to analyze the effects of scouring under very extreme conditions.

The first series of simulations (namely PO_4) is performed adopting a deck mass m_1 of 264 Mg. Under such vertical load, the achieved FS_v is equal to 3 before scouring, reducing to 2.9 and 2.1 due to local and general scour, respectively. Interestingly, the simulation performed under general scour conditions starts to accumulate substantial rotations (i.e. larger than 0.01 rad) even under the pure vertical load of the deck mass. As opposed to the vertical push tests performed to define the vertical capacity, in the lateral pushover simulations, the vertical load corresponding to the deck mass is progressively applied to the footing under loading control. If the degrees of freedom of the rigid pier are not externally "fixed", any numerical imperfection produces a very small initial rotation. Such rotation is usually negligible and does not affect the results of the simulations. However, for very heavily loaded slender structures, this very small initial rotation implies non-negligible $\Delta M(\delta)$ acting on the footing due to second-order effects. The $\Delta M(\delta)$ produced by the numerical imperfection induces a further rotation on structures with reduced capacity (as in the case of general scour) which leads in turn to an increase of $\Delta M(\delta)$. Under these conditions, the pier may become unstable due to $P-\delta$ effects. It should be noted that this instability, caused in the simulations by very small numerical imperfections, may also occur in real structures. Any initial rotation of the pier (due, for example, to a small structural imperfection) would in fact produce a non-negligible $\Delta M(\delta)$, which, in turn, could produce a further rotation of the pier. As a consequence, the structure may accumulate significant rotations and eventually collapse, even under the dead load of the structure.

It is worth mentioning that the simplified numerical model here developed does not consider the presence of the superstructure. As noticed by previous Authors (e.g. Tanasić and Hajdin, 2018), the superstructure can be seen as an additional resisting system if sufficient redundancy is present in the structural scheme. As a consequence, in such extreme conditions, it could reduce the accumulation of permanent rotations, decreasing the failure probability of the bridge (see Section 3.1.2.3 for further details). The drawback is that the redistribution of the loadings will generate additional "parasite" actions on other parts of the bridge.

The results obtained for the other two conditions (i.e. unscoured and after local scour) are presented in Figure 8.9 in terms of $M-\theta$ and $w-\theta$ responses. By observing the curves, it is interesting to notice that also the foundation subjected to local scour accumulates a small, but not-negligible, initial rotation. This rotation,

equal to about 0.001 rad, always takes place towards the upstream direction due to the geometric asymmetry of the scour hole. The reduction of the moment capacity induced by local scour is more pronounced with respect to the case of a heavily loaded caisson (as presented in Figure 8.6). However, such a reduction is not sufficient to lead to the collapse of the pier and the caisson foundation still presents a residual capacity to withstand external loadings. Both the scoured and the unscoured caisson presents a marked accumulation of settlement for the entire range of rotations investigated. The increase of the vertical load, and the consequent reduction of FS_v, brings the caisson into the sinking dominated-regime.

The second series of simulations (namely PO_5) considers a deck mass m_1 of 410 Mg, thus achieving a FS_v equal to 2 before scouring, reducing to 1.9 and 1.4 due to local and general scour, respectively. Figure 8.10 reports the response of the unscoured foundation in terms of $M-\theta$ and $w-\theta$ responses. The moment capacity of the foundation is now substantially reduced with respect to the previous case. The increase of the vertical load acting on the base of the footing, together with the increase of $P-\delta$ effects, becomes indeed predominant on the beneficial effect due to the reduction of the load eccentricity.

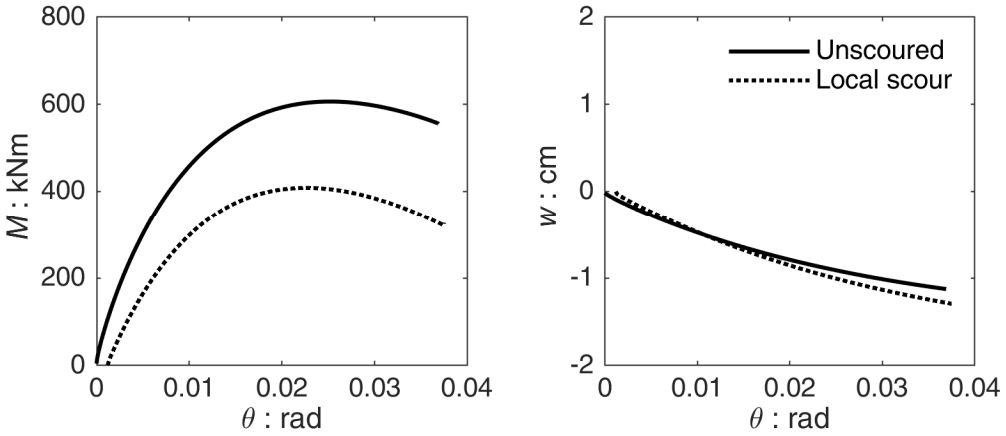

Figure 8.9: Rocking response of a very heavily loaded ($FS_{v,unsc} \approx 3$) caisson foundation before and after scouring in terms of external overturning moment-rotation $M-\theta$ curves and settlement-rotation $w-\theta$ curves.

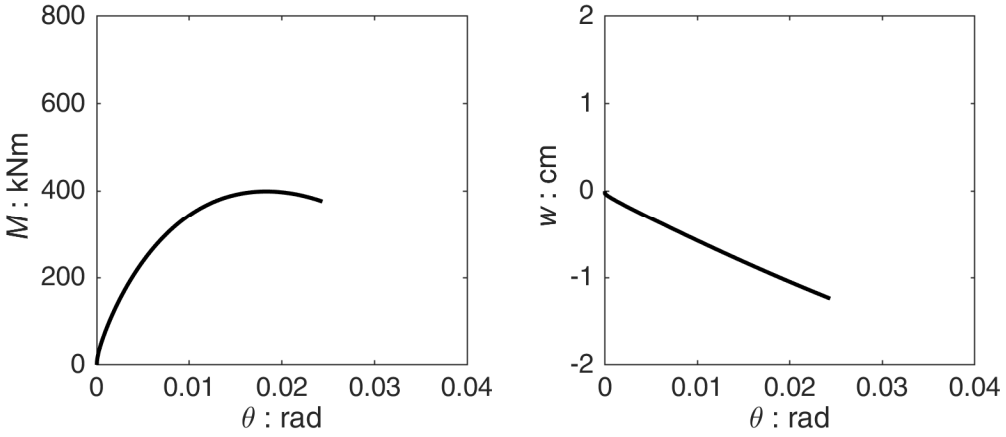

Figure 8.10: Rocking response of a very heavily loaded ($FS_{v,unsc} \approx 2$) caisson foundation before and after scouring in terms of external overturning moment-rotation $M-\theta$ curves and settlement-rotation $w-\theta$ curves.

As a consequence, extensive yielding takes place below the foundation, leading to a progressive, almost monotonic, increase of the settlement w with increasing rotation. For this situation, not only general scour but also local scour reduces the capacity of the foundation enough to make the bridge pier unstable, leading to the accumulation of significant permanent rotations (close to the failure rotation of 0.02 rad).

8.2.4 Discussion

The influence of FS_v on the effects of scouring on the moment capacity of the structure is first considered. As discussed in Section 7.3.4, the $M-\theta$ curves are used to define the horizontal pushover capacity of the structures, implicitly considering the second-order effects. In particular, to allow for direct comparison among the different cases M_{ult} is defined as the external moment necessary to produce a rotation $\theta = 0.02\,\text{rad}$.

Figure 8.11.a plots the M_{ult} as a function of both the scouring conditions and the vertical safety factor (before scouring) $FS_{v,unsc}$. Figure 8.11.b reports instead the corresponding total moment M_{tot} acting on the footing, computed including second-order ($P-\delta$) effects. Finally, the actual moment capacity normalized to the one observed before scouring $M_{ult}/M_{ult,unsc}$ is presented in Figure 8.11.c.

For decreasing $FS_{v,unsc}$ (and, thus, increasing vertical loads V), the M_{ult} for the unscoured foundation increases due to the reduction of the load eccentricity (Figure 8.11.a-b). However, soon after its maximum is reached (for a $FS_{v,unsc}$ of about 4) the detrimental consequence of the increase of $P-\delta$ effects leads to a rapid reduction of the capacity against external loadings.

A similar trend is also observed for the foundation subjected to local scour. In absolute terms, the reduction of M_{ult} due to local scour is almost constant for $FS_{v,unsc} \geq 4$ (Figure 8.11.a-b). However, its relative importance becomes more significant for lightly loaded foundations, where the bearing capacity resistance is reduced and the lateral resisting mechanism is predominant (Figure 8.11.c).

For very heavily loaded foundations ($FS_{v,unsc} \leq 3$) local scour induces the accumulation of an initial rotation due to just the dead mass of the superstructure. As a consequence, the total moment $M_{ult} + P\delta$ starts to decrease (Figure 8.11.b), inducing a fast decay of the moment capacity M_{ult} and, for $FS_{v,unsc} = 2$, the instability of the pier (Figure 8.11.a).

As opposite to local scour, the reduction of M_{ult} induced by general scour is influenced by the vertical load also for larger safety factors (Figure 8.11.a). General scour affects also the base resistance of the caisson. Consequently, for increasing vertical loads (and thus decreasing $FS_{v,unsc}$) the reduction of M_{ult} due to general scour always increases in absolute terms (Figure 8.11.a). Such a reduction is sufficient to induce the instability of the pier due to its self-weight even for severe, but not extreme, loading conditions (i.e. $FS_{v,unsc} \leq 3$).

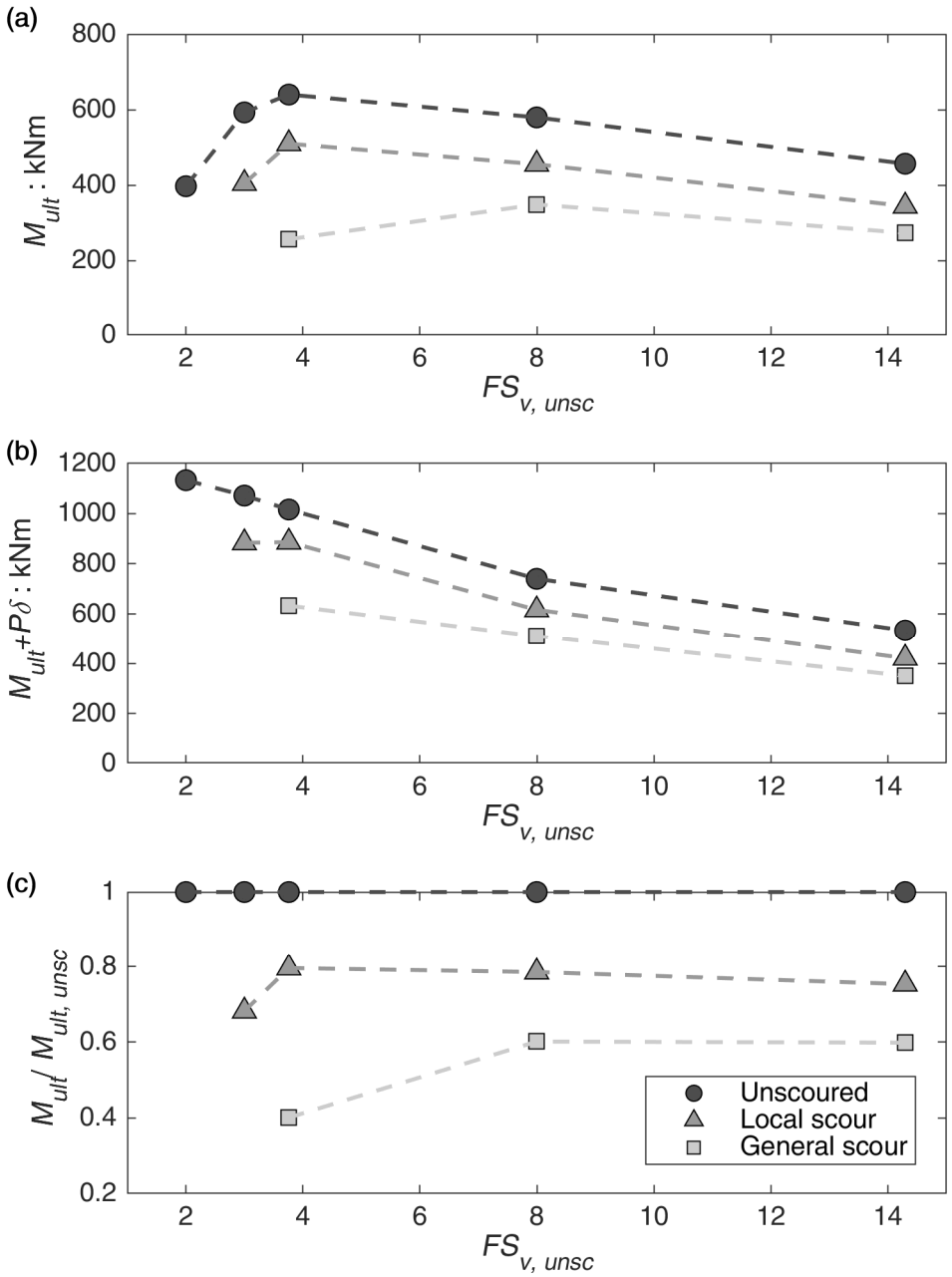

Figure 8.11: Influence of the vertical safety factor $FS_{v,unsc}$ on the rocking response of caisson foundations with $d/D_f = 1$ before and after scouring: (a) moment capacity M_{ult}; (b) moment capacity plus second-order effects $M_{ult} - P\delta$; (c) normalized moment capacity $M_{ult}/M_{ult,unsc}$. Values computed for a rotation $\theta = 0.02\,\text{rad}$.

The considerations regards the effects of scouring on the resisting mechanisms are summarized Figure 8.12 in terms of normalized base $M_{base}/M_{base,unsc}$ and sides $M_{sides}/M_{sides,unsc}$ resisting moments at failure (i.e. for a rotation of 0.02 rad). The effect of local scour on the base mechanism is almost irrelevant for all the $FS_{v,unsc}$ considered (Figure 8.12.a). A slight reduction is observed for $FS_{v,unsc} = 3$, probably due to the initial rotation accumulated by the structure in this condition. Conversely, general scour affects the resisting moment given by the bearing capacity mechanism. As the vertical load increases (and $FS_{v,unsc}$ decreases), the reduction becomes progressively more relevant, leading to decay of M_{base} of about 30% for $FS_{v,unsc} = 3$.

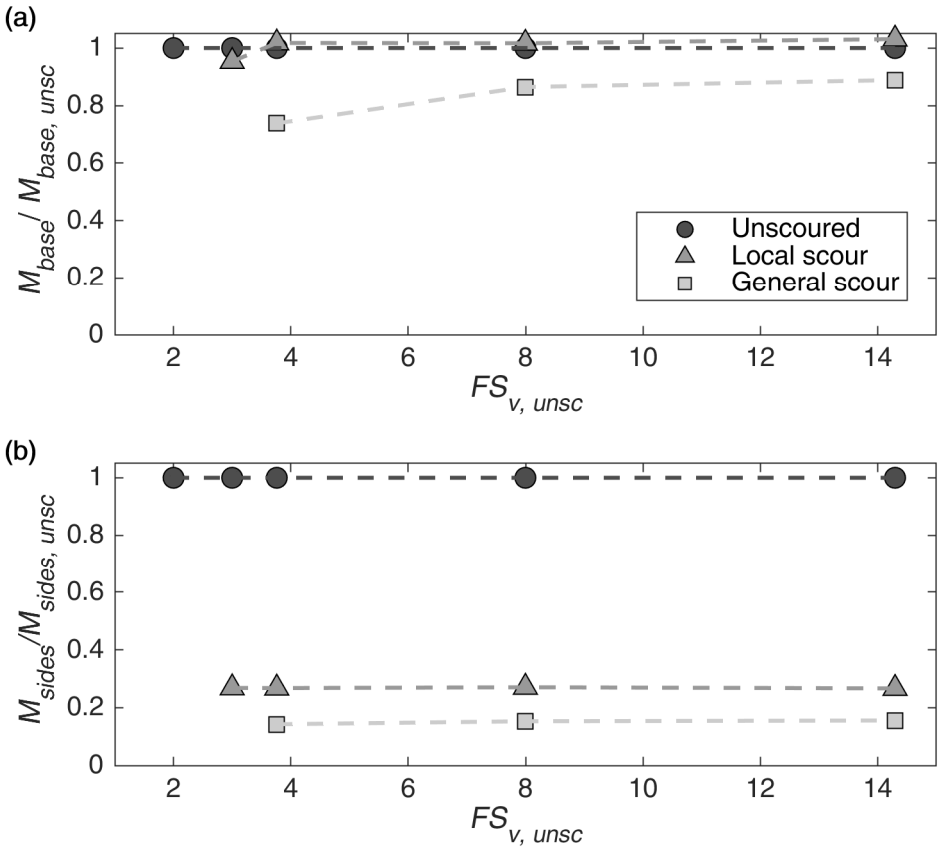

Figure 8.12: Influence of the vertical safety factor $FS_{v,unsc}$ on the rocking response of caisson foundations with $d/D_f = 1$ before and after scouring: (a) normalized base resisting moment $M_{base}/M_{base,unsc}$; (b) normalized sides resisting moment $M_{sides}/M_{sides,unsc}$. Values computed for a rotation $\theta = 0.02\,\text{rad}$.

On the other side, the $FS_{v,unsc}$ does not influence the effects of general and local scour on the lateral resisting mechanism (Figure 8.12.b). For the entire range of $FS_{v,unsc}$ investigated, the reduction of M_{sides} is almost constant and equal to 70 and 80%, respectively for the local and general scour conditions.

Unavoidably, the adverse effects of scouring also affect the small-strain response of the foundation. Figure 8.13.a plots the secant rocking monotonic stiffness $K_{r,m}$ obtained for a rotation of 0.001rad, as a function of $FS_{v,unsc}$. The stiffness is also presented normalized to the corresponding unscoured value $K_{r,m}/K_{r,m\,unsc}$ in Figure 8.13.b. Within the range of $FS_{v,unsc}$ here examined (i.e. between 2 and 14), $K_{r,m}$ at small rotations seems not to be particularly sensitive to the vertical load for the unscoured case (Figure 8.13.a). The stiffness just slightly increases, with decreasing $FS_{v,unsc}$, due to the reduction of the load eccentricity.

Conversely, the reduction of the stiffness induced by local and general scour seems to be influenced by $FS_{v,unsc}$ (Figure 8.13.a-b). In particular, the $K_{r,m}/K_{r,m\,unsc}$ ratio for the foundation subjected to local scour is quite stable (and equal to about 0.8) for $FS_{v,unsc} \geq 4$, while it rapidly reduces for larger vertical loads. Similarly, for the general scour condition the $K_{r,m}/K_{r,m\,unsc}$ ratio is initially almost stable and equal to 0.55, while it starts to decrease for $FS_{v,unsc} \leq 4$.

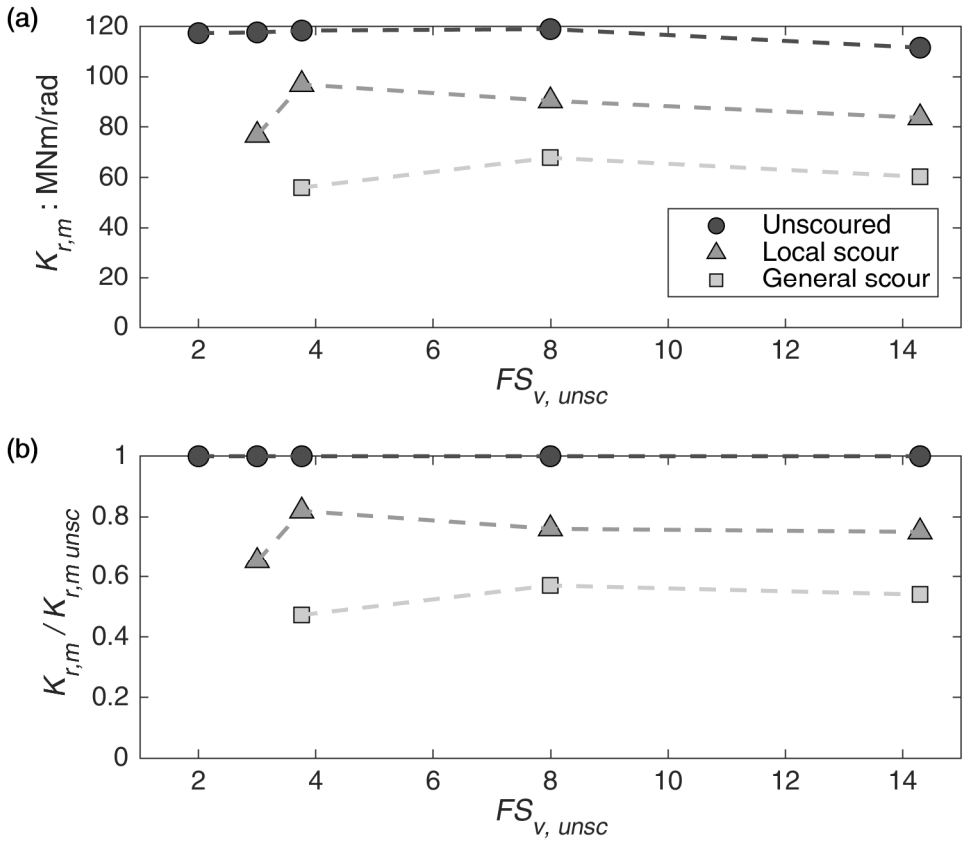

Figure 8.13: Influence of the vertical safety factor $FS_{v,unsc}$ on the rocking response of caisson foundations with $d/D_f = 1$ before and after scouring: (a) small-strain monotonic rocking stiffness $K_{r,m}$; (b) normalized small-strain monotonic rocking stiffness $K_{r,m}/K_{r,m\,unsc}$. Values computed for a rotation $\theta = 0.001\,\text{rad}$.

As discussed in Section 8.2.4, for heavily loaded foundations the reduction of the capacity of the footing due to scouring, together with the increase of the vertical load (and thus of $P-\delta$ effects), may lead to the accumulation of a small, but not-negligible, permanent rotation. The latter causes a more pronounced initial soil yielding below the foundation which may result, in turn, in a reduction of the initial rocking stiffness of the footing.

In summary, the vertical safety factor (before scouring) $FS_{v,unsc}$ defines the loading condition in the soil below the footing. For reasonable values of $FS_{v,unsc}$ (i.e. ≥ 4), an increase of the vertical load implies a larger unscoured moment capacity due to the reduction of the load eccentricity. This holds also for the foundation subjected to local scour, as the localized erosion mainly affects the lateral resisting mechanism, which is less relevant with increasing V. However, this is not the case of the foundation subjected to general scour. A global erosion of the riverbed leads to a pronounced decrease of the actual FS_v. If a heavily loaded foundation is considered ($FS_{v,unsc} \approx 4$), such a decrease may lead to a substantial reduction of the base resisting moment M_{base} and, also due to the increase of the second-order effects, to a smaller moment capacity M_{ult}.

In the limit case of a very heavily loaded foundation ($FS_{v,unsc} \leq 3$), the increase of second-order effects becomes predominant, counterbalancing the positive impact

of the smaller load eccentricity. As a consequence, the moment capacity of the structure starts reducing. Under this condition, the bridge pier may become unstable due to the combined action of scouring (which further reduces M_{ult}) and $P-\delta$ effects. Such instability is more likely for foundation subjected to general scour, even though it still can take place for very heavily loaded foundations subjected to extreme local scour.

8.3 Influence of the slenderness ratio

The slenderness ratio d/D_f of the caisson foundation basically affects the relative importance of the two resisting mechanisms acting during the lateral pushover of the bridge pier. The predominant resisting mechanism for a moderately loaded (i.e. $FS_{v,unsc} \approx 8$) caisson with $d/D_f = 1$ is the bearing capacity mechanism developing below the base of the footing. The base mechanism is however affected just slightly by local scour (i.e. the FS_v reduces to 7.7), while more significant effects are induced by general scour (i.e. the FS_v reduces to 5.6). As a consequence, significant differences are observed between the responses of foundations subjected to local or general scour. Such differences are even more pronounced for increasing vertical loads.

However, this is not necessarily the case of caisson foundations characterized by $d/D_f > 1$. As also noticed by previous studies (e.g. Zafeirakos and Gerolymos, 2016), an increase of the slenderness ratio d/D_f leads to a reduction of the contribution of the base resistance to the overall capacity of the footing. The sidewall capacity (which is affected by both local and general scour) becomes then the predominant resisting mechanism.

Consequently, foundations with different d/D_f could show a different response. The influence of d/D_f on the effects of scouring should then be carefully analyzed. To this end, reference is made in the following to two series of pushover simulations (i.e. PO_6 and PO_7 of Table 8.1), conducted on caisson foundations with $FS_{v,unsc} \approx 8$ and d/D_f equal to 2 and 4, respectively.

It is clear that an increase in the slenderness ratio d/D_f implies also a reduction of the normalized (with respect to the initial embedment depth) scour depth d_s/d of the footing. The hydraulic scenario considered in this research has produced an average local scour depth d_s of about 1 m, which is also adopted as a reference condition to study the effects of general scour. Such a value is mainly influenced by the flow intensity $\overline{v}/U_c$ and the flow shallowness y/D_c, which are independent of the embedment depth of the caisson (see Section 2.3.1 and Section 5.2 for further details). Consequently, the scour depth is the same for all the models, but its normalized value d_s/d changes, being equal to 0.5 for the reference case and reducing to 0.25 and 0.125 for the two additional series of simulations.

8.3.1 Pure vertical loading

The vertical response of caisson foundations with $d/D_f > 1$ is initially investigated through some vertical push simulations. Specifically, six simulations are carried out to study the two caissons characterized by d/D_f equal to 2 and 4, before and after local and general scour.

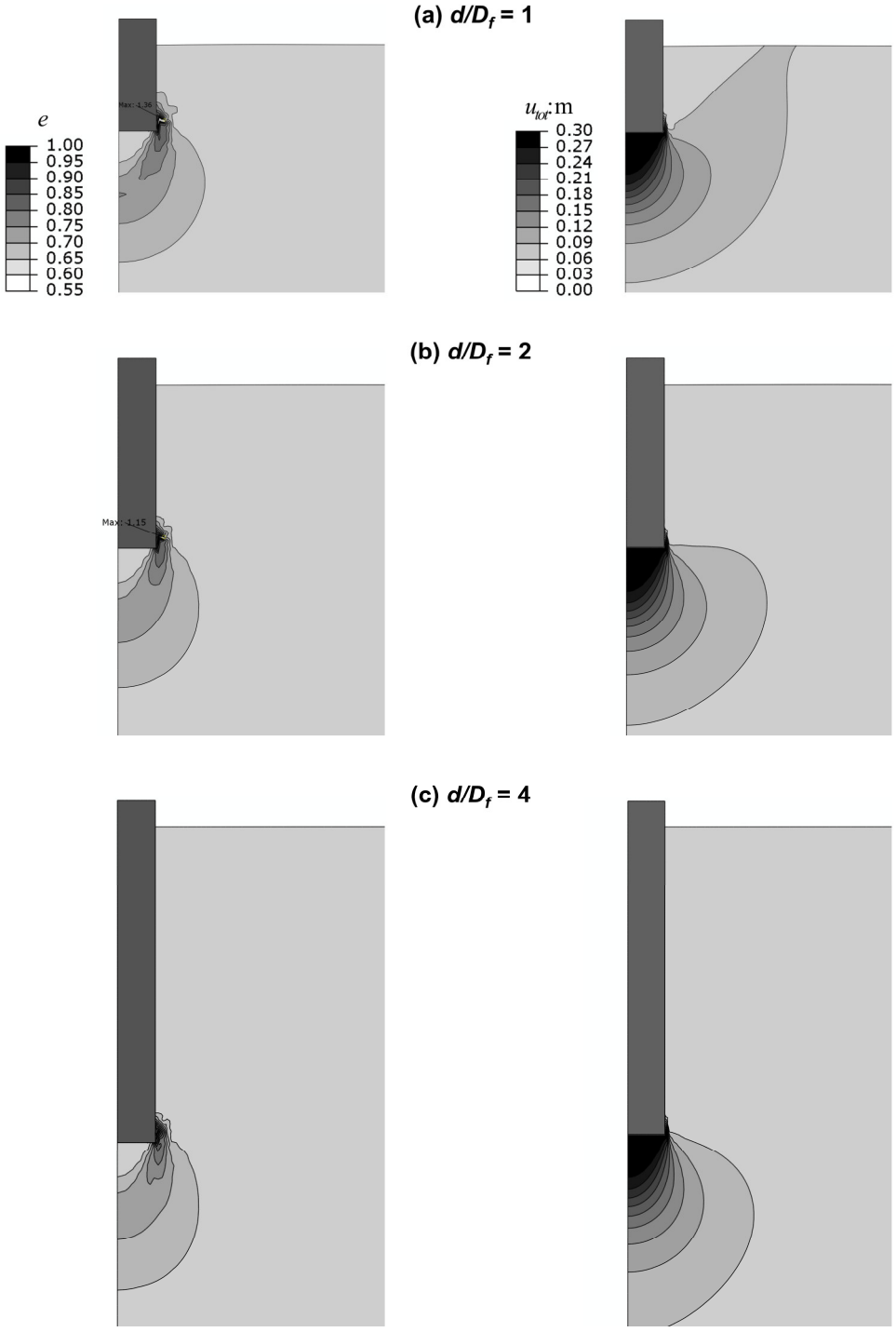

Figure 8.14: Deformed mesh with superimposed void ratio e (left figures) and total displacement u_{tot} (rigth figures) contours for the unscoured condition: (a) caisson with $d/D_f = 1$; (b) caisson with $d/D_f = 2$; (c) caisson with $d/D_f = 4$. Imposed vertical displacement of 0.3 m.

Figure 8.14 compares the failure mechanisms of the three caissons in terms of void ratio e and total displacement u_{tot} contours for an imposed vertical displacement $w = 0.3\,\text{m}$. The comparison is presented for the unscoured condition, but similar conclusions can be drawn by observing the results of the other simulations.

According to Vesic (1973, 1975), three failure mechanisms can occur for a shallow or an embedded foundation: (i) general shear failure, (ii) local shear failure, and (iii) punching shear failure. The occurrence of one rather another depends on the slenderness ratio d/D_f of the footing, together with the relative density of the sand. As also discussed in detail in Section 7.2.4, for the reference case (characterized by $d/D_f = 1$ and $D_R \approx 80\%$) a local shear failure is expected for all the conditions examined, although the foundation subjected to general scour shows a transition towards a general failure. For $d/D_f = 1$, the displacement field involves also the sand along the sides of the footing up to the soil surface, even though to a very small extent (Figure 8.14.a). Conversely, as the slenderness ratio d/D_f increases, the failure mechanism becomes deeper and involves a smaller portion of the soil below the base of the footing. For a $d/D_f = 2$ for instance, the displacement field does not reach the ground surface (Figure 8.14.b). Eventually, for the footing with $d/D_f = 4$, soil yielding takes place in a very localized zone just below the footing, suggesting the transition towards a punching failure mechanism.

These observations are confirmed by the tangent vertical stiffness-settlement $K_v - w$ and load-settlement $V - w$ responses shown in Figure 8.15 and Figure 8.16, respectively for the caissons with d/D_f equal to 2 and 4. As also observed for the simulations performed for the reference case (see Figure 7.6.b), a load plateau cannot be identified in the $V - w$ curves for both the caissons with d/D_f equal to 2 and 4 (Figure 8.15.b and Figure 8.16.b, respectively).

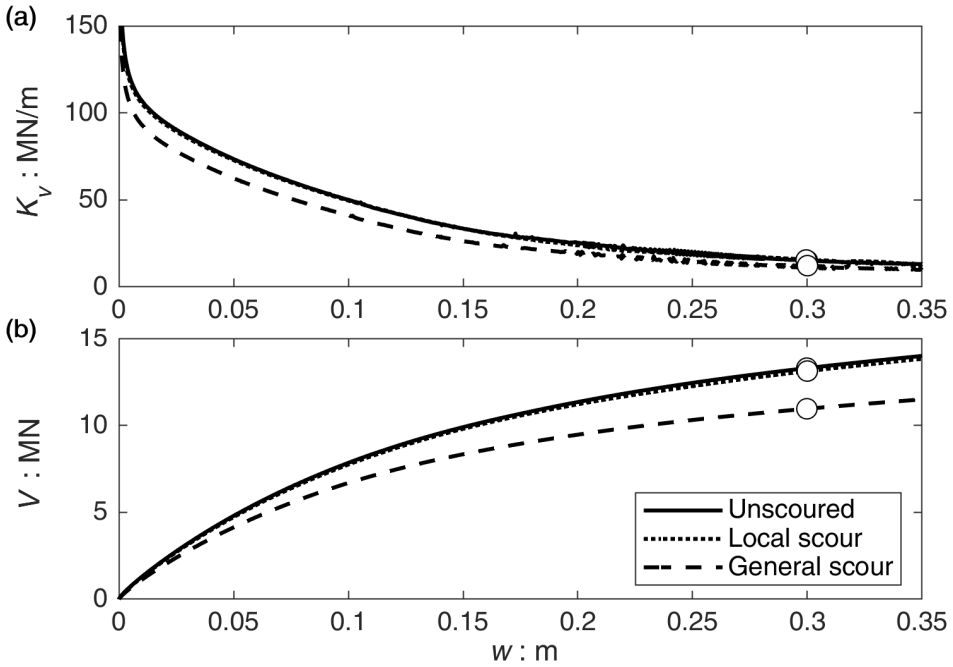

Figure 8.15: Vertical response of the caisson foundation with $d/D_f = 2$ before and after scouring: (a) tangent vertical stiffness-settlement $K_v - w$ curves; (b) load-settlement $V - w$ response.

However, the $K_v - w$ curves do not show a clear transition between the almost linear and the strongly nonlinear branches, as opposed to the foundation with $d/D_f = 1$ (Figure 8.15.a and Figure 8.16.a). Moreover, for $w > 0.3\,\text{m}$ the K_v tends to a constant value substantially larger than the residual one observed for $d/D_f = 1$ (see Figure 7.6.a), especially for the foundation with $d/D_f = 4$ (Figure 8.16.a).

Therefore, it is not possible to identify a point after which the failure mechanism can be considered fully developed. Such behaviour is consistent with a punching type failure mechanism, characterized by a progressive hardening of the response without a dramatic break in the load-settlement $V - w$ curves.

In the absence of a clear plateau, the ultimate vertical load V_{ult} is identified as the load necessary to produce a settlement w_{ult} of 0.3 m. This value was also adopted for the reference case (see Section 7.2.4.2) and corresponds to a normalized settlement w_{ult}/D_f equal to 15%, which coincides approximately with the initiation point of the hardening regime. The V_{ult} values are reported in Table 8.1 for the two corresponding pushover tests (i.e. PO_6 and PO_7). Such values are used to define the deck masses to obtain a vertical safety factor before scouring equal to the one adopted for the reference case (i.e. $FS_{v,unsc} \approx 8$).

Before scouring, the two caissons exhibit a V_{ult} equal to 13.3 and 21.7 MN, respectively for d/D_f equal to 2 and 4. As d/D_f increases (and d_s/d decreases), the influence of local scour on the pure vertical bearing capacity of the footing vanishes. As a consequence, the curves (and the V_{ult} values) characteristic of the foundations subjected to local scour are almost coincident with the corresponding unscoured ones. At the same time, also the effect of general scour tends to decrease. Nevertheless, its occurrence produces a not negligible reduction of V_{ult} of 17% when $d/D_f = 2$, reducing to 9% for the caisson with $d/D_f = 4$.

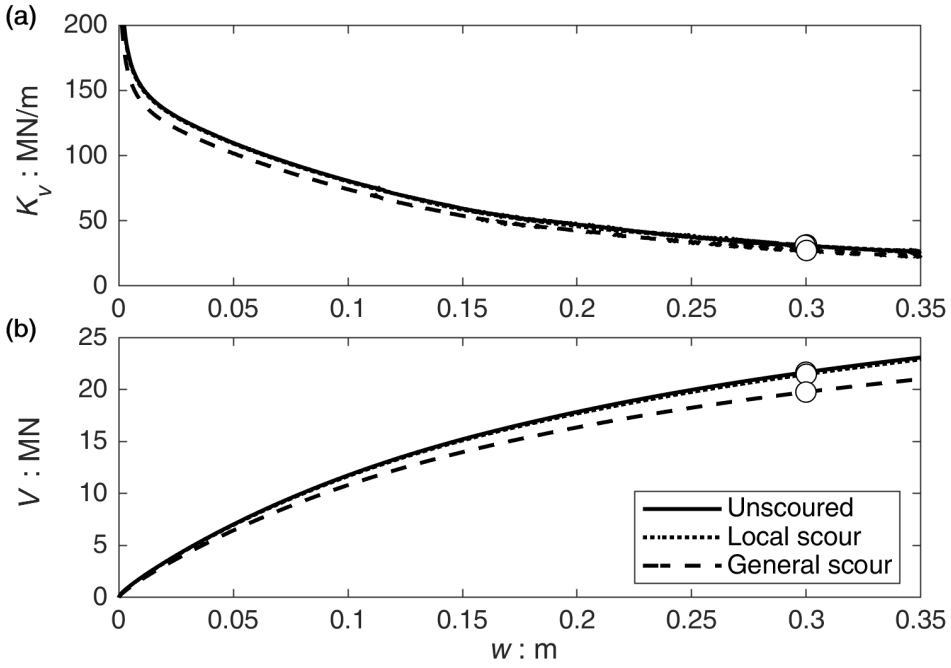

Figure 8.16: Vertical response of the caisson foundation with $d/D_f = 4$ before and after scouring: (a) tangent vertical stiffness-settlement $K_v - w$ curves; (b) load-settlement $V - w$ response.

8.3.2 Lateral monotonic pushover

This section compares in-depth the lateral monotonic response of a deep caisson foundation ($d/D_f = 4$, simulations PO_7 of Table 8.1) with the reference case of a shallow caisson ($d/D_f = 1$, simulations PO_1 of Table 8.1). The aggregated results obtained from all the simulations are instead discussed in the next section.

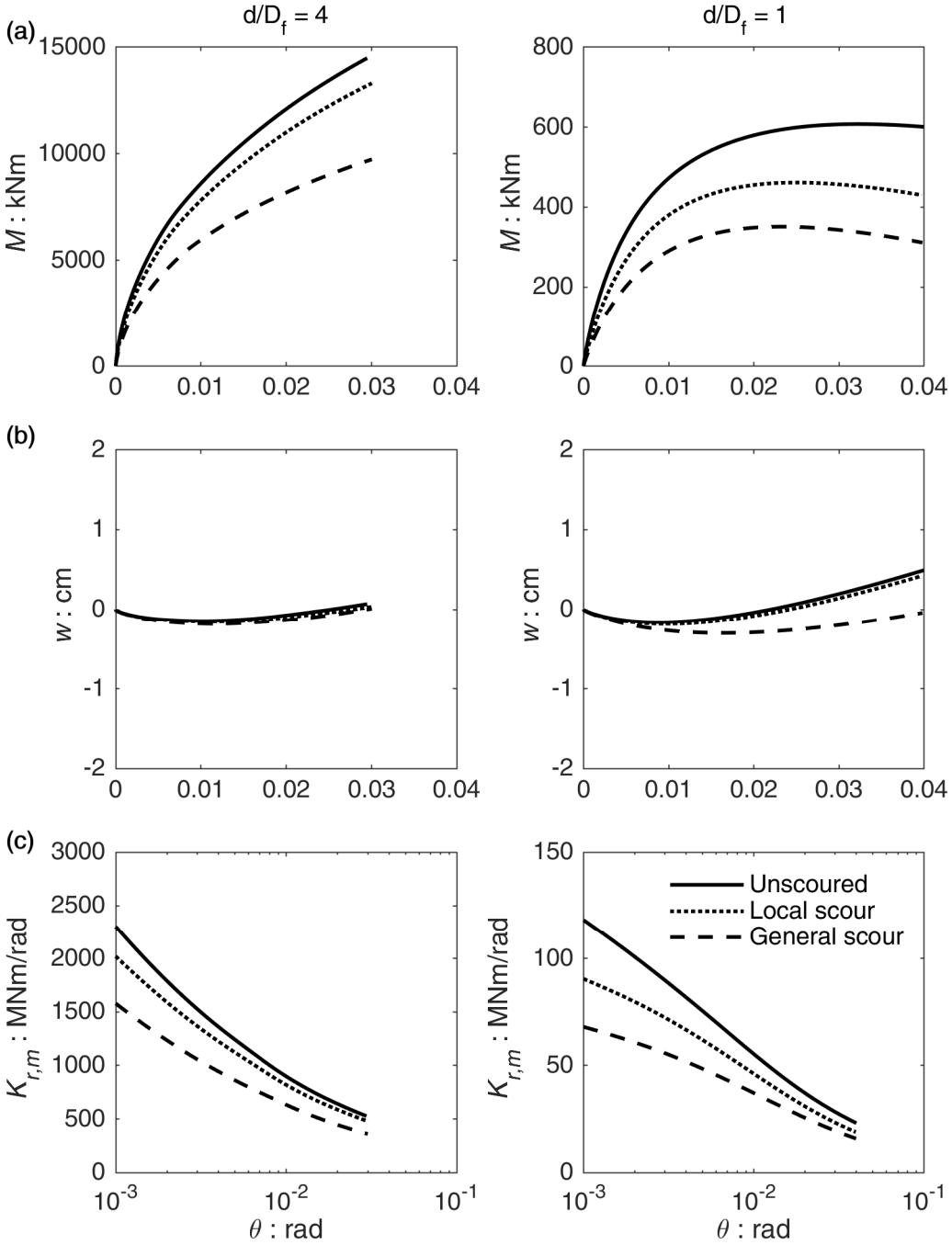

Figure 8.17: Comparison between the rocking response of caisson foundations with $d/D_f = 4$ (left figures) and $d/D_f = 1$ (right figures) before and after scouring: (a) external overturning moment-rotation $M - \theta$ curves; settlement-rotation $w - \theta$ curves; (c) rocking monotonic stiffness-rotation $K_{r,m} - \theta$ curves.

Figure 8.17 plots the rocking responses before and after scouring in terms of external overturning moment-rotation $M-\theta$ curves, settlement-rotation $w-\theta$ curves, and rocking monotonic stiffness-rotation $K_{r,m}-\theta$ curves. It is worth mentioning that, for consistency, the overturning moment is always computed by considering as a reference point the centre of the base of the footing.

As expected, the caisson with $d/D_f=4$ presents a significant increase of the moment capacity for all the scouring conditions examined (Figure 8.17.a). Such an increase is enough to fully compensate for the larger $P-\theta$ effects suffered by the deep footing (due to the increase of both the deck mass and the load arm). The external overturning moment M thus progressively increases for the entire range of rotations here investigated, as opposite respect the caisson with $d/D_f=1$ for which the $P-\theta$ effects becomes predominant for $\theta>0.02\,\text{rad}$.

Although the increase of the embedment depth implies a consistent reduction of the normalized scour depth d_s/d, the effects of scouring on the capacity of the structure are still significant (Figure 8.17.a). In particular, the reduction of the unscoured moment capacity M_{ult} is about 10% if the footing is subjected to local scour, increasing up to 30% after general scour. By comparing the two families of curves, it appears evident that the response of the foundation after local scour is closer to the unscoured one for the caisson with $d/D_f=4$.

Interestingly, the settlement-rotation $w-\theta$ response seems not to be affected by scouring for the caisson with $d/D_f=4$ (Figure 8.17.b). As for the footing with $d/D_f=1$, the curves assume the typical trend expected for moderately loaded foundations, without showing a clear tendency to sink or uplift. Nevertheless, the three curves are almost coincident in contrast to the reference case, suggesting that the effects of general scour on the bearing capacity mechanism tends to vanish with increasing d/D_f (and decreasing d_s/d).

As regards the $K_{r,m}-\theta$ curves (Figure 8.17.c), the stiffness of the deep caisson is clearly much higher in respect to the one observed for the reference case. However, its response falls in the highly nonlinear range (characterized by a fast decay of $K_{r,m}$) even for relatively small rotations. As a matter of fact, the displacements induced in the soil along the sides of the footing increase with increasing embedment depths. Consequently, the soil along the sides of the deep caisson experiences larger shear strains for a given rotation, triggering more rapidly the material nonlinearity. The latter is also confirmed by the comparison between the void ratio contours for the two caissons, presented respectively in Figure 7.17 and Figure 8.19.

The previous observations can be analyzed in light of the $M_{base}-\theta$ and $M_{sides}-\theta$ curves reported in Figure 8.18. The resisting moment exerted by the bearing capacity mechanism is practically not affected by scouring for the caisson with $d/D_f=4$ (Figure 8.18.a). This is also consistent with the results of the vertical push tests, which predict a reduction of the vertical capacity V_{ult} due to general scour equal just to the 9% for the deep caisson. Conversely, the effects of scouring on the lateral resisting moment M_{sides} (the predominant resisting mechanism for deep caissons) are significant also for the footing with $d/D_f=4$ (Figure 8.18.b).

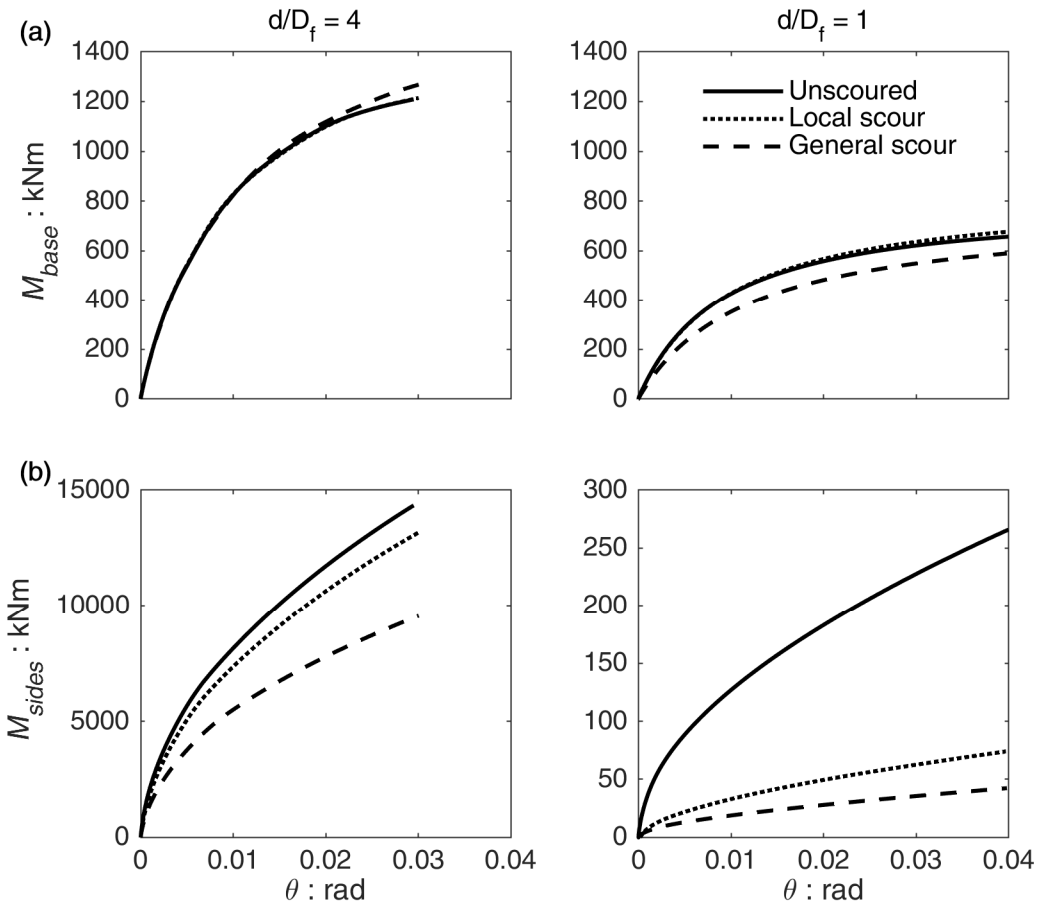

Figure 8.18: Comparison between the rocking response of caisson foundations with $d/D_f = 4$ *(left figures) and* $d/D_f = 1$ *(right figures) before and after scouring: (a) base resisting moment-rotation* $M_{base} - \theta$ *curves; (b) sides resisting moment-rotation* $M_{sides} - \theta$ *curves.*

Although general scour does not affect particularly the base resisting mechanism of the caisson with $d/D_f = 4$, the differences with local scour seems to be more pronounced concerning the reference case. Such behaviour can be explained by observing the failure mechanisms taking place in the soil close to the deep caisson.

Figure 8.19 plots the deformed mesh with superimposed void ratio e and total displacement u_{tot} contours for a rotation of 0.02 rad. As the embedment depth increases, the volume of soil involved in the lateral failure mechanism also increases, reducing the effects of the local erosion around the footing. This is not the case of general scour, which leads to the removal of a constant thickness sand layer.

The u_{tot} contours reported in Figure 8.19 also reveal that the deeper caisson is not rotating around the centre of its base, but the rotation pole is inside the footing at a certain depth. As suggested by Zafeirakos and Gerolymos (2016), the evolution of the rotation pole during a pushover test can be assessed by referring to the depth of the pole z_p, normalized to the embedment depth d.

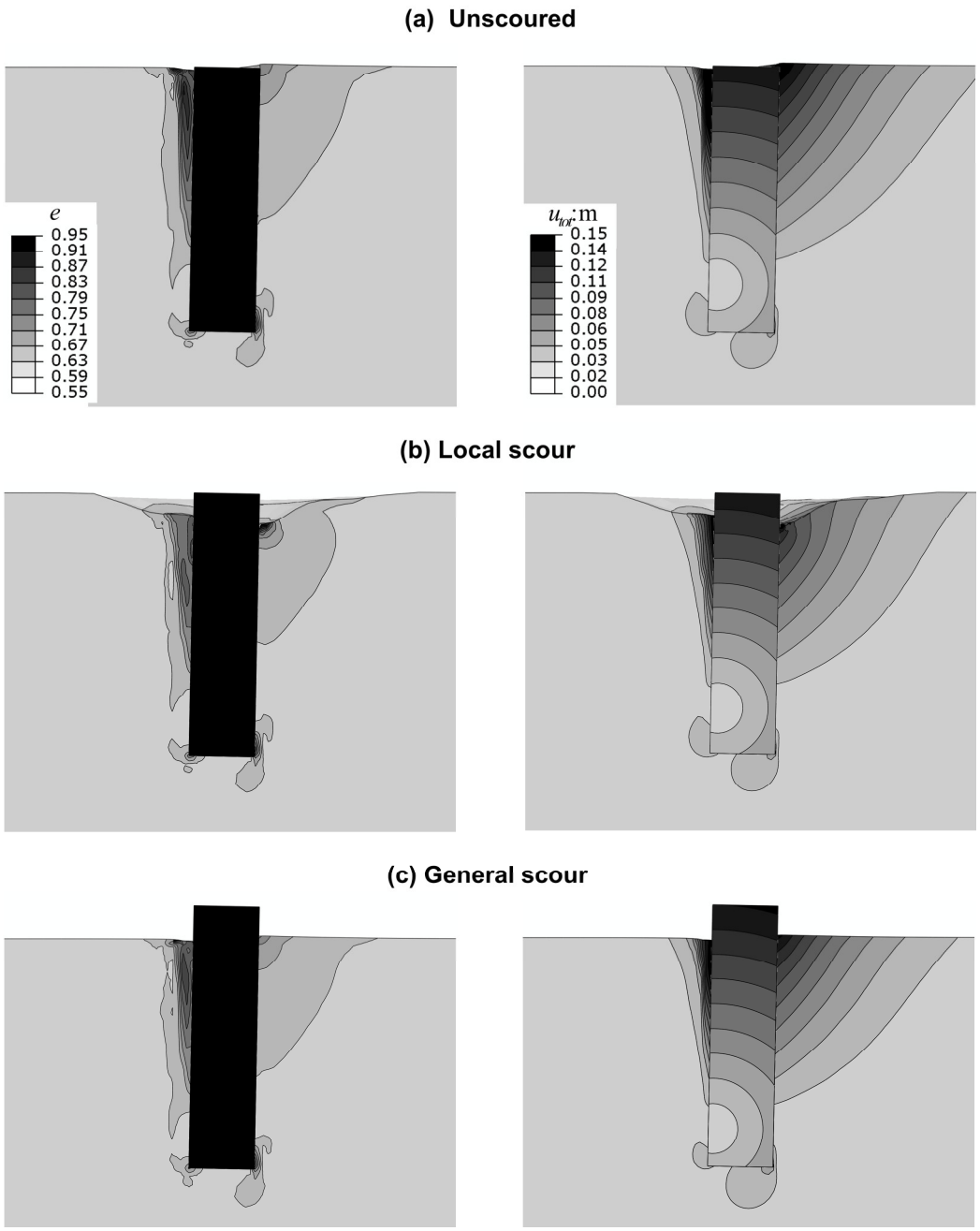

Figure 8.19: Deformed mesh with superimposed void ratio e (left figures) and total displacement u_{tot} (right figures) contours for an imposed rotation of 0.02 rad: (a) unscoured foundation; (b) foundation subjected to local scour; (c) foundation subjected to general scour. Deep caisson foundation with $FS_{v,unsc} = 8$ and $d/D_f = 4$.

Within a small-displacements framework, the z_p of a rigid caisson can be computed as (Zafeirakos and Gerolymos, 2016):

$$z_p \approx \frac{\delta u_p}{\delta \theta_p} \tag{8.1}$$

being δu_p and $\delta\theta_p$ the incremental horizontal translation and rotation, respectively (see also the schemes reported on the left of Figure 8.20).

Figure 8.20 compares the evolution of the z_p/d ratio with θ for the two caissons as obtained from the numerical simulations. The rotation pole of the caisson

with $d/D_f = 1$ is initially placed just below the foundation (Figure 8.20.a). The $w-\theta$ curves presented in Figure 8.17 reveal in fact that the foundation, during the first branch of its rocking response, accumulates plastic settlements due to progressive soil yielding.

However, for increasing θ, the soil dilatancy becomes predominant and the foundation starts to uplift. As a consequence, the depth z_p tends to decrease (i.e. the rotation pole moves up). At very high rotations (i.e. when the failure mechanism is fully developed), z_p reaches the base of the footing. As suggested by Fröhlich (1936), such a condition indicates that the maximum lateral resistance can be attained from the soil along the pushing side of the caisson.

It is interesting to notice that the effects of scouring induce a slight lowering of the rotation pole, especially for the general scour condition. For shallow caissons, general scour affects the bearing capacity mechanism, increasing the amount of settlement accumulated and increasing, in turn, the depth of the pole z_p.

The rocking response of the deep caisson is dominated by the lateral resisting mechanism. For this situation, the maximum lateral force (which may be attained if the caisson rotates around its base) would overcome the sum of the external horizontal force H plus the base sliding resistance. As a consequence, the lateral resistance can just partially be attained (See Appendix A.2 for further details), and the rotation pole raises (Figure 8.20.b).

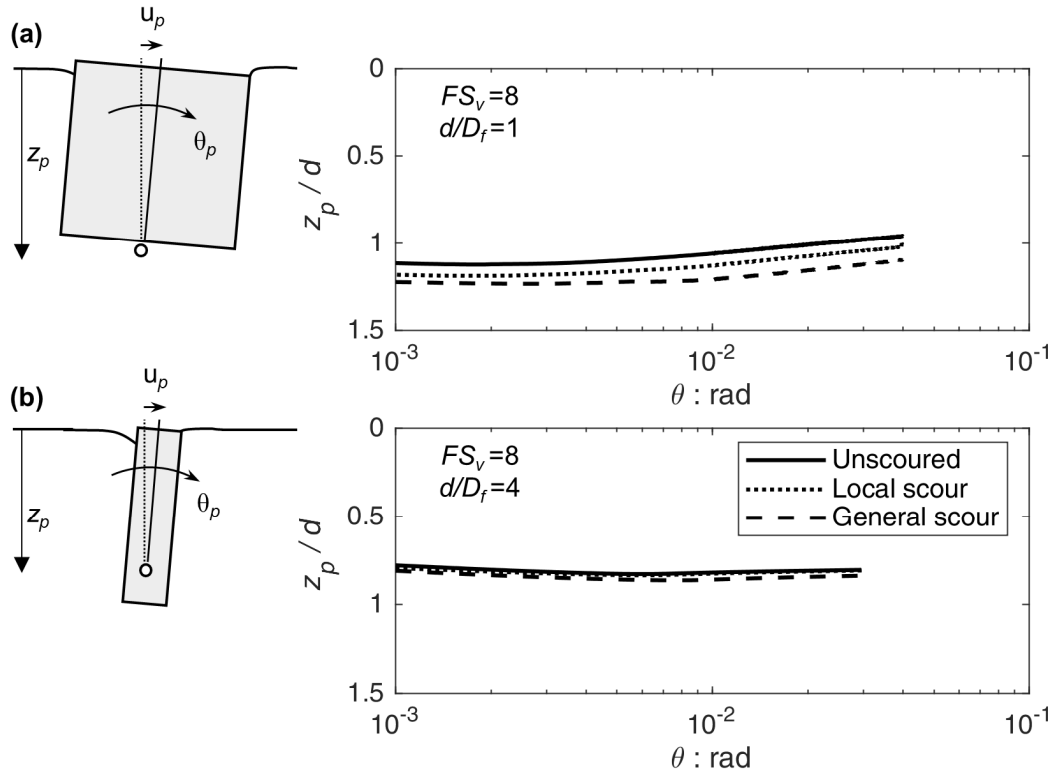

Figure 8.20: Comparison between the rocking response of caisson foundations with $d/D_f = 1$ (a) and $d/D_f = 4$ (b) before and after scouring in terms of the evolution of the normalized depth to rotation pole z_p/d.

As shown in Figure 8.18, neither local nor general scour affects the bearing capacity mechanism of the deeper caisson. Moreover, the foundation does not accumulate significant settlement (or uplifting) with increasing θ (Figure 8.17.b). As consequence, the z_p / d ratio for the deep caisson is almost constant (and <1) with increasing θ for all the scouring conditions.

8.3.3 Discussion

The comparison between the rocking responses of the two limit conditions (i.e. a shallow caisson with $d/D_f = 1$ and a slender one with $d/D_f = 4$) has shown that the effects of scouring are strongly influenced by the embedment depth d. Such influence is discussed and analyzed in this section by referring to the results obtained for the three foundations with $FS_{v,unsc} = 8$ and d/D_f equal to 1, 2, and 4.

Figure 8.21.a reports the moment capacity M_{ult} (computed for a rotation of 0.02 rad) as a function of the slenderness ratio d/D_f. In absolute terms, an increase of the embedment d has a very strong impact on the response of the footing. To focus on the scouring effects it is possible to refer to the normalized (with respect to the unscoured condition) moment capacity of the footing $M_{ult}/M_{ult,unsc}$, reported as a function of d/D_f in Figure 8.21.b. As the embedment d increases, the normalized scour depth d_s/d progressively decreases. Consequently, it would be reasonable to expect that also the effects of scouring would progressively decrease.

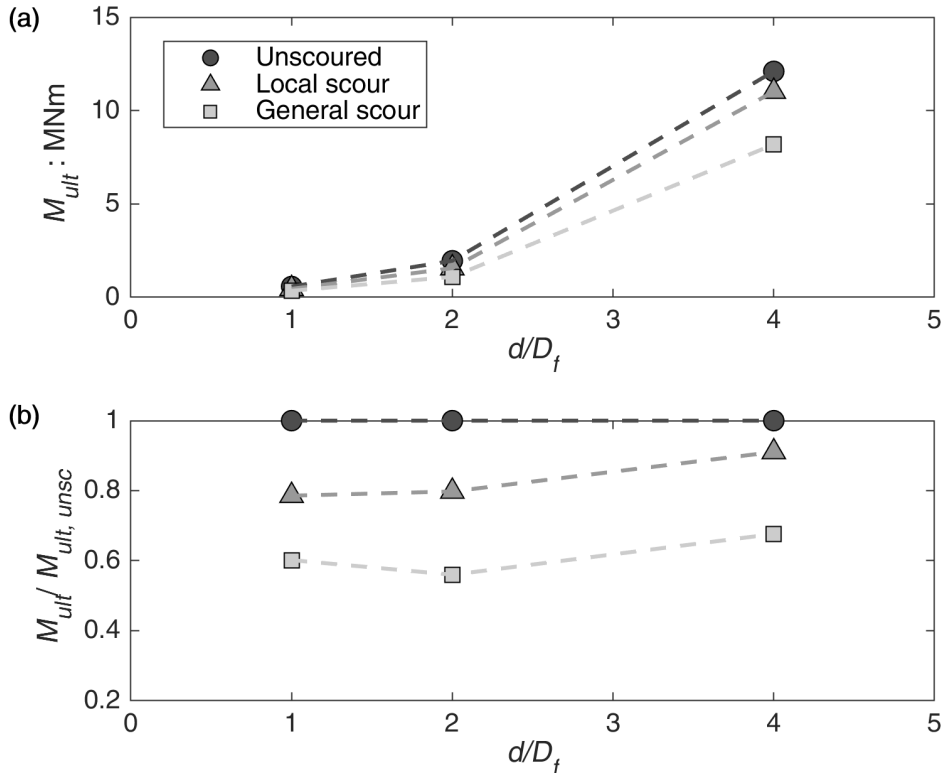

Figure 8.21: Influence of the slenderness ratio d/D_f on the rocking response of caisson foundations with $FS_{v,unsc} = 8$ before and after scouring: (a) moment capacity M_{ult}; (b) normalized moment capacity $M_{ult}/M_{ult,unsc}$. Values computed for a rotation $\theta = 0.02$ rad.

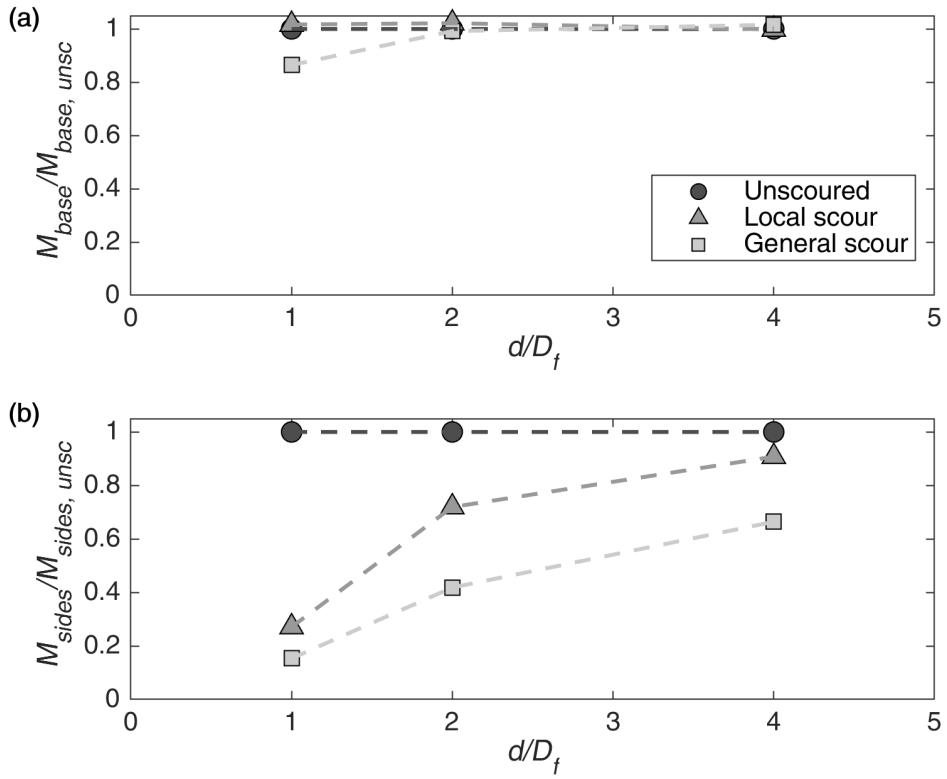

Figure 8.22: Influence of the slenderness ratio d/D_f on the rocking response of caisson foundations with $FS_{v,unsc}=8$ before and after scouring: (a) normalized base resisting moment $M_{base}/M_{base,unsc}$; (b) normalized sides resisting moment $M_{sides}/M_{sides,unsc}$. Values computed for a rotation $\theta=0.02\,\text{rad}$.

However, this is not the case of the foundation with d/D_f equal to 2, for which the reduction of the capacity due to local and general scour is equivalent, or even higher, to the one obtained for the shallow caisson (with $d/D_f=1$). For larger embedment depths (as in the case of the deep caisson with $d/D_f=4$) the reduction of d_s/d becomes instead predominant, and the effects of scouring decrease (especially for the local scour condition).

Such behaviour can be explained by looking at the resisting moments exerted by the two different mechanisms. Figure 8.22 plots the normalized base $M_{base}/M_{base,unsc}$ and lateral $M_{sides}/M_{sides,unsc}$ moments obtained for a rotation of 0.02 rad, as a function of the slenderness ratio d/D_f . As previously discussed, the effects of scouring on the vertical capacity vanish with increasing d/D_f (and decreasing d/d_s). No significant reduction is thus induced on M_{base} , even for the caisson with $d/D_f=2$ (Figure 8.22.a). Nevertheless, the lateral resisting mechanism (which is more deeply affected by scouring) becomes predominant on the base one with increasing d/D_f . Therefore, the impact of both general and local scour on the moment capacity M_{ult} increases for caisson with $d/D_f=2$, although their effect on M_{sides} reduces with d/D_f .

Finally, Figure 8.23 reports the influence of the slenderness ratio d/D_f on the small-strain (i.e. for a conventional rotation $\theta=0.001\,\text{rad}$) rocking monotonic secant stiffness $K_{r,m}$. The trends reported in the plot are consistent with the responses observed in terms of moment capacity for high rotations (Figure 8.21).

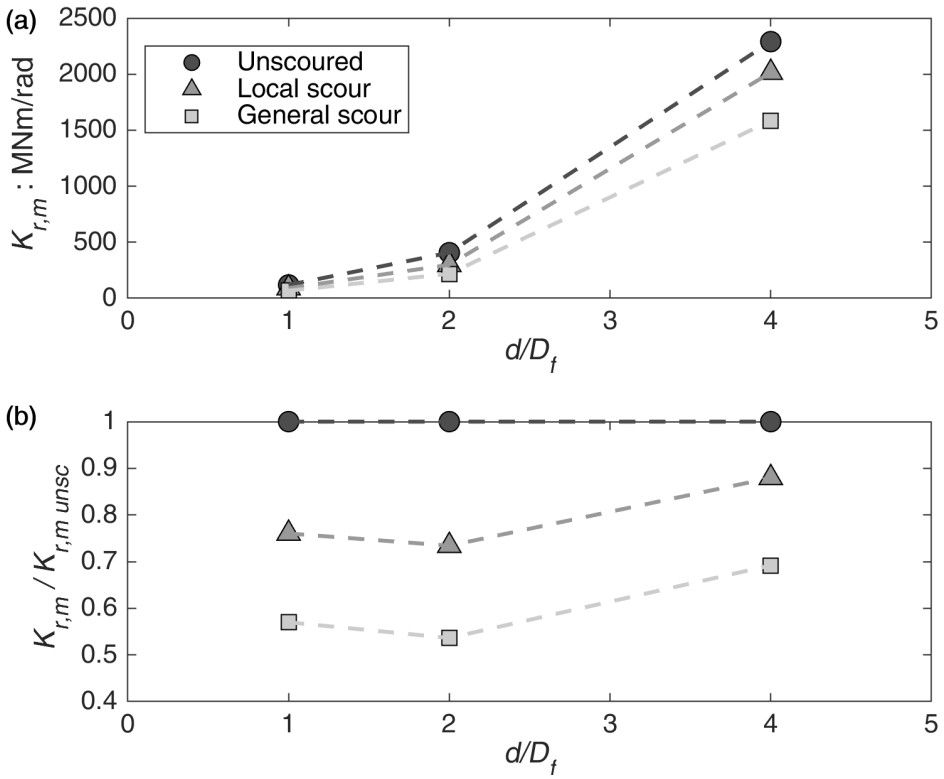

Figure 8.23: Influence of the slenderness ratio d/D_f on the rocking response of caisson foundations with $FS_{v,unsc} = 8$ before and after scouring: (a) small-strain monotonic rocking stiffness $K_{r,m}$; (b) normalized small-strain monotonic rocking stiffness $K_{r,m}/K_{r,m\,unsc}$. Values computed for a rotation $\theta = 0.001\,\text{rad}$.

The marked increase of the lateral resisting moment with d/D_f produces a rise up of $K_{r,m}$ before scouring from 120 MNm/rad (for the caisson with $d/D_f = 1$) to about 2400 MNm/rad (for the caisson with $d/D_f = 4$). Local scour induces a decrease of $K_{r,m}$ of about 25% for the caissons with d/D_f equal to 1 and 2, reducing to about 10% for deep caisson. The effects of general scour are more pronounced, with a stiffness reduction varying from 45% to 30%. These results suggest that vibration-based techniques could be a viable option to effectively monitor the evolution of the scour depth, even for relatively deep foundations.

Broadly speaking, the main aspect arising, once again, from the results of the simulations is the importance of the hydraulic scenario, and, thus, of the shape of the scour hole. With increasing slenderness ratio d/D_f (and, thus, decreasing normalized scour depth d_s/d), the contribution of the base resisting mechanisms to the overall capacity of the system tends to decrease. Moreover, the impact of general scour on FS_v tends to vanish. As a consequence, one would expect a similar response from the foundations subjected to general and local scour and, in general, a smaller reduction of the performance of the footing due to scouring.

However, this is not necessarily true, especially for foundations with intermediate slenderness ratios (i.e. $d/D_f = 2$). For these foundations, the impact of scouring on the lateral resisting mechanism (which is now the predominant one) is still very significant, leading to a strong reduction of the overall capacity of the system.

Moreover, the larger amount of soil involved in the lateral failure mechanism enhances the discrepancies between the effects of general and local scour. It may therefore be concluded that it is of crucial importance to model appropriately the geometry corresponding to the actual hydraulic scenario responsible for the local (or general) erosion of soil.

Chapter 9

Conclusions and Recommendation

This study dealt with the response of bridge piers subjected to flood-induced scour, in an attempt to quantify the impact of soil erosion on the performance of the structure. In particular, the study considered as base case a slender pier supported by a cylindrical caisson founded on dense sand.

In this respect, the first objective of the research was to develop an experimental approach to assess the influence of scouring on the mechanical response of the pier. A hybrid 2-step methodology was developed for this purpose. The first step models the hydraulic process of local scour around the pier in 1*g* using a Miniaturized Tidal Generator recently developed at the ETH Zurich (Jones and Anastasopoulos, 2020). The results of the experimental tests serve then as a basis to reproduce the actual shape of the scour hole in physical models suitable for testing in a geotechnical drum centrifuge. The mechanical consequences of scouring are then investigated under proper stress scaling in the second step. This experimental approach has the advantage of studying the mechanical problem as a direct consequence of the hydraulic phenomenon, without introducing any further hypothesis or assumption regards the expected depth and shape of the scour hole.

The 2-step methodology was applied to study the performance of a prototype bridge pier before and after scouring. The results have shown the significant impact of foundation scour, in particular on the lateral response of the pier. Furthermore, the observed differences among the different hydraulic scenarios considered (i.e. local and general scour) have proven the importance of linking a well-defined hydraulic scenario to its mechanical consequences.

The second part of the study was devoted to the numerical modelling of the mechanical consequences of scouring. The analyses were carried out adopting an advanced constitutive model (i.e. the Severn-Trent model, Gajo and Muir Wood, 1999b, a; Gajo, 2010) to simulate the sand behaviour which was calibrated independently on a set of element tests. Subsequently, the numerical model was validated using the results of the centrifuge tests. The analyses gave also the

opportunity to investigate the effects of scouring on the different resistant mechanisms exerted by the soil around the foundation. Finally, the validated model was used to perform a parametric analysis to extend the results of the study to more general conclusions. In particular, the simulations focused on the effects of scouring on foundations characterized by different vertical loading conditions and slenderness ratios.

In the following, the main conclusions of the research are discussed and summarized. Still many aspects regard the scour phenomenon and its mechanical consequences need to be investigated. Some recommendations are then given at the end of the section, including suggestions on future experimental and numerical studies.

9.1 Conclusions

The main aspect that emerges from the physical modelling of the phenomenon is its significant impact on the lateral performance of caisson foundations. The hydraulic scenario considered in the experimental tests has produced extensive local scour around the caisson foundation. Such a scenario corresponds to an extreme, but reasonable, hydraulic condition. However, its mechanical consequences on the response of the footing are detrimental.

Based on the results of both the centrifuge tests and the numerical simulations, the following main conclusions can be drawn on the effects of scouring on the performance of bridge piers supported on caisson foundations.

Lateral and vertical monotonic capacity

Local scour has a limited effect on the vertical response of the prototype foundation (i.e. a cylindrical caisson characterized by $d/D_f = 1$ and $FS_{v,unsc} \approx 8$) investigated in the experimental tests, but it reduces its moment capacity M_{ult} by 19% to 38%, depending on the direction of loading. Conversely, general scour (i.e. the removal of a constant thickness soil layer) also affects the vertical capacity of the footing. In addition, its impact on the lateral response of the pier is even more pronounced, leading to a reduction of the moment capacity M_{ult} of about 48%.

The results of the numerical analyses performed on the same prototype bridge pier confirm these differences. The simulations of the vertical push tests show that general scour leads to a reduction of FS_v from about 8 to 5.6 (i.e. 30%), while local scour has an almost negligible effect on FS_v (as also shown by the centrifuge tests). Consequently, under lateral loading local scour mainly affects the sidewall resisting moment M_{sides} whereas general scour also reduces the resistance exerted by the soil below the footing M_{base}. For a caisson with $d/D_f = 1$, the predominant resisting mechanism is the bearing capacity one, the overall lateral monotonic response of the foundation therefore strongly depends on the type of hydraulic condition considered (i.e. general or local scour).

Slow-cyclic lateral capacity

The slow-cyclic lateral response of the foundation shows a significant overstrength when compared to the monotonic backbone curve and the corresponding M_{ult}. Such overstrength is mainly attributed to the hardening of the sand response and the increase of embedment due to settlement accumulation. Under fully drained conditions, the application of multiple loading cycles leads to an increase of the secant soil stiffness along the loading direction. With increasing loading cycles, however, the soil tends to a steady-state and the volumetric strain accumulation, as well as the secant stiffness evolution, begins to level off. Such sand behaviour is responsible for the initial hardening of the foundation stiffness with multiple loading cycles. The differences between the monotonic and the cyclic response, quantified through the moment overstrength ratio r_M, are even more pronounced when the pier is subjected to foundation scour. In particular, local scour leads to a moderate increase of r_M while the effect of general scour is more pronounced. This is mainly attributed to the drastic increase of the embedment ratio due to the progressive accumulation of settlement.

Rate of settlement accumulation under cyclic loading

The centrifuge tests and the numerical simulations have shown that the amount of settlement accumulated during cyclic loading increases slightly due to local scour. Conversely, the erosion of a constant thickness soil layer leads to a substantial accumulation of permanent settlement.

These observations can be explained by considering the evolution of the rate of settlement accumulation $\overline{w}_c$ with increasing rotation amplitudes. For small cyclic rotations, the vertical response under cyclic loadings of a moderately loaded foundation (as in the case of the prototype bridge pier) is mainly dominated by sand densification. As a consequence, the (small) initial accumulation of settlements is not significantly influenced by scouring. For larger rotations, the bearing capacity mechanism begins to mobilize, and soil yielding becomes the controlling factor. Under this condition, the settlement accumulation is partially counterbalanced by the dilative tendency typical of dense sands. After a certain rotation, the sand dilation becomes predominant and the rate of settlement accumulation tends to stabilize or even reduce. For a given rotation amplitude, the two mechanisms prevail on each other depending on the vertical safety factor FS_v of the footing. General scour leads to a reduction of FS_v of about 30%. Such reduction tips the balance, for intermediate rotations, in favour of the settlement accumulation. Conversely, local scour does not affect FS_v. For this hydraulic condition, the equilibrium between the two mechanisms remains unchanged and the amount of permanent settlements does not significantly increase.

Rocking stiffness degradation and damping ratio curves

The degradation of the secant cyclic (and monotonic) rocking stiffness with rotation and the corresponding hysteretic damping ratio offer a convenient way to assess the

nonlinear foundation response. Moreover, the rocking stiffness curves can be used to quantify the differences between the monotonic and the cyclic response of the foundation.

The comparison between the cyclic secant stiffness $K_{r,c}$ curves and the monotonic ones $K_{r,m}$ reveals that the previously discussed overstrength (due to the application of multiple loading cycles) leads to a significant increase in the stiffness of the footing. Nevertheless, the trends are consistent between cyclic and monotonic tests. With increasing rotation amplitudes, both $K_{r,c}$ and $K_{r,m}$ progressively decrease due to the soil nonlinear behaviour. For the entire range of θ (even at very small rotations), general scour leads to a pronounced reduction of the rocking stiffness of the system; conversely, the effect of local scour is moderate (but still significant).

Despite the geometric asymmetry of the scour hole, the direction of loading (i.e. upstream or downstream) does not significantly affect the experimental $K_{r,m}$ curves measured for the local scour condition. This is consistent with the shape of the $M-\theta$ loops, which are only slightly skewed. Such behaviour can be explained by looking at the results of the numerical simulations of the slow-cyclic lateral pushovers. Local scour mainly reduces the lateral resisting moment M_{sides}, which is effectively affected by the loading direction. However, the larger contribution to the moment capacity of the footing is given by the base resisting mechanism. Consequently, the importance of the loading direction tends to vanish when the two resisting moments (i.e. M_{base} and M_{sides}) are summed up to obtain the total moment M_{tot} which defines the monotonic (or cyclic) rocking stiffness. It is worth mentioning that this consideration holds for the prototype cylindrical caisson here considered (characterized by a slenderness ratio $d/D_f = 1$ and a $FS_{v,unsc} \approx 8$). Foundations with different characteristics (for instance characterized by larger $FS_{v,unsc}$ or d/D_f) may present a stronger asymmetric response, according to the relative importance of the lateral resisting mechanism.

The hysteretic damping ratio $\xi_{r,h}$ quantifies the amount of energy dissipated by the soil-structure system within each loading cycle. The centrifuge tests show that the $\xi_{r,h}$ increases with rotation θ due to the soil nonlinear behaviour, reaching a maximum of 0.4 to 0.5. As opposed to $K_{r,c}$, $\xi_{r,h}$ seems to be practically insensitive to scouring. These observations are partially confirmed by the results of the numerical simulations. Minor differences are in fact observed in the numerical $\xi_{r,h}-\theta$ curves due to general and local scour. The removal of soil along the sides of the footing slightly reduces the amount of energy dissipated within each loading cycle. Such small effects may not have been detected by the experimental tests due to the uncertainties affecting the experimental estimation of $\xi_{r,h}$.

Influence of the vertical safety factor

The vertical load V (and, thus, the vertical safety factor before scouring $FS_{v,unsc}$) affects mainly the bearing capacity mechanism developing below the base of the foundation. The base resisting moment M_{base} tends to increase (for $FS_{v,unsc} \geq 2$) with increasing V due to the reduction of the load eccentricity. Conversely, M_{sides}

is not influenced by the vertical load V. As a consequence for a relatively shallow caisson ($d/D_f = 1$), the predominant resisting mechanism during the lateral pushover of the structure depends on the vertical loading condition. For heavily loaded bridge piers ($FS_{v,unsc} \approx 4$), M_{base} largely prevails on M_{sides}. General scour (which also affects the bearing capacity mechanism) has then a huge impact on the capacity of the footing, while the effect of local scour is more moderate. The two hydraulic scenarios, therefore, produce quite different mechanical consequences. Conversely, M_{sides} becomes more relevant for lightly loaded bridge piers ($FS_{v,unsc} \approx 14$), reducing the differences between the two scenarios.

The vertical safety factor FS_v also defines the settlement regime shown by the caisson foundation during the lateral pushover. For the lightly loaded bridge pier ($FS_{v,unsc} \approx 14$), the response of the footing is unavoidably uplifting-dominated, regardless of scouring. Conversely, the vertical response of the heavily loaded caisson ($FS_{v,unsc} \approx 4$) is strongly influenced by scouring. For the unscoured foundation and the one subjected to local scour, the amount of settlement accumulated rapidly increases for small θ. However, its rate tends to decrease with increasing θ. On the other side, the response of the foundation after general scour is sinking-dominated and the permanent settlement monotonically increases for the entire range of θ. The latter can be attributed to the decrease of the actual vertical safety factor FS_v (i.e. from 4 to 2.6) due to general scour, which brings the footing into the sinking-dominated regime.

An additional effect associated with lower vertical safety factors $FS_{v,unsc}$ is the increase of second-order ($P-\delta$) effects. The vertical load V is defined by the deck mass m_1, which produces an additional moment $\Delta M(\delta)$ with increasing θ due to $P-\delta$ effects. For slender structures (such as bridge piers), such effects can be substantial. In particular, in the case of very heavily loaded foundations ($FS_{v,unsc} \leq 3$) even a very small initial rotation produces a non-negligible $\Delta M(\delta)$. In such condition, the reduction of the lateral capacity due to scour may result to the instability of the pier, which may, in turn, accumulates permanent rotations and eventually collapse, even under just the dead load of the structure.

Influence of the slenderness ratio

For a given hydraulic scenario characterized by a certain expected scour depth d_s, an increase of the slenderness ratio d/D_f of the caisson implies a decrease of the normalized scour depth d_s/d. Consequently, it would be reasonable to expect that deeper foundations are less sensitive to scouring. This certainly applies to very deep caissons with $d/D_f \geq 4$, but it is not necessarily the case of foundations characterized by intermediate slenderness ratios. As d/D_f increases, the predominant resisting mechanism becomes the lateral one, which is mostly affected by both general and local scour. Therefore, the impact of scouring on the total moment capacity M_{ult} may (initially) increase with d/D_f despite the reduction of normalized scour depth d_s/d.

The same considerations apply also to the secant rocking stiffness $K_{r,m}$ of the system. Local scour induces a decrease of $K_{r,m}$ (obtained at small rotations

$\theta = 0.001\,\text{rad}$) of about 25% for the shallow ($d/D_f = 1$) and the intermediate ($d/D_f = 2$) caissons, reducing to about 10% for the deep ($d/D_f = 4$) foundation. The effects of general scour are instead more pronounced, with a stiffness reduction varying from 45% to 30%. These results suggest that vibration-based techniques could be a viable option to effectively monitor the evolution of the scour depth, even for relatively deep foundations.

Overall, what emerges from the physical modelling of both the aspects (i.e. the *hydraulic* problem and its *mechanical* consequences) of the phenomenon is that the effects of *local scour* on the foundation response are significantly different from those of *general scour*. Such effects can be successfully predicted by numerical models only if the actual geometry of the problem, which depends on the hydraulic scenario, is carefully reproduced.

However, in practice the shape of the local scour hole is typically neglected, making no distinction between local and general scour. The evolution of the scour process is usually simulated by progressively removing soil layers of constant thickness – a simplification considered to be conservative. Considering static loading, the results of this study confirm this hypothesis, indicating, however, that such a simplifying assumption can be over-conservative.

This is not necessarily the case for dynamic loading. Nonlinear soil–foundation response has been shown to be potentially beneficial for the seismic response of the superstructure (e.g., Gazetas et al., 2003; Pecker, 2003; Gajan et al., 2005; Gajan and Kutter, 2008; Anastasopoulos et al., 2010; Loli et al., 2014), something that can be of great relevance for the seismic retrofit of existing bridges. The reduction of foundation moment capacity M_{ult} leads to a reduction of inertia loading of the superstructure, at the cost of increased settlement. The simplifying assumption of general scour is therefore problematic, as the underestimation of M_{ult} (compared to local scour conditions) will lead to an *underestimation* of the inertia loading of the structure (*un-conservative*) and an *overestimation* of permanent settlement (*over-conservative*). These observations can have major implications on the seismic retrofit of existing bridges, calling for realistic modelling of the physical phenomenon to link the hydraulic scenario responsible for foundation scour to its mechanical consequences on the performance of the structure.

9.2 Recommendation for Future Research

A major contribution of this research was the development of an experimental methodology to investigate the mechanical problem as a direct consequence of the local scour process. The hybrid methodology “decouples” the two problems: in the first step the hydraulic process is analyzed in 1*g* using a Miniaturised Tidal Generator (MTG); the second step studies the mechanical problem in a geotechnical centrifuge under proper stress-scaling. The main advantage of this approach is the possibility of studying the problem without introducing any assumption on the local scour hole.

The decoupled approach represents a good balance between the reliability of the results and the feasibility of physical model tests. Nevertheless, the methodology is based on two underlying assumptions: (1) 1*g* experiments are appropriate to reproduce the hydraulic scouring process; and (2) the scouring process does not strongly influence the void ratio of the remaining soil. The first hypothesis is widely adopted in hydraulic experiments, where small and medium scale tests are conducted to study the scour phenomenon and the results are analyzed according to dimensionless quantities (e.g., Melville and Raudkivi, 1996; Coleman, 2005; Moreno et al., 2016). The second hypothesis is considered reasonable, especially in clear-water conditions where no sediments are transported by the river or the material is transported in suspension (Melville and Coleman, 2000). These assumptions could be relaxed through the direct (fully coupled) physical modelling of both the hydraulic and the mechanical part of the problem in a geotechnical centrifuge. The direct modelling approach would however require an MTG mounted in the geotechnical centrifuge, which is not currently feasible. The development of such a new apparatus would be the best option to simulate the entire process as realistically as possible.

As regards the numerical simulations, the analyses have proven that it is possible to predict the mechanical consequences of scouring for a wide range of problems, providing that the scour hole geometry is carefully reproduced. However, an aspect that is just partially captured by the numerical model is the hardening effect due to multiple loading cycles. Such progressive hardening leads to a substantial increase of the moment capacity under drained conditions, but it could be detrimental under undrained (or partially drained) conditions due to the pore-pressure build-up resulting from the kinematic constriction of zero volumetric strains (e.g. Zhu et al., 2013; Cox et al., 2014; Tasiopoulou et al., 2021). When dealing with problems that mainly involve a small number of loading cycles of different amplitudes, this aspect is not very relevant. However, it becomes significant when a large number of loading cycles of almost constant amplitude is applied to the structure. This is for instance the case of foundations used to support offshore wind turbines, which are typically subjected to wind/wave loadings. These types of structures are also prone to foundation scour, although the hydraulic scenario is quite different from the one analyzed in the present research. A specific study is therefore necessary to evaluate the impact of scouring on these types of structures, with due consideration of the effects of multiple loading cycles on the sand response.

Besides these specific suggestions regards numerical and experimental future developments, the main general aspect that necessitates further investigations is the influence of scouring on the dynamic response of bridge piers. This aspect is particularly relevant as budget constraints often prevent the immediate retrofitting of scoured bridges after floods, increasing the vulnerability of the structure to subsequent extreme events. Consequently, several studies have been recently developed to assess specific combined risks for bridge management (e.g. Alampalli and Ettouney, 2008). Nevertheless, a great research effort is still required to investigate the seismic performance of bridge piers subjected to foundation scour. It is also

crucial to study the dynamic response of scoured foundations bearing in mind the differences between local and general scour and, generally speaking, between different hydraulic scenarios.

Furthermore, the relevance of the actual hydraulic scenario may have major implications also on the vibration-based techniques recently proposed to monitor the evolution of the dynamic response of bridges due to scour (e.g., Foti and Sabia, 2010; Briaud et al., 2011; Prendergast and Gavin, 2014; Bao and Liu, 2017). The results of this research have confirmed that the erosive process leads to a significant reduction of the foundation stiffness. The latter can, in turn, be effectively used to infer the actual scour depth. Nevertheless, the extent of the stiffness reduction strongly depends on the hydraulic scenario considered (i.e. *general* or *local* scour). Moreover, the asymmetry of the local scour hole may result in a different dynamic response of the footing depending on the loading direction considered. Neglecting the actual shape of the local scour hole may, thus, imply an erroneous estimate of the scour depth, not necessarily on the safe side.

In this respect, it would be useful to assess the potential of dynamic structural testing in monitoring the effects of foundation scour through centrifuge tests, to properly account for the soil-structure interaction. Availing of the known scouring conditions, physical models may serve as a basis to develop novel vibration-based techniques. However, to date, very few experimental studies have been carried out under proper stress-scaling (Kariyawasam et al., 2020). Eventually, the effectiveness of such techniques has to be assessed through field testing. As also recognized by previous studies (Briaud et al., 2011), the actual site conditions may indeed significantly differ from the controlled conditions in laboratory due to the presence of incoherent noise and the difficulties in applying an impulsive force to the structure with sufficient energy content. It is therefore crucial to test the applicability of the developed techniques also on real case studies.

Appendix A

Approaches for predicting the capacity of caisson foundations

This appendix briefly summarizes the main approaches adopted in the common practice to estimate the capacity of caisson foundations against both vertical and horizontal actions. The method is presented with a view on the main resisting mechanisms exerted by the soil. The attention is focused on the specific case here considered, i.e. a cylindrical caisson foundation supported on dense sand and loaded under drained conditions.

A.1 Bearing capacity

The approach usually adopted to compute the bearing capacity $q_{\lim}$ of caisson foundations under drained conditions is based on the well-known three-term expression introduced by Terzaghi (1943).

The soil behaviour is assumed to be rigid, perfectly-plastic with a Mohr-Coulomb failure criterion. Within these assumptions, the bearing capacity can be computed considering the three resisting components: the weight of the soil below the foundation, the cohesion offered by the soil along the failure surface and the additional contribution provided by the overburden pressure applied in correspondence of the foundation base. The total bearing capacity is thus obtained, as an approximation, by superposition of the three effects.

The method is applied by referring to the general expression proposed by Brinch Hansen (1970), which takes into account also the effects of several factors on the bearing capacity of the foundation:

$$q_{\lim} = \frac{1}{2}\gamma' B_{eq} N_\gamma s_\gamma i_\gamma b_\gamma g_\gamma d_\gamma + c' N_c s_c i_c b_c g_c d_c + q' N_q s_q i_q b_q g_q d_q \qquad \text{(A.1)}$$

where: γ' is the unit weight of the soil under buoyancy; B_{eq} is the equivalent base of the foundation for which the vertical load is centred; q' is the effective

overburden pressure applied at the foundation base; N_γ, N_c and N_q are the bearing capacity factors; $s_{\gamma,c,q}$, $i_{\gamma,c,q}$, $b_{\gamma,c,q}$, $g_{\gamma,c,q}$, $d_{\gamma,c,q}$ are corrective factors, respectively, for the shape of the foundation, the load inclination, the base inclination, the slope of the soil, and the presence of soil along the sides of the foundation.

In the specific case here considered of a caisson foundation supported on sand under drained conditions, Eq. (A.1) can be rewritten as follows:

$$q_{\lim} = \frac{1}{2}\gamma' B_{eq} N_\gamma s_\gamma i_\gamma d_\gamma + q' N_q s_q i_q d_q \tag{A.2}$$

where the effective overburden pressure q' is computed as $\gamma' d$, with d equal to the embedment depth of the caisson. According to Prandtl (1921) and Caquot and Kerisel (1953), the bearing capacity factors are computed as follows:

$$N_q = \frac{1+\sin\varphi'}{1-\sin\varphi'} e^{\pi \tan\varphi'} \tag{A.3}$$

$$N_\gamma = 2\left(N_q + 1\right)\tan\varphi' \tag{A.4}$$

As previously discussed, the initial area of the footing has to be reduced to an equivalent area as a function of the net load eccentricity e_n, such that the vertical load is centred (Meyerhof, 1951). In particular, the eccentricity e_n can be written as:

$$e_n = \frac{M_{tot} - M_{sides}}{V} \tag{A.5}$$

where: M_{tot} is the total moment acting on the caisson, computed concerning the base of the footing; M_{sides} is the resisting moment given by the soil thrusts acting along the sidewalls of the foundation; V is the total vertical load. It is worth mentioning that the total moment should include also the additional moment $\Delta M(\delta)$ given by second-order (i.e. $P-\delta$) effects.

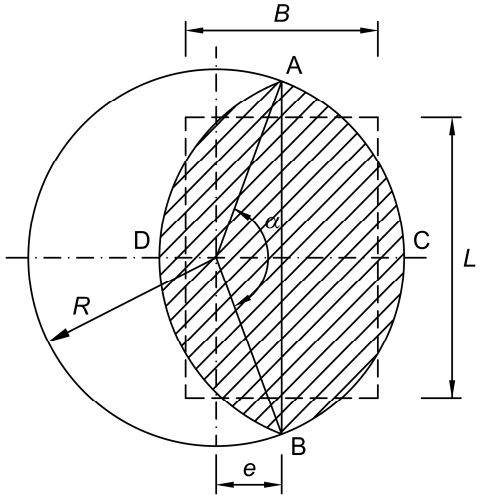

$$e = \frac{M}{N}$$

$$\frac{B}{L} = \frac{DC}{AB}$$

$$h = R - e$$

$$\text{Area}(B \cdot L) = 2 \cdot \left[R^2 \cdot \cos^{-1}\left(\frac{R-h}{R}\right) - (R-h)\left(2R \cdot h - h^2\right)^{0.5}\right]$$

Figure A.1: Equivalent rectangular area of an eccentrically loaded circular foundation (from Lancellotta et al., 2020).

For a circular foundation, the equivalent dimensions B_{eq} and L_{eq} are defined considering an equivalent rectangle constructed with the same aspect ratio of the actual base, so that the geometric centre coincides with the load centre (Figure A.1).

The tridimensionality of the failure mechanism induced by a circular footing is considered through the corrective factors s_γ and s_q, for which Vesic (1975) proposed the following expressions:

$$s_\gamma = 1 + 0.4\frac{B_{eq}}{L_{eq}} \tag{A.6}$$

$$s_q = 1 + \frac{B_{eq}}{L_{eq}}\tan\varphi' \tag{A.7}$$

while the corrective factors for the load inclination i_γ and i_q are computed according to Vesic (1973):

$$i_\gamma = \left(1 - \frac{H}{N + B_{eq}L_{eq}c'\cot\varphi'}\right)^{\frac{2+\frac{B_{eq}}{L_{eq}}}{1+\frac{B_{eq}}{L_{eq}}}+1} \tag{A.8}$$

$$i_q = \left(1 - \frac{H}{N + B_{eq}L_{eq}c'\cot\varphi'}\right)^{\frac{2+\frac{B_{eq}}{L_{eq}}}{1+\frac{B_{eq}}{L_{eq}}}} \tag{A.9}$$

being H the horizontal force acting on the foundation.

Finally, the contribution of the soil above the base of the footing is taken into account through the factors d_γ and d_q (after Brinch Hansen, 1970, and Vesic, 1973):

$$d_\gamma = 1 \tag{A.10}$$

$$\begin{aligned} d_q &= 1 + 2\tan\varphi'\left(1-\sin\varphi'\right)^2\frac{d}{B_{eq}} && d \le B_{eq} \\ d_q &= 1 + 2\tan\varphi'\left(1-\sin\varphi'\right)^2\tan^{-1}\left(\frac{d}{B_{eq}}\right) && d > B_{eq} \end{aligned} \tag{A.11}$$

with d equal to the embedment depth of the caisson.

Eq. (A.2) provides an estimation of the bearing capacity at the tip of the caisson foundation. A further contribution to the total bearing capacity is given by the friction along the sides of the footing. For a cylindrical caisson, this contribution can be expressed as (Kulhawy, 1991):

$$Q_{sides} = \pi D_f \int_0^d \gamma' z K(z)\tan(\delta)\,dz \tag{A.12}$$

where: D_f is the diameter of the caisson; δ is the friction angle at the soil-foundation interface; $K(z)$ is the coefficient of horizontal soil stress. This contribution is anyway usually negligible for relatively shallow (i.e. $d/D_f \approx 1$) foundations (e.g. Brandl, 1985; Gaudio, 2017).

The approach previously introduced is based on the assumption of a rigid, perfectly-plastic constitutive law for the soil with a Mohr-Coulomb failure criterion. However, the mechanical behaviour of granular materials is known to be both pressure- and density-dependent. For a sand in a dense state, the peak friction angle

φ'_{peak} is a function of both the initial void ratio and the effective confining pressure of the soil. For a bearing capacity problem, the state of the sand below the foundation varies due to the progressive increase of the load. Consequently, the contribution of the dilatancy to the soil resistance and, in turn, to the peak friction angle φ'_{peak} is not constant. A practical approach to estimate the peak friction angle φ'_{peak} consists of applying an iterative procedure as proposed by De Beer (1970). A first tentative $\varphi'_{peak}{}^{1}$ is assumed and the corresponding bearing capacity $q_{\lim}{}^{1}$ is computed. The equivalent confining pressure at failure $p'_{f}{}^{1}$ is obtained as (De Beer, 1970):

$$p'_{f} = \frac{1}{4}\left(q_{\lim} + 3q'\right)\left(1 - \sin\varphi'_{peak}\right) \tag{A.13}$$

A second tentative $\varphi'_{peak}{}^{2}$ can then be computed according to the Bolton (1986) relationship:

$$\varphi'_{peak} = \varphi'_{cs} + 3\left[D_R\left(10 - \ln p'_{f}\right) - 1\right] \tag{A.14}$$

where φ'_{cs} is the critical state friction angle of the soil, while D_R is the relative density. The iterative process continues as long as convergency is reached.

Such a method gives an estimation of the peak friction angle φ'_{peak} for bearing capacity problems. However, it should be considered that, due to the progressive failure, in a given instant the soil state is different throughout the slip surface. Moreover, for a horizontally-loaded caisson foundation, the problem is twofold given that, additionally to the bearing capacity mechanism, the resistant mechanism given by the soil thrusts at the sides of the footing is also mobilized. Consequently, it is not straightforward to define an "operative" friction angle φ'. An intermediate value between the peak friction angle φ'_{peak} and the critical state friction angle φ'_{cs} is usually adopted for design purposes.

A.2 Sides resistance

The abovementioned procedure is useful to estimate the bearing capacity of the foundation. The procedure however has been originally developed for shallow foundations with low embedment-to-diameter d/D_f ratios. In the case of a caisson foundation, the horizontal thrusts (as well as the corresponding resisting moment M_{sides}) given by the soil at the sides of the footing are not negligible and should therefore be considered.

A practical approach to estimate M_{sides} has been proposed by Fröhlich (1936). The method, recently adopted also by other Authors (e.g. Lanzano et al., 2011; Gaudio, 2017; Gaudio and Rampello, 2019), is based on the hypothesis of a rigid rotation of the caisson foundation. The effective horizontal stress σ_h' at the sides of the foundation is computed assuming a parabolic distribution defined as a function of the passive thrust coefficient K_P.

In particular, the method distinguishes between two different cases: the rotation centre at the base of the footing and above the base of the footing (Figure A.2). The first case (Figure A.2.a) takes place if Eq. (A.15) is verified, so if the maximum

soil thrust H_{sides} is lower or equal to the other horizontal forces acting on the foundation.

$$H + V \cdot \tan\varphi' \geq H_{sides} = \frac{1}{6} K_P \gamma' D_f d^2 \tag{A.15}$$

In such a condition, the sides resisting moment M_{sides} can be computed as:

$$M_{sides} = \frac{1}{12} K_P \gamma' D_f d^3 \tag{A.16}$$

Conversely, if Eq. (A.15) is not verified, the rotation centre will be above the base of the caisson (Figure A.2.b) and the resisting moment M_{sides} will be:

$$M_{sides} = \frac{1}{12} K_P \gamma' D_f d^3 + \frac{\left(H + V \cdot \tan\varphi'\right) \cdot d}{4} \tag{A.17}$$

Several limitations affect the estimation of M_{sides}. First of all, if a foundation supported on dense sand is considered, the passive thrust coefficient K_P has again to be defined as a function of an "operative" friction angle φ'. Secondarily, the approach is based on the assumption that the full passive resistance is mobilized at the head of the foundation. However, a significant rotation of the structure is necessary to mobilize the passive earth resistance (e.g. James and Bransby, 1970). From a performance-based perspective, such a rotation is probably higher than the maximum one attainable for the structure. Consequently, it may not be possible to reach the maximum lateral resistance without exceeding the Ultimate Limit State for the structure.

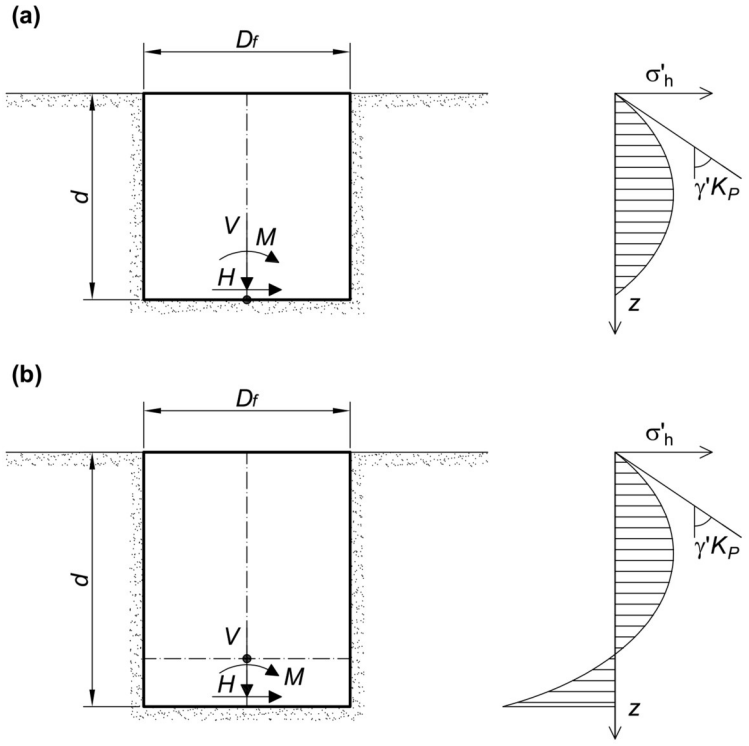

Figure A.2: Horizontal stress distribution at the sides of the caisson; (a) rotation centre above the base; (b) rotation centre at the base (modified from Gaudio, 2017, after Fröhlich, 1936).

References

Abate G, Caruso C, Massimino M, Maugeri M (2008) *Evaluation of shallow foundation settlements by an elasto-plastic kinematic-isotropic hardening numerical model for granular soil*. Geomechanics and Geoengineering: An International Journal 3:27-40

Abate G, Massimino M, Maugeri M, Wood DM (2010) *Numerical modelling of a shaking table test for soil-foundation-superstructure interaction by means of a soil constitutive model implemented in a FEM code*. Geotechnical and geological engineering 28:37-59

Alampalli S, Ettouney M (2008) *Multihazard applications in bridge management*. International Bridge and Structure Management:356

Alarcon-Guzman A, Leonards G, Chameau J (1988) *Undrained monotonic and cyclic strength of sands*. Journal of Geotechnical Engineering 114:1089-1109

Alipour A, Shafei B *Performance assessment of highway bridges under earthquake and scour effects*. In: Proceedings of the 15th world conference on earthquake engineering, 2012. pp 24-28

Anastasopoulos I, Gazetas G, Loli M, Apostolou M, Gerolymos N (2010) *Soil failure can be used for seismic protection of structures*. Bulletin of Earthquake Engineering 8:309-326

Anastasopoulos I, Kourkoulis R, Gelagoti F, Papadopoulos E (2012) *Rocking response of SDOF systems on shallow improved sand: An experimental study*. Soil Dynamics and Earthquake Engineering 40:15-33

Ansari S, Kothyari U, Ranga Raju K (2002) *Influence of cohesion on scour around bridge piers*. Journal of Hydraulic Research 40:717-729

Argyris J, Faust G, Szimmat J, Warnke E, Willam K (1974) *Recent developments in the finite element analysis of prestressed concrete reactor vessels*. Nuclear Engineering and Design 28:42-75

Arneson L, Zevenbergen L, Lagasse P, Clopper P (2012) *Evaluating scour at bridges: Hydraulic Engineering Circular No. 18*. Washington DC, USA

ASTM International (2014) *ASTM D854-14, Standard Test Methods for Specific Gravity of Soil Solids by Water Pycnometer*. ASTM International, West Conshohocken, PA

ASTM International (2015) *ASTM D4015-15, Standard Test Methods for Modulus and Damping of Soils by Fixed-Base Resonant Column Devices*. ASTM International, West Conshohocken, PA

ASTM International (2016) *ASTM D4254-16, Minimum Index Density and Unit Weight of Soils and Calculation of Relative Density*. ASTM International, West Conshohocken, PA

ASTM International (2017) *ASTM D2487-17, Standard practice for classification of soils for engineering purposes (Unified Soil Classification System)*. ASTM International, West Conshohocken, PA

ASTM International (2020) *ASTM D7181-20, Standard Test Method for Consolidated Drained Triaxial Compression Test for Soils*. ASTM International, West Conshohocken, PA

Ballio F, Bianchi A, Franzetti S, Mancini M *Vulnerabilità idraulica di ponti fluviali (in Italian)*. In: XXVI Convegno di Idraulica e Costruzioni Idrauliche, 1998. pp 69-80

Banerjee S, Ganesh Prasad G (2013) *Seismic risk assessment of reinforced concrete bridges in flood-prone regions*. Structure and Infrastructure Engineering 9:952-968

Bao T, Liu Z (2017) *Vibration-based bridge scour detection: a review*. Structural Control and Health Monitoring 24:e1937

Bateni SM, Borghei S, Jeng D-S (2007) *Neural network and neuro-fuzzy assessments for scour depth around bridge piers*. Engineering Applications of Artificial Intelligence 20:401-414

Been K, Jefferies M, Hachey J (1991) *The critical state of sands*. Geotechnique 41:365-381

Been K, Jefferies MG (1985) *A state parameter for sands*. Géotechnique 35:99-112

Bishop AW, Green GE (1965) *The influence of end restraint on the compression strength of a cohesionless soil*. Geotechnique 15:243-266

Bolton M (1986) *The strength and dilatancy of sands*. Geotechnique 36:65-78

Brandimarte L, Montanari A, Briaud J-L, D'Odorico P (2006) *Stochastic flow analysis for predicting river scour of cohesive soils*. Journal of hydraulic engineering 132:493-500

Brandimarte L, Paron P, Di Baldassarre G (2012) *Bridge pier scour: A review of processes, measurements and estimates*. Environmental Engineering and Management Journal 11:975-989

Brandl H *Bearing capacity of piers and piles with large diameters*. In: Eleventh International Conference on Soil Mechanics and Foundation Engineering, San Francisco, 12-16 August 1985. Balkema (AA),

Breusers H (1966) *Conformity and time scale in two-dimensional local scour*.

Breusers H, Nicollet G, Shen H (1977) *Local scour around cylindrical piers*. Journal of Hydraulic Research 15:211-252

Breusers H, Raudkivi AJ (1991) *Scouring*. AA Balkema,

Briaud J-L, Chen H-C, Li Y, Nurtjahyo P (2004) *SRICOS-EFA method for complex piers in fine-grained soils*. Journal of geotechnical and geoenvironmental engineering 130:1180-1191

Briaud J-L, Chen H-C, Li Y, Nurtjahyo P, Wang J (2005) *SRICOS-EFA method for contraction scour in fine-grained soils*. Journal of geotechnical and geoenvironmental engineering 131:1283-1294

Briaud J-L et al. (2011) *Realtime monitoring of bridge scour using remote monitoring technology*. Texas Transportation Institute,

Briaud J-L et al. (1999a) *SRICOS: Prediction of scour rate at bridge piers*. Texas Transportation Institute, The Texas A&M University, College Station, Texas, USA Report:2937-2931

Briaud J-L, Ting FC, Chen H, Gudavalli R, Perugu S, Wei G (1999b) *SRICOS: Prediction of scour rate in cohesive soils at bridge piers*. Journal of Geotechnical and Geoenvironmental Engineering 125:237-246

Brinch Hansen J (1970) *A revised and extended formula for bearing capacity*.

Buchheister JA (2009) *Verflüssigungspotenzial von reinem und siltigem Sand unter multiaxialer Belastung (in German)*. vol Ph.D. Dissertation No. 18312. ETH Zurich, Zurich, Switzerland. doi:10.3929/ethz-a-006020660

Bühler F, Perrey S, Anastasopoulos I, Adamidis O, Sakellariadis L, Sieber M (2019) *Element test characterisation of Perth sand*. ETH Zurich, Institute for Geotechnical Engineering

Caquot A, Kerisel J *Sur le terme de surface dans le calcul des fondations en milieu pulverulent*. In: Proc. 3rd Int. Conf. on SMFE, 1953. pp 336-337

Carrera A (2008) *Mechanical behaviour of Stava tailings*. Politecnico di Torino

Casagrande A (1936) *Characteristics of cohesionless soils affecting the stability of slopes and earth fills*. J Boston Society of Civil Engineers 23:13-32

Casagrande A (1976) *Liquefaction and cyclic deformation of sands: a critical review*. Harvard Soil Mechanics Series, Harvard University, Cambridge, Massachusetts

Cascante G, Vanderkooy J, Chung W (2003) *Difference between current and voltage measurements in resonant-column testing*. Canadian Geotechnical Journal 40:806-820

Castro G (1969) *Liquefaction of sands*. ph D Thesis, Harvard Soil Mech

Chabert J, Engeldinger P (1956) *Study of scour around bridge piers*. Rep Prepared for the Laboratoire National d'Hydraulique

Chen C-C, Wu W-H, Shih F, Wang S-W (2014) *Scour evaluation for foundation of a cable-stayed bridge based on ambient vibration measurements of superstructure*. NDT & E International 66:16-27

Chiew YM (1984) *Local scour at bridge piers*. ResearchSpace@ Auckland

Chortis G, Askarinejad A, Prendergast L, Li Q, Gavin K (2020) *Influence of scour depth and type on p–y curves for monopiles in sand under monotonic lateral loading in a geotechnical centrifuge*. Ocean Engineering 197:106838

Ciancimino A, Jones L, Sakellariadis L, Anastasopoulos I, Foti S (2021) *Experimental assessment of the performance of a bridge pier subjected to flood-induced foundation scour*. Géotechnique doi:http://doi.org/10.1680/jgeot.20.P.230

Ciancimino A et al. (2019) *Dynamic characterization of fine-grained soils in Central Italy by laboratory testing*. Bulletin of Earthquake Engineering:29 doi:https://doi.org/10.1007/s10518-019-00611-6

Coleman SE (2005) *Clearwater local scour at complex piers*. Journal of Hydraulic Engineering 131:330-334

Coop M (2005) *On the mechanics of reconstituted and natural sands*. In: Deformation characteristics of geomaterials. CRC Press, pp 36-65

Corti R, Diambra A, Wood DM, Escribano DE, Nash DFT (2016) *Memory Surface Hardening Model for Granular Soils under Repeated Loading Conditions*. Journal of Engineering Mechanics 142:04016102 doi:doi:10.1061/(ASCE)EM.1943-7889.0001174

Cox JA, O'Loughlin CD, Cassidy M, Bhattacharya S, Gaudin C, Bienen B (2014) *Centrifuge study on the cyclic performance of caissons in sand*. International Journal of Physical Modelling in Geotechnics 14:99-115

Dafalias YF, Manzari MT (2004) *Simple plasticity sand model accounting for fabric change effects*. Journal of Engineering mechanics 130:622-634

Darendeli MB (2001) *Development of a new family of normalized modulus reduction and material damping curves*. PhD Dissertation, University of Texas at Austin

Dargahi B (1990) *Flow field and local scouring around a cylinder*.

De Beer E (1970) *Experimental determination of the shape factors and the bearing capacity factors of sand*. Geotechnique 20:387-411

Delatte NJ (2008) *Beyond failure: Forensic case studies for civil engineers*. American Society of Civil Engineers,

Desrues J, Chambon R, Mokni M, Mazerolle F (1996) *Void ratio evolution inside shear bands in triaxial sand specimens studied by computed tomography*. Géotechnique 46:529-546

Dietz JW, Wittke W (1969) *Kolkbildung in feinen oder leichten Sohlmaterialien bei strömendem Abfluß*. Inst. für Wasserbau und Kulturtechnik, Versuchsanst. für Wasserbau" Theodor …,

Dobry R, Ladd R, Yokel FY, Chung RM, Powell D (1982) *Prediction of pore water pressure buildup and liquefaction of sands during earthquakes by the cyclic strain method*. vol 138. National Bureau of Standards Gaithersburg, MD,

Dobry R, Vucetic M (1987) *Dynamic properties and seismic response of soft clay deposits*.

Elsaid A, Seracino R (2014) *Rapid assessment of foundation scour using the dynamic features of bridge superstructure*. Construction and Building Materials 50:42-49

Ettema R (1980) *Scour at bridge piers*.

Ettema R, Melville BW, Constantinescu G (2011) *Evaluation of bridge scour research: Pier scour processes and predictions*.

Fotherby LM, Jones JS *The influence of exposed footings on pier scour depths*. In: Hydraulic Engineering, 1993. ASCE, pp 922-927

Foti S, Sabia D (2010) *Influence of foundation scour on the dynamic response of an existing bridge*. Journal of bridge engineering 16:295-304

Foti S, Sabia D (2011) *Influence of foundation scour on the dynamic response of an existing bridge*. Journal of Bridge Engineering 16:295-304

Fröhlich H (1936) *Beitrag zur Berechnung von Mastfundamenten (in German)*. Ernst & Sohn, Berlin

Gajan S, Kutter BL (2008) *Capacity, settlement, and energy dissipation of shallow footings subjected to rocking*. Journal of Geotechnical and Geoenvironmental Engineering 134:1129-1141

Gajan S, Kutter BL (2009) *Effects of moment-to-shear ratio on combined cyclic load-displacement behavior of shallow foundations from centrifuge experiments*. Journal of Geotechnical and Geoenvironmental Engineering 135:1044-1055

Gajan S, Kutter BL, Phalen JD, Hutchinson TC, Martin GR (2005) *Centrifuge modeling of load-deformation behavior of rocking shallow foundations*. Soil Dynamics and Earthquake Engineering 25:773-783

Gajo A (2010) *Hyperelastic modelling of small-strain stiffness anisotropy of cyclically loaded sand*. International journal for numerical and analytical methods in geomechanics 34:111-134

Gajo A (2017) *Fortran subroutine in a format of user defined material (UMAT) of implementation of the Severn-Trent model*.

Gajo A, Bigoni D (2008) *A model for stress and plastic strain induced nonlinear, hyperelastic anisotropy in soils*. International journal for numerical and analytical methods in geomechanics 32:833-861

Gajo A, Muir Wood D (1999a) *A kinematic hardening constitutive model for sands: the multiaxial formulation*. International journal for numerical and analytical methods in geomechanics 23:925-965

Gajo A, Muir Wood D (1999b) *Severn–Trent sand: a kinematic-hardening constitutive model: the q–p formulation*. Géotechnique 49:595-614

Ganesh Prasad G, Banerjee S (2013) *The impact of flood-induced scour on seismic fragility characteristics of bridges*. Journal of Earthquake Engineering 17:803-828

Garnier J et al. (2007) *Catalogue of scaling laws and similitude questions in geotechnical centrifuge modelling*. International Journal of Physical Modelling in Geotechnics 7:1

Gaudio D (2017) *Interazione dinamica terreno-struttura di pozzi di fondazione di pile di ponti e viadotti (in Italian)*. Sapienza, University of Rome

Gaudio D, Rampello S (2019) *The influence of soil plasticity on the seismic performance of bridge piers on caisson foundations*. Soil Dynamics and Earthquake Engineering 118:120-133

Gaudio D, Rampello S (2020) *Equivalent seismic coefficients for caisson foundations supporting bridge piers*. Soil Dynamics and Earthquake Engineering 129:105955

Gawin D, Sanavia L (2010) *Simulation of cavitation in water saturated porous media considering effects of dissolved air*. Transport in porous media 81:141

Gazetas G, Anastasopoulos I, Adamidis O, Kontoroupi T (2013) *Nonlinear rocking stiffness of foundations*. Soil Dynamics and Earthquake Engineering 47:83-91

Gazetas G, Apostolou M *Nonlinear soil–structure interaction: foundation uplifting and soil yielding*. In: Proceedings Third UJNR Workshop on Soil-Structure Interaction, 2004. pp 29-30

Gazetas G, Apostolou M, Anastasopoulos J *Seismic uplifting of foundations on soft soil, with examples from Adapazari (Izmit 1999 earthquake)*. In: BGA International Conference on Foundations: Innovations, observations, design and practice: Proceedings of the international conference organised by British Geotechnical Association and held in Dundee, Scotland on 2–5th September 2003, 2003. Thomas Telford Publishing, pp 37-49

Georgopoulos I, Vardoulakis I (2005) *Corrections on the specimen volume changes and axial force in the Wykeham Farrance triaxial cell*. Internal Report,

Graf WH (1998) *Fluvial hydraulics: Flow and transport processes in channels of simple geometry*. vol 551.483 G7.

Hancu S *Sur le calcul des affouillements locaux dams la zone des piles des ponts*. In: Proceedings of the 14th IAHR congress, Paris, France, 1971. pp 299-313

Hardin BO, Black WL (1966) *Sand stiffness under various triaxial stresses*. Journal of Soil Mechanics & Foundations Div 92

Hardin BO, Drnevich VP (1972) *Shear modulus and damping in soils: design equations and curves*. Journal of Soil Mechanics & Foundations Div 98:667-692

Hardin BO, Richart F (1963) *Elastic wave velocities in granular soils*. Journal of Soil Mechanics & Foundations Div 89

Hoffmans GJ, Verheij HJ (1997) *Scour manual*. vol 96. CRC press,

Hsu C-C, Vucetic M (2004) *Volumetric threshold shear strain for cyclic settlement*. Journal of geotechnical and geoenvironmental engineering 130:58-70

Hwang SK (1997) *Dynamic properties of natural soils*. PhD Dissertation, University of Texas at Austin

Imhof D (2004) *Risk assessment of existing bridge structures*. University of Cambridge

Isenhower WM (1979) *Torsional simple shear/resonant column properties of San Francisco Bay mud*. University of Texas at Austin

Isenhower WM, Stokoe K (1981) *Strain-rate dependent shear modulus of San Francisco Bay mud*. Paper presented at the Int Conf on Recent Advances in Geotechnical Earthquake Engineering and Soil Dynamics, St. Louis, Missouri,

Ishibashi I, Zhang X (1993) *Unified dynamic shear moduli and damping ratios of sand and clay*. Soils and Foundations 33:182-191

Ishihara K (1993) *Liquefaction and flow failure during earthquakes*. Geotechnique 43:351-451

Iwasaki T, Tatsuoka F, Takagi Y (1978) *Shear moduli of sands under cyclic torsional shear loading*. Soils and Foundations 18:39-56

Jain SC (1981) *Maximum clear-water scour around circular piers*. Journal of the Hydraulics Division 107:611-626

Jaky J (1944) *The coefficient of earth pressure at rest (A nyugalmi nyomas tenyezoje, In Hungarian)*. J Soc Hung Eng Arch (Magyar Mernok es Epitesz-Egylet Kozlonye):355-358

James R, Bransby PL (1970) *Experimental and theoretical investigations of a passive earth pressure problem*. Geotechnique 20:17-37

Johnson PA, Torrico EF (1994) *Scour around wide piers in shallow water*. Transportation Research Record:66-70

Jones JS, Kilgore RT, Mistichelli MP (1992) *Effects of footing location on bridge pier scour*. Journal of Hydraulic Engineering 118:280-290

Jones L, Anastasopoulos I *Development of an Apparatus for the Simulation of Coastal Structures Subjected to Tsunami*. In: Proceedings of the 16th European Conference on Earthquake Engineering (16ECEE), 2018. European Association for Earthquake Engineering, p 11482

Jones L, Anastasopoulos I (2020) *Miniaturised Tsunami Generator to model the Interaction of Tsunamis with Coastal infrastructure*. International Journal of Physical Modelling in Geotechnics:35 doi:10.1680/jphmg.19.00021

Kariyawasam K, Fidler P, Talbot J, Middleton C (2019) *Field assessment of ambient vibration-based bridge scour detection*. Structural health monitoring Stanford, CA, USA:374-338

Kariyawasam KD, Middleton CR, Madabhushi G, Haigh SK, Talbot JP (2020) *Assessment of bridge natural frequency as an indicator of scour using centrifuge modelling*. Journal of Civil Structural Health Monitoring 10:861-881

Kennedy JF (1995) *The albert shields story*. Journal of Hydraulic Engineering 121:766-772

Khosronejad A, Kang S, Sotiropoulos F (2012) *Experimental and computational investigation of local scour around bridge piers*. Advances in Water Resources 37:73-85

Kim DS (1991) *Deformational characteristics of soils at small to intermediate strains from cyclic test*. PhD dissertation, University of Texas at Austin

Kirkpatrick W, Belshaw D (1968) *On the interpretation of the triaxial test*. Geotechnique 18:336-350

Klinga JV, Alipour A (2015) *Assessment of structural integrity of bridges under extreme scour conditions*. Engineering Structures 82:55-71

Kodaka T, Higo Y, Kimoto S, Oka F (2007) *Effects of sample shape on the strain localization of water-saturated clay*. International journal for numerical and analytical methods in geomechanics 31:483-521

Kokkali P, Anastasopoulos I, Abdoun T, Gazetas G *Static and cyclic rocking on sand: centrifuge versus reduced-scale 1 g experiments*. In: Geotechnical Earthquake Engineering: Géotechnique Symposium in Print 2015, 2015. ICE Publishing, pp 155-170

Kokusho T (1980) *Cyclic triaxial test of dynamic soil properties for wide strain range*. Soils and foundations 20:45-60

Kokusho T, Yoshida Y, Esashi Y (1982) *Dynamic properties of soft clay for wide strain range*. Soils and Foundations 22:1-18

Konrad J-M (1998) *Sand state from cone penetrometer tests: a framework considering grain crushing stress*. Geotechnique 48:201-215

Konrad J (1993) *Undrained response of loosely compacted sands during monotonic and cyclic compression tests*. Géotechnique 43:69-89

Kowalczyk P, Gajo A *Effects of Pore Pressure on Wandering in Structural Natural Frequency*. In: International Conference of the International Association for Computer Methods and Advances in Geomechanics, 2020. Springer, pp 715-722

Kulhawy FH (1991) *Drilled shaft foundations*. In: Foundation engineering handbook. Springer, pp 537-552

Lade P *Localization effects in triaxial tests on sand*. In: Luger PAVaHJ (ed) International Union of Theoretical and Applied Mechanics. Symposium on Deformation and Failure of Granular Materials, Rotterdam, 1982. Balkema, pp 461-472

Lagasse P, Schall J, Johnson F, Richardson E, Chang F (1995) *Stream stability at highway structures (2d ed.): Federal Highway Administration, Hydraulic Engineering Circular No. 20*. Publication FHWA-IP-90-014, Washington, DC

Lagasse PF, Richardson EV (2001) *ASCE compendium of stream stability and bridge scour papers*. Journal of Hydraulic Engineering 127:531-533

Lancellotta R, Ciancimino A, Costanzo A, Foti S (2020) *Progettazione geotecnica: Secondo l'Eurocodice 7 e le Norme Tecniche per le Costruzioni 2018 (in Italian)*. HOEPLI EDITORE,

Lanzano G, Mancini M, Fabbrocino G, Santucci De Magistris F *Modellazione di fondazioni a cassone per la valutazione e adeguamento sismico dei ponti esistenti*. In: IARG 2011, Incontro Annuale dei Ricercatori di Geotecnica, 2011.

Lanzo G, Vucetic M, Doroudian M (1997) *Reduction of shear modulus at small strains in simple shear*. Journal of Geotechnical and Geoenvironmental Engineering 123:1035-1042

Laue J, Nater P, Springman SM *Preparation of soil samples in drum centrifuges*. In: International Conference on Physical Modelling in Geotechnics/ICPGM'02, St. John's, New Foundland, Canada, 10-12 July 2002, 2002. Balkema, pp 143-148

Laursen EM (1963) *An analysis of relief bridge scour*. Journal of the Hydraulics Division 89:93-118

Li Q, Askarinejad A, Gavin K (2020) *The impact of scour on the lateral resistance of wind turbine monopiles: an experimental study*. Canadian Geotechnical Journal

Li S, He S, Li H, Jin Y (2017) *Scour depth determination of bridge piers based on time-varying modal parameters: application to Hangzhou Bay bridge*. Journal of Bridge Engineering 22:04017107

Liang F, Wang C, Yu X (2019) *Widths, types, and configurations: Influences on scour behaviors of bridge foundations in non-cohesive soils*. Marine Georesources & Geotechnology 37:578-588

Liang F, Zhang H, Huang M (2017) *Influence of flood-induced scour on dynamic impedances of pile groups considering the stress history of undrained soft clay*. Soil Dynamics and Earthquake Engineering 96:76-88

Lin C, Bennett C, Han J, Parsons RL (2010) *Scour effects on the response of laterally loaded piles considering stress history of sand*. Computers and Geotechnics 37:1008-1014

Lin C, Han J, Bennett C, Parsons RL (2014a) *Behavior of laterally loaded piles under scour conditions considering the stress history of undrained soft clay*. Journal of Geotechnical and Geoenvironmental Engineering 140:06014005

Lin C, Han J, Bennett C, Parsons RL (2014b) *Case history analysis of bridge failures due to scour*. In: Climatic effects on pavement and geotechnical infrastructure. pp 204-216

Liu H-K (1957) *Mechanics of sediment-ripple formation*. Journal of the Hydraulics Division 83:1-23

Liu H (1958) *Closure: Mechanics of sediment ripple formation*. Journal of the Hydraulics Division 84:5-31

Liu HY, Abell JA, Diambra A, Pisanò F (2018) *Modelling the cyclic ratcheting of sands through memory-enhanced bounding surface plasticity*. Géotechnique 69:783-800 doi:10.1680/jgeot.17.P.307

Lo Presti D, Pallara O, Lancellotta R, Armandi M, Maniscalco R (1993) *Monotonic and cyclic loading behavior of two sands at small strains*. Geotechnical Testing Journal 16:409-424

Lo Presti DC *Proprietà dinamiche dei terreni*. In: XIV CGT, Torino, 1989. Politecnico di Torino, pp 1-62

Lo Presti DC *Discussion on" threshold strain in Soils"*. In: X ECSMFE on Deformation of Soils and Displacements of Structures, Firenze, Italy, 1991. AA Balkema, pp 1282-1283

Lo Presti DC, Jamiolkowski M, Pallara O, Cavallaro A, Pedroni S (1997) *Shear modulus and damping of soils*. Geotechnique 47:603-617

Loli M, Knappett JA, Brown MJ, Anastasopoulos I, Gazetas G (2014) *Centrifuge modeling of rocking-isolated inelastic RC bridge piers*. Earthquake engineering & structural dynamics 43:2341-2359

Macky G (1990) *Survey of roading expenditure due to scour*. CR 90_09, Department of Scientific and Industrial Research, Hydrology Centre, Christchurch, New Zealand

Madabhushi G (2014) *Centrifuge modelling for civil engineers*. CRC Press,
Matešić L, Vucetic M (2003) *Strain-rate effect on soil secant shear modulus at small cyclic strains*. Journal of geotechnical and geoenvironmental engineering 129:536-549
MathWorks (2020) *MATLAB and Curve Fitting Toolbox*. Release 2018a edn., Natick, Massachusetts, United States
May R, Ackers J, Kirby A (2002) *Manual on scour at bridges and other hydraulic structures*. vol 551. Ciria London,
McManus K, Davis R (1997) *Dilation-induced pore fluid cavitation in sands*. Géotechnique 47:173-177
Melville B, Sutherland A (1988) *Design method for local scour at bridge piers*. Journal of Hydraulic Engineering 114:1210-1226
Melville BW (1997) *Pier and abutment scour: integrated approach*. Journal of hydraulic Engineering 123:125-136
Melville BW, Chiew Y-M (1999) *Time scale for local scour at bridge piers*. Journal of Hydraulic Engineering 125:59-65
Melville BW, Coleman SE (2000) *Bridge scour*. Water Resources Publication, Highlands Ranch, CO, USA.
Melville BW, Raudkivi AJ (1996) *Effects of foundation geometry on bridge pier scour*. Journal of Hydraulic Engineering 122:203-209
Meng J, Rix G (2003) *Reduction of equipment-generated damping in resonant column measurements*. Géotechnique 53:503-512
Menq F-y (2003) *Dynamic properties of sandy and gravelly soils*.
Meyerhof G (1951) *The ultimate bearing capacity of foudations*. Geotechnique 2:301-332
Molina-Gómez F, da Fonseca AV, Ferreira C, Camacho-Tauta J (2020) *Dynamic properties of two historically liquefiable sands in the Lisbon area*. Soil Dynamics and Earthquake Engineering 132:106101
Morales P (2015) *River dyke failure modeling under transient water conditions*. vol 247. vdf Hochschulverlag AG,
Moreno M, Maia R, Couto L (2016) *Prediction of equilibrium local scour depth at complex bridge piers*. Journal of Hydraulic Engineering 142:04016045
Mortezaie A, Vucetic M (2016) *Threshold shear strains for cyclic degradation and cyclic pore water pressure generation in two clays*. Journal of Geotechnical and Geoenvironmental Engineering 142:04016007
Muir Wood D (2004) *Geotechnical modelling*. E & FN Spon,
Muntasir Billah A, Shahria Alam M (2015) *Seismic fragility assessment of highway bridges: a state-of-the-art review*. Structure and infrastructure engineering 11:804-832
Muraro S, Jommi C (2019) *Implication of end restraint in triaxial tests on the derivation of stress–dilatancy rule for soils having high compressibility*. Canadian Geotechnical Journal 56:840-851
Nater P (2005) *Belastungs- und Verformungsverhalten von geschichteten Bodensystemen unter starren Kreisfundationen. (in German)*. ETH Zurich
Neill CR (1967) *Mean-velocity criterion for scour of coarse uniform bed-material*. Paper presented at the 12th IAHR Congress, Fort Collins, CO,
Neill CR (1968) *A re-examination of the beginning of movement for coarse granular bed materials*. Hydraulics Research Station Wallingford, England,
Nemat-Nasser S (1980) *On behavior of granular materials in simple shear*. Soils and Foundations 20:59-73

Nemat-Nasser S, Tobita Y (1982) *Influence of fabric on liquefaction and densification potential of cohesionless sand*. Mechanics of Materials 1:43-62

Ni S-H (1987) *Dynamic properties of sand under true triaxial stress states from resonant column/torsional shear tests*. Ph D Dissertation, The University of Texas at Austin

Olson RE, Campbell LM, Lee K, Seed HB, Turnbull JM, Poulos S (1964) *Discussion of "Importance of Free Ends in Triaxial Testing"*. Journal of the Soil Mechanics and Foundations Division 90:167-179

Ovesen NK *The scaling law relationship - Panel discussion*. In: Proc. 7th European Conference on Soil Mechanics and Foundation Engineering, Brighton, 1979. pp 319-323

Pallara O (1995) *Comportamento sforzi-deformazioni di due sabbie soggette a sollecitazioni monotone e cicliche (in Italian)*. Politecnico di Torino

Panagiotidou AI, Gazetas G, Gerolymos N (2012) *Pushover and seismic response of foundations on stiff clay: analysis with p-delta effects*. Earthquake Spectra 28:1589-1618

Parola A, Mahavadi S, Brown B, El Khoury A (1996) *Effects of rectangular foundation geometry on local pier scour*. Journal of Hydraulic Engineering 122:35-40

Pecker A *Aseismic foundation design process, lessons learned from two major projects: the Vasco de Gama and the Rion Antirion bridges*. In: ACI International Conference on Seismic Bridge Design and Retrofit. La Jolla, California, 2003.

Poulos SJ (1981) *The steady state of deformation*. Journal of Geotechnical and Geoenvironmental Engineering 107

Prandtl L (1921) *Uber die Harte plastischer Korper. Nachr. Ges. Wiss. Goettingen, Math*. Phys Kl:7485

Prendergast LJ, Gavin K (2014) *A review of bridge scour monitoring techniques*. Journal of Rock Mechanics and Geotechnical Engineering 6:138-149

Prendergast LJ, Hester D, Gavin K, O'sullivan J (2013) *An investigation of the changes in the natural frequency of a pile affected by scour*. Journal of Sound and Vibration 332:6685-6702

Priestly M, Seible F, Calvi G (1996) *Seismic Design and Retrofit of Bridges*. John Wiley & Sons, Chichester,

Puci I (1999) *Un'indagine di laboratorio sul comportamento non drenato della sabbia di Toyoura (in Italian)*. Politecnico di Torino

Qi M, Li J, Chen Q (2016a) *Comparison of existing equations for local scour at bridge piers: parameter influence and validation*. Natural Hazards 82:2089-2105

Qi WG, Gao F, Randolph MF, Lehane BM (2016b) *Scour effects on p–y curves for shallowly embedded piles in sand*. Géotechnique 66:648-660

Randolph M, Hope S *Effect of cone velocity on cone resistance and excess pore pressures*. In: Effect of cone velocity on cone resistance and excess pore pressures, 2004. Yodogawa Kogisha Co. Ltd, pp 147-152

Remaud D (1999) *Pieux sous charges latérales: étude expérimentale de l'effet de groupe*. Université de Nantes

Richardson E, Davis S (2001) *Evaluating scour at bridges: Hydraulic Engineering Circular No. 18*. Washington DC, USA

Richart FE, Hall JR, Woods RD (1970) *Vibrations of soils and foundations*.

Roscoe KH, Schofield A, Wroth aP (1958) *On the yielding of soils*. Geotechnique 8:22-53

Rotisciani G, Miliziano S (2014) *Guidelines for calibration and use of the Severn-Trent sand model in modeling cantilevered wall-supported excavations*. International Journal of Geomechanics 14:04014029

Rouse H (1939) *Experiments on the mechanics of sediment suspension*.

Rowe P, Barden L, Lee I (1964) *Energy components during the triaxial cell and direct shear tests*. Geotechnique 14:247-261

Rowe PW (1962) *The stress-dilatancy relation for static equilibrium of an assembly of particles in contact*. Proceedings of the Royal Society of London Series A Mathematical and Physical Sciences 269:500-527

Rowe PW, Barden L (1964) *Importance of free ends in triaxial testing*. Journal of the Soil Mechanics and Foundations Division 90:1-27

Santamarina JC, Rinaldi VA, Fratta D, Klein KA, Wang Y-H, Cho GC, Cascante G (2005) *A survey of elastic and electromagnetic properties of near-surface soils*. Near-surface geophysics 1:71-87

Schwerzmann N (2019) *Centrifuge study on pile foundations under axial loading*. ETH Zurich

Seed H, Idriss I (1970) *Soil moduli and damping factors for dynamic response analyses, Report no. EERC 70-10*. Earthquake Engineering Research Center, University of California, Berkeley, California

Seed HB, Wong RT, Idriss I, Tokimatsu K (1986) *Moduli and damping factors for dynamic analyses of cohesionless soils*. Journal of geotechnical engineering 112:1016-1032

Shen HW, Schneider VR, Karaki S (1969) *Local scour around bridge piers*. Journal of the Hydraulics Division

Sheng D, Westerberg B, Mattsson H, Axelsson K (1997) *Effects of end restraint and strain rate in triaxial tests*. Computers and Geotechnics 21:163-182

Sheppard D, Melville B, Demir H (2014) *Evaluation of existing equations for local scour at bridge piers*. Journal of Hydraulic Engineering 140:14-23

Sheppard D, Renna R (2005) *Bridge scour manual*. Florida Department of Transportation, Florida

Shibuya S, Mitachi T, Fukuda F, Degoshi T (1995) *Strain rate effects on shear modulus and damping of normally consolidated clay*. Geotechnical testing journal 18:365-375

Shields A (1936) *Application of similarity principles and turbulence research to bed-load movement*.

Shinozuka M, Feng MQ, Lee J, Naganuma T (2000) *Statistical analysis of fragility curves*. Journal of engineering mechanics 126:1224-1231

Shockley WG, Ahlvin RG *Nonuniform conditions in triaxial test specimens*. In: Research conference on shear strength of cohesive soils, 1960. ASCE, pp 341-357

Silver ML, Seed HB (1971) *Volume changes in sands during cyclic loading*. Journal of Soil Mechanics & Foundations Div

Springman SM, Laue J, Boyle R, White J, Zweidler A (2001) *The ETH Zurich geotechnical drum centrifuge*. International Journal of Physical Modelling in Geotechnics 1:59-70

Stokoe K, Darendeli M, Andrus R, Brown L *Dynamic soil properties: laboratory, field and correlation studies*. In: Proc. 2nd Int. Conf. Earthquake Geotech. Engg, 1999. pp 811-846

Stoll RD, Kald L (1977) *Threshold of dilation under cyclic loading*. Journal of the Geotechnical Engineering Division 103:1174-1178

Storey C, Delatte N (2003) *Lessons from the collapse of the schoharie creek bridge*. In: Forensic Engineering (2003). pp 158-167

Sumer BM, Hatipoglu F, Fredsøe J (2007) *Wave scour around a pile in sand, medium dense, and dense silt*. Journal of waterway, port, coastal, and ocean engineering 133:14-27

Systèmes Dassault (2020) *ABAQUS/CAE software package*.

Tabata K, Vucetic M *Threshold shear strain for cyclic degradation of three clays*. In: 5th Int. Conf. on Recent Advances in Geotechnical Earthquake Engineering and Soil Dynamics, Missouri Univ. of Science and Technology, San Diego, May 24th - May 29th 2010.

Taeseri D, Laue J, Anastasopoulos I (2018) *Non-linear rocking stiffness of embedded foundations in sand*. Géotechnique:1-16

Tanasić N, Hajdin R (2018) *Management of bridges with shallow foundations exposed to local scour*. Structure and Infrastructure Engineering 14:468-476

Tasiopoulou P, Chaloulos Y, Gerolymos N, Giannakou A, Chacko J (2021) *Cyclic lateral response of OWT bucket foundations in sand: 3D coupled effective stress analysis with Ta-Ger model*. Soils and Foundations

Tasiopoulou P, Gerolymos N (2016a) *Constitutive modeling of sand: Formulation of a new plasticity approach*. Soil Dynamics and Earthquake Engineering 82:205-221

Tasiopoulou P, Gerolymos N (2016b) *Constitutive modelling of sand: a progressive calibration procedure accounting for intrinsic and stress-induced anisotropy*. Géotechnique 66:754-770

Taylor D (1941) *Cylindrical compression research program on stress-deformation and strength characteristics of soils*. MIT 7th Progress Report to Water Experiments Station

Taylor DW (1942) *Research on consolidation of clays*. vol 82. Massachusetts Institute of Technology,

Terzaghi K (1943) *Theoretical soil mechanics*. John Wiley & Sons, New York

Thornton-Tomasetti (1987) *Overview Report, Investigation of the New York State Thruway Schoharie Creek Bridge Collapse*. Thornton-Tomasetti,

Toth E, Brandimarte L (2011) *Prediction of local scour depth at bridge piers under clear-water and live-bed conditions: comparison of literature formulae and artificial neural networks*. Journal of Hydroinformatics 13:812-824

Tsujimoto T (1987) *Local scour around bridge piers in rivers and its protection works*. 金沢大学工学部紀要 20:p11-21

Tu W, Huang M, Gu X, Chen H-P (2020) *Nonlinear dynamic behavior of laterally loaded composite caisson-piles foundation under scour conditions*. Marine Georesources & Geotechnology 38:1265-1280

Verdugo R, Ishihara K (1996) *The steady state of sandy soils*. Soils and foundations 36:81-91

Vesic AS (1973) *Analysis of ultimate loads of shallow foundations*. ASCE Journal of Soil Mechanics & Foundations Div 99:45-73

Vesic AS (1975) *Bearing capacity of shallow foundations*. In: ed.s WaF (ed) Foundation engineering handbook. Van Nostran Reinhold, New York, pp 121-147

Vucetic M *Soil properties and seismic response*. In: Proc. 10th World Conference on Earthquake Engineering, 1992. pp 1199-1204

Vucetic M (1994) *Cyclic threshold shear strains in soils*. Journal of Geotechnical engineering 120:2208-2228

Vucetic M, Dobry R (1991) *Effect of soil plasticity on cyclic response*. Journal of geotechnical engineering 117:89-107

Wang Y-H, Cascante G, Santamarina JC (2003) *Resonant column testing: the inherent counter emf effect*. Geotechnical Testing Journal 26:342-352

Wang Z, Dueñas-Osorio L, Padgett JE (2014a) *Influence of scour effects on the seismic response of reinforced concrete bridges*. Engineering structures 76:202-214

Wang Z, Padgett JE, Dueñas-Osorio L (2014b) *Risk-consistent calibration of load factors for the design of reinforced concrete bridges under the combined effects of earthquake and scour hazards*. Engineering Structures 79:86-95

Wang Z, Song W, Li T *Combined fragility surface analysis of earthquake and scour hazards for bridge*. In: Proceedings of the 15th World Conference on Earthquake Engineering, Lisbon, Portugal, 2012. pp 24-28

Wardhana K, Hadipriono FC (2003) *Analysis of recent bridge failures in the United States*. Journal of performance of constructed facilities 17:144-150

Whitman RV, Healy KA (1962) *Shear Strength of Sands During Rapid Loadings*. Journal of the Soil Mechanics and Foundations Division 88:99-132

WJE W, Janney, Elstner Associates , MR MRCE (1987) *Collapse of Thruway Bridge at Sehoharie Creek, Final Report*. New York State Thruway Authority,

Woods RD *Measurement of dynamic soil properties*. In: From Volume I of Earthquake Engineering and Soil Dynamics--Proceedings of the ASCE Geotechnical Engineering Division Specialty Conference, June 19-21, 1978, Pasadena, California. Sponsored by Geotechnical Engineering Division of ASCE in cooperation with:, 1978. vol Proceeding.

Yalin MS (1972) *Mechanics of sediment transport [by] M. Selim Yalin*.

Yang Z (2005) *Investigation of fabric anisotropic effects on granular soil behavior*. Hong Kong University of Science and Technology

Youd TL (1972) *Compaction of sands by repeated shear straining*. Journal of Soil Mechanics & Foundations Div 98

Yu P, Richart Jr F (1984) *Stress ratio effects on shear modulus of dry sands*. Journal of Geotechnical Engineering 110:331-345

Zafeirakos A, Gerolymos N (2013) *On the seismic response of under-designed caisson foundations*. Bulletin of Earthquake Engineering 11:1337-1372

Zafeirakos A, Gerolymos N (2014) *Towards a seismic capacity design of caisson foundations supporting bridge piers*. Soil Dynamics and Earthquake Engineering 67:179-197

Zafeirakos A, Gerolymos N (2016) *Bearing strength surface for bridge caisson foundations in frictional soil under combined loading*. Acta Geotechnica 11:1189-1208

Zanke U (1978) *Zusammenhänge zwischen Strömung und Sedimenttransport. Teil 1: Berechnung des Sedimenttransportes-allgemeiner Fall*. EV,

Zhang C, Zhang X, Huang M, Tang H (2019) *Responses of caisson-piles foundations to long-term cyclic lateral load and scouring*. Soil Dynamics and Earthquake Engineering 119:62-74

Zhu B, Byrne B, Houlsby G (2013) *Long-term lateral cyclic response of suction caisson foundations in sand*. Journal of Geotechnical and Geoenvironmental Engineering 139:73-83